GDSA Repository Systems Analysis Investigations in FY 2023

Spent Fuel and Waste Disposition

Sandia National Laboratories

Additional Disclaimer for work covering the feasibility of Direct Disposal of Dual Purpose Canisters:

<p style="text-align:center">**APPENDIX E**</p>
<p style="text-align:center">**NFCSC DOCUMENT COVER SHEET[1]**</p>

Name/Title of
Deliverable/Milestone/Revision No.: GDSA Repository Systems Analysis Investigations in FY
2023

Work Package Title and Number: GDSA Repository Systems Analysis SF-23SN01030409

Work Package WBS Number: 1.08.01.03.04

Responsible Work Package Manager: Tara LaForce _Tara LaForce_____ (Name/Signature)

Date Submitted

Quality Rigor Level for Deliverable/Milestone[2]	☐ QRL-1 ☐ Nuclear Data	☐ QRL-2	☒ QRL-3	☐ QRL-4 Lab QA Program[3]

This deliverable was prepared in accordance with

_____ *(Participant/National Laboratory Name)*

QA program which meets the requirements of

    ☐ DOE Order 414.1   ☐ NQA-1   ☐ Other

This Deliverable was subjected to:

☒ Technical Review   ☐ Peer Review

Technical Review (TR) **Review Documentation Provided**	**Peer Review (PR)** **Review Documentation Provided**
☒ Signed TR Report or,	☐ Signed PR Report or,
☐ Signed TR Concurrence Sheet or,	☐ Signed PR Concurrence Sheet or,
☒ Signature of TR Reviewer(s) below	☐ Signature of PR Reviewer(s) below

Name and Signature of Reviewers

Kristopher Kuhlman _K. Kuhlman_____ _____

_____ _____

_____ _____

NOTE 1: *Appendix E should be filled out and submitted with the deliverable. Or, if the PICS:NE system permits, completely enter all applicable information in the PICS:NE Deliverable Form. The requirement is to ensure that all applicable information is entered either in the PICS:NE system or by using the NFCSC Document Cover Sheet.*

- *In some cases there may be a milestone where an item is being fabricated, maintenance is being performed on a facility, or a document is being issued through a formal document control process where it specifically calls out a formal review of the document. In these cases, documentation (e.g., inspection report, maintenance request, work planning package documentation or the documented review of the issued document through the document control process) of the completion of the activity, along with the Document Cover Sheet, is sufficient to demonstrate achieving the milestone.*

NOTE 2: *If QRL 1, 2, or 3 is not assigned, then the QRL 4 box must be checked, and the work is understood to be performed using laboratory QA requirements. This includes any deliverable developed in conformance with the respective National Laboratory / Participant, DOE or NNSA-approved QA Program.*

NOTE 3: *If the lab has an NQA-1 program and the work to be conducted requires an NQA-1 program, then the QRL-1 box must be checked in the work Package and on the Appendix E cover sheet and the work must be performed in accordance with the Lab's NQA-1 program. The QRL-4 box should not be checked*

EXECUTIVE SUMMARY

This report describes specific activities in the Fiscal Year (FY) 2023 associated with the Geologic Disposal Safety Assessment (GDSA) Repository Systems Analysis (RSA) work package funded by the Spent Fuel and Waste Science and Technology (SFWST) Campaign of the U.S. Department of Energy Office of Nuclear Energy (DOE-NE), Office of Spent Fuel and Waste Disposition (SFWD).

High-level purpose of this work:

The overall objective of the GDSA RSA work package is to develop generic deep geologic repository concepts and system performance assessment (PA) models in several potential host-rock environments (crystalline, argillite, salt, and unsaturated alluvium), and to simulate and analyze these generic repository concepts and models using the GDSA Framework toolkit and other tools as needed. The specific goals are to:

- Develop the technical bases for representing generic repository reference case concepts for deep geologic disposal in the four potential host-rocks, including potential disposal of high-decay heat waste packages.

- Reference case development, simulation, and analysis for potential host-rocks, including coupled processes in the engineered barrier system (EBS), disturbed rock zone (DRZ) and natural barrier system as needed. This goal includes:

    o Incorporating relevant near field and far field processes as well as geologic/material properties and stratigraphic information developed in conjunction with geologic framework models (GFMs).

    o Supporting and collaborating closely with the other GDSA work packages, in particular the Framework, PFLOTRAN Development, Sensitivity Analysis Uncertainty Quantification (SA/UQ), and Los Alamos National Laboratories (LANL) Geologic Modeling work packages.

    o Exercising the simulation tools and methodologies under development by GDSA for PA modelling.

- Lead and participate in international collaborations in reference case development simulation and analysis.

FY23 Accomplishments:

The main accomplishments in FY23 are:

- Lead Task F of the international collaboration DECOVALEX-2023 (https://decovalex.org) on PA modelling from 2020-present (Section 2).

    o The main deliverable this financial year has been a publicly available task specification that contains all information necessary to create simplified PA models of a crystalline and a domal salt repository in collaboration with our 13 international partner teams. This is in a separate report (LaForce et al., 2023a).

    o Simulation and analysis of the final Sandia National Laboratory (SNL) in-house models for the DECOVALEX crystalline (Section 2.2) and domal salt (Section 2.3) conceptual models.

- For FY23 the RSA and SA/UQ work packages decided to focus on the development of a new argillite (shale) PA model. The updated model (Section 3.1) includes updated model parameters,

additional simulation quantities of interest, and new waste package heat inventories. The results of this work include:

- o Deterministic modelling of scenarios that include radionuclide heat representative of the spread of in-inventory dual-purpose canisters (DPCs) in the United States (Section 3.2). The results of this study demonstrate that layout of the waste packages impacts radionuclide transport.

- o Successful execution of all simulation model runs for an uncertainty study utilizing the Next Generation Workflow (NGW) (Section 3.3) in support of the SA/UQ work package.

- Collaborative development of a workflow to integrate the geological models of unsaturated alluvium developed by the LANL GDSA-Geologic Modeling work package into RSA disposal simulations (Section 4.1). Results of this work will be in a separate report (LaForce et al., 2023b)

- Utilization of the in-house automated meshing software VoroCrust in a prototype NGW sensitivity analysis that utilizes nested sampling to incorporate multiple realizations of large-scale geological features as well as sampled flow properties (Section 5). This work indicates that, for the prototype model, the subsurface geological structure has a first-order impact on tracer distribution in the subsurface.

- Continued development and maintenance of VoroCrust and experimentation with simulations on the VoroCrust meshes.

- o Creation of a beta capability to mesh individual waste packages (Section 6.1).

- o Testing the accuracy and speed of simulations using our in-house simulator PFLOTRAN on VoroCrust meshes and comparison of the results with the results on hexahedral meshes that have traditionally been used for GDSA RSA calculations (Section 6.2). The results of this study indicate that simulations on VoroCrust meshes are always reasonably accurate, even on examples where it is not possible to achieve accurate simulations on hexahedral meshes.

Next Steps:

- Major deliverables for this project in FY24 will be the final DECOVALEX reports and conference presentations. There will be several journal publications in FY24 associated with each task in addition to the two final reports. We have also requested funding to continue the two subtasks in DECOVALEX-2027, which would allow us to continue to lead this international collaboration for a further four years.

- Further development of the shale PA case in collaboration with the SA/UQ work package to include distributions of radionuclide inventory and DPC thermal output to be representative of in inventory DPCs in the uncertainty workflow.

- Continue to test VoroCrust meshing and incorporate it into increasingly realistic NGW uncertainty studies of the shale PA case.

ACKNOWLEDGEMENTS

This page is intentionally left blank.

CONTENTS

This page is intentionally left blank.

LIST OF FIGURES

LIST OF TABLES

VERSION INFORMATION

This report is an annual update of a series of Geologic Disposal Safety Assessment (GDSA) Repository Systems Analysis (RSA) status reports. It describes specific activities in the FY23. RSA has also written two M4 reports in FY23, SAND2022-10439R and SANDXXXX. There have been four previous RSA status updates 2019-2022: SAND2019-11942R, SAND2020-12028 R, SAND2021-11691 R, and SAND2022-12771 R. This report presents new results of the RSA work package, referencing materials from the previous reports and other GDSA reports whenever possible without repeating them.

This page is intentionally left blank.

ABREVIATIONS/ACRONYMS

AMSL	above mean sea level
DCDM	dual continuum disconnected matrix
DECOVALEX	DEveloping COupled models and their VALidation against Experiments
DFN	discrete fracture networks
DOE-NE	U.S. Department of Energy Office of Nuclear Energy
DPC	dual-purpose canister
DRZ	disturbed rock zone
EBS	engineered barrier system
ECPM	equivalent continuous porous medium
GDSA	Geologic Disposal Safety Assessment
GFM	geologic framework model
GIRT	Global Implicit Reactive Transport
HLW	high-level radioactive waste
HPC	high-performance computer
LANL	Los Alamos National Laboratory
LHS	Latin Hypercube Sampling
NGW	next generation workflow
NWT	nuclear waste transport
PA	performance assessment
PWR	pressurized water reactor
QoI	quantities of interest
R&D	research and development
RD&D	research, development, and demonstration
ROM	run-of-mine
RSA	repository systems analysis
SA/UQ	Sensitivity Analysis and Uncertainty Quantification
SFWD	Spent Fuel and Waste Disposition
SFWST	Spent Fuel and Waste Science and Technology
SNF	spent nuclear fuel
SNL	Sandia National Laboratories
UFD	Used Fuel Disposition
UQ	uncertainty quantification
UZ	unsaturated zone

This page is intentionally left blank.

1. INTRODUCTION

This report describes specific activities in the Fiscal Year (FY) 2023 associated with the Geologic Disposal Safety Assessment (GDSA) Repository Systems Analysis (RSA) work package funded by the Spent Fuel and Waste Science and Technology (SFWST) Campaign of the U.S. Department of Energy Office of Nuclear Energy (DOE-NE), Office of Spent Fuel and Waste Disposition (SFWD).

The SFWST Campaign is conducting research and development (R&D) on geologic disposal of spent nuclear fuel (SNF) and high-level radioactive waste (HLW). Two of the highest priorities for SFWST disposal R&D are design concept development and disposal system performance assessment (PA) modeling (DOE 2012, Table 6). Generic design (or reference-case) concepts being considered for SNF and HLW disposal since 2010 include mined repository concepts in bedded salt, argillite (clay, shale, or mudstone), and crystalline rock. Additional investigations began five years ago on a potential mined repository in unsaturated alluvium. Since 2019, the PA R&D has given a greater emphasis to simulating disposal of higher decay-heat waste packages containing 21, 24, or 37 pressurized water reactor (PWR) assemblies.

Prior development and accomplishments are summarized at a high-level in Mariner et al. (2019), with much more detail provided in Mariner et al. (2018), Mariner et al. (2017), Mariner et al. (2016), Mariner et al. (2015), Sevougian et al. (2016), Sevougian et al. (2014), Sevougian et al. (2013), Sevougian et al. (2012), Freeze et al. (2013), and Vaughn et al. (2013). Previous reports specific to the RSA work package that are the building blocks for the present research are Sevougian et al. (2019a), Sevougian et al. (2019b), LaForce et al. (2020), LaForce et al. (2021), and LaForce et al. (2022a).

Sassani et al. (2021) details a 5-year research R&D plan that "provides a strategic guide to the work within the research, development, and demonstration (RD&D) technical areas, focusing on the highest priority technical thrusts" for the SFWST Campaign. The plan discusses the need to focus on four areas (Sassani et al., 2021):

- capabilities development and demonstration,

- international collaboration and underground research laboratories,

- engineered barrier system (EBS) representations, and

- evaluation of potential direct disposal of large, high-energy waste packages.

Figure 1-1 shows the flow of information and the role of PA in RD&D. The objective of the GDSA RSA work package is to develop generic deep geologic repository concepts and PA models in line with the current 5-year plan (Sassani et al., 2021) for several host-rock environments, and to simulate and analyze these generic repository concepts and models using the GDSA Framework toolkit shown in Figure 1-2 (Mariner et al., 2020), and other tools as needed, in particular the Next Generation Workflow (NGW). The RSA work package focuses primarily on the reference case components, technical bases, and process models, as indicated by the dashed blue lines in Figure 1-1. The long-term goals of the RSA work package are to:

- Develop the technical bases for representing generic repository reference case concepts for deep geologic disposal in the four potential host-rocks, including potential disposal of high-decay heat waste packages.

- Reference case development, simulation, and analysis for potential host-rocks, including coupled processes in the EBS, disturbed rock zone (DRZ) and natural barrier system as needed. This goal includes:

- o Incorporating relevant near field and far field processes as well as geologic/material properties and stratigraphic information developed in conjunction with geologic framework models (GFMs).

  - o Supporting and collaborating closely with the other GDSA work packages, in particular the Framework, PFLOTRAN Development, Sensitivity Analysis Uncertainty Quantification (SA/UQ), and Los Alamos National Laboratories (LANL) Geologic Modeling work packages.

  - o Exercising the simulation tools and methodologies under development by GDSA for PA modelling.

- Lead and participate in international collaborations in reference case development simulation, and analysis.

The piece of the GDSA framework addressed by RSA in FY23 is flow and transport modelling and investigating integration of improved geology and VoroCrust meshing software into the workflow. The work accomplished in FY23 applies to the goals of capabilities development and demonstration, international collaboration, and evaluation of disposal of large, high-energy waste packages. The specific goals for FY23 were:

- Lead DEveloping COupled models and their VALidation against Experiments (DECOVALEX) international collaboration in development and simulation of Crystalline and Salt PA reference cases and conduct internal simulations of both cases.

- Conduct statistical shale PA SA/UQ analyses in collaboration with the SA/UQ and GDSA Framework work packages. This has two subtasks:

  a. Utilize Dakota and the NGW to update the 2019 case.

  b. Incorporate geological uncertainty a simplified shale model using the NGW and VoroCrust meshing.

- Collaborate with LANL to initiate the implementation of a safety assessment model for the unsaturated alluvium case with uncertain and realistic geology in GDSA.

- Training and Outreach. Attend, as appropriate, training (e.g., classes/workshop in Python, meshing, simulation and analysis software, and computational and analysis methods) and conferences with direct benefit to GDSA.

The accomplishments in FY23 discussed in this report are:

- Lead Task F of the international collaboration DECOVALEX-2023 (https://decovalex.org) on PA modelling from 2020 to present (Section 2).

  - o The main deliverable in FY23 has been a publicly available task specification that contains all information necessary to create simplified PA models of a crystalline and a domal salt repository. This was developed in collaboration with our 13 international partner teams and is in separate reports (LaForce et al., 2022b, 2023a).

  - o Simulation and analysis of the final SNL in-house models for the DECOVALEX crystalline (Section 2.2) and domal salt (Section 2.3) conceptual models.

- For FY23 the RSA and SA/UQ work packages decided to focus on the development of a new argillite (shale) PA model. The updated model (Section 3.1) includes additional sampled parameters, additional simulation output quantities of interest, utilizing the NGW to automate the workflow, a coarser mesh, and new waste package heat inventories. The results of this work include:

- o   Deterministic modelling of scenarios that include radionuclide heat representative of the spread of in-inventory dual-purpose canisters (DPCs) in the United States (Section 3.2). Several possible layouts of the waste packages in the repository have been proposed, and it has been shown that layout can have an impact on downstream transport of radionuclides.

- o   Successful execution of all simulation model runs for an uncertainty study utilizing the NGW (Section 3.3) in support of the SA/UQ work package.

- Development of a workflow in collaboration with LANL to integrate the geological models of unsaturated alluvium developed by the LANL GDSA-Geologic Modeling work package into RSA disposal simulations (Section 4.1). Results of this work are in a separate M4 report (LaForce et al., 2023b)

- Utilization of the in-house automated meshing software VoroCrust in an NGW sensitivity analysis that incorporates multiple realizations of large-scale geological features (Section 5). This model utilizes nested sampling wherein 30 simulations of flow parameters are simulated on three geological model meshes. The results of this simplified simulation study indicate that geological structure has a first-order impact on distribution of tracers in the subsurface.

- Testing the accuracy and speed of simulations using our in-house simulator PFLOTRAN on VoroCrust meshes, and comparison of the results with the results on flexed hexahedral meshes that have traditionally been used for GDSA RSA calculations (Section 6). This study indicates that simulations on VoroCrust meshes are always reasonably accurate, even for the example problems it is not possible to get accurate simulated solutions using hexahedral meshes.
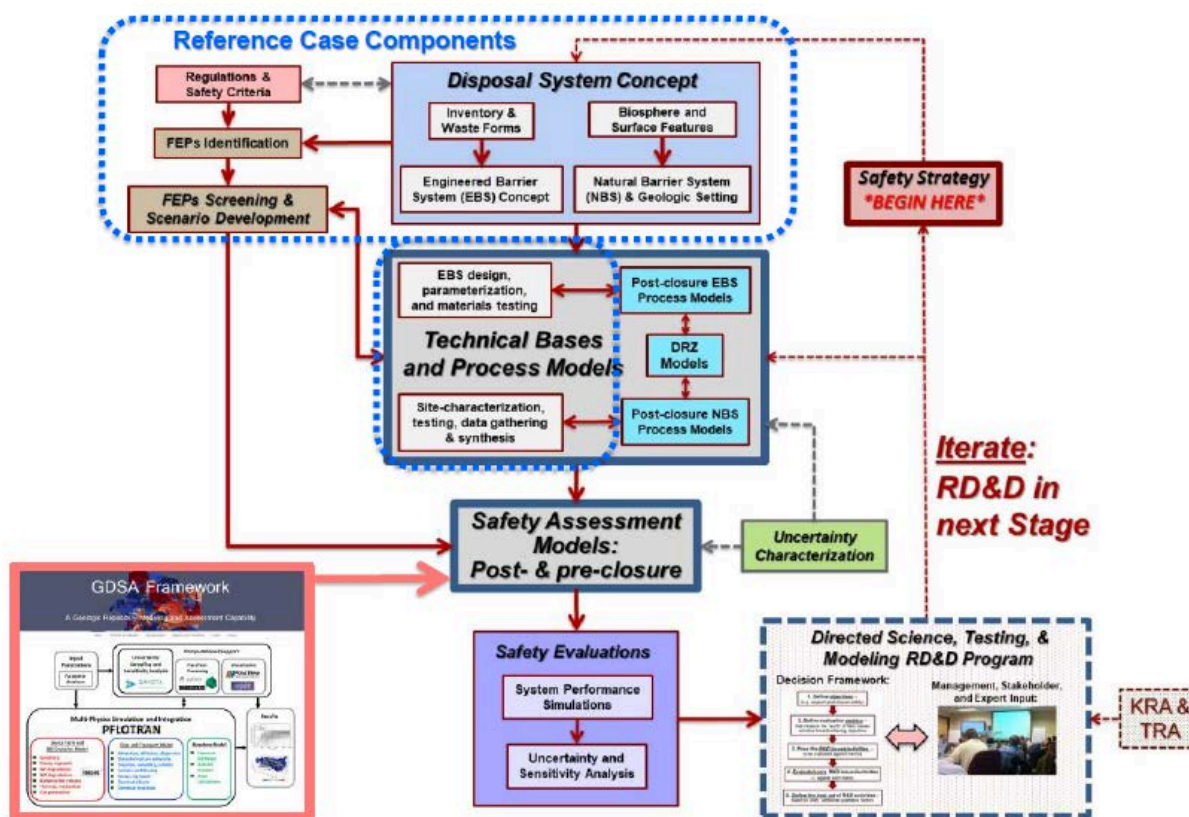
Figure 1-1.   **Information flow and the role of PA for RD&D prioritization during a single stage of repository development. (Sevougian et al., 2019b)**
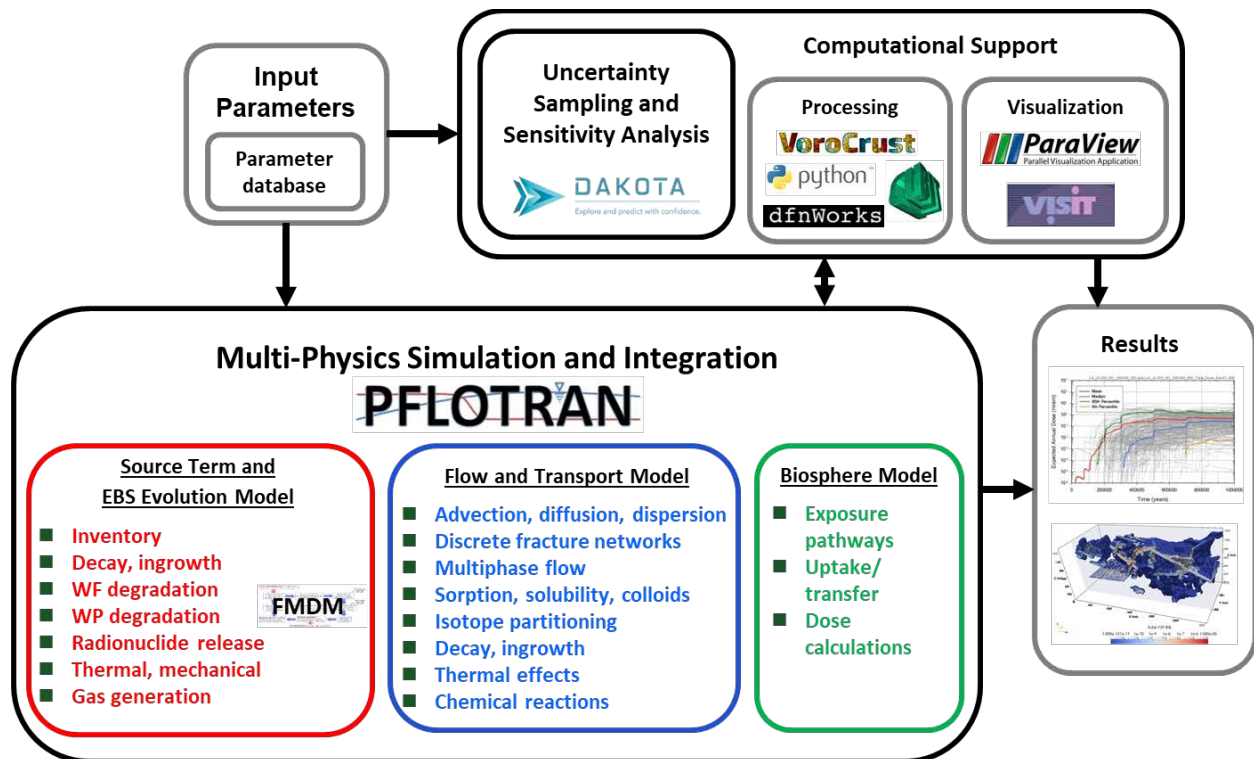
Figure 1-2. Schematic the GDSA Framework. The RSA work package focuses primarily on flow and transport modelling, but also works closely with VoroCrust, dfnWorks, and Dakota for processing and computational support. (Mariner et al., 2020)

2.   DECOVALEX REFERENCE CASES

2.1   DECOVALEX Task Overview/Management

DECOVALEX (DEveloping COupled models and their VALidation against Experiments; https://decovalex.org) is an international collaboration initiated in 1992 for the purpose of improving understanding of the coupled thermal, hydrological, and mechanical processes affecting repository evolution. DECOVALEX activities run in four-year phases. Sandia National Laboratory (SNL) is leading Task F, on behalf of the DOE's Spent Fuel and Waste Science and Technology (SFWST) Campaign, for the DECOVALEX-2023 phase. SNL also hosted the 6th DECOVALEX-2023 hybrid workshop in Albuquerque, NM on Nov 7-10, 2022.

Task F of DECOVALEX-2023 (LaForce et al., 2023a) focuses on comparison of models and methods used for post-closure performance assessment (PA). The goal is to test and build confidence in models, methods, and software used for post-closure PA and to identify additional research and development needed to improve PA methodologies. Task F includes more than 50 participants from nine countries and 19 organizations. The countries are Canada, Czech Republic, Germany, Korea, Netherlands, Sweden, Taiwan, United Kingdom, and The United States.

In Task F, two hypothetical repositories are being developed: one in crystalline rock (F1) and the other in salt (F2). In the first year, nine teams from six countries participated in the crystalline repository and benchmarking exercises. In the second year (2021), Task F1 gained one additional team. Task F2 was initiated six months later than Task F1, in August 2020, and has five teams from five countries. In year two, the focus of the tasks was on development of the conceptual reference case, benchmark, and preliminary simulations. During the third year (2022), the Task F1 and F2 groups have further refined the reference case specifications and produced the 10th revision to the task specification (LaForce et al., 2023a). The teams within these groups are currently finalizing their simulation studies and the focus has now turned to model comparison. The SNL simulation modelling accomplishments in the past year for both tasks are highlighted in the subsections below.

Task F1 added to its benchmarks, implemented waste package failure scenarios, and included a radionuclide source term. The previous discrete fracture network (DFN) benchmarks were redefined to ensure a 24-hour flux-based pulse of tracers. Also, a new continuous point source DFN benchmark was adopted. A radionuclide source term benchmark was also added to test radioactive decay and ingrowth, waste package failure, instant release fractions, waste form degradation, and radionuclide solubility. New reference case simulations include all source term processes, specify one waste package failure at time zero at a specific location due to an undetected defect, and failure of all waste packages at 50,000 years due to a conservative assumption about the effects of glaciation. Preliminary results indicate clear differences between the teams in mean radionuclide releases from the repository and mean mass fluxes to the hillslope and low point over time. Differences may or may not decrease as the simulations mature, as reasons for differences are identified, and as implementation errors are discovered.

Task F2 has defined 34 flow and transport quantities of interest (QoI) for PA model comparison and they are now narrowing this down to a smaller number of informative comparisons for the final report and future publications. All five teams have submitted preliminary calculations for these QoI and all models indicate that no radionuclides reach the surface. Differences in some of the comparisons at points within the repository are greater between the teams and are believed to be the result of different levels of fidelity of salt creep in the models.

An extension of Task F, including salt and crystalline cases, has been proposed to the sponsors for DECOVALEX-2027. This continuation will provide numerous opportunities for learning new modeling approaches, developing new models for use in PA simulations, testing uncertainty and sensitivity analysis

methods, comparing PA methods, including additional physics, and exchanging ideas with modelers in other programs.

2.2   Crystalline Reference Case

2.2.1   Benchmarks

Teams participating in the Crystalline Task F1 completed several benchmark cases related to flow and transport through fractured rock. The benchmark cases provide an opportunity to understand differences in model implementation that affect how a problem can be specified, what results can be obtained, and the influence modeling choices have on calculated values of performance measures in relatively simple systems. The benchmarks involving DFNs were recently updated to 24-hour flux-based injections in order to perform moment analysis on the tracer concentrations in the domain. First and second moments provide mean and variance of tracer travel times for each tracer in each simulation, respectively. Apparent retardation factors of the sorbing tracer are calculated from first moment ratios. In addition, two new benchmarks were added. First, a continuous point source on the four-fracture plus stochastic fracture system and second, a radionuclide source term calculation. The benchmarks are described in more detail in LaForce et al. (2021) and Revision 10 of the task specification (LaForce et al., 2023a)

2.2.1.1   Four Fractures

The four-fracture test problem provided an opportunity for teams to practice generating deterministic fractures, upscaling to an equivalent continuous porous medium (ECPM), and simulating particle tracking (if desired). The test problem is based on an example provided with dfnWorks (Hyman et al., 2015); it includes advection and diffusion of a conservative tracer through four fractures within a cubic domain. It is assumed flow and transport only occur in the fractures; matrix diffusion is neglected. Groundwater flow is simulated by a steady state (saturated, single-phase) flow driven by a pressure gradient along the x-axis. Constant pressure (Dirichlet) boundary conditions are applied on the inflow and outflow faces. For simplicity, the effect of gravity is not included. No-flow boundary conditions are applied at all other faces of the domain. A Dirichlet boundary condition lasting for one day, of 1 mol/L of the tracer is set along the single fracture on the west face (x = -500) of the domain at time zero; the concentration at the west face is zero for all other times. The tracer was modeled using three different methods: (1) A particle tracking DFN approach, (2) an advection-diffusion equation (ADE) DFN approach, and (3) an ADE ECPM approach. First and second moments of particle travel times across the domain are found in Table 2-1 and mass breakthrough curves are shown in Figure 2-1. Overall, the three methods show good agreement with one another.

Table 2-1.   **First and second moments for particle travel times in the four-fracture problem.**

Method	1st Moment [yr]	2nd Moment [yr²]
DFN Particle Tracking	1.069	3.153
DFN ADE	1.009	2.337
ECPM ADE	1.052	1.968
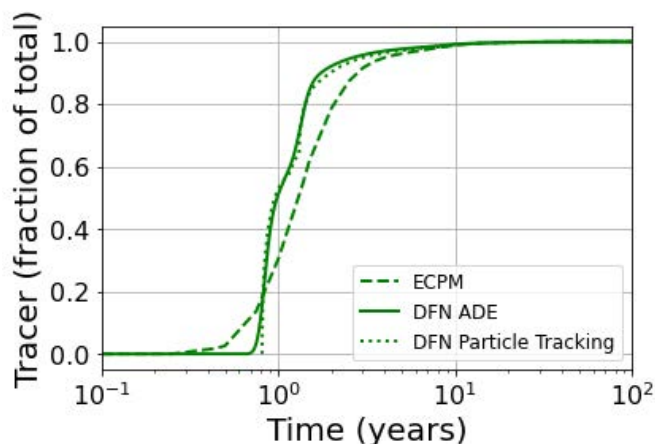
Figure 2-1.   Breakthrough curves for the four-fracture benchmark using three different modelling methods.

2.2.1.2   *Four-Fractures Plus Stochastic Fractures*

The four-fracture benchmark case is then extended by adding stochastically generated fracture sets to the model domain. The stochastically generated fractures were provided to the teams. The problem uses the same assumptions for flow and transport as the four-fracture benchmark case and the domain extent remains the same. The DFN particle tracking method is not used on this example. First and second moments of particle travel times across the domain are found in Table 2-2 and mass breakthrough curves are shown in Figure 2-2. The first moments are quite similar but there is a large difference in the second moments. This could be due to false connections in the ECPM and the averaging out of fracture properties compared to the DFN.

Table 2-2.   First and second moments for particle travels times in the four-fracture plus stochastic fractures problem.

Method	1st Moment Conservative Tracer [yr]	1st Moment Decaying Tracer [yr]	1st Moment Sorbing Tracer [yr]	2nd Moment Conservative Tracer [yr^2]	2nd Moment Decaying Tracer [yr^2]	2nd Moment Sorbing Tracer [yr^2]
DFN ADE	1.01	0.804	4.92	399	4.04	3480
ECPM ADE	1.02	0.853	5.19	28.6	6.20	737
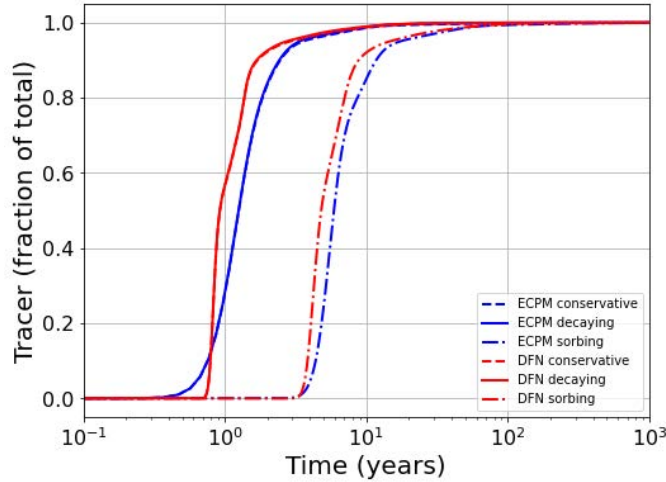
Figure 2-2.   Breakthrough curves for four-fracture plus stochastic fractures benchmark.

A second benchmark using the four-fracture plus stochastic fracture domain and tracers was created that simulates plume development from a continuous point source, as might happen for a slowly degrading waste form of a failed waste package. For this benchmark, the tracers are introduced continuously at a constant rate at a point source. The point source has coordinates (-500.0, 7.0, 248.25). First and second moments are found in Table 2-3 and flux-based breakthrough curves are shown in Figure 2-3. The breakthrough curves for the point source were calculated from the flux entering the domain at each time step divided by the flux exiting at each timestep. This differs from the previous breakthrough curves which looked at the initial mass that entered the domain divided by the amount that has exited. The DFN has higher first and second moments than the ECPM. Similar to the flux-based injection, this could be due to false connections in the ECPM and large tailing in the DFN due to tracer spending more time in the stochastic fractures.

Table 2-3.   First and second moments for the continuous point source benchmark on the four-fracture plus stochastic fracture domain.

Method	1st Moment Conservative Tracer [yr]	1st Moment Decaying Tracer [yr]	1st Moment Sorbing Tracer [yr]	2nd Moment Conservative Tracer [yr²]	2nd Moment Decaying Tracer [yr²]	2nd Moment Sorbing Tracer [yr²]
DFN ADE	1.64	1.28	8.14	846	305	6360
ECPM	0.883	0.799	4.47	10.4	3.33	271
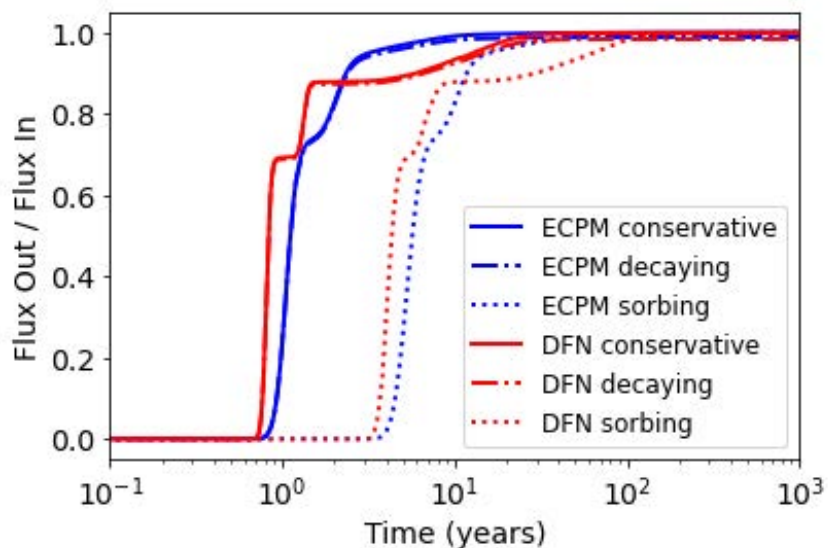
Figure 2-3.   **Breakthrough curves for four-fracture plus stochastic fractures with continuous point source.**

2.2.1.3   *Radionuclide Source Term*

The radionuclide source term depends on rates of radioactive decay and ingrowth, the timing of waste package breach, and degradation properties of spent nuclear fuel (SNF). Depending on implementation, limitations on radionuclide solubility within the waste canister may be accounted for in the source term model or considered separately. A test case for the source term is defined in LaForce et al. (2023a, Section 5.3) to test the effects of the following on radionuclide release from the waste form:

   (1).   Radioactive decay and ingrowth

   (2).   Waste package breach time

   (3).   Instant release fraction

   (4).   Fuel matrix degradation rate

   (5).   Solubility limitations

Results of this test case are evaluated as follows:

   (1).   Activities of the radionuclides in the ^{245}Cm to ^{229}Th decay chain are shown to match the activities calculated in Anttila (2005, Table 2.2.2.4) at 5, 30, 102, 103, 104, 105, and 106 years as shown in Figure 2-4.

   (2).   Waste package breach is shown to occur at 3,000 years.

   (3).   As indicated in Figure 2-5, an immediate transfer of 3% of the ^{99}Tc is shown to be released from the fuel when the waste package breaches.

   (4).   The fuel matrix is shown not to degrade before waste package breach and is shown to be 64% degraded at one million years (Figure 2-5); the expected degradation is 63.1% based on analytical solution. In addition, radionuclide release from fuel degradation is shown to be congruent.

   (5).   Aqueous concentrations are shown to be limited by prescribed elemental solubility limits as appropriate in Figure 2-6. A solubility-limited aqueous concentration of an isotope is reduced

by the presence of other isotopes of the same element. However, for this test problem the concentrations of other isotopes are assumed negligible.

The internal calculation tracking number for these simulations and figures is 230501-RNSOURC-01.
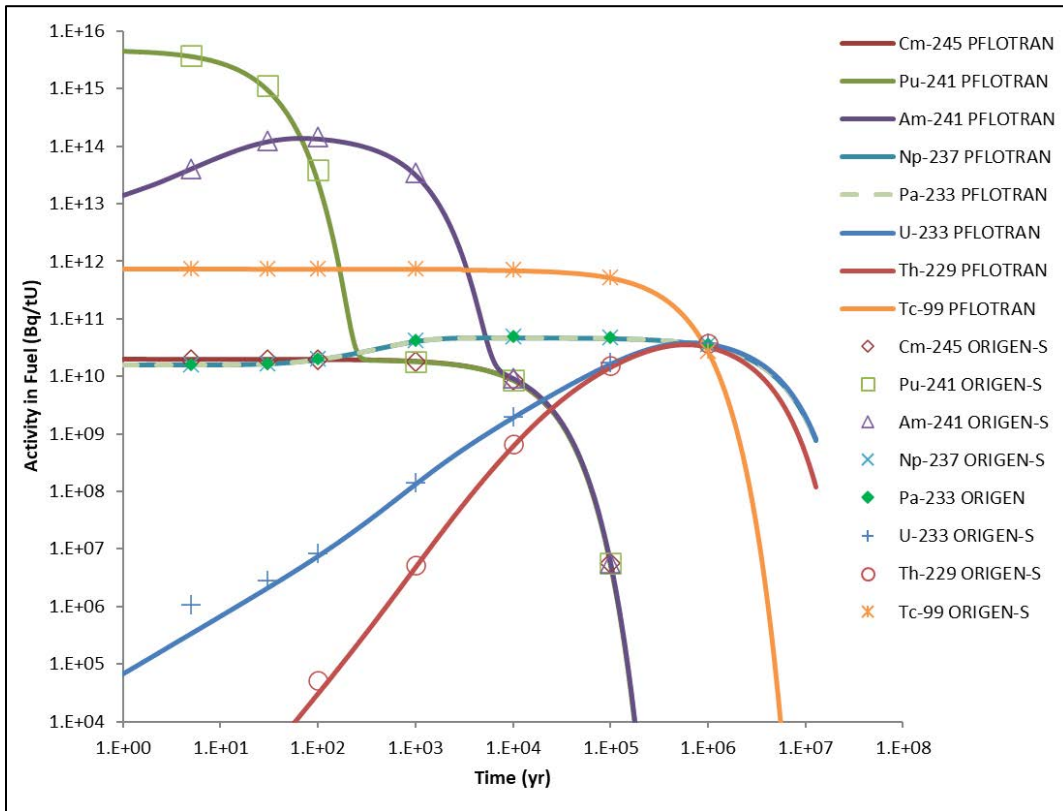
Figure 2-4. **Calculated decay and ingrowth for the radionuclide source term benchmark compared to ORIGEN-S calculations of Anttila (2005, Table 2.2.2.4).**
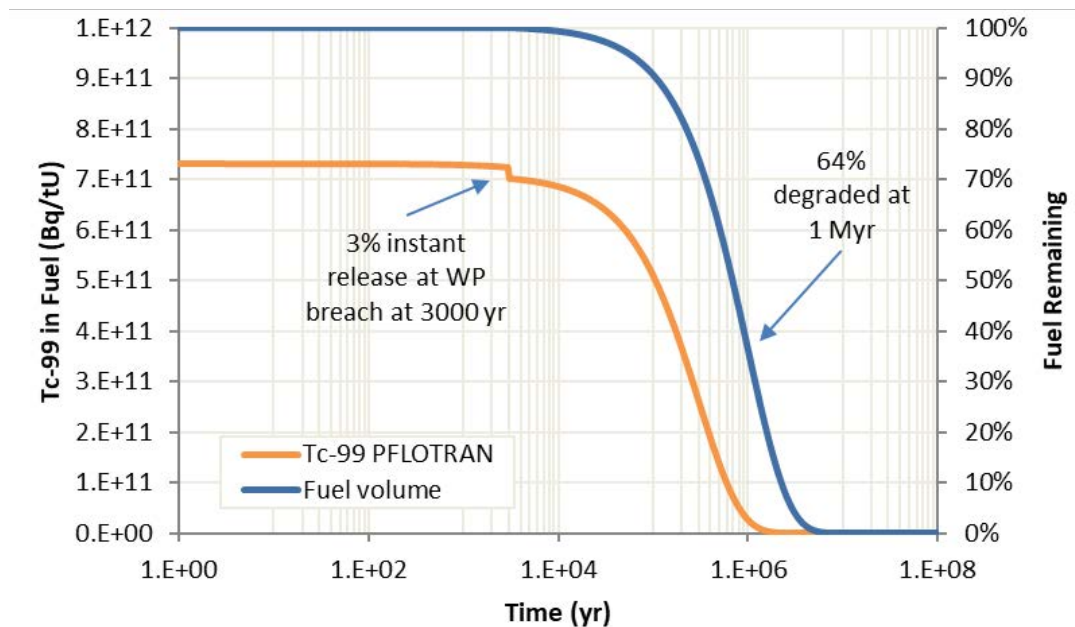
Figure 2-5. Calculated ^{99}Tc activity in the fuel and fuel volume remaining over time in the radionuclide source term benchmark.
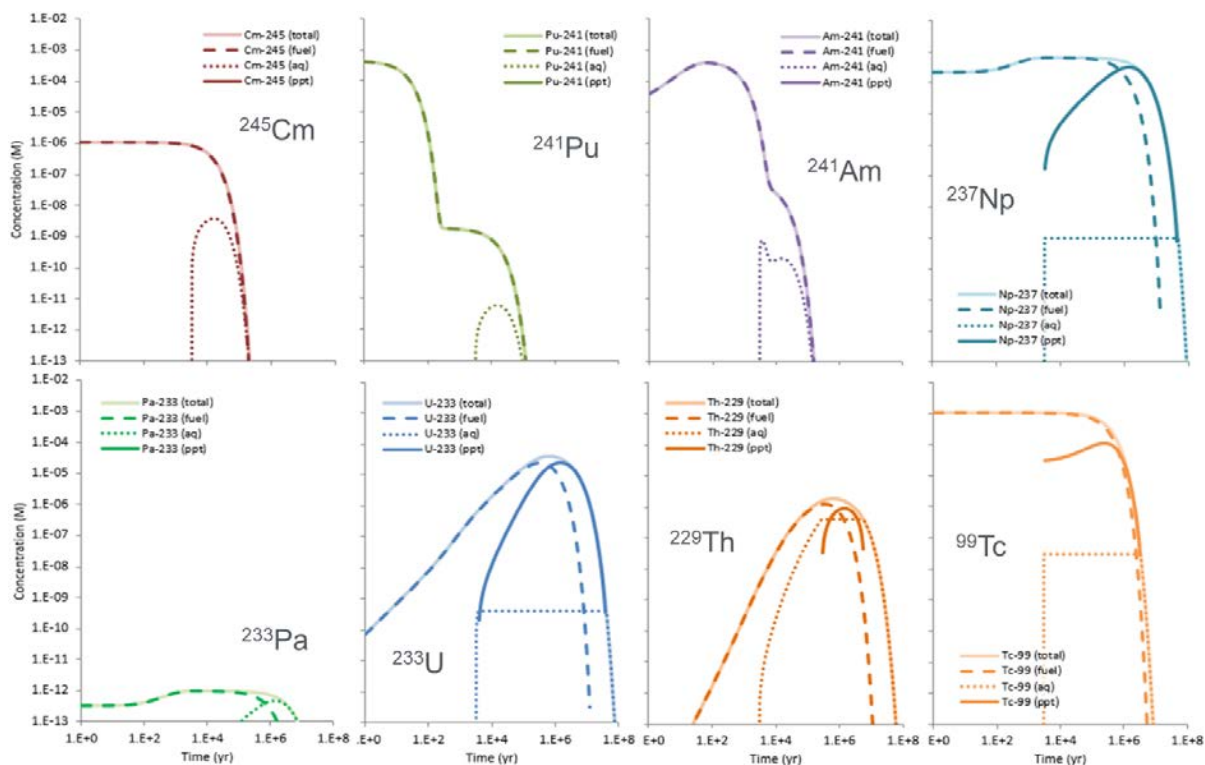
Figure 2-6. Calculated phase partitioning of radionuclide source term benchmark as affected by release and solubility limitations.

2.2.2   Full Reference Case

The Task F1 reference case for a mined repository in fractured crystalline rock is defined in the Task Specification revision 10 (LaForce et al., 2023a). The reference case assumes isothermal conditions, steady state flow, and two different transport scenarios. The first, modeling two conservative tracers upon simultaneous breach of all the canisters in the repository, and the second modeling a radionuclide decay chain where one waste package fails at the beginning of the simulation and the rest fail at 50,000 years. Teams ran the simulation on ten different stochastic fracture realizations and compared tracer transport and steady state flow across the top boundary of the model domain.

The SNL team ran the ten different fracture realizations of the reference case using two different methods. One using an ECPM and the second using a dual continuum disconnected matrix (DCDM) which is described in more detail in Nole et al. (2023). The DFN (created using dfnWorks) was upscaled to an ECPM using two different upscaling lengths, 20 m and 25 m. An overview of the repository discretization and upscaling can be found in LaForce et al. (2022a). Using the upscaled porosities from the 25 m grid the DCDM was then discretized. First, the 20 m vs 25 m ECPM grid was analyzed and then the 25 m ECPM was compared to the 25 m DCDM. Table 2-4 shows the mean steady state water fluxes at the three surfaces of interest (Figure 2-7) for all ten fracture realizations. The 25 m grid has slightly higher magnitude fluxes at the high point and low point, as expected. The larger grid size increases false connections in the domain but runs six times faster than the 20 m grid using eight nodes and 288 processors on a parallel super-computer.

Table 2-4.   Mean and standard deviation for the water fluxes on the three surfaces of interest for the 10 realizations of the crystalline reference case.

Surface	Mean Flux 20 m grid [kg/y]	Standard Deviation 20 m grid [kg/y]	Mean Flux 25 m grid [kg/y]	Standard Deviation 25 m grid [kg/y]
High Point	-643643	104755	-733756	125180
Hillslope	-21756	111360	-1959	123889
Low Point	665399	119680	735715	122949
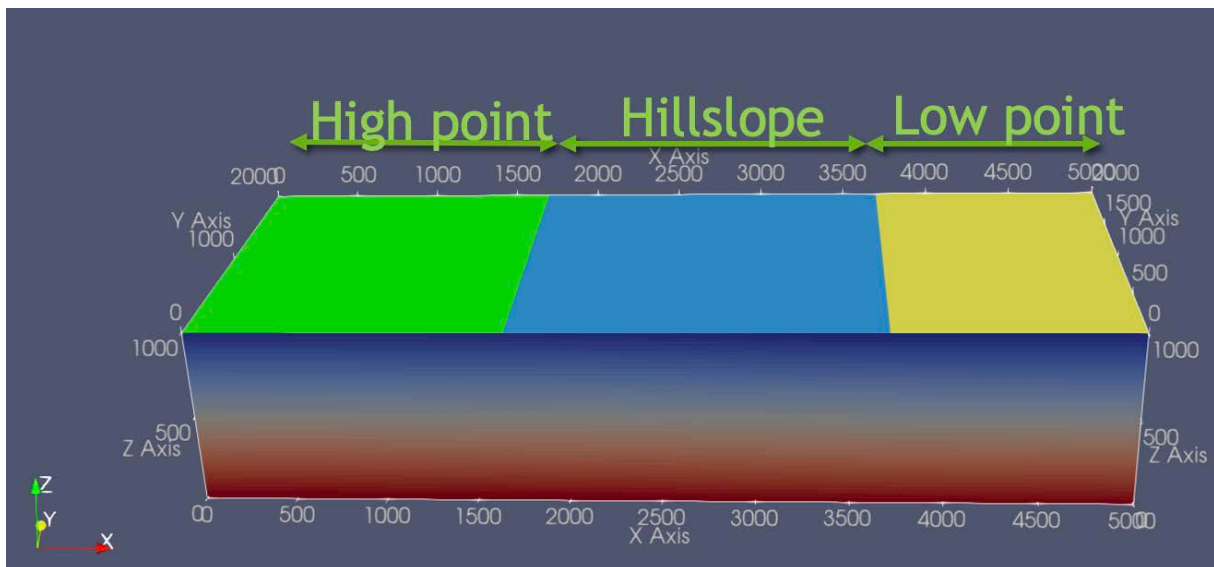
Figure 2-7. Domain for the crystalline reference case and 3 surfaces of interest defined.

2.2.2.1   *Conservative Tracers on the 20 m grid vs 25 m ECPM grid*

The source terms for the tracers were simulated in PFLOTRAN using the Waste Form Process Model. All waste packages fail at the beginning of the simulation, after which the conservative tracers were simulated by the Reactive Transport model in PFLOTRAN. Tracer 1 is instantly released, and Tracer 2 is released at a fractional rate of 10^{-7}/year. Figure 2-8 shows the mass remaining in the repository for the 20 m grid. The mass remaining of Tracer 2 had to be post processed since the mass balance file output by PFLOTRAN does not include the amount remaining in the waste packages. There is little variance between fracture realizations early on. At the end of the simulation, the difference increases to about ~0.1 moles for Tracer 1 and ~0.001 moles for Tracer 2. When comparing the mass in the repository for different upscaling lengths (Figure 2-9), we see that there is more mass remaining in the repository for the 25 m grid compared to the 20 m grid. The 25 m repository is ~15 m larger in the x-direction than the 20 m grid, due to the discretization limits in Cubit.
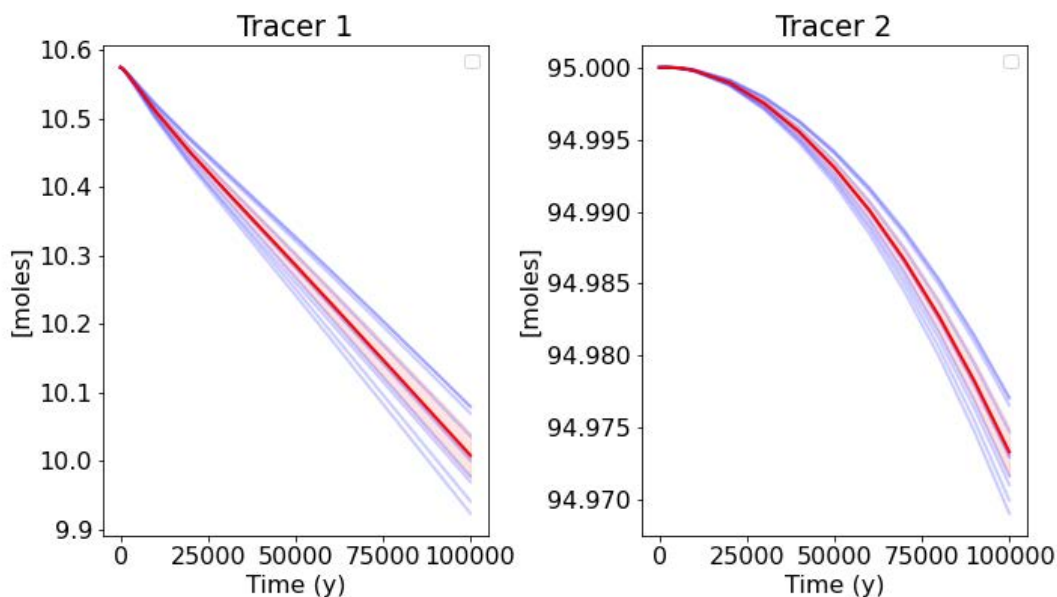
Figure 2-8.   **Mass remaining in the repository for the 20 m grid. Bold red line is the mean, shaded red area is the 95% confidence interval, and blue lines represent fracture realizations.**
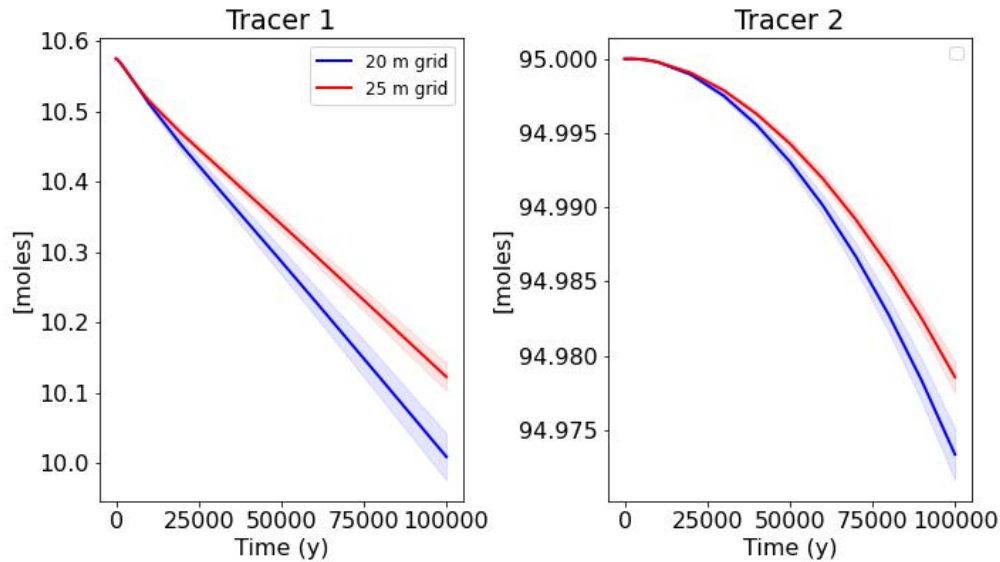
Figure 2-9. **Mean and 95% confidence interval of mass remaining in the repository for the 20 m grid (blue) and 25 m grid (red).**

The cumulative mass (moles) and mass flow rate (moles/year) across the hillslope for the 20 m grid can be seen in Figure 2-10. We see a large difference in the realizations with a range of ~ 0.035 moles for Tracer 1 cumulative mass. There is a steady increase of mass flow for Tracer 2 while Tracer 1 has a spike in the beginning of the simulation and then steadily increases. When comparing the different upscaling lengths (Figure 2-11) we see no difference in the mean and 95% confidence intervals except at late times where the 20 m grid is slightly higher than the 25 m grid.
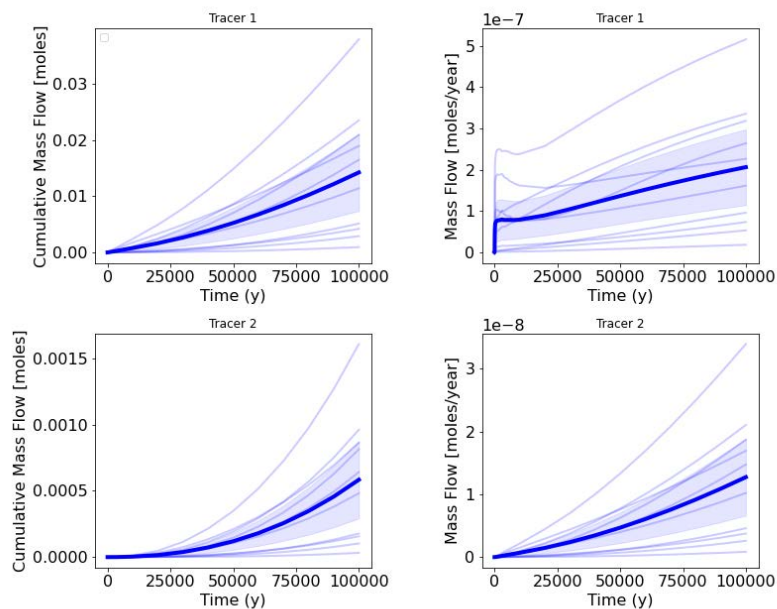
Figure 2-10. **Cumulative mass (moles) and mass flow (moles/year) across the hillslope for the 20 m grid. Light blue shade represents 95% confidence interval of the mean.**
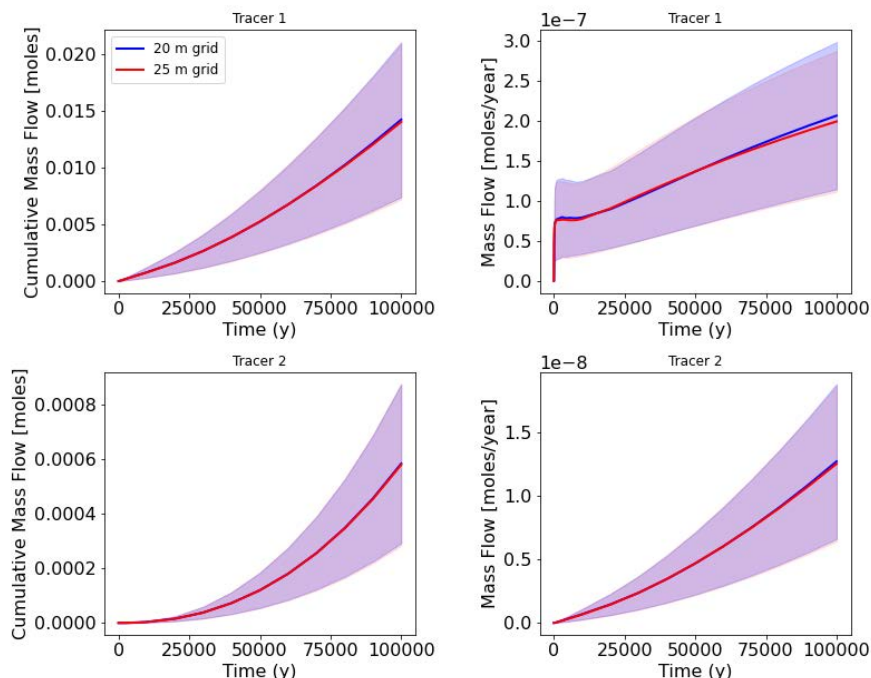
Figure 2-11.   **Cumulative mass (moles) and mass flow (moles/year) across the hillslope for the 20 m grid (blue) and 25 m grid (red). Light red and blue shading represent 95% confidence interval of the mean.**

The cumulative mass flow and mass flow rate for the low point for the 20 m grid is plotted in Figure 2-12. We see significant variance in the realizations with a range of ~0.05 mole. As expected, the low point has higher fluxes than the hillslope and the tracer is concentrating in the south-west portion of the low point surface (Figure 2-13). Comparing the two upscaling lengths across the low point (Figure 2-14) the 25 m grid has a slightly higher mean which is likely due to more false connections occurring in the domain. However, the means and 95% confidence intervals are still quite close to each other, proving the 25 m grid to be advantageous over the 20 m grid due to the faster run time.
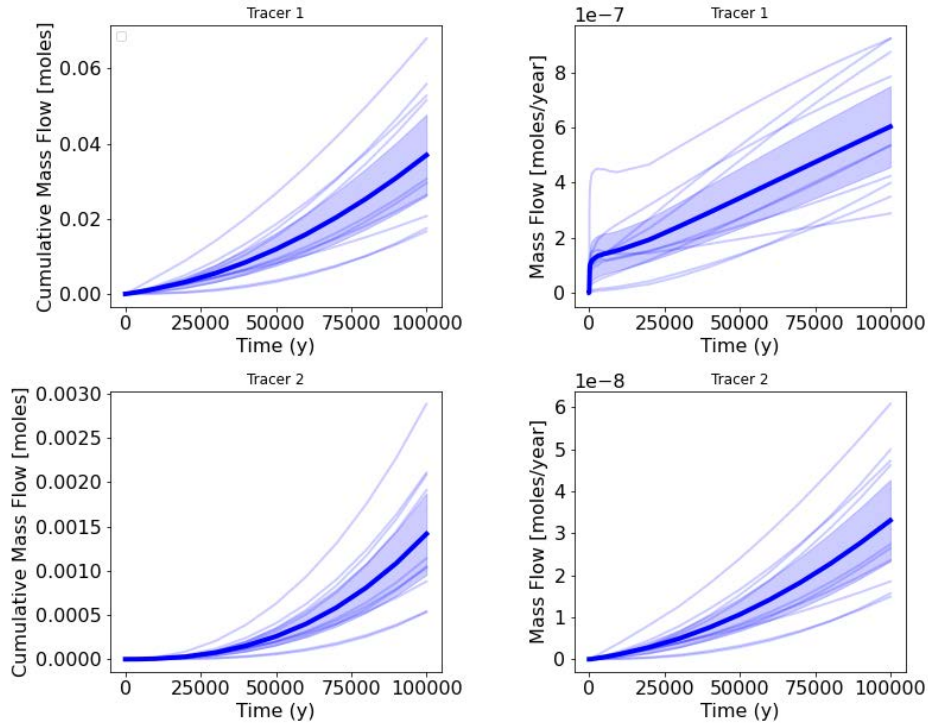
Figure 2-12. Cumulative mass (moles) and mass flow (moles/year) across the low point for the 20 m grid. Light blue shade represents 95% confidence interval of the mean.
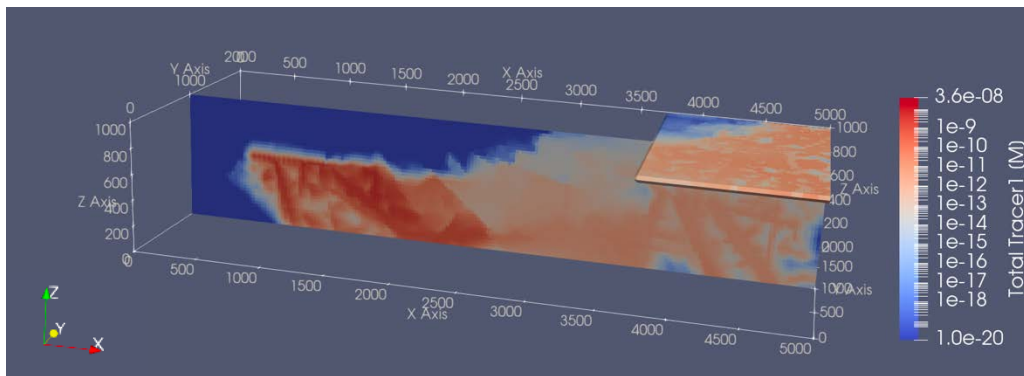
Figure 2-13. Tracer 1 at 100,000 years for realization one.
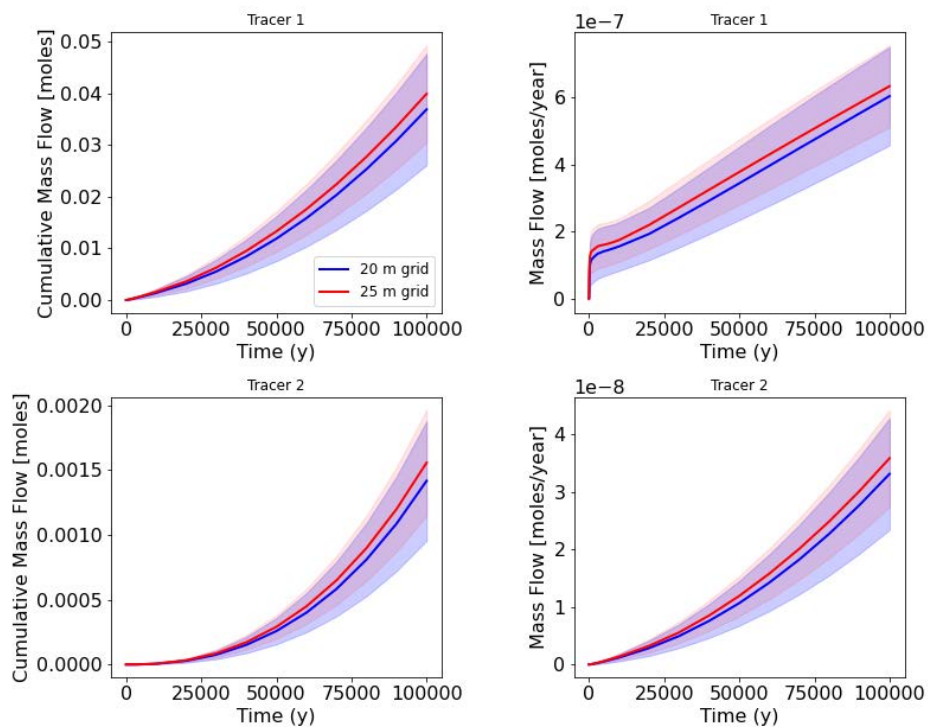
Figure 2-14.   **Mean (solid line) and 95% confidence interval (shaded area) for the cumulative mass (moles) and mass flow (moles/year) across the low point for the 20 m grid (blue) and 25 m grid (red).**

To obtain the maximum tracer flux over the hillslope and low point, observation points across the entire two surfaces were post processed to find maximum mass flow at 100,000 years. Each realization resulted in a different maximum flux location on the surface. The results for the hillslope calculated using both grid sizes is shown in Figure 2-15. The means and 95% confidence interval of the 25 m grid overlap with the 20 m grid, with realization 9 having the highest cumulative mass flow and mass flow rate on both grid sizes. Looking at a slice through the domain at this point we see a large stochastic fracture intersecting a deterministic fracture which is likely causing the high mass flow. Looking at the maximum mass flow results for the low point (Figure 2-16), the 25 m grid is visibly higher than the 20 m grid with realization 9 again having the highest mass flow. Taking a slice in the domain where this maximum mass flow occurs (not shown) indicates that it is due to a large stochastic fracture cluster in realization 9.
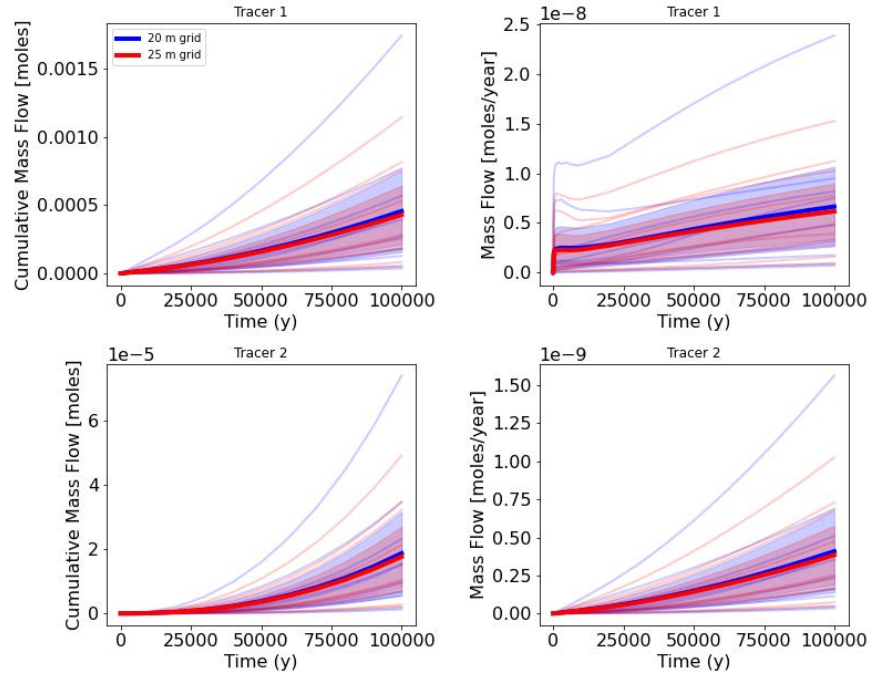
Figure 2-15. **Maximum cumulative mass (moles) and mass flow (moles/year) across the hillslope for the 20 m grid (blue) and 25 m grid (red). Light red and blue shade represent 95% confidence interval of the mean.**
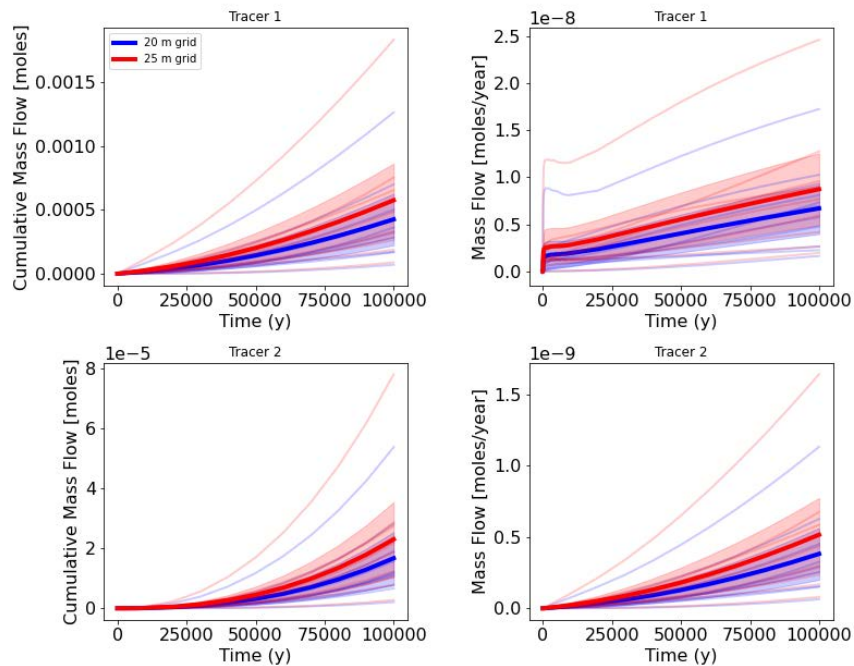
Figure 2-16. **Maximum cumulative mass (moles) and mass flow (moles/year) across the low point for the 20 m grid (blue) and 25 m grid (red). Light red and blue shade represent 95% confidence interval of the mean.**

Two observation points on the hillslope and low point were also selected to compare concentrations. These locations represent places where deterministic fractures intersect with the top surface. Figure 2-17 shows the results comparing the two grid sizes and realizations. We see a large range in realizations, ~1.59×10^{-13} M for Tracer 1 on the hillslope and ~1.15×10^{-11} M for Tracer 1 on the low point. However, all concentrations remain low with nothing higher than 10^{-10} M.
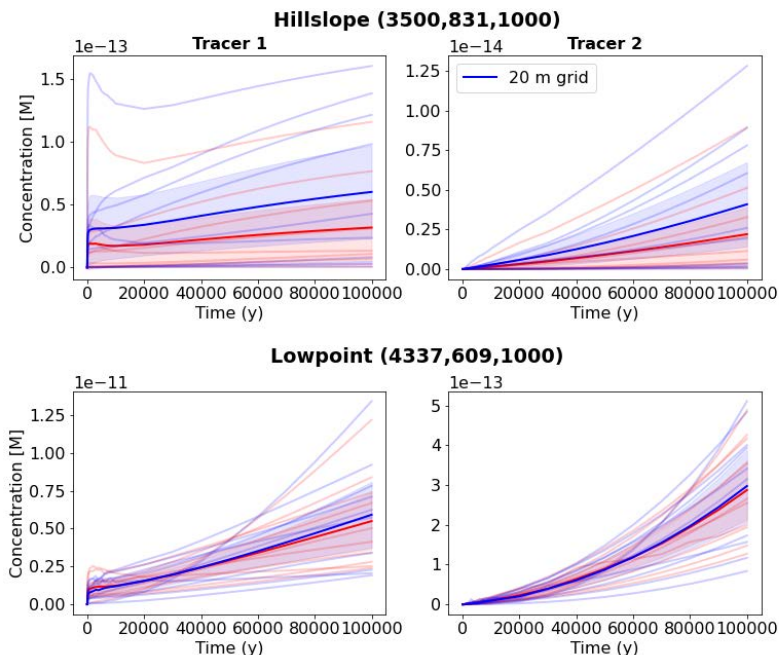
Figure 2-17.   **Observation points on the hillslope and low point comparing the 20 m grid (blue) and 25 m grid (red). Light red and blue shade represent 95% confidence interval of the mean. (X,Y,Z) coordinates of the flux location given in figure title.**

2.2.2.2   *Conservative tracers on the 25 m ECPM and DCDM grid*

The DCDM model results were compared to the ECPM 25 m grid model results. The DCDM model was not included over the repository region. Outside the repository region, cells that had no fractures intersecting them were made inactive. The secondary continuum was discretized using 100 cells with matrix properties as stated in the task specification. Figure 2-18 shows the mean and 95% confidence intervals of the fluxes over the hillslope comparing the ECPM and DCDM models. The DCDM shows slightly higher means of at the hillslope than the ECPM but similar confidence intervals. At 100,000 years the cumulative mass flow for Tracer 1 for the DCDM is about ~0.005 moles higher. The similarity in confidence intervals could be due to the large variance in realizations. Figure 2-19 shows the fluxes over the low point, where the DCDM is very similar to the ECPM. Although the DCDM represents fracture-matrix diffusion at the cm scale, the effective diffusion coefficient specified in the task specification is quite low ($10 \times 10^{-13.7}$ m^2/s), therefore it is not surprising that the ECPM and DCDM give similar results on the low point.
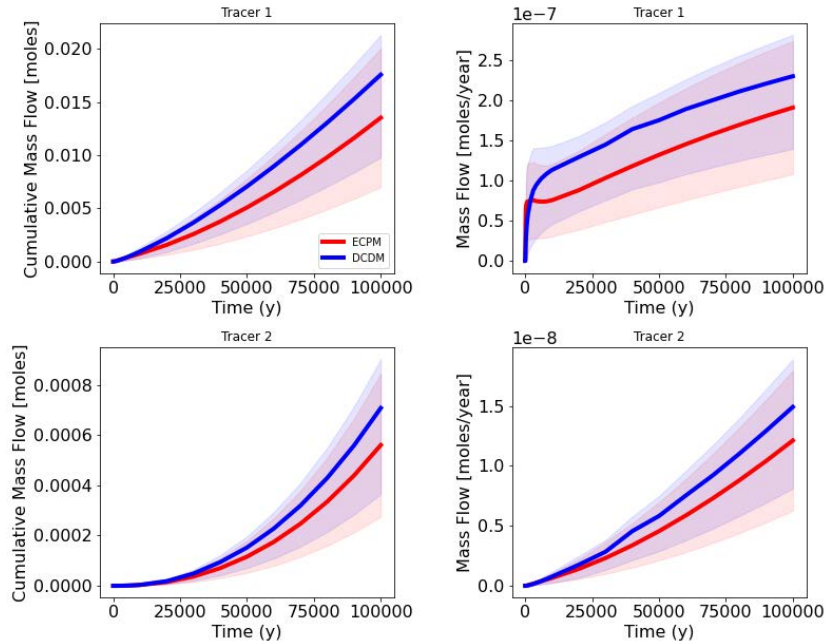
Figure 2-18. Means and 95% confidence intervals for the DCDM (blue) and ECPM (red) for the fluxes over the hillslope. Light red and blue shade represent 95% confidence interval of the mean.
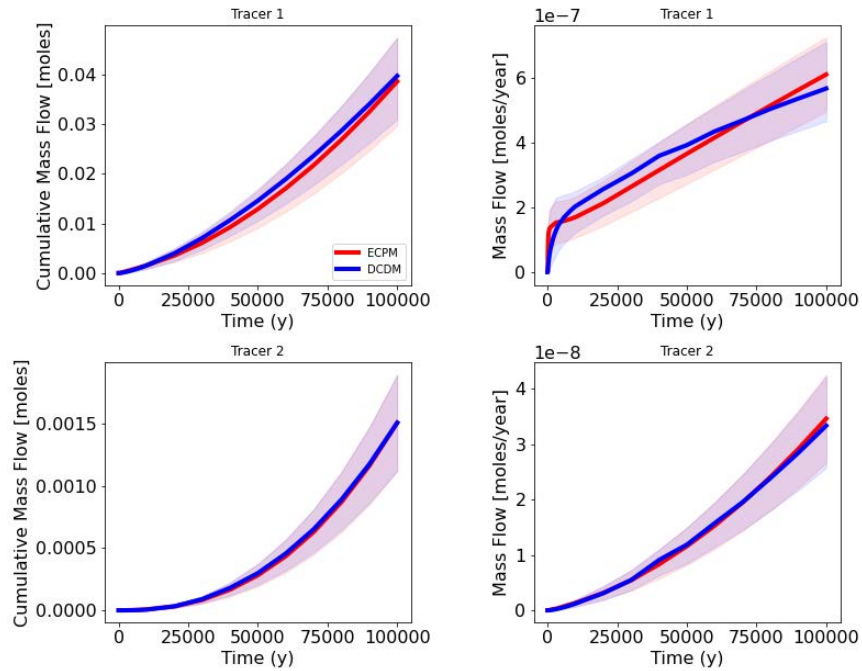
Figure 2-19. Means and 95% confidence intervals for the DCDM (blue) and ECPM (red) for the fluxes over the low point. Light red and blue shade represent 95% confidence interval of the mean.

2.2.2.3   Radionuclide Inventory and Waste Package Failure Scenario

For the radionuclide inventory of the reference case, teams looked at the decay, ingrowth, sorption, and solubility limits of ^{129}I and the decay chain of ^{238}U (^{238}U $\rightarrow$ ^{234}U $\rightarrow$ ^{230}Th $\rightarrow$ ^{226}Ra) modeled using data from the KURT (KAERI Underground Research Tunnel) site (Cho et al., 2016). Additionally, two waste package failure scenarios are modeled simultaneously:

(1). One waste package fails at time zero due to an undetected defect. For this iteration, the waste package that fails will be the fourth one in the center drift immediately south of the access tunnel.

(2). All remaining intact waste packages fail at year 50,000 due to glacial effects.

It is conservatively assumed that the waste packages provide no containment after failure (as if they disappear and there are no internal barriers such as cladding). The same output metrics for the conservative tracers are used to examine the radionuclide inventory. The radionuclide inventory was implemented on the ECPM 25 m grid for all ten realizations. The Used Fuel Disposition (UFD) Decay Process Model was used to simulate the radionuclide behavior in the simulation.

The radionuclide mass left in the repository was found to be the same for all realizations (Figure 2-20). This could be due to the larger portion of tracer remaining in the waste package compared to the conservative tracers, or the adsorption occurring in the buffer. Figure 2-20 shows ^{129}I at 40,000 years and then at 60,0000 years after all waste packages breach. We see a decrease in ^{129}I and ^{238}U at 50,000 years after all the waste packages breach but an increase in ^{226}Ra and ^{230}Th from decay and ingrowth, while ^{234}U shows a steady decrease throughout the entire simulation.
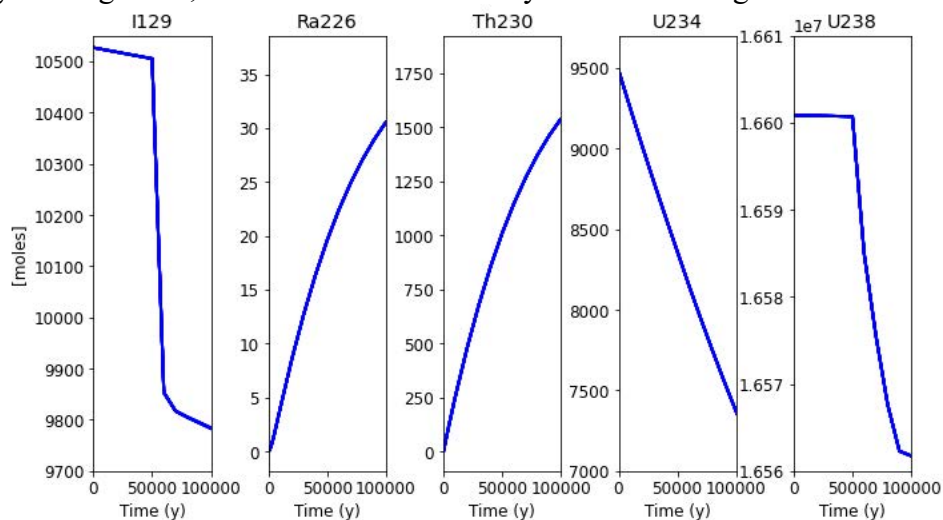
Figure 2-20.   **Mass remaining in the repository for the radionuclide inventory. No difference seen between realizations.**

The cumulative mass flow and mass flow across the hillslope are plotted in Figure 2-21. The fluxes show no observable amount before 50,000 years, and then we observe a spike in the flux after all the waste packages breach. There is a large difference between the realizations, a range in ~1 mole for ^{129}I and ~20 moles for ^{238}U. The cumulative mass flow and mass flow rate across the low point plotted to one million years is shown in Figure 2-22. When plotted to a million years we see that the mass flow ^{129}I is still increasing but for all other radionuclides it has started to decrease, and the maximum mass flow occurred at ~200,000 years. A wide difference in realizations remains with more than 40 moles range for ^{129}I and ~5,000 moles range for ^{238}U. The observation points for the hillslope and low point are plotted in Figure

2-23 to one million years. [129]I shows the highest concentration with the largest realization reaching over 4.0×10^{-9} M and 1.5×10^{-11} M at the hill slope and low point observation point respectively. [226]Ra and [230]Th are not plotted because not a significant amount of concentration has been observed at these points.
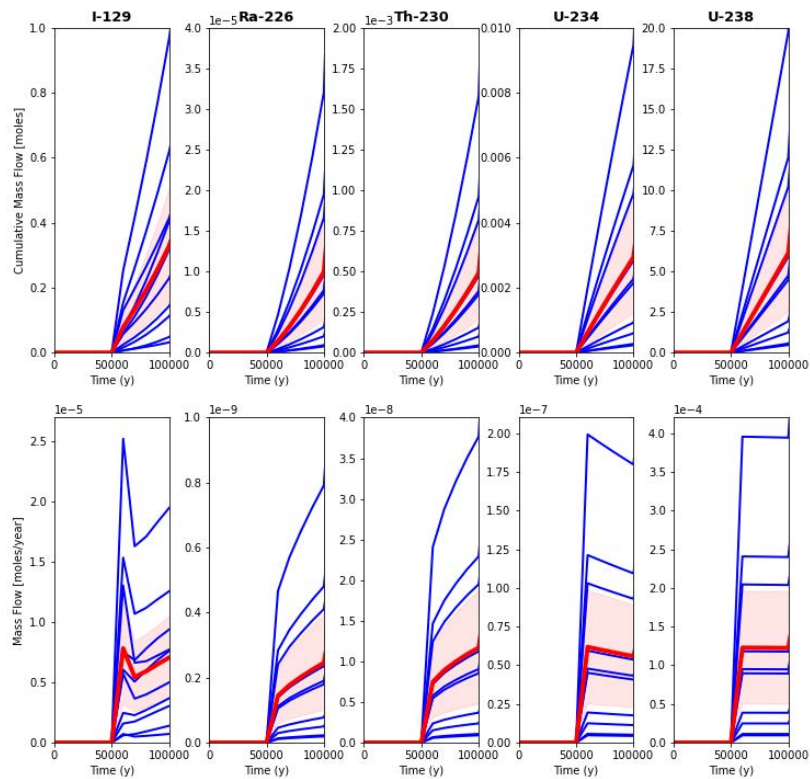
Figure 2-21. The cumulative mass flow (top) and mass flow (bottom) across the hill slope for radionuclide inventory to 100,000 years. Blue lines indicate realizations, red line is mean, red shaded area is 95% confidence interval.
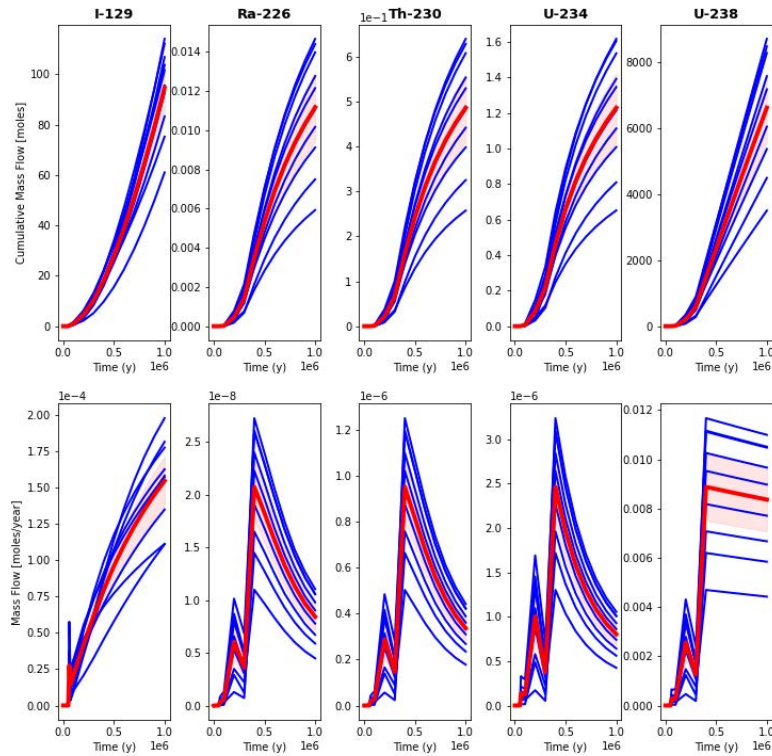
Figure 2-22. The cumulative mass flow (top) and mass flow rate (bottom) across the low point for radionuclide inventory to 1,000,000 years. Blue lines indicate realizations, red line is mean, red shaded area is 95% confidence interval.
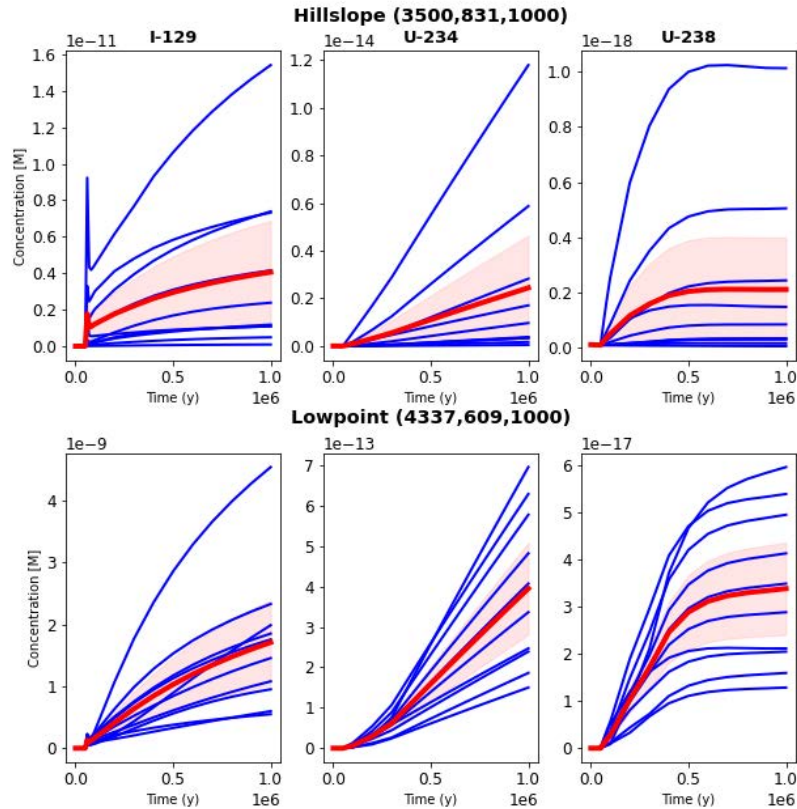
Figure 2-23. Radionuclide concentrations at the observation points on the hillslope (top) and low point (bottom) for the radionuclide inventory. Blue lines indicate realizations, red line is mean, red shaded area is 95% confidence interval.

2.3 Salt Reference Case

2.3.1 Reference Case Summary

The salt reference scenario presented here does not focus on an undisturbed scenario for a salt repository. It has been shown through multiple performance assessments: RESUS, KOMTESS, ISIBEL and VSG (Bollingerfehr et al., 2008; Beuth et al., 2012; Bollingerfehr et al., 2017; Bollingerfehr et al., 2018; Bertrams et al., 2020a), that there are no radiological consequences within 1,000,000 years for disposal in undisturbed salt formations because of their very low permeability and moisture content. Additionally, the integrity of rock salt is given for at least 1,000,000 years for salt rock barriers greater than 200 m in thickness (which is the scenario presented here), which provides no pathway through permeable anhydrite, boudinage, or isolated salt blocks. As a result, here we present a disturbed scenario in which the shaft seals fail 1,000 years after repository closure, allowing an influx of brine down the shafts and into the repository.

This work is a part of the DECOVALEX 2023 Task F2 (LaForce et al., 2023a), which is a staged development of models building up to a full PA. This stepwise process is done to ensure the consistency between each team's modeling efforts as complexities are added. The planned staged development was:

(1). Flow + radionuclide mobilization and transport (problem description will include variably saturated initial conditions)

(2). include drift convergence (salt creep and backfill consolidation will be considered)

(3). include heat flow and temperature-dependence of drift convergence

(4). include model uncertainty in backfill consolidation model

(5). include gas generation

The final task specification (Revision 10) includes in detail the teams' efforts to date for only steps one and 2, with steps 3 through 5 to be proposed as part of a future DECOVALEX task (LaForce et al., 2023a). Here we present the modelling efforts and progress made by SNL within the current DECOVALEX task. As a result, the reader will be referred to the final task specification (LaForce et al., 2023a) for more detailed discussions on model concept and development throughout Section 2.3.

2.3.2 Geologic Setting

The salt reference case considers a mined repository for SNF and vitrified high-level radioactive waste (HLW) in a salt dome. The generic geological cross section of a salt dome developed for the RESUS project (Bertrams et al., 2020a) is simplified to six homogeneous geologic units for use in this reference case (Figure 2-24). It is assumed that the salt dome geometry shown in Figure 2-24 extends for 9 km perpendicular to the plane of the cross section. The ground surface is at about 50 m above mean sea level (amsl) and the top of the salt dome is roughly -150 m amsl. The base of the salt diapir is at about -3150 m amsl and is underlain by basement rock, which extends to the base of the section at about -5,500 m amsl. The repository is mined at a depth of 850 m below the ground surface, such that the floor of the repository is at an elevation of -800 m amsl.
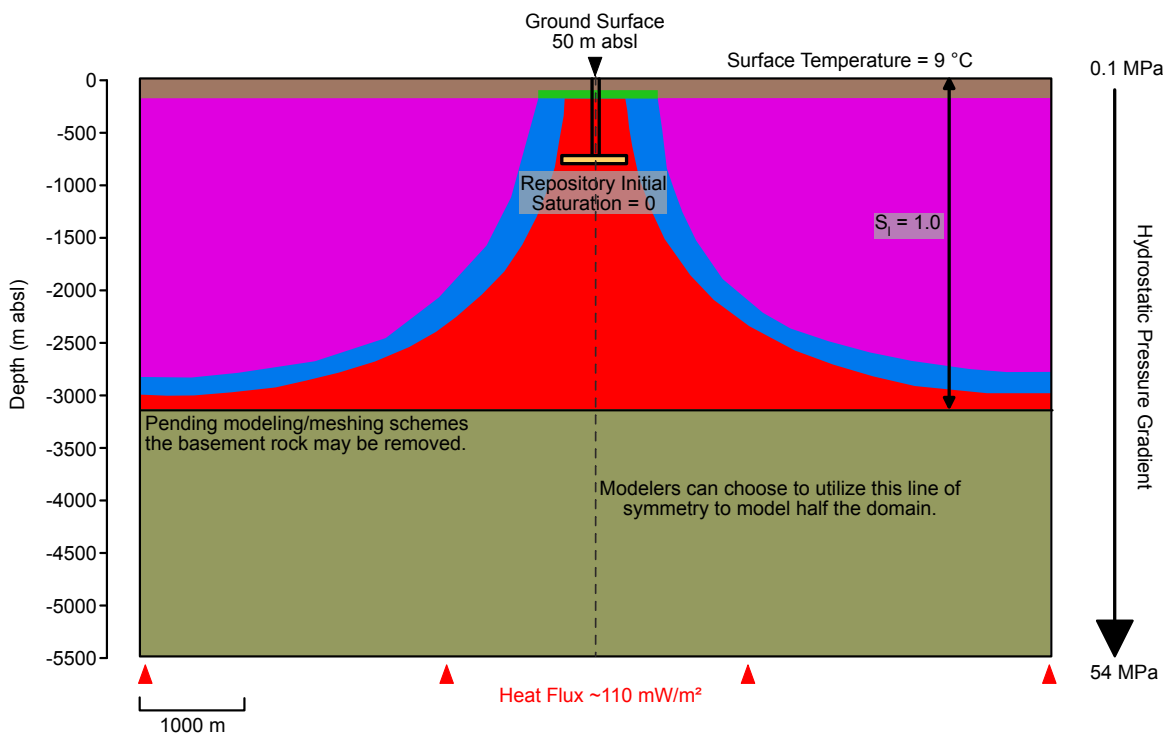
Figure 2-24. **Geologic cross-section of simplified salt dome with initial conditions shown for fluid pressure and fluid saturation (Edited from LaForce et al., 2023a)**

2.3.3   Repository

The floor of the repository is located at a depth of 850 m below the ground surface (-800 m amsl). The repository is oriented so that the emplacement drifts are perpendicular to the orientation of the salt dome in Figure 2-24. With the repository oriented this way and positioned in the center of the salt dome, it results in a line of symmetry through the repository and salt dome that is utilized here to reduce the computational resources required for simulation. The repository is accessed by two shafts that extend vertically out of the salt dome formation through the cap rock and to the surface.

Within the repository there are three sets of 25 emplacement drifts with a drift spacing of 35 m center–to–center. The waste package spacing for the two sets of SNF drifts is 3 m end–to–end in an emplacement drift 90 m long with a total of 10 waste packages per drift for a total of 500 POLLUX-10 waste packages. The vitrified waste emplacement area consists of 25 emplacement drifts with 35 m center-to-center drift spacing. Each 45 m long drift contains 10 vertical boreholes with a center–to–center spacing of 4.5 m; two waste packages per borehole gives a total of 500 vitrified waste packages (Figure 2-25).

The dimensions of all emplacement drifts and access tunnels within the repository are the same, at 7 m width and 4 m height. The infrastructure has a total volume of 240,000 m^3, with dimensions of 240 m × 250 m × 4 m.
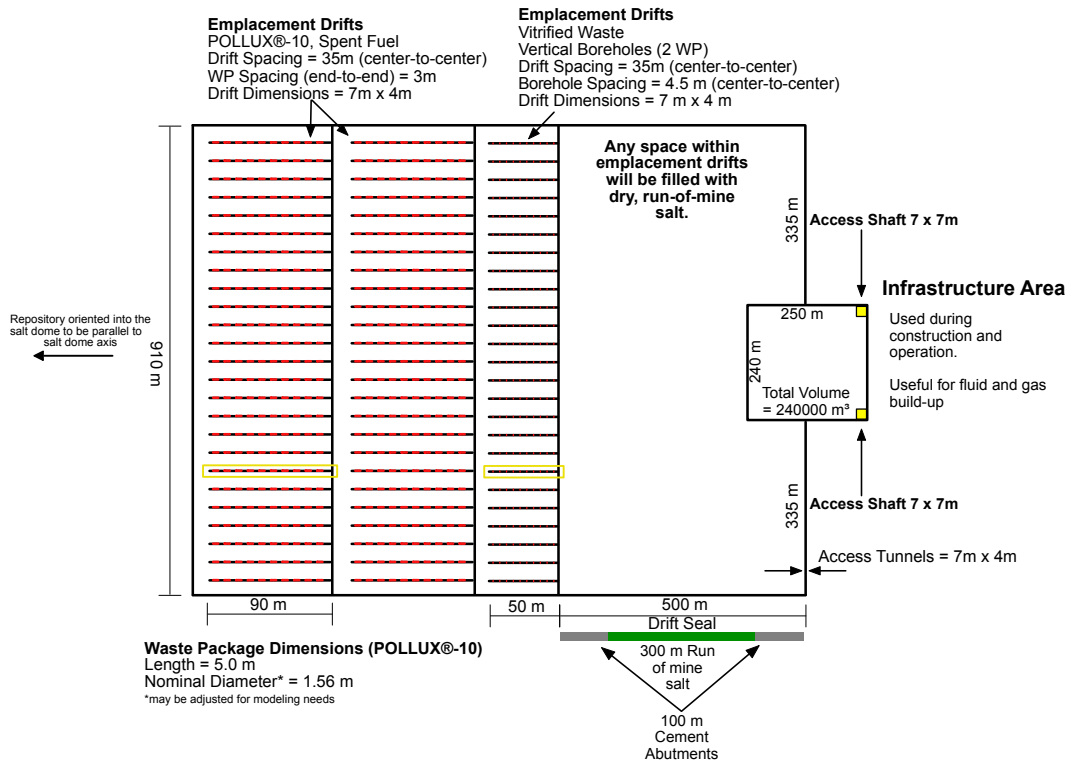
Figure 2-25.   Map view schematic of the salt reference case repository.

2.3.4   Inventory

The salt reference case assumes small inventories of SNF and HLW to reduce the computational burden. For the same reason, the radionuclides included in transport simulations are limited to a two mobile, long-lived fission products, ^{129}I and ^{99}Tc, and a single transuranic decay chain ($^{238}U \rightarrow {}^{234}U \rightarrow {}^{230}Th \rightarrow {}^{226}Ra$). Additionally, three non-sorbing conservative tracers are modeled. Tracers 1 and 2 exist only in the SNF waste packages and Tracer 3 exists only in the HLW glass. The complete inventories and release mechanisms can be found in LaForce et al. (2023a, Section 4.5).

2.3.5   Model Development

2.3.5.1   *Cartesian Meshing (Geologic formations and repository layout)*

The workflow used here to create the cartesian mesh utilizes PFLOTRAN's internal structured meshing method. Inputs for the cartesian mesh include the total dimensions of the model domain with the number of grid cells in the X, Y, and Z directions. The current model domain is 490 m × 932 m × 940 m, consisting of 4,309,900 grid cells. The dimensions of each grid cell are 7 m × 3.557 m × 4 m. These dimensions were chosen to match the height and width of the drifts and shaft proposed for the Task F2 repository. The final mesh (Figure 2-26) utilizes ½ symmetry to reduce computational demand associated with the given repository scenario. The model domain contains 24 SNF disposal drifts, 12 HLW drifts, a drift seal of two 100 m cement abutments with 300 m run-of-mine (ROM) salt in-between them, an infrastructure area, a simplified shaft seal (homogenous material properties), and an overburden layer where an aquifer is located.

While steps were taken to reduce the complexity of the meshing and simulations described above, additional assumptions are made to help with numerical convergence:

   (1).   Only the domal salt geologic formation is accounted for explicitly in the model.

   (2).   Drifts are meshed, but individual waste packages are not. Each disposal drift is treated as one waste package containing the sum of all radionuclides from each waste package within an individual drift.

   (3).   Shaft and drift seals are simplified into one homogeneous material.
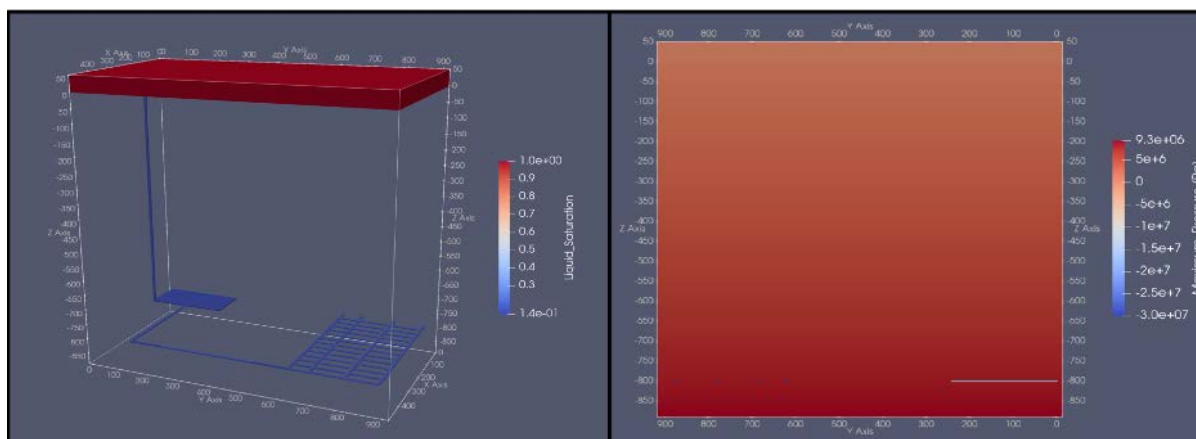
Figure 2-26.   The repository, shaft, and overlying aquifer showing initial fluid saturation (left). A Y-Z plane view of the model domain (right) illustrates liquid pressure is hydrostatic within the intact salt and negative within the repository to achieve 20% initial liquid saturation.

2.3.6   Flow and Transport Methods

PFLOTRAN Richards' mode is chosen to simulate mass transport within the repository which assumes a single phase, variably saturated, isothermal system. The Richards' set of equations are chosen by the participating teams in DECOVALEX Task F keep computational requirements low and to allow for alike comparisons. The initial pressure and saturation profiles are shown in Figure 2-26. Initial conditions for fluid pressure are hydrostatic from the surface at 50 m amsl at 101325 Pa to 9.6 MPa at 890 m amsl (940 m below land surface). The initial fluid pressure conditions within the repository are -30 MPa, this is due to the use of Richards' flow. In order to set an initial liquid saturation near 20% within the repository a

negative liquid pressure is required to result in a capillary pressure associated with liquid saturation less than 100%. In order to simulate radionuclide release and transport the Global Implicit Reactive Transport (GIRT) mode is utilized in PFLOTRAN along with two process models: (1) Waste Form Process Model represents waste package degradation and waste form dissolution for the simulation of a nuclear waste repository and (2) Used Fuel Disposition Decay Process Model performs radionuclide isotope decay, ingrowth, and phase partitioning, for the simulation of a nuclear waste repository.

2.3.6.1   Geomechanic Implementation and Simplification

LaForce et al. (2023a) describes in detail the implementation for drift convergence based on Gorleben data (Bertrams et al., 2020b) as computed by LOPOS (LaForce et al., 2023a). The resulting drift convergence rate and resulting porosity as a function of time are shown in Tables 7-1 through 7-3 of LaForce et al. (2023a). Permeability is also defined as a function of time with a Kozeny-Carmen type equation (LaForce et al., 2023a, Eq. 4-20). With the geomechanical limitations of the current version of PFLOTRAN, simplifications are made to implement some of the geomechanical effects of drift convergence. Porosity does not change with time; this simplification is important for the conservation of mass in PFLOTRAN. Instead, here we make a stepped permeability change with time. At 1,000 years when the shaft fails, the drift convergence is considered complete resulting in any crushed salt within the repository to assume the properties of intact salt, in this case permeability ($10^{-17} \rightarrow 10^{-21}$ m^2). This assumption speeds up the drift convergence process with respect to permeability as described in LaForce et al. (2023a). When porosity decreases, pore fluid pressure increases, and due to the much higher compressibility of the gas phase, water saturation eventually increases. As pore fluid pressure increases it causes the pressure gradient from the shaft to the drifts to decrease, resulting in slower brine flow within the repository. In future simulations a stepped permeability change with time may be used to match drift convergence more accurately.

2.3.7   Flow Results

Figure 2-27 illustrates how the repository re-saturates slowly over time. At 500 years (Figure 2-27(A)), the shaft is slowly becoming saturated starting near the surface and liquid is migrating down towards the repository. The drifts leading away from the infrastructure area towards the disposal drifts have also increased in saturation slightly. This is due to a small amount of brine inflow from the intact salt surrounding the disposal drifts. Once the shaft seal fails at 1,000 years, the bulk permeability of the shaft seal increases by two orders of magnitude. This can be seen in Figure 2-27(B) at 2,500 years, the shaft is fully saturated, the infrastructure area is becoming saturated, as well as the drifts near the infrastructure area. Figure 2-27(C) and Figure 2-27(D) illustrates how the remaining drifts become saturated at 5,000 and 10,000 years, respectively. The entire repository is 100% liquid saturated by 15,000 years.
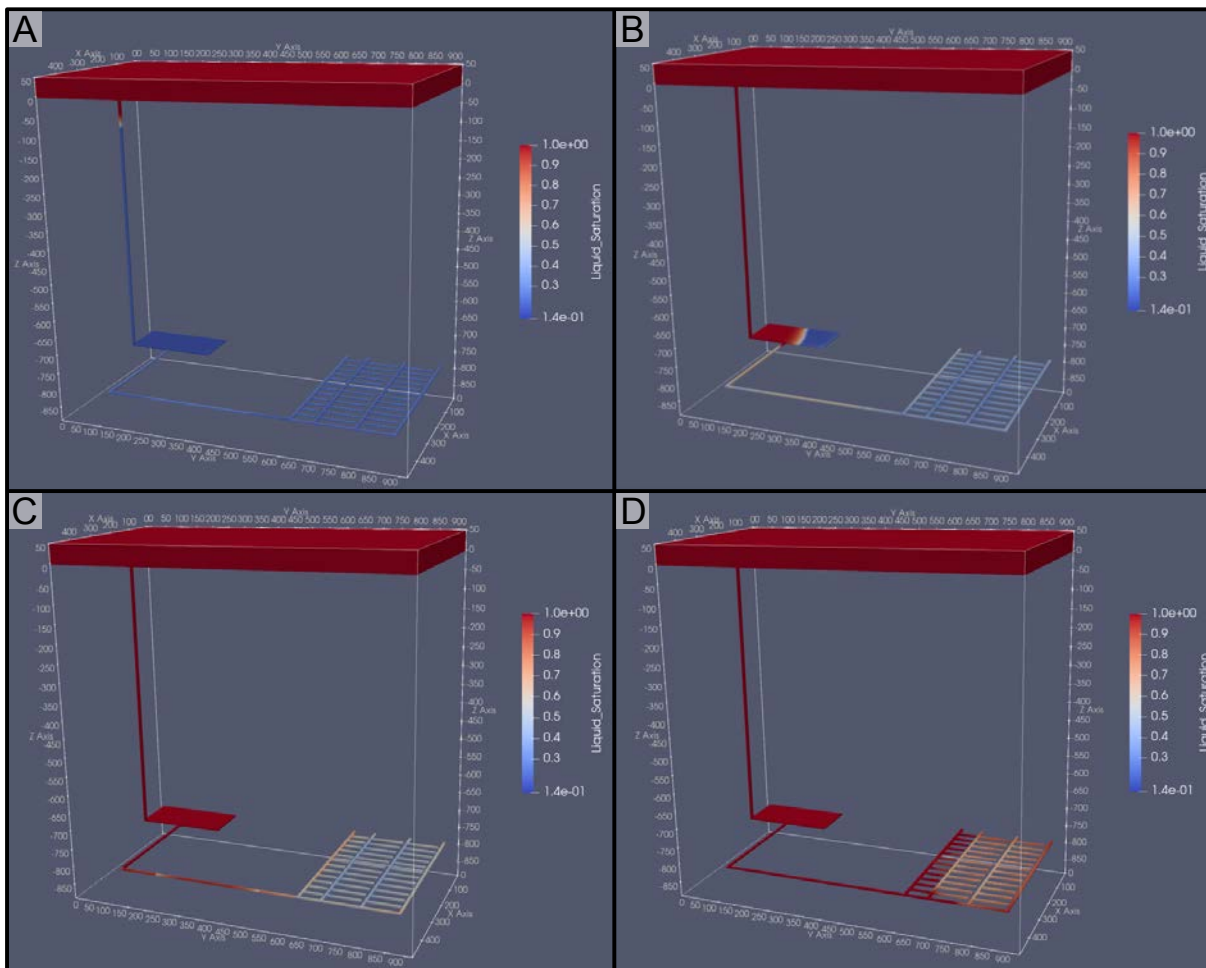
Figure 2-27. **Liquid saturation in the repository at (A) 500 years, (B) 2,500 years, (C) 5,000 years, and (D) 10,000 years.**

Figure 2-28 helps illustrate the evolution of liquid saturation within the repository by showing liquid saturation over time at six regions of interest. Before the shaft seal fails, the ROM salt and disposal drifts begin to slowly saturate due to slow brine inflow from the intact salt. The infrastructure area does not begin to saturate, due to brine inflow from the intact salt, because it is a large area with higher porosity and the inflow from the intact salt is negligible. After 1,000 years when the shaft seal fails, the infrastructure area begins to re-saturate rapidly. As the infrastructure area becomes saturated with water from the surface, the flow then begins to move through the repository to the drift seal closest to the shaft, the ROM salt in the drift seal, the drift seal nearest to the waste, the vitrified waste drift, and finally the HLW drifts all become fully saturated.
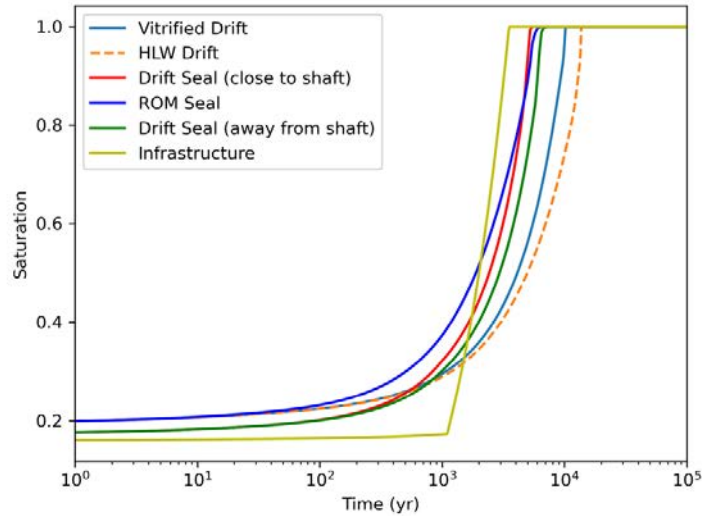
Figure 2-28.   Liquid saturation over time at regions of interest within the repository

2.3.8   Tracer and Radionuclide Concentrations

Tracer and radionuclide transport within the repository is limited to the disposal drifts, the first cement drift seal, and the ROM salt within the drift seal (Figure 2-29 through Figure 2-32). There is no appreciable amount of tracer or radionuclide transport past the drift seal into the infrastructure area or the shaft. Radionuclide and tracer mass within the first grid cell of the 100 m cement abutment of the drift seal closest to the waste is shown in Figure 2-29, where Tracer 3 (1.2×10^{-5} moles) and ^{99}Tc (3.8×10^{-6} moles) are most abundant. These results are intuitive given that Tracer 3 and ^{99}Tc have the shortest distance to travel from the vitrified waste drift to the seal, they are released instantly and have low/no retardation and do not decay.
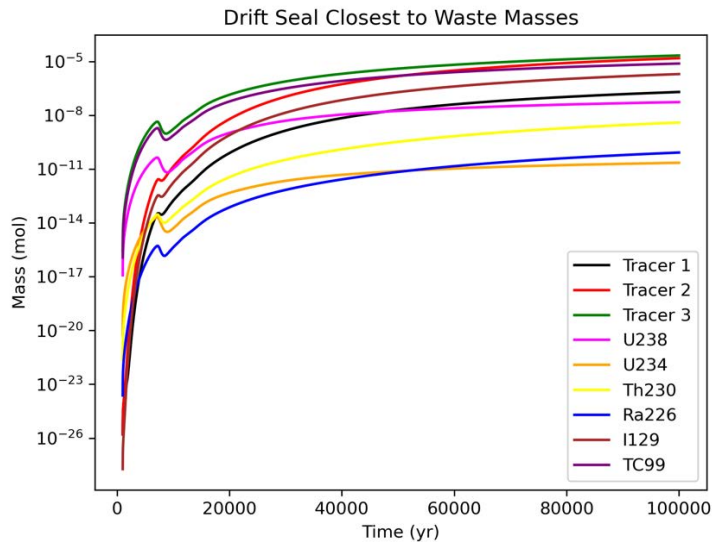
Figure 2-29.   Radionuclide and tracer masses within the concrete abutment of the drift seal closest to the waste disposal drifts.

Figure 2-30 shows the tracer and radionuclide masses in the first grid cell of the ROM salt between the two cement abutments within the drift seal. Like Figure 2-29, Tracer 3 and ^{99}Tc are the most abundant radionuclides, but their total masses have decreased by two to three orders of magnitude. This highlights the effectiveness of the drift seal for the given scenario and material properties.
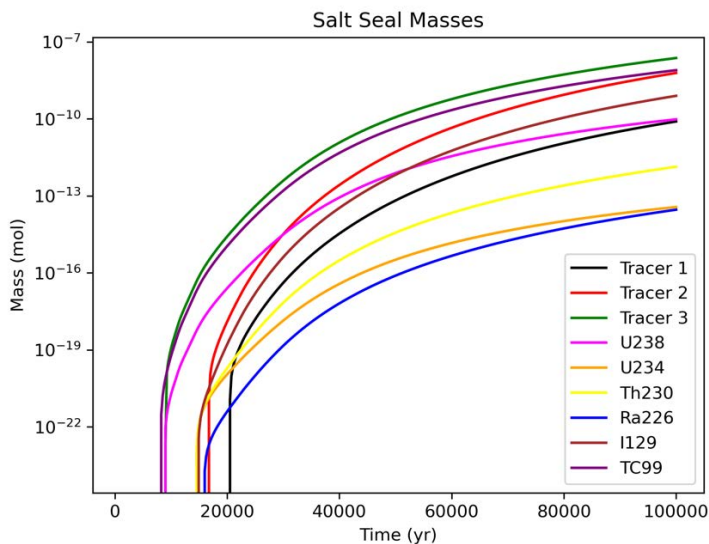
Figure 2-30.   Radionuclide and tracer masses within the run-of-mine salt between the two concrete abutments within the drift seals

Finally, moving onto the drift seal closest to the shaft (Figure 2-31) and the shaft seal 25 m above the infrastructure area (Figure 2-32), we see no radionuclides transported past the drift seal. The values shown in Figure 2-31 and Figure 2-32 are insignificant, with the most abundant radionuclide at ~10^{-20} moles. Additionally, multiple tracer and radionuclide data plot directly on top of each other, resulting in Figure 2-31 and Figure 2-32 appearing to only have three different curves. This highlights how small the changes in radionuclide and tracer mass over the 100,000-year simulation.
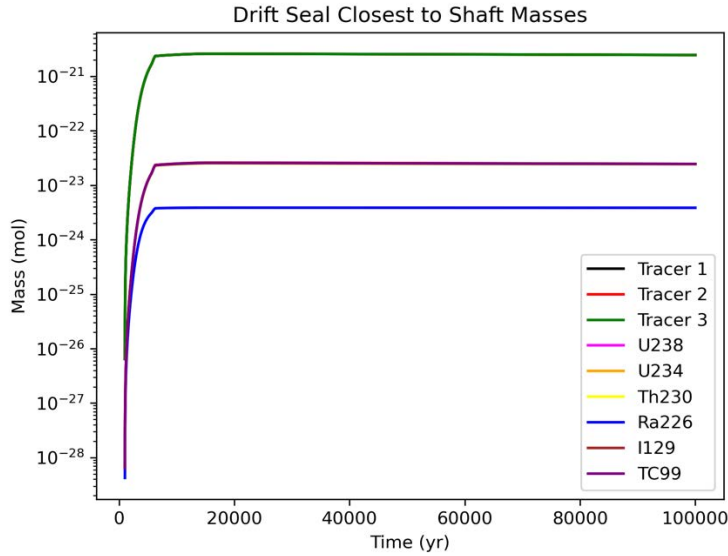
Figure 2-31. **Radionuclide and tracer masses within the concrete abutment within the drift seal closest to the shaft. Note that some curves are not seen because the data plot on top of one another.**
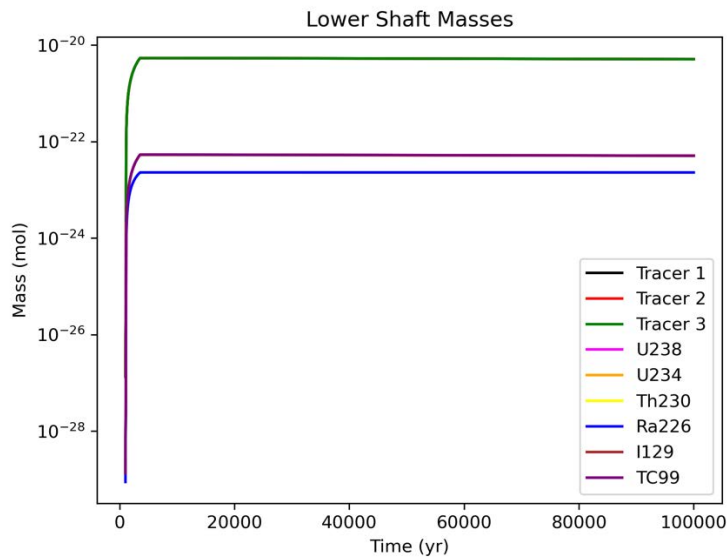
Figure 2-32. **Radionuclide and tracer masses within the shaft 25 meters above the infrastructure area. Note that some curves are not seen because the data plot on top of one another.**

2.4   Summary

Previous PAs have shown that there are no radiological consequences within 1,000,000 years for disposal in undisturbed salt formations because of their very low permeability and moisture content. As a result, we present a PA of a shaft failure scenario to force the repository to re-saturate rapidly. The shaft failure scenario has provided interesting results in terms of pressure and saturation evolution within the repository for the teams of DECOVALEX 2023 Task F2 to compare against. Even with the shaft seal failing after only 1,000 years, radionuclide transport is contained to the disposal drifts and part of the drift seal. The current PA provides promising results highlighting the robustness of a salt dome waste repository, but more work is required. As mentioned above, this is a staged development of models building up to a full PA. The addition of heat flow and temperature-dependence of drift convergence, model uncertainty in backfill consolidation model, and potentially gas generation need to be incorporated. As PFLOTRAN development continues a few of the simplifications made here may be improved upon, such as salt creep and individual discretization of the waste packages.

This page is intentionally left blank.

3.   SHALE PERFORMANCE ASSESSMENT CASE

Clay-rich sedimentary strata have been considered a potential medium for disposal of radioactive waste in the United States (U.S.) since the forerunner to the DOE introduced a program to develop radioactive waste disposal technology in 1976 (Shurr, 1977; Gonzales & Johnson, 1985; Rechard et al., 2011). Clay-rich formations are an attractive disposal medium due to their low permeability, high sorption capacity, typically reducing porewaters (which limit radionuclide solubility), and ability to deform plastically, which promotes self-healing of fractures. The U.S. hosts several marine sedimentary sequences containing thick beds of clay-rich sediments potentially suitable for deep geologic disposal of radioactive waste (Gonzales & Johnson,1985; Perry et al., 2014; Perry & Kelley, 2017). This section builds on the generic shale/argillite/clay reference case reported in Mariner et al. (2017), the shale Geologic Framework Model (GFM) presented in Sevougian et al. (2019a), the deterministic shale reference case in Sevougian et al. (2019b), and the stochastic reference case in Swiler et al. (2019). The conceptual geological model is developed in Sevougian et al. (2019b) and is unchanged in the present work.

One primary goal of updating this reference case is to automate running the performance assessment (PA) by utilizing the Next Generation Workflow (NGW) of Dakota. Several smaller changes are implemented, such as having an open boundary at the north edge of the domain, additional monitoring points in and around the repository to study near-field processes, and inclusion of additional epistemic uncertain parameters. A coarser mesh simulation is also conducted in support of a multi-fidelity model study for the Geologic Disposal Safety Assessment (GDSA) Sensitivity Analysis and Uncertainty Quantification (SA/UQ) work package.

The largest change from the 2019 shale PA model (Sevougian et al., 2019b; Swiler et al., 2019) is the focus on waste package thermal output. This includes a deterministic study of PA simulations with heat distributions that are representative of as loaded dual-purpose canisters (DPCs) in inventory in the U.S. The reason for this year's focus on hotter waste packages is that the mixture of 24 and 37 DPCs in Sevougian et al. (2019b) and Swiler et al. (2019) is too hot on average to be representative of current waste packages in inventory (Jones et al., 2021) and does not include any waste packages representative of the 90% hottest waste packages in inventory. Thus, implementing a wider and more representative range of waste package heats improves the realism of the PA case. It also tests the conceptual model of the repository and the capability of the simulator on the hottest waste packages that could reasonably be expected in a repository.

Heat energy emitted from DPCs can cause pressurization and thermal stressing in the repository system due to the thermal expansion of trapped pore fluids and poroelastic deformation of host rocks, respectively. These heat-driven multiphysics coupled processes can influence hydro-thermal flow and radionuclide transport in both near- and far-field of the repository as well as alter thermo-hydro-mechanical characteristics of host rocks (Yu et al., 2014; Zhang et al., 2017).

In the near-field, the engineered barrier system (EBS) and host rock influence each other thermally by heat flow, hydraulically by single- or multi-phase fluid flow, mechanically by buffer swelling, and chemically by exchange of radioactive solutes between groundwater and pore water in the EBS and host rock. In the far-field, radioactive isotopes released from the breached canisters will migrate, and the transport rate of radionuclides will be controlled by in-situ hydraulic and geological conditions (e.g., direction of groundwater flow, presence of hydraulic pathways).

Section 3.1 discusses the current shale conceptual and simulation model, including the changes from the 2019 case. Section 3.2 discusses the impact of utilizing waste package heat distributions that are representative of loaded DPCs in inventory in the U.S. Section 3.3 discusses the set of 50 stochastically-generated simulations that were run in support of the GDSA SA/UQ work package.

3.1 Model Description, Base Case, and Variant Results

The methodology used to develop the shale GFM is documented in detail in Sevougian et al. (2019a). The Pierre Shale was chosen as the basis of the shale conceptual model due to its large areal extent, thickness (>400 meters), accessible depth, stable tectonic history, and desirable mechanical and hydrologic properties (Perry & Kelley, 2017).

3.1.1 Numerical Model Setting

3.1.1.1 Model Domain

The computational domain is 7,215 m (x-axis) × 2,055 m (y-axis) × 1,200 m (z-axis) and represents a shale-hosted repository system in a layered formation (Figure 3-1A). The center of repository with the waste packages is located at depth of 402.5 m below land surface, the top of the model domain. The numerical domain consists of approximately 9.88×10^6 unstructured grid cells, of which 4.6×10^6 are the finer cells in and around the repository to resolve repository-scale features (Figure 3-1B). The repository is discretized into volumetric cells of size $5/3 \times 5/3 \times 5/3$ m^3, while most of other regions are discretized into $15 \times 15 \times 15$ m^3 cells for the base case and $45 \times 45 \times 45$ m^3 cells for the coarse model case. A waste package, consisting of three $5/3 \times 5/3 \times 5/3$ m^3 cells aligned in the y-direction, is surrounded by the bentonite buffer with a thickness of 5/3 m, representing a compacted mixture of 70% bentonite and 30% quartz sand. The voids of access drifts and shafts are filled with the buffer material to reduce the transport of radionuclides and corrosive reactants. The disturbed rock zone (DRZ) has a thickness of 5/3 m and is defined as the portion of the damaged host rock adjacent to the EBS.
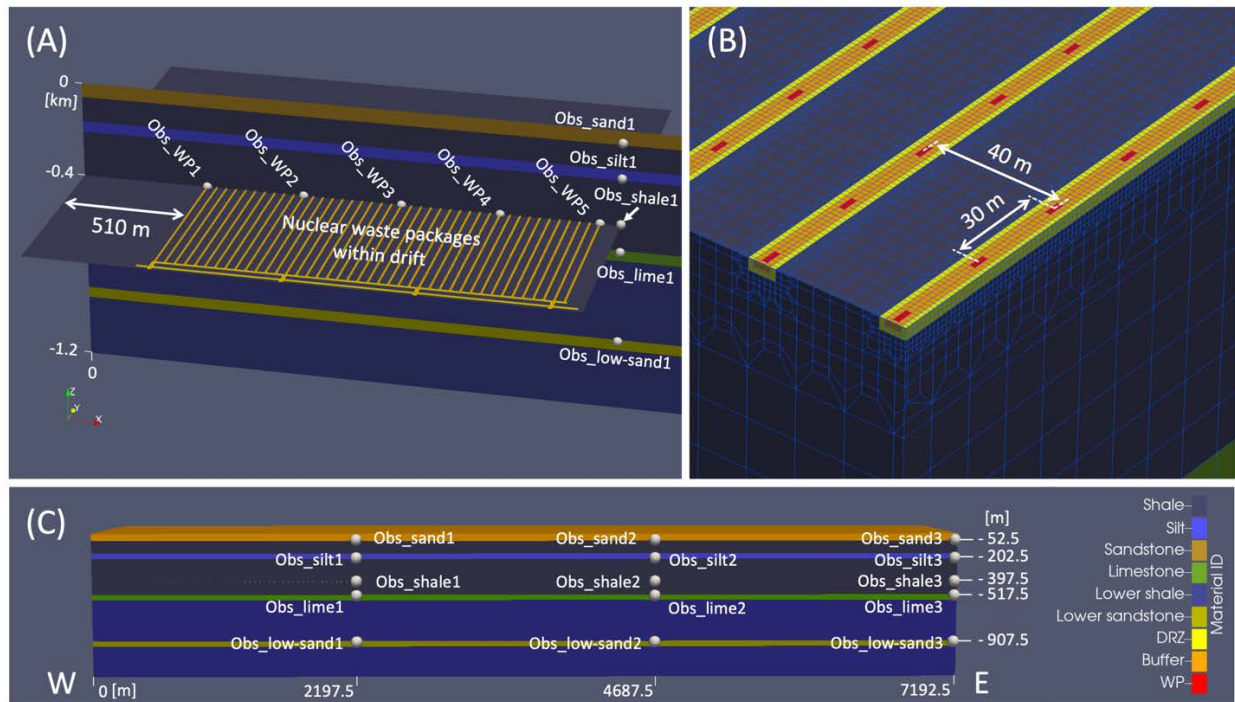
Figure 3-1. **(A) Cross-section of the model domain with xy-plane of waste packages and zx--plane. (B) Numerical domain sliced laterally through the waste packages, approximately at depth z = 404 m with mesh shown. (C) Observation points at layers in the whole domain. The temporal evolution of physical quantities is reported at the observation points in x-direction at depth of 402.5 m as well as in z--direction.**

Prior to installing waste forms, the localized DRZ experiences durable (but not necessarily permanent) perturbations of hydrological and/or mechanical characteristics of the host rock (e.g., fracture opening) due to excavation for the repository. In this model, the initial enhancement of hydraulic diffusivity by excavation-driven fracturing is represented implicitly by assigning one order of magnitude larger permeability than the permeability used for the host rock to the DRZ. Note that the use of stress-dependent DRZ permeability function may describe the short term (less than 10^3 years) and near-field impact of hydro-thermal flow, driven by heat pulse from waste packages, on hydraulic characteristics of the DRZ (Chang et al., 2021; Sasaki & Rutqvist, 2021; Chang et al., 2022), but this is not implemented in this study.

The natural barrier system comprises the DRZ and the shale formation surrounding the repository. This field-scale model includes interbedded high-permeability layers (i.e., silt, sandstone and limestone sequences) above and below the shale host rock (Figure 3-1A & C), such that long-term heat-driven flow and transport in a vertical direction may release radioactive nuclides into the far-field along these conductive paths. The hydro-thermal properties of all materials in the base case model are constant over time as given in Table 3-1.

Table 3-1.   Flow, thermal, and van Genuchten parameters for the reference model.

Flow and thermal properties							
	Buffer	**DRZ**	**Host shale**	**Sandstone***	**Silt**	**Limestone**	**Lower shale**
Porosity	0.35	0.2	0.2	0.2	0.2	0.1	0.1
Permeability [m^2]	1×10^{-20}	1×10^{-18}	1×10^{-19}	1×10^{-13}	1×10^{-17}	1×10^{-14}	1×10^{-20}
Density [kg/m^3]	2700	2700	2700	2700	2700	2700	2700
Heat capacity [J/(kg-K)]	830	1005	1005	830	830	830	1005
Dry thermal conductivity [W/(K-m)]	0.6	0.6	0.6	1.0	0.8	1.0	0.6
Wet thermal conductivity [W/(K-m)]	1.5	1.2	1.2	3.1	1.4	2.6	1.2
Initial gas saturation	0.7	0.0	0.0	0.0	0.0	0.0	0.0
Residual liquid saturation	0.1	0.1	0.1	0.1	0.1	0.1	0.1
Residual gas saturation	0.1	0.1	0.1	0.1	0.1	0.1	0.1
van Genuchten saturation function							
alpha [1/Pa]	6.25×10^{-8}	6.67×10^{-7}	6.67×10^{-7}	1×10^{-4}	6.67×10^{-7}	1×10^{-4}	6.67×10^{-7}
Lambda	0.375	0.333	0.333	0.5	0.333	0.5	0.333

* The lower sandstone layer has the same properties of the sandstone layer.

3.1.1.2   Initial and Boundary Conditions

Initial pressures and temperatures throughout the model domain are calculated by applying a liquid flux of 0 m/s and an energy flux of 60 m-W/m^2 to the base of the domain and holding temperature (10 °C) and approximately atmospheric pressure constant at the top of the domain and allowing the simulation to run to 10^6 years. Pressure decreases from west (left) to east (right) with a head gradient of -0.0013 m/m. This setting results in initial conditions that represent a geothermal temperature gradient, hydrostatic pressure gradient in the vertical direction, and a horizontal pressure gradient that drives flow from west to east. The whole geologic formation is fully saturated with water, while in the repository the buffer sections are unsaturated initially ($S_{gi,buffer} = 0.7$). The chemical/radioactive transport is solved for 18 radionuclides listed in Table 3-2, and initial concentrations of all radionuclides in all cells are 10^{-20} mol/L.

Table 3-2. Inventory of selected radionuclides.

Isotope	Atomic Weight [g/mol]	Decay constant [1/s]	Inventory [g/g-waste]*	
			24-PWR†	37-PWR‡
^{241}Am	241.06	5.08×10^{-11}	9.45×10^{-4}	9.42×10^{-4}
^{243}Am	243.06	2.98×10^{-12}	9.57×10^{-5}	1.86×10^{-4}
^{238}Pu	238.05	2.56×10^{-10}	8.40×10^{-5}	1.33×10^{-4}
^{239}Pu	239.05	9.01×10^{-13}	4.43×10^{-3}	5.14×10^{-3}
^{240}Pu	240.05	3.34×10^{-12}	1.78×10^{-3}	2.84×10^{-3}
^{242}Pu	242.06	5.80×10^{-14}	3.92×10^{-4}	5.67×10^{-4}
^{237}Np	237.05	1.03×10^{-14}	6.03×10^{-4}	1.05×10^{-3}
^{233}U	233.04	1.38×10^{-13}	1.82×10^{-8}	4.61×10^{-8}
^{234}U	234.04	8.90×10^{-14}	2.25×10^{-4}	4.18×10^{-4}
^{236}U	236.05	9.20×10^{-16}	3.29×10^{-3}	4.37×10^{-3}
^{238}U	238.05	4.87×10^{-18}	6.48×10^{-1}	6.32×10^{-1}
^{229}Th	229.03	2.78×10^{-12}	4.19×10^{-12}	1.84×10^{-11}
^{230}Th	230.03	2.75×10^{-13}	5.19×10^{-8}	1.26×10^{-7}
^{226}Ra	226.03	1.37×10^{-11}	2.12×10^{-11}	7.04×10^{-11}
^{36}Cl	35.97	7.30×10^{-14}	2.44×10^{-7}	3.48×10^{-7}
^{99}Tc	98.91	1.04×10^{-13}	6.36×10^{-4}	8.89×10^{-4}
^{129}I	128.9	1.29×10^{-15}	1.50×10^{-4}	2.17×10^{-4}
^{135}Cs	134.91	9.55×10^{-15}	3.37×10^{-4}	5.36×10^{-4}

*[g/g-waste] = [g-isotope/MTHM]/ [g-waste/MTHM], where [g-waste] = [g-all isotope] and MTHM is metric tons initial heavy metal.

† 40 Gwd/MTHM burn-up, 100-year OoR (out of reactor)

‡ 60 Gwd/MTHM burn-up, 150-year OoR

This model was run in PFLOTRAN GENERAL and Global Implicit Reactive Transport (GIRT) modes, which solves two-phase (liquid-gas) miscible flow and solute transport coupled to energy for unsaturated conditions in waste packages and buffer, which have been used for multi-scale and multi-physics PA simulations of geological nuclear waste repository systems (Sevougian et al., 2019b; Mariner et al., 2020; Mariner et al., 2021; LaForce et al., 2020; LaForce et al., 2021; LaForce et al., 2022a).

3.1.1.3   Spent Fuel Inventory

This field-scale models assume that the spent fuel inventory consists entirely of pressurized water reactor (PWR) spent nuclear fuel (SNF) assemblies, each containing 0.435 MTHM (metric tons initial heavy metal). In the two simulation studies, two DPC waste package configurations are considered, the 24-PWR and 37-PWR waste packages. Table 3-2 shows the radionuclide inventory at the time of emplacement by assuming an initial enrichment of 3.72 wt % ^{235}U, 40 GWd/MTHM burn-up, and 100-year OoR (out-of-reactor) surface storage for 24-PWR and of 4.73 wt % ^{235}U, 60 GWd/MTHM burn-up, and 150-year OoR storage for 37-PWR.

3.1.1.4   Chemical Environment: Solubility and Adsorption

This study assumes homogeneous solubility limits throughout the whole domain that neglects near-field complexity within the repository system (Sevougian et al., 2019b). Adsorption is modeled using a linear isotherm; distribution of a solute between the aqueous and adsorbed phase is characterized by the distribution coefficient Kds given in Table 3-3, where the concentration in the adsorbed phase is proportional to the concentration in the aqueous phase. The details of procedure to generate the material-specific Kd values are found in Mariner et al. (2017).

Table 3-3.   Chemical environment setting.

Element	Solubility limit [mol/L]	Kd [kg-water/m³-bulk]		
		Shale*	**Buffer**	**Aquifer†**
Am	4×10^{-7}	1.08×10^{8}	2.11×10^{7}	2.17×10^{5}
Pu	2×10^{-7}	1.94×10^{6}	1.76×10^{6}	1.09×10^{6}
Np	4×10^{-9}	1.94×10^{6}	1.76×10^{6}	3.44×10^{6}
U	7×10^{-7}	1.73×10^{7}	1.76×10^{6}	1.88×10^{3}
Th	6×10^{-7}	1.73×10^{7}	5.27×10^{6}	6.43×10^{6}
Ra	1×10^{-7}	2.16×10^{6}	1.76×10^{6}	Non-adsorbing
Cl	Infinitely soluble	Non-adsorbing		
Tc	4×10^{-9}	2.48×10^{6}	2.00×10^{8}	1.22×10^{5}
I	Infinitely soluble	Non-adsorbing		
Cs	Infinitely soluble	8.64×10^{5}	6.67×10^{5}	1.22×10^{6}

* For DRZ, Host/lower shale and silt layers.

† For sandstone and limestone layers.

3.1.1.5   Waste Package Breach and Waste Form Dissolution

To introduce the onset of waste form breach, the model defines a canister vitality which is a normalized measure of remaining time or remaining canister wall thickness before canister breach. The PFLOTRAN simulation implements the waste package degradation model (Mariner et al., 2016) that calculates normalized remaining canister thickness at each time step by the following equation:

$$\log_{10} R_{eff} = \log_{10} R + C\left(\frac{1}{333.15} - \frac{1}{T(t,\mathbf{x})}\right)$$ **Eq. 3-1**

where R [1/year] is a base canister vitality degradation rate, C is a canister material constant ($C = 1500$ for 316L stainless steel), and T [K] is the local temperature. The values of R are sampled at the beginning of the simulation, for each waste form, by sampling on a truncated log normal distribution with a mean of 4.5 $\log_{10}$(-1/year), a standard deviation of 0.5 $\log_{10}$(-1/year) and an upper limit of -3.5 $\log_{10}$(1/year).

The canister vitality is initialized to 1 and is reduced at each time step by the effective degradation rate. Once canister vitality drops below zero (the canister thickness becomes zero), the canister is considered breached and the waste form object inside the canister begins dissolving. The remaining radionuclide inventory in each waste package is calculated at each time since the time of waste package breach in PFLOTRAN by either instant- or slow-release fraction of each radionuclide.

The instant-release fraction is due to the accumulation of certain fission products in void spaces of the waste form, while the slow-release fraction is due to fuel matrix (UO_2) dissolution, which is modeled using a fractional dissolution rate for the waste form bulk (or matrix), in units of fractional volume per time of the remaining volume. (10^{-7} 1/year in this study). This study uses a non-zero instant-release fraction for ^{36}Cl, ^{99}Tc, ^{129}I, and ^{135}Cs (Table 3-4), and zero for all other radionuclides in the simulations.

Table 3-4.   Waste form release rate.

Isotope	Instant release fraction
^{36}Cl	0.16
^{99}Tc	0.07
^{129}I	0.1
^{135}Cl	0.1
Other isotopes	0.0

3.1.2   Coarser Mesh Development

The multifidelity UQ work in the GDSA SA/UQ work package (Swiler et al., 2023) creates a need for a coarser mesh version of the shale reference case. The original mesh developed using Cubit (Skroch et al., 2021) by Sevougian et al. (2019a) generates a model domain consisting of 9,888,556 grid cells. The coarse mesh (Figure 3-2) developed this FY with Cubit is 5,726,548 grid cells, which has about 60% fewer elements than the original mesh. Once the coarse mesh was implemented in PFLOTRAN (Hammond et al., 2014) material IDs were assigned in the repository/shafts, DRZ, drift and waste package materials, and were all checked and verified to be assigned to 'good' hex cells instead of the refined 'zig-zag' cells found in the outer repository region. These 'zig-zag' cells are used to transition to larger grid cells and can be seen in Figure 3-5 just outside the repository region. An additional check was performed to verify that observation points assigned within several material layers in the model domain were still in the correct strata.

Initial PFLOTRAN test simulations using the coarse mesh failed due to a bug reading in the unstructured grid. The GDSA PFLOTRAN DEVELOPMENT work package investigated the issue and generated a new PFLOTRAN branch (rosie/unstructured-grid-fix) that resolved the issue by adding a right had rule check for all point combinations in quad face. This fix has been merged to the master version of PFLOTRAN (Nole et al., 2023).
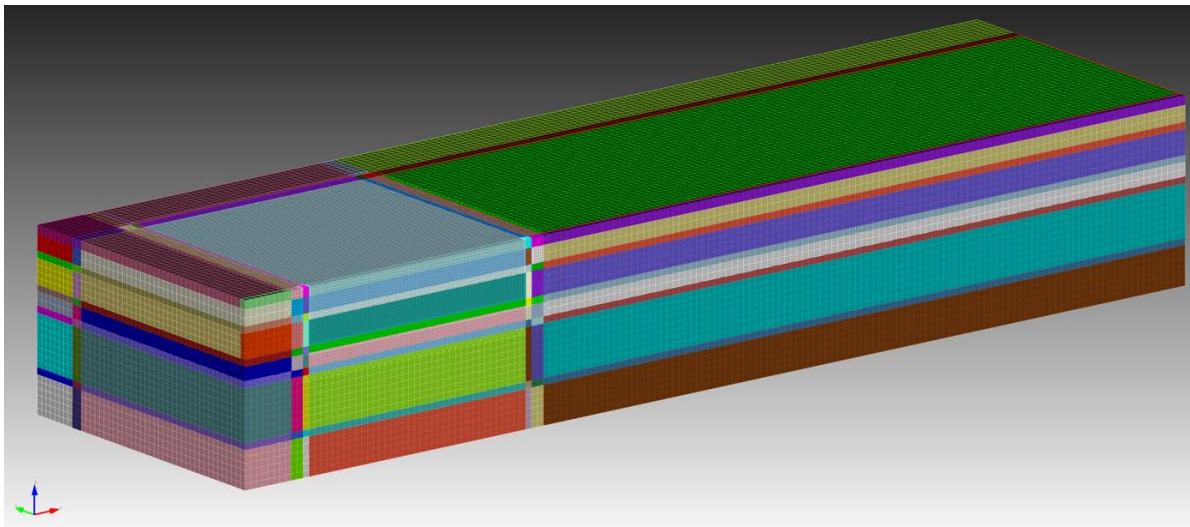
Figure 3-2.   Coarser mesh for the shale model developed and generated with the use of CUBIT meshing software.

3.1.2.1   New simulation mesh

Figure 3-3 through Figure 3-8 show comparisons between the original and newly developed coarser mesh visualized using ParaView (Ayachit, 2015). The primary difference between the two meshes is that the coarse mesh has a far-field grid cell size of $45 \times 45 \times 45$ m while the original mesh has a far-field grid cell size of $15 \times 15 \times 15$ m. Grid cell refinement at the waste package, buffer, and DRZ has not changed from the original mesh discussed in Section 3.1.1.1. The grid cell refinement in the shale material has changed slightly but the main difference can be seen in the grid cells away from the repository region which are much larger. Four material layers (lower sandstone, limestone, siltstone, sandstone) that originally consisted of a minimum of three grid cells vertically in the z-direction now consist of a single vertical grid cell in the coarser mesh (Figure 3-4). Due to larger grid cells away from the repository region within the model domain of the coarser mesh, coordinates for observation points of interest have changed. An example of this is included in Figure 3-3, where a white sphere representing the location of observation point sand_obs3 is located within the original and coarse meshes.
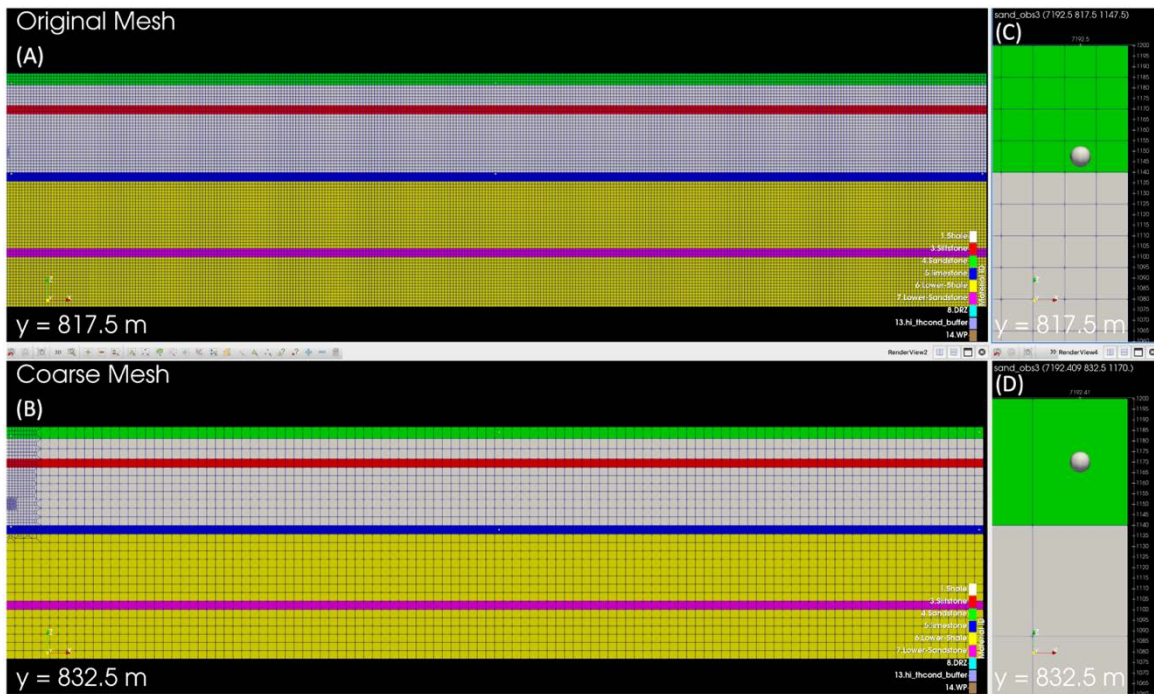
Figure 3-3. Comparison between original mesh from Sevougian et al. (2019a) and the newly developed coarser mesh visualized in ParaView. (A) shows a slice through the y-normal of the model domain in the original finer mesh, (B) slice through the y-normal of the model domain in the coarse mesh, (C) close-up of sand_obs3 in the original mesh, (D) a close-up of sand_obs3 in the coarse mesh.
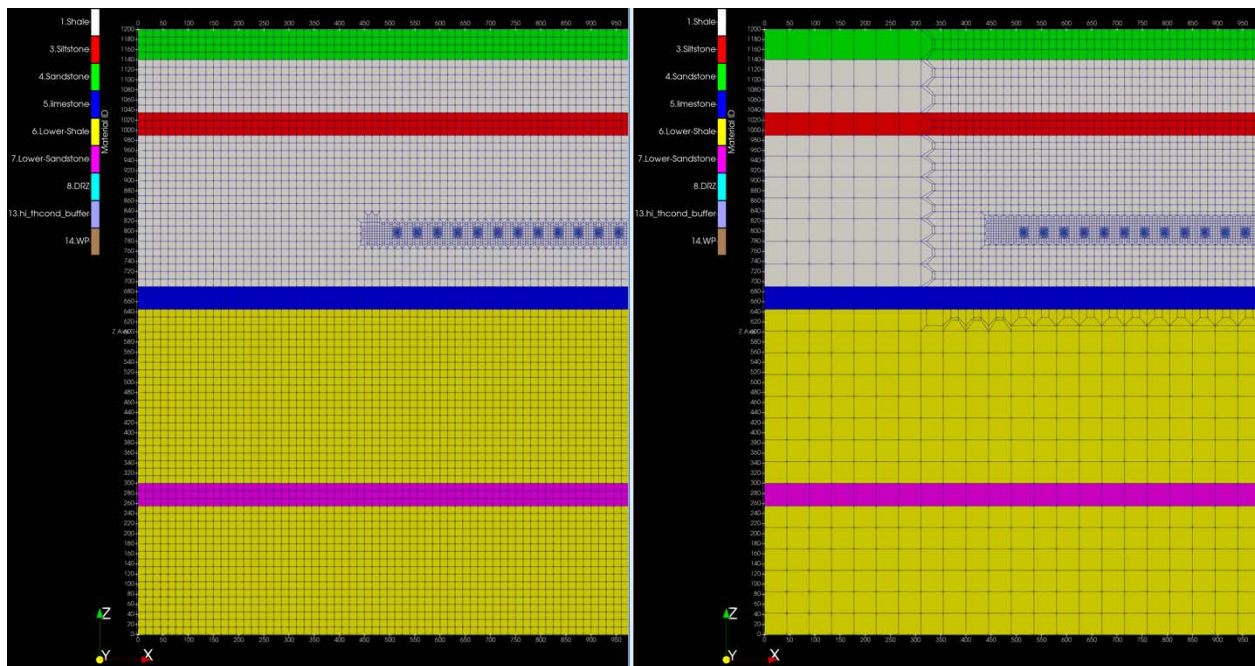
Figure 3-4. XZ slice through model domain comparison between original mesh (left) and the newly developed coarser mesh (right) visualized in ParaView.
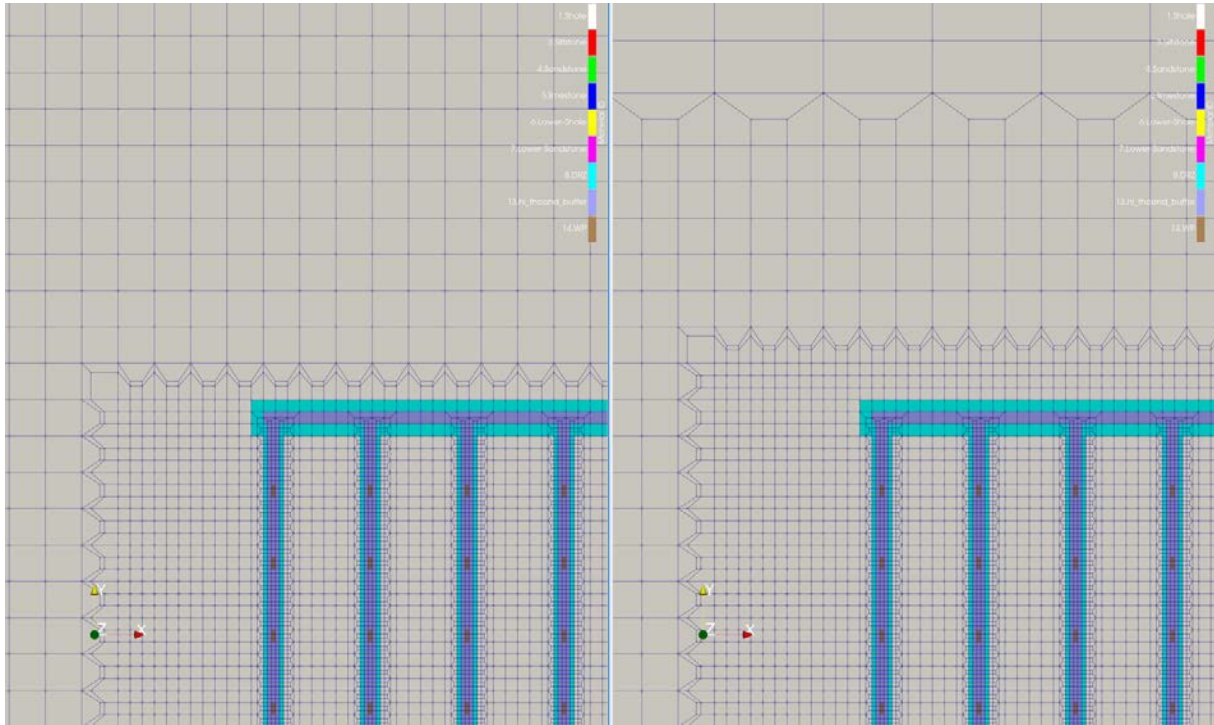
Figure 3-5. Close-up of the north-west corner of the repository on an XY slice at the repository level comparing the original mesh (left) and the newly developed coarser mesh (right) visualized in ParaView.
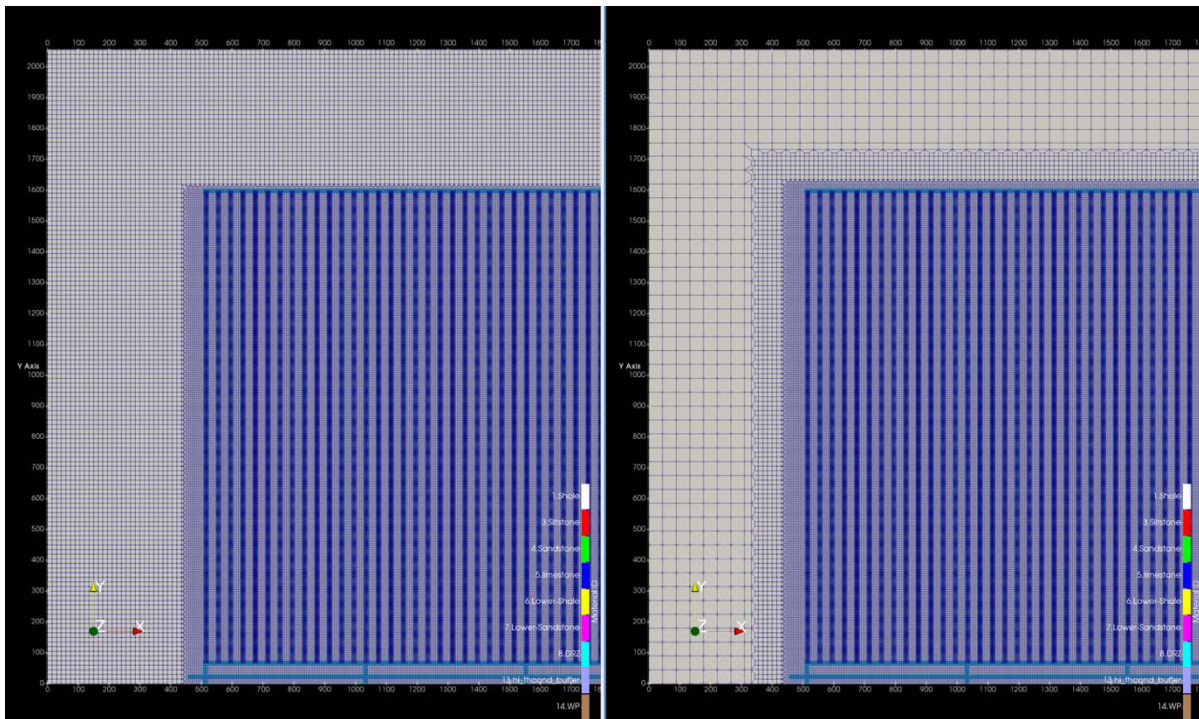
Figure 3-6. XY slice through the repository showing the comparison between original mesh (left) and the newly developed coarser mesh (right) visualized in ParaView.
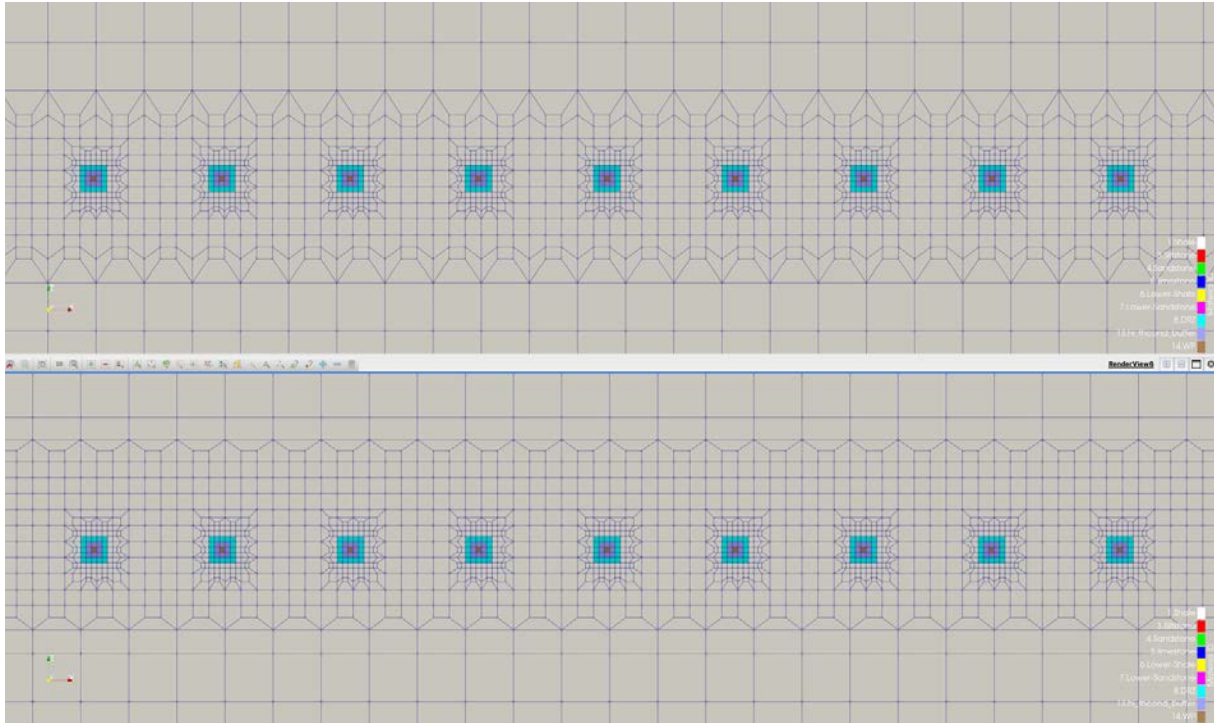
Figure 3-7. Close-up XZ slice through the center of repository comparing the original mesh (top) and the newly developed coarser mesh (bottom) visualized in ParaView.
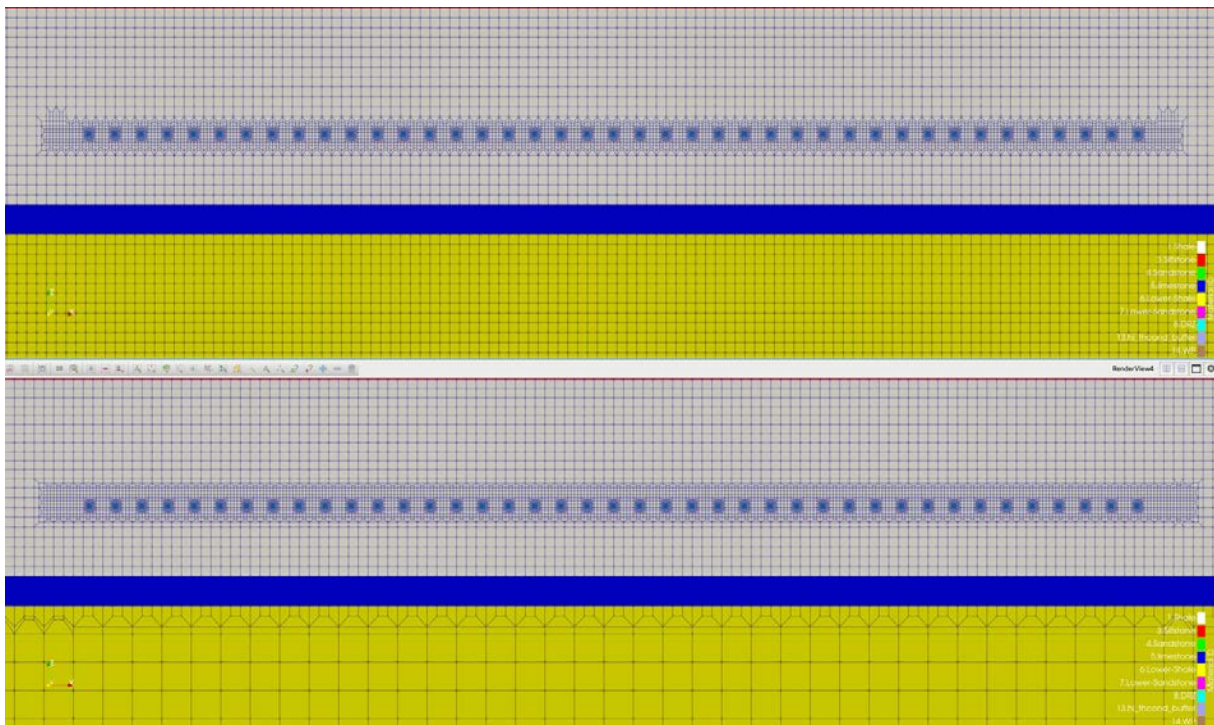
Figure 3-8. XZ slice through the center of the repository comparing the original mesh (top) and the newly developed coarser mesh (bottom) visualized in ParaView.

3.1.2.2   *Comparison of results on the original and coarse mesh*

There are two goals in comparing the fine and coarse mesh simulations. The first is to investigate the decrease runtime on the coarser mesh. The second is to determine differences in total ^{129}I concentration at one million years at observation points of interest in the model domain.

Figure 3-9 and Figure 3-10 show slices through the repository in the shale material layer colored by total ^{129}I concentration at one million years for the original mesh and two coarser mesh simulations set with varying maximum timestep size of 5,000 years and 10,000 years. There are slight differences between the finer and coarser meshes but the ^{129}I concentrations do not vary greatly for the most part.

Table 3-5 includes data values for total ^{129}I concentration at one million years for quantity of interest (QoI) at specific observation points in the model domain for the original mesh with a max timestep size of 1,000 years, coarse mesh with max timestep size of 5,000 years and a second coarse mesh simulation with max timestep size set to 10,000 years. Concentrations at sand_obs1 and lime_obs1 do not vary greatly between the three simulations since these observation points are near the repository. Very low concentrations were seen at lime_obs2 and lime_obs3 for all three simulations. Higher ^{129}I concentration can be seen on the coarser mesh at the sandstone material layer observation points downstream of the repository. Observation point sand_obs3, which is located towards the east end of the model domain, saw a two order of magnitude difference in ^{129}I concentration between the three cases. This increase in ^{129}I can be associated with increased numerical dispersion due to the larger grid cells present in the coarser mesh away from the repository region.

The runtime for the original mesh was 6.66 hours (1024 cores), for the coarse mesh with 5,000-year max timesteps ran in 4.03 hours (540 cores), and for the coarse mesh with 10,000-year max timesteps ran in 2.73 hours (540 cores). Thus, the goal of significantly decreasing the simulation time by coarsening the mesh was achieved. The impact of the coarser mesh will be investigated in a future multi-fidelity study by the SA/UQ work package.
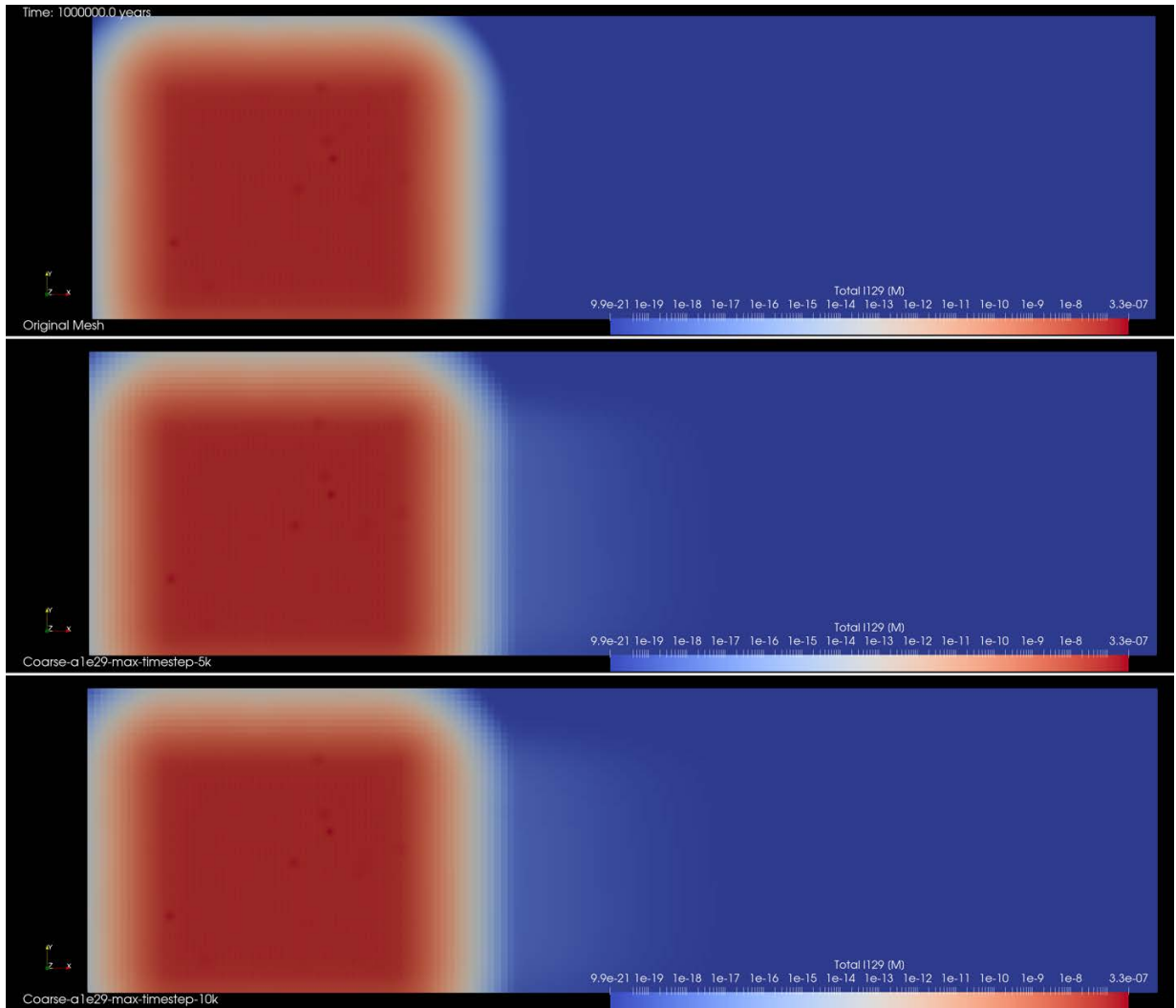
Figure 3-9. **XY slice through the repository in the shale material layer colored by total ^{129}I at one million years for the original mesh (top) and two coarser mesh simulations set with a max timestep size of 5,000 years (middle) and 10,000 years (bottom).**
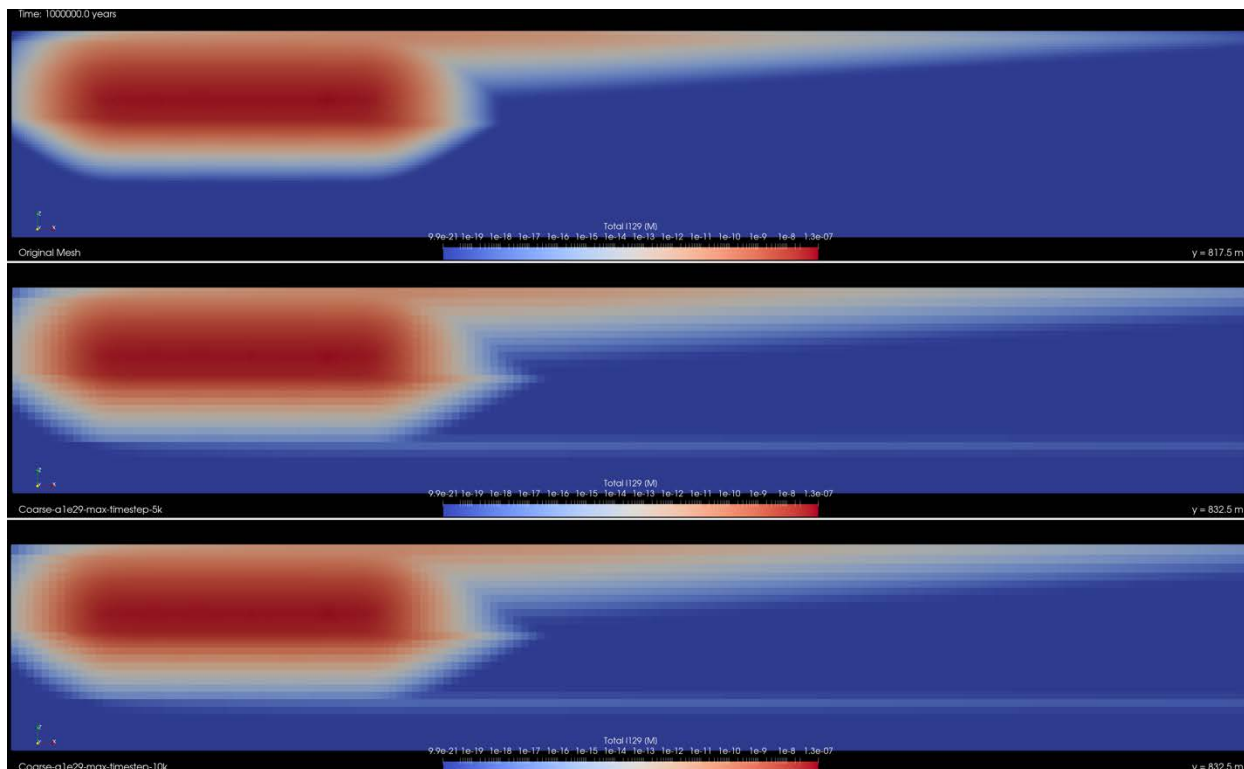
Figure 3-10.   **XZ slice through the model domain and colored by total ^{129}I at one million years for the original mesh (top, y slice at 817.5 m) and two coarser mesh simulations set with a max timestep size of 5,000 years (middle, y slice at 832.5 m) and 10,000 years (bottom, y slice at 832.5 m).**

Table 3-5.   **Quantity of interest (QoI) comparison of original shale mesh against two coarse meshes varying in maximum timestep size of 5,000 years and 10,000 years.**

Original shale mesh vs coarse mesh QoI results	RUN		
	Original mesh max timestep size 1 k years	Coarse mesh max timestep size 5 k years	Coarse mesh max timestep size 10 k years
QoI			
Final_I129_sand_obs1_M	1.846425e-11	1.873255e-11	1.874605e-11
Final_I129_sand_obs2_M	2.595711e-14	7.314595e-14	7.323536e-14
Final_I129_sand_obs3_M	1.102527e-19	2.452893e-17	2.474267e-17
Final_I129_lime_obs1_M	1.051554e-08	1.126031e-08	1.125953e-08
Final_I129_lime_obs2_M	9.986944e-21	9.985230e-21	9.986486e-21
Final_I129_lime_obs3_M	9.985379e-21	9.983390e-21	9.984646e-21

3.1.3   Open Northern Boundary

The shale model in Sevougian et al. (2019a) originally had both the north and south (y minimum and maximum) boundaries no-flow and insulated, meaning no set boundary condition for either face of the model domain in PFLOTRAN. A reassessment of modeling assumptions resulted in only keeping the south boundary closed to make a reflective boundary which effectively doubles the repository, through

symmetry. Additionally setting a no flow and insulated boundary condition for the north face (y maximum) of the model would create an infinite array of repositories in the north/south direction through symmetry, which is not physically realistic. Setting the northern boundary open to solute diffusion will result in a less conservative calculation of radionuclide concentration at downstream observation points because concentrations can now diffuse out across the north boundary.

A BOUNDARY_CONDITION card was set for the north face (y maximum) in PFLOTRAN that includes an initial FLOW_CONDITION block that sets flow parameters. Within this block, a sub-block called LIQUID_PRESSURE DIRICHLET was set which specifies a fixed pressure is used along with pressure data taken from a DATASET called from within the PFLOTRAN input deck that is applied at the boundary. This dataset is a hydrostatic boundary pressure that is set to as low as 0.106 MPa initially at the top edge of the boundary and up to about 11.956 MPa at the bottom edge of the boundary. Similarly, a sub-block called TEMPERATURE DIRICHLET is also used within this boundary condition that specifies a temperature [°C] applied at the boundary using a hydrostatic temperature dataset. This hydrostatic boundary temperature dataset has an initial 10°C set at the top edge of the boundary and a 51°C max initial temperature set to the bottom edge of the boundary. Lastly, a gas mole fraction of 10^{-8} is applied at the boundary.

Figure 3-11 shows an XY view into the top layer of the shale model domain that compares the effect of setting the north boundary closed or open. Stream tracer tubes are shown within ParaView visuals for both simulations. For the open north boundary condition simulation visual, stream tracer tubes near the north face curve into the edge of the model domain and at one point even cross out of the domain through the north face.
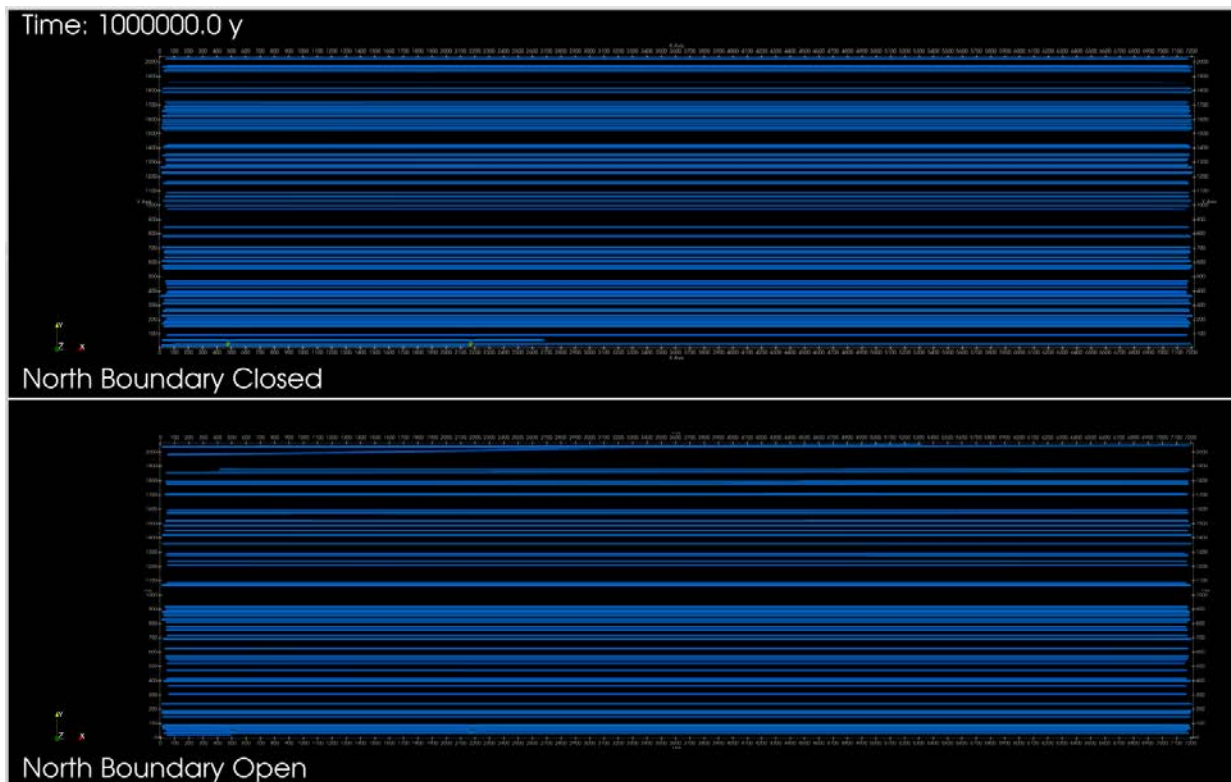
Figure 3-11. **XY view of stream tracer tubes into the top layer of shale model domain comparing the closed north boundary case (top) against the open north boundary case (bottom) at 1-million-year simulation time.**

A quick analysis was also performed, which involved looking at Figure 3-9 that had no north boundary condition applied. The analysis focused on the north wall and a small symmetry effect of ^{129}I concentration cumulating on the north wall can be seen. The solution to resolve this symmetry effect was to set a boundary condition for the north wall. This analysis also determined that the distance between the repository and the west and north faces of the model was too small since the current set up could allow for concentrations to leak out too quickly out of the model domain and give biased results. This analysis supports future extension of the distance by at least 30% between the repository edge and both the west and north boundaries. Another consideration for future work is to increase the domain size in all directions and move away from the symmetric model assumption as the model complexity increases.

Table 3-6 compares QoI data for final ^{237}Np and ^{129}I molar concentrations at several observation points of interest for both the closed and open north boundary condition shale simulations. The concentration of ^{237}Np and ^{129}I at these observation points differ slightly, or not at all.

Table 3-6.   QoI data comparison between having the north boundary closed versus open.

QoI	North-Boundary Closed	North-Boundary Open
Final_Np237_sand_obs1_M	9.86E-20	1.01E-19
Final_I129_sand_obs1_M	1.85E-11	1.85E-11
Final_Np237_sand_obs2_M	9.83E-20	1.01E-19
Final_I129_sand_obs2_M	2.60E-14	3.68E-14
Final_Np237_sand_obs3_M	9.82E-20	1.01E-19
Final_I129_sand_obs3_M	1.10E-19	2.27E-19
Final_Np237_lime_obs1_M	6.54E-20	6.68E-20
Final_I129_lime_obs1_M	1.05E-08	1.05E-08
Final_Np237_lime_obs2_M	6.54E-20	6.68E-20
Final_I129_lime_obs2_M	9.99E-21	9.99E-21
Final_Np237_lime_obs3_M	6.53E-20	6.67E-20
Final_I129_lime_obs3_M	9.99E-21	9.99E-21

Figure 3-12 through Figure 3-15 show ParaView visualizations of the shale model domain comparing the effect of setting the north boundary open or closed. Visuals are set at 1-million-year simulation time and are colored by total ^{129}I molar concentration. Figure 3-13 looks at the ground surface in the shale model domain, where noticeable differences are seen in the west half of the model between the closed and open north boundary simulations, though the difference is much smaller on the other XY slices (Figure 3-14) and the south face of the model (Figure 3-15).
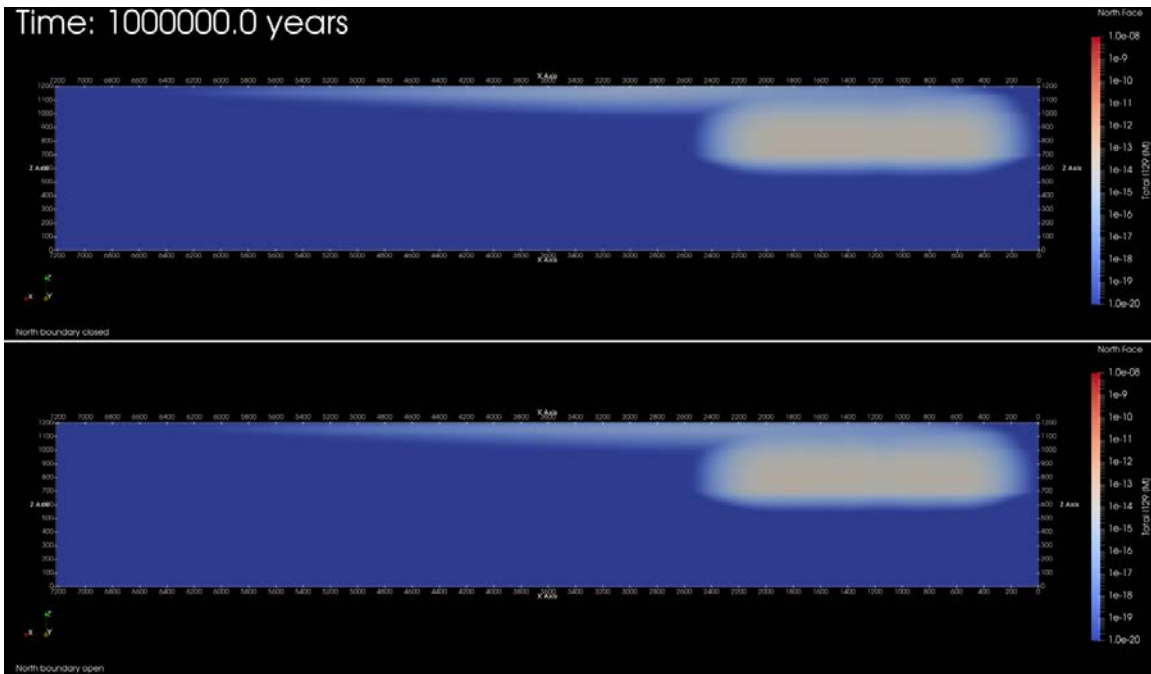
Figure 3-12. North face of shale model domain comparing the closed north boundary case (top) against the open north boundary case (bottom). (Flow is from right to left because that is the direction of increasing x in this view) Both visuals are colored by total [129]I molar concentration at 1-million-year simulation time.
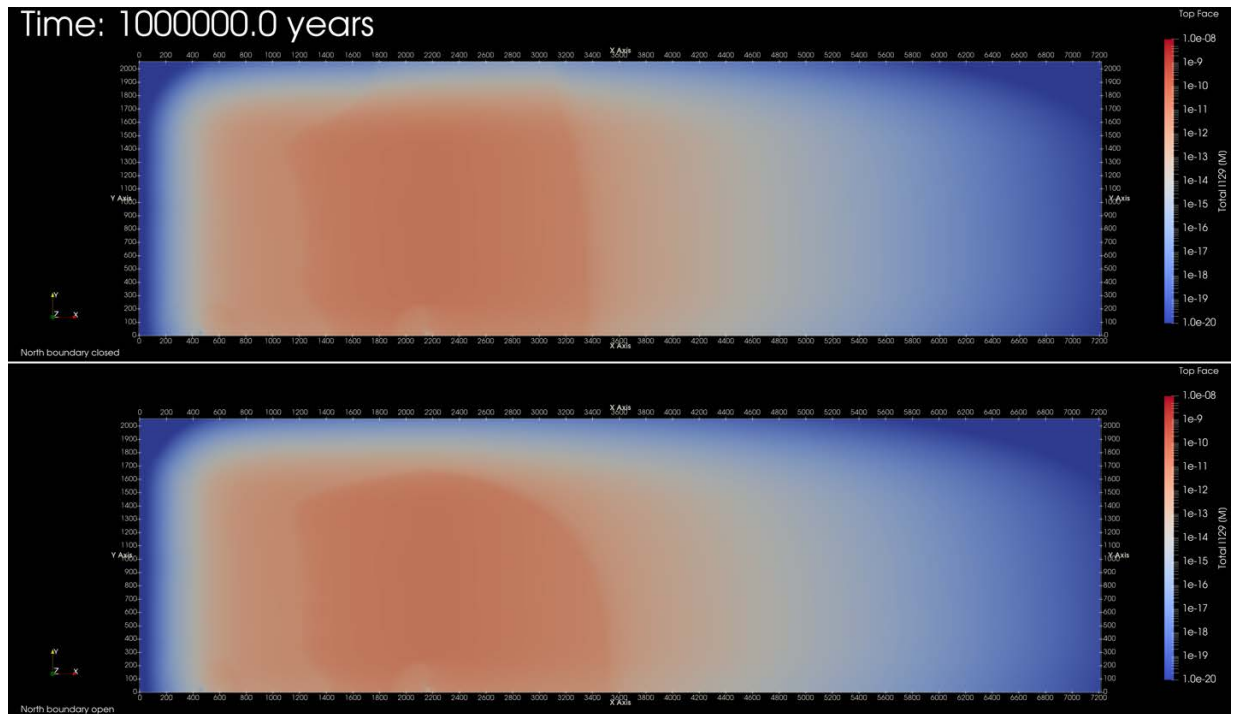
Figure 3-13. Top face (surface) of the shale model domain comparing the closed north boundary case (top) against the open north boundary case (bottom). Both visuals are colored by total [129]I molar concentration at 1-million-year simulation time.
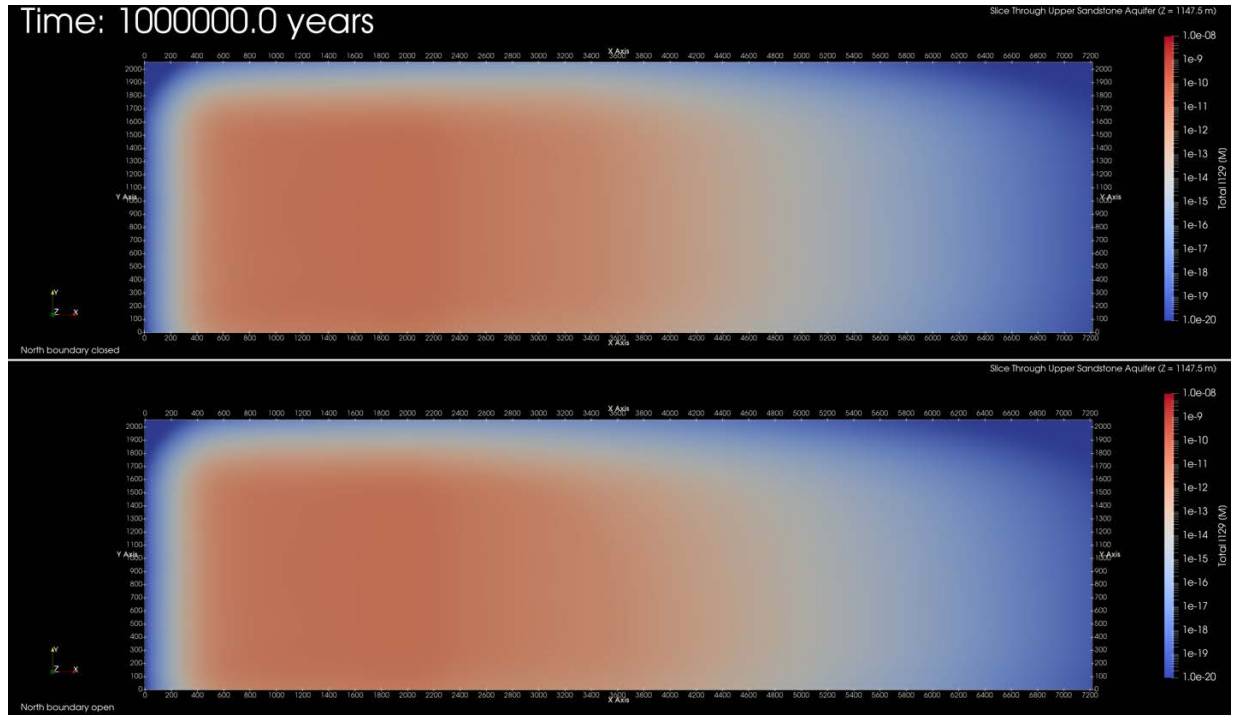
Figure 3-14.   **Slice through upper sandstone aquifer material layer of shale model domain comparing the closed north boundary case (top) against the open north boundary case (bottom). Both visuals are colored by total [129]I molar concentration at 1-million-year simulation time.**
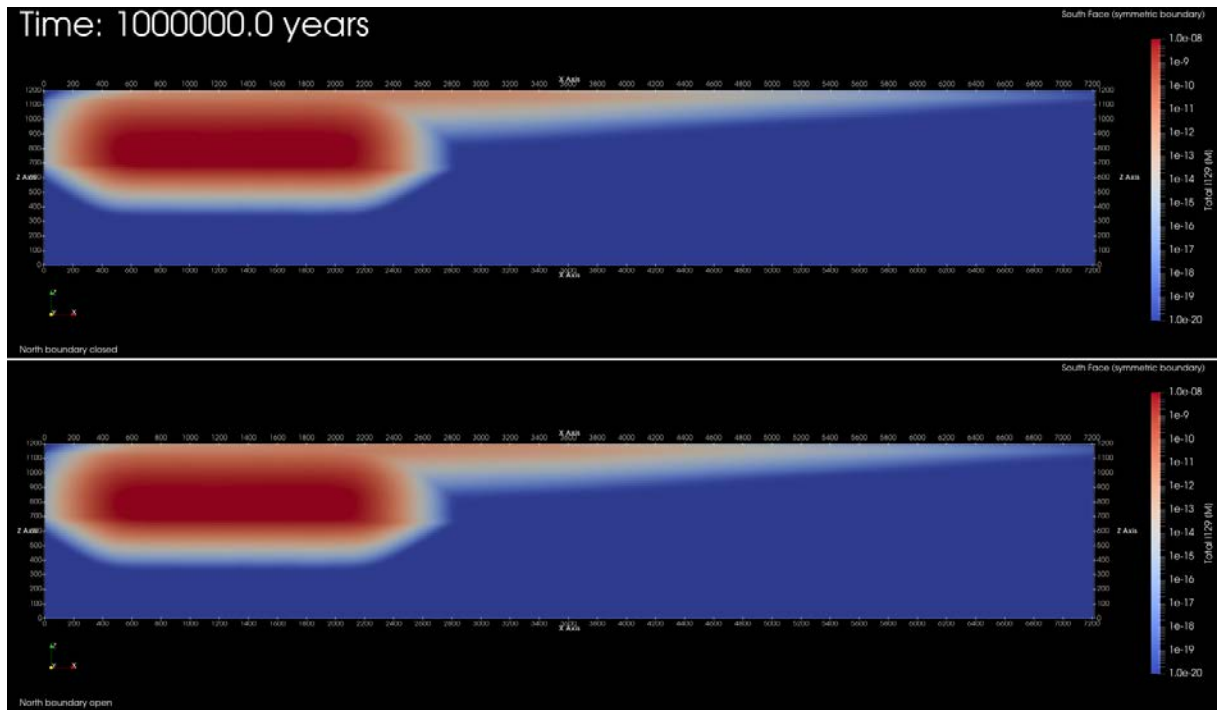
Figure 3-15.   **South face of shale model domain comparing the closed north boundary case (top) against the open north boundary case (bottom). Both visuals are colored by total [129]I molar concentration at 1-million-year simulation time.**

3.1.4 Ignoring the engineered buffer and using crushed rock backfill

A single shale simulation with crushed rock backfill material properties, instead of engineered buffer, was set up to address a Nuclear Waste Technical Review Board comment letter from the Summer 2022 meeting. The original base case shale PA model set a porosity of 0.35 for the buffer material while the modified buffer used a higher porosity (0.5). Buffer permeability was not changed because of numerical instabilities observed in the simulation when very high buffer permeability was included in the model.

Figure 3-16 shows the location of four of the five QoI that this study will focus on for comparing the base case and modified porosity simulations. Observation point pwr_wp2 is located towards the center of the repository in the centermost grid cell of a waste package; pwr_bf2 is located in the buffer (or crushed rock backfill for the modified porosity simulation) directly east of pwr_wp2; pwr_drz2 similarly is located directly east of pwr_wp2 and pwr_bf2 in the disturbed rock zone; shale_obs1 is located in the shale material layer east of the center edge of the repository. Figure 3-17 is an XZ slice through the repository colored by material ID showing the location of all five observation points. Within this figure, the fifth observation point called lime_obs3 is visible and is located at the far east end of the model domain within the limestone material layer.

Figure 3-18 shows total ^{129}I at the five observation points of interest over the course of the 1-million-year simulation for both the base case (base) and modified porosity (mod) simulations. Simulation results show concentrations of ^{129}I are nearly identical, varying at times at specific observation points. Table 3-7 lists ^{129}I molar concentration at 1 million years at the observation points of interest for both simulations. At 1 million years simulation time, the concentration at pwr_wp2 for the base case is slightly higher and can be attributed to the lower porosity of 0.35 in the original buffer material. A lower porosity in the buffer for the base case simulation inhibits ^{129}I from transporting out of the waste package region as rapidly as compared to the modified 0.5 porosity case.

ParaView visualizations of an XY slice through the repository colored by total ^{129}I molar concentration at 3,000, 5,000, 10,000, and 100,000 years for both the base case and modified porosity simulations are shown in Figure 3-19. A subtle difference can be seen in the 3,000-, 5,000-, and 10,000-year visualizations. At these early times in the simulation, several waste packages have already breached and ^{129}I is confined to the immediate vicinity of the breached waste packages. The difference between the two cases can be seen in plume of the ^{129}I concentration in the north and south directions. The modified porosity case sees a slight increase in ^{129}I through the crushed rock with a porosity of 0.5 compared to the buffer 0.35 porosity in the base case. By 1,000,000 years, ^{129}I concentrations at the repository for both cases look identical.

An XZ slice through the center of the repository colored by total ^{129}I molar concentration at 3,000, 10,000, 100,000, and 1,000,000 years for both the base case and modified porosity simulations are shown in Figure 3-20 through Figure 3-23. No noticeable differences can be seen within these visuals. Both cases see a higher ^{129}I concentration around the repository region as well as through the limestone material layer that is consistent through to the end of the east side of the model domain.

Differences in ^{129}I between the two cases at observation points and in the repository region are minimal. A future simulation should consider further changes to the crushed rock backfill material such as characteristic curves, altering thermal conductivity values (wet and dry), and changing in the permeability.
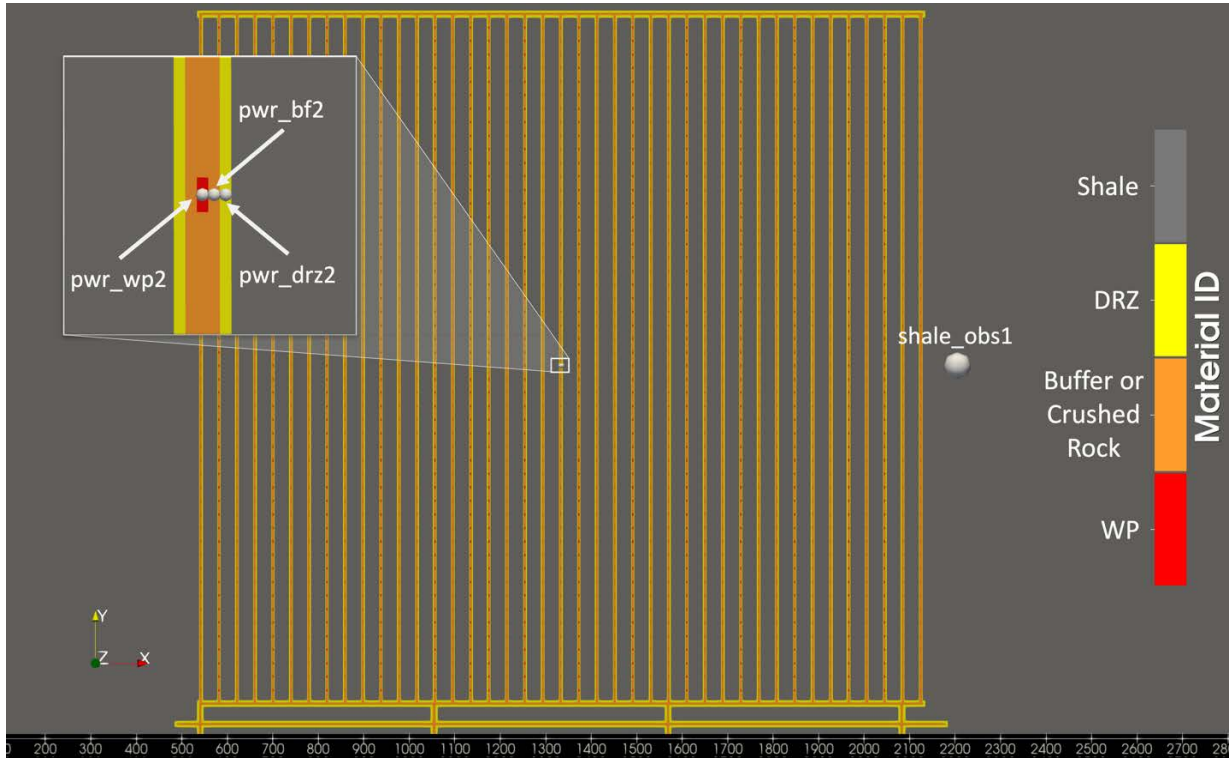
Figure 3-16.   XY slice through the repository colored by material ID showing the location of four observation points in and around the repository.
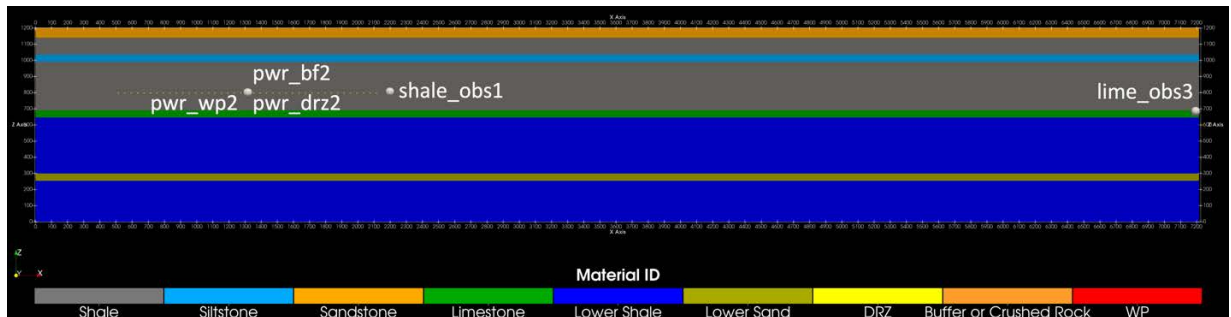
Figure 3-17.   XZ slice through the repository colored by material ID showing the location of five observation points of interest.
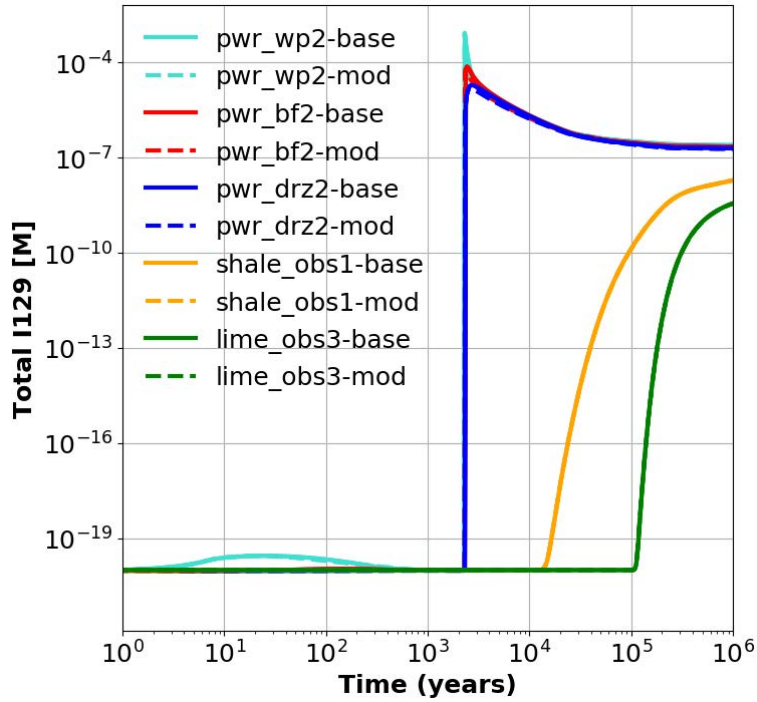
Figure 3-18. Total ^{129}I molar concentration at the observation points of interest over the course of the 1-million-year simulation for both the base case (base) and modified porosity (mod) simulations.

Table 3-7. Total ^{129}I molar concentrations at several observation points of interest at 1-million-year simulation time for both the base case and modified porosity simulations.

Simulation	Total ^{129}I molar Concentration at specified observation points				
	pwr_wp2	**pwr_bf2**	**pwr_drz2**	**shale_obs1**	**lime_obs3**
Base Case	2.48E-07	2.23E-07	2.00E-07	1.93E-08	3.63E-09
Crushed Rock Backfill (modified porosity 0.5)	2.18E-07	2.04E-07	1.90E-07	1.93E-08	3.61E-09
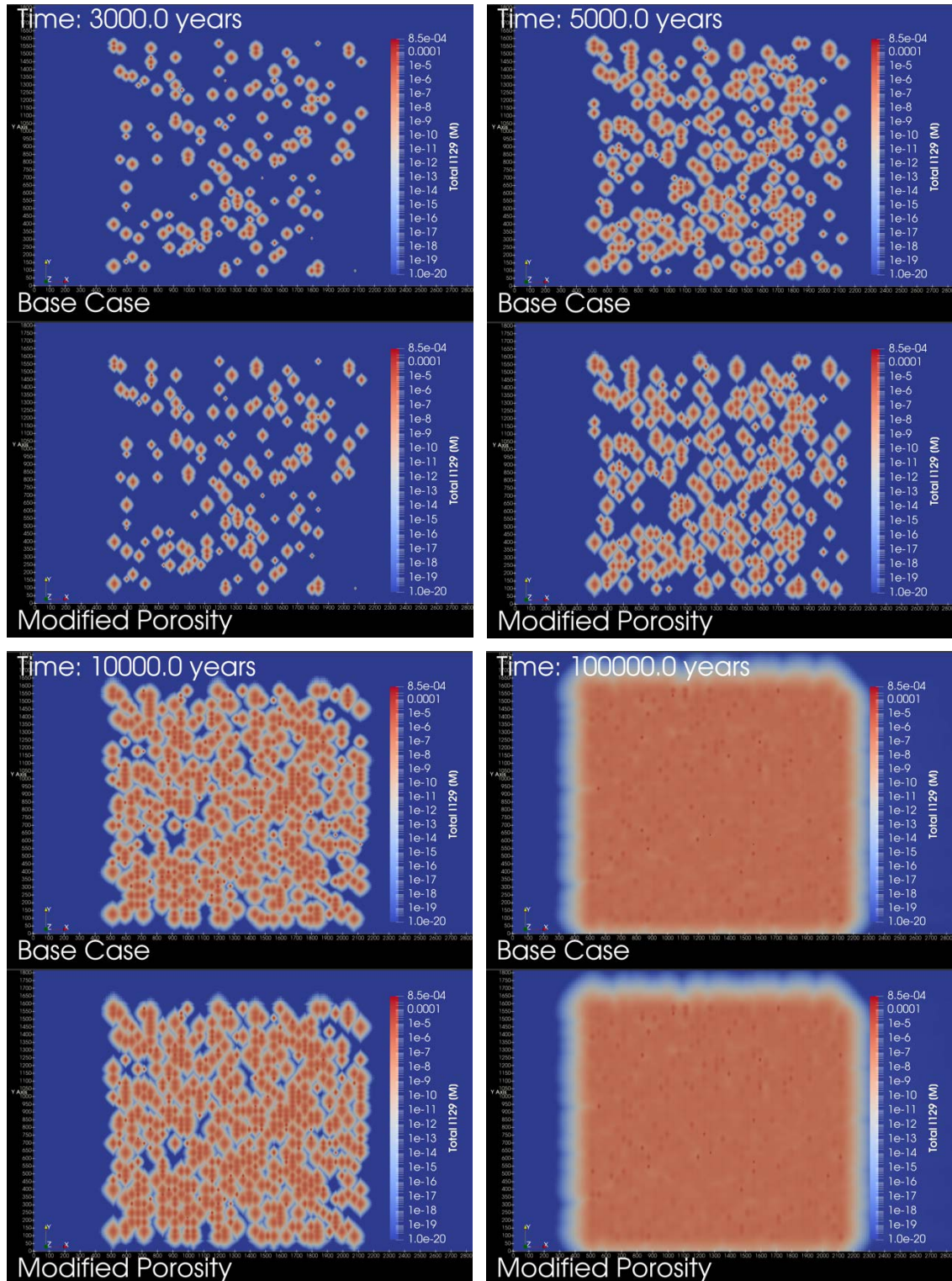
Figure 3-19.   **XY slice through the repository colored by total ^{129}I molar concentration at 3,000, 5,000, 10,000, and 100,000- years for the base case and modified porosity simulations.**
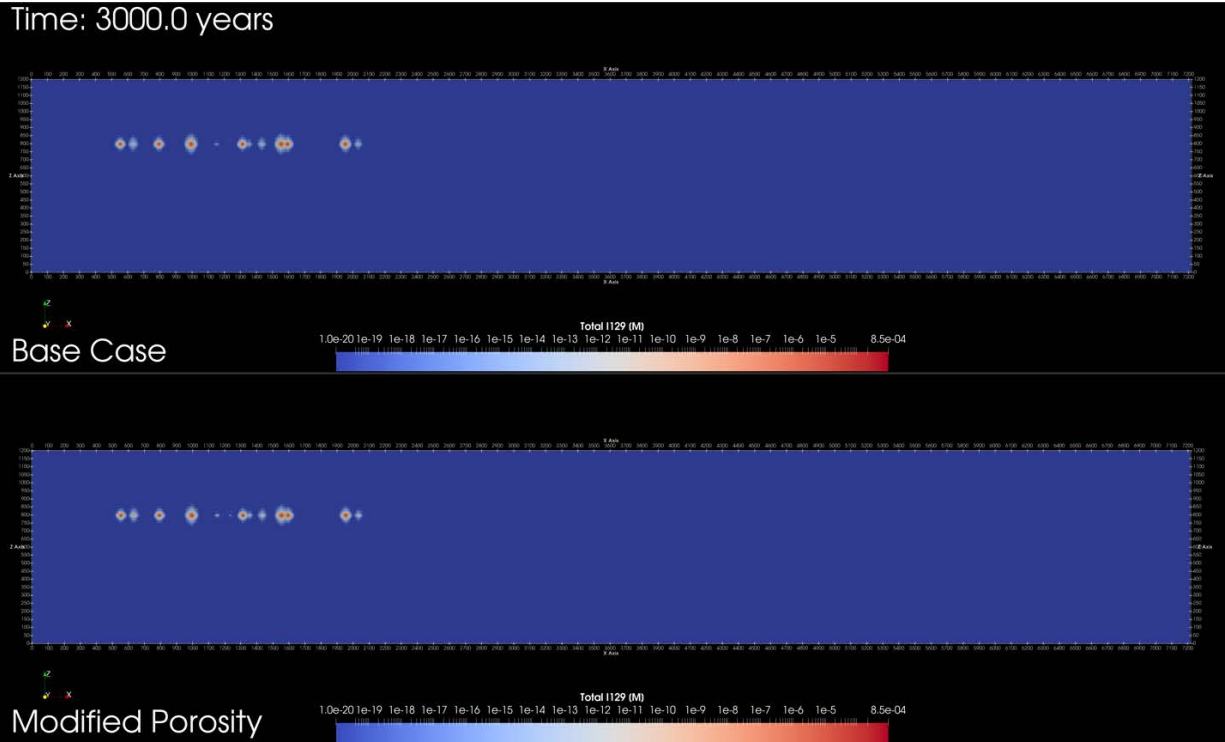
Figure 3-20, **XZ slice through the center of the repository colored by total ^{129}I molar concentration at 3,000 years for the base case (top) and modified porosity (bottom) simulations.**
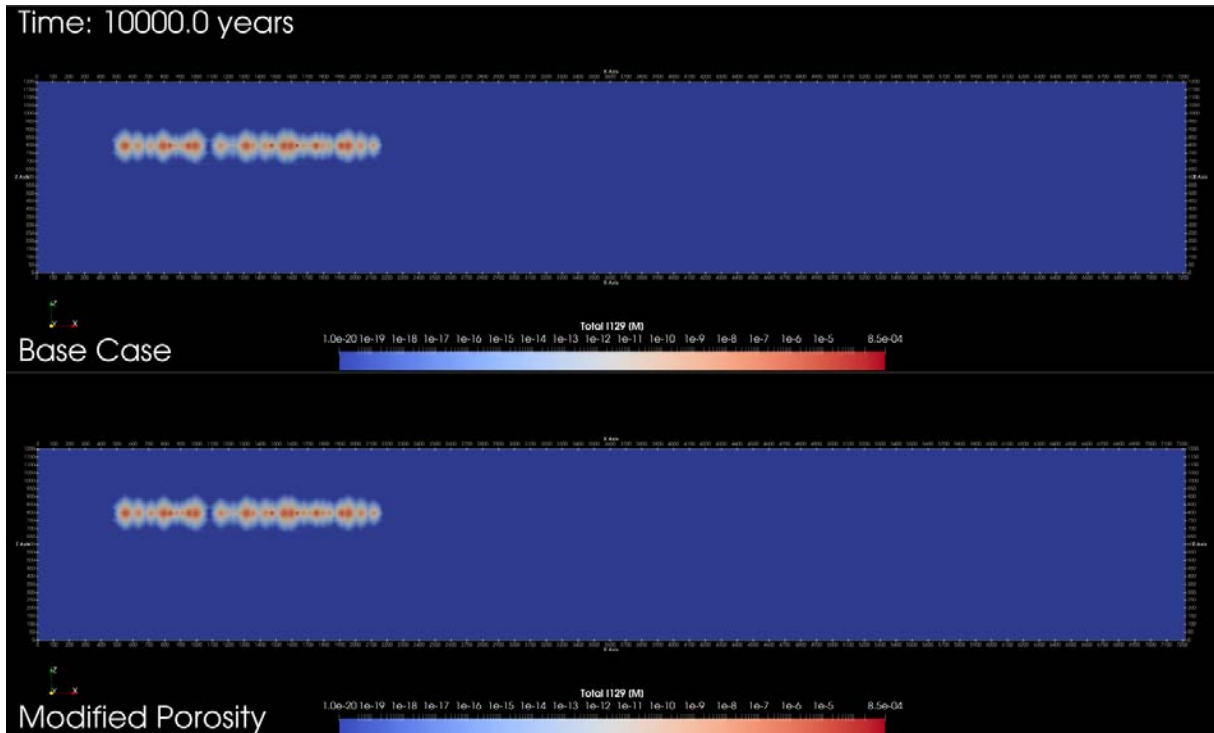
Figure 3-21. XZ slice through the center of the repository colored by total ^{129}I molar concentration at 10,000 years for the base case (top) and modified porosity (bottom) simulations.
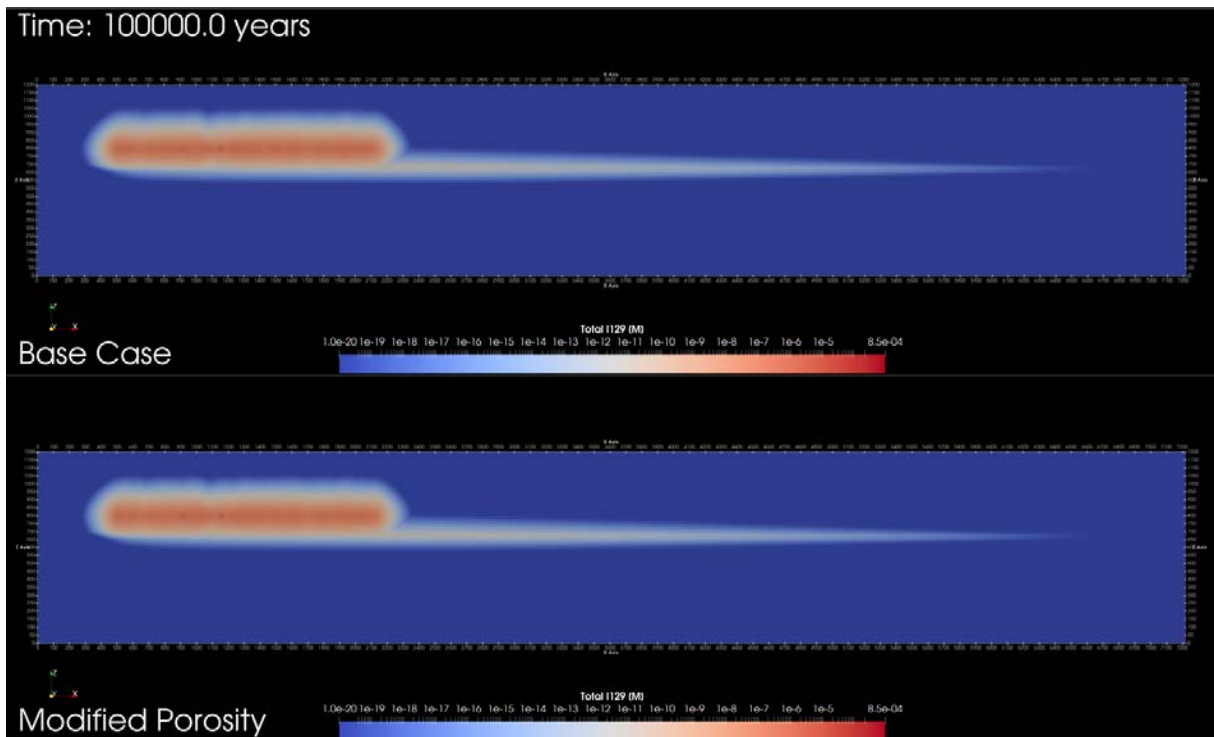
Figure 3-22. XZ slice through the center of the repository colored by total ^{129}I molar concentration at 100,000 years for the base case (top) and modified porosity (bottom) simulations.
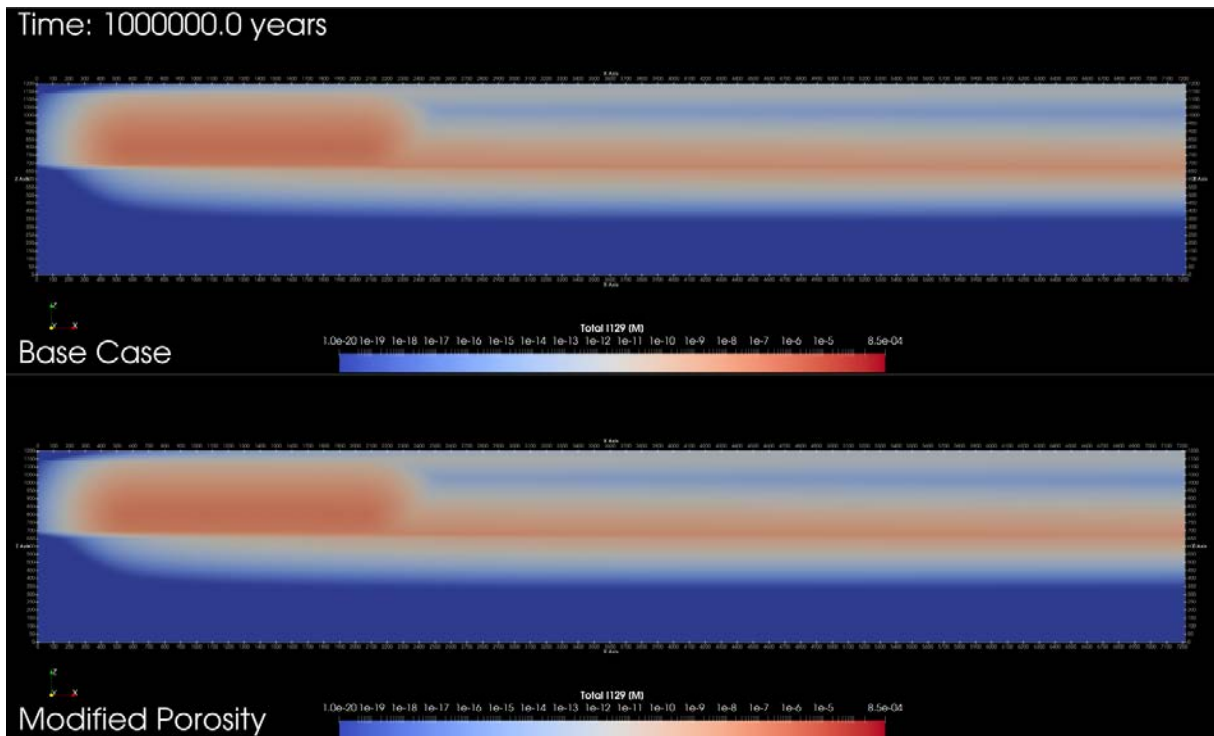
Figure 3-23.   XZ slice through the center of the repository colored by total ^{129}I molar concentration at 1,000,000 years for the base case (top) and modified porosity (bottom) simulations.

3.2   Deterministic Study Incorporating Heat Source Distribution

In this study, we performed a sensitivity test with variation in spatial distribution of heat sources with respect to the direction of groundwater flow to investigate nonuniform thermal impacts on hydro-thermal flow and long-term transport of radionuclides in the near- and far-field of the repository system. Uneven heat energy emitted from multiple heat sources can affect advective transport of radionuclides through the engineered and/or natural barriers as well as diffusive transport into the host rock, potentially influencing the long-term performance of the repository system as heat and radioactivity decay. Heat-driven thermo-hydro-chemical (THC) coupling processes in a shale-hosted repository system bounded by multiple geologic layers for 10^6 years after completion of waste-package installation are simulated using PFLOTRAN, which is a massively parallel open source, reactive multi-phase flow and transport simulator designed to leverage massively-parallel high-performance computing (Lichtner & Hammond, 2012).

3.2.1   Heat Source Distribution

3.2.1.1   *Waste Package: Heat Source*

In PFLOTRAN we must assume the whole waste package volume is a porous medium. The waste package porosity is set equal to the fraction of void space (50%) and the permeability is 10^{-16} m^2, several orders of magnitude higher than that of the surrounding materials, so that water and air can flow out of the waste package (rather than thermal pressurization of the interior of the waste package). The installed package consists of a stainless-steel canister and a stainless steel overpack, and thus, the thermal properties of stainless steel are implemented for the waste package (Shelton,1934).

To see the effect of less and greater heat from the waste package on near- and far-field hydro-thermal coupled processes, a sensitivity test is performed by implementing the 10th, 50th, 75th, 90th, 95th, and 99th percentiles of frequency distribution of heat outputs as heat source which are obtained from as-loaded

DPCs in the United States. More details of the procedure generating the heat curve are found in the recent report of Jones et al. (2021, Section 1 & Table 1-2).
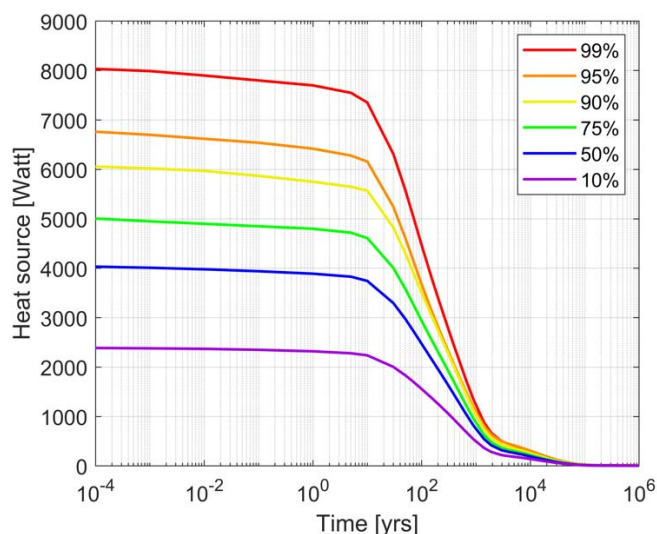
Figure 3-24   **Transient decay heat curves for six types of waste package heat source term: 10th, 50th, 75th, 90th, 95th, and 99th percentiles of frequency distribution of heat outputs (Jones et al., 2021).**

Figure 3-24 shows the transient decay heat curves estimated based on six types of heat outputs for representative DPCs from calendar year 2100 to 10^6 years. In the PFLOTRAN simulation, the energy (watts per waste package volume) entering the model domain is updated as a function of time according to values in a lookup table of each heat source.

3.2.1.2   *Spatial Distribution of Waste Packages*

This study aims to show how the spatial variation of waste packages with different heat emission influences hydro-thermal flow and corresponding radioactive transport in near- and far-field of the repository. The waste packages are assumed to be uniformly distributed within each drift (30 m center-to-center distance along y-axis) and drifts are equally spaced (40 m center-to-center distance along x-axis), such that total 2,050 waste packages are placed in the model domain as shown in Figure 3-25(A).
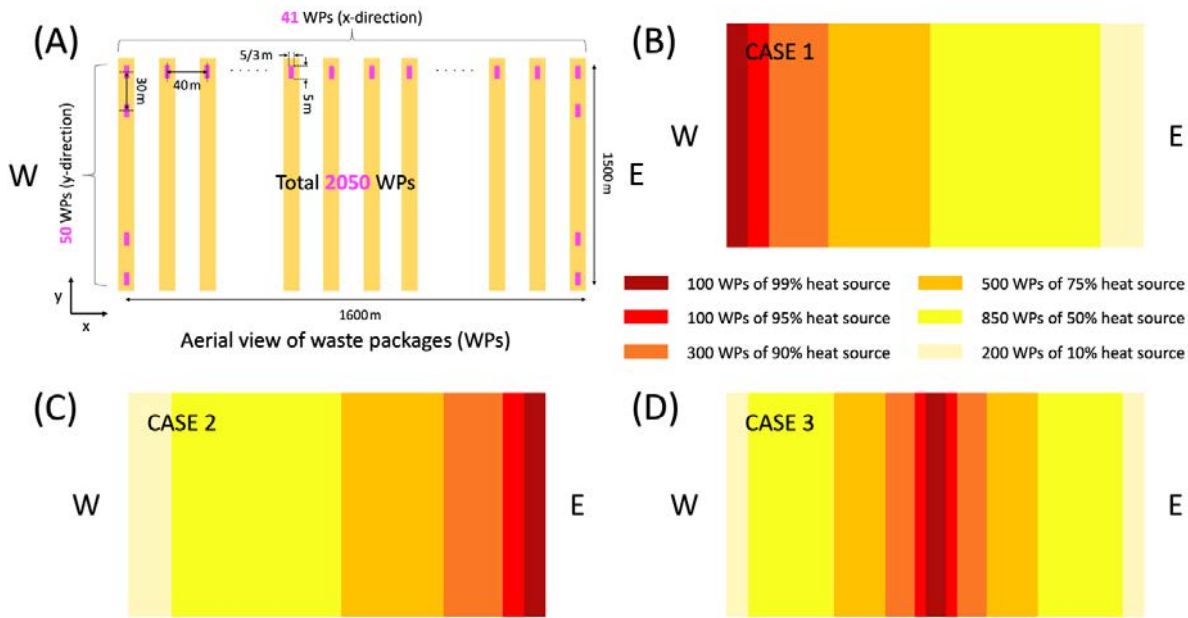
Figure 3-25. **(A) Map view of the repository. The groundwater flows from left to right (west to east). (B to D) Schematic description of three scenarios with spatial variation in the six types of heat sources. For case 3, half the waste packages from the 10th to 99th percentile heat sources are arranged symmetrically around the center where 99th percentile heat sources are located.**

Based on the geometry of drifts and direction of groundwater flow in this model, we define three cases with variation in the location of six types of heat sources: (1) CASE 1: progressively cooler waste packages from west to east, (2) CASE 2: progressively hotter waste packages from west to east, and (3) CASE 3: half the waste packages from the 10th to 99th percentile heat sources are arranged symmetrically around the center, which has the hottest 99th percentile waste packages (Figure 3-25(B) to (D)).

3.2.2 Spent Fuel Inventory

This field-scale model assumes that the spent fuel inventory consists entirely of PWR SNF assemblies and implements two DPC waste package configurations: 24-PWR and 37-PWR waste packages. The lower burn-up fuel (40 GWd/MTHM in this study) is emplaced in 24-PWR waste packages, while higher burn-up fuel (60 GWd/MTHM) is emplaced in 37-PWR waste packages.

Table 3-2 shows the radionuclide inventory at the time of emplacement. The transient heat flow out of the 10th, 50th, and 75th percentiles heat curves are assigned radionuclide inventory representative of the 24-PWR waste packages, while the 90th, 95th, and 99th percentiles heat curves have the 37-PWR radionuclide inventory. Note that all waste packages are uniformly distributed with the same drift spacing, while only the inventory varies depending on the amount of heat energy.

3.2.3 Results Incorporating Heat Source Distribution

The simulation results show the spatio-temporal evolution of hydro-thermal quantities (e.g., temperature, pressure, and liquid saturation) and total concentration of selected isotope species in the aqueous phase at the observation points indicated in the Figure 3-1 for three cases of spatial distribution of heat sources as

shown in Figure 3-25. For the near-field analysis, three locations of observation points are selected: west edge, middle, and east edge of the repository system.

3.2.3.1   Hydro-thermal flow

The canisters containing heat-emitting nuclear waste will perturb the thermal field around the waste packages and affect the rate of resaturation of engineered buffer corresponding to the magnitude of the heat pulse, as shown in the previous model of single waste package (Chang et al., 2022).

The presence of multiple waste packages with variation in amounts of heat generated from different types of canisters needs to consider hydro-thermal interaction among waste packages that will control the near-field behavior of engineered and natural barriers.
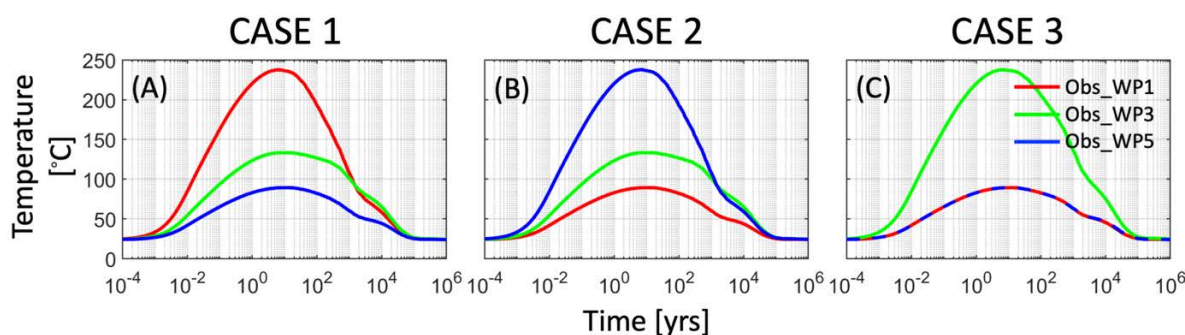
Figure 3-26.   Evolution of temperature within selected waste packages: WP1 (west edge), WP3 (middle), and WP5 (east edge) as shown in Figure 3-1(A) for three cases.

The PFLOTRAN simulation results show that the waste package temperature peaks at approximately 7 years of simulation time, reaching a high value of 237 °C (Figure 3-26), where the 99th percentile of heat sources are placed. CASE 3, where the greatest heat sources are located in the middle of the repository and surrounded by cooler heat sources, causes symmetric heat flow outwards, such that almost identical temperature changes are observed at both edges of the repository (red and blue lines in Figure 3-26(C)).

Figure 3-27 shows the temporal evolution of temperature, pressure, and saturation of gas phase, and liquid mobility at the selected observation points within the buffer cell nearest each waste package for the three cases. The maximum temperature (~175 °C) is observed at about 20 years of simulation time, but the spatial variation in heat sources determines the location of region experiencing intense thermal flow (Figure 3-27(A) to Figure 3-27(C)).
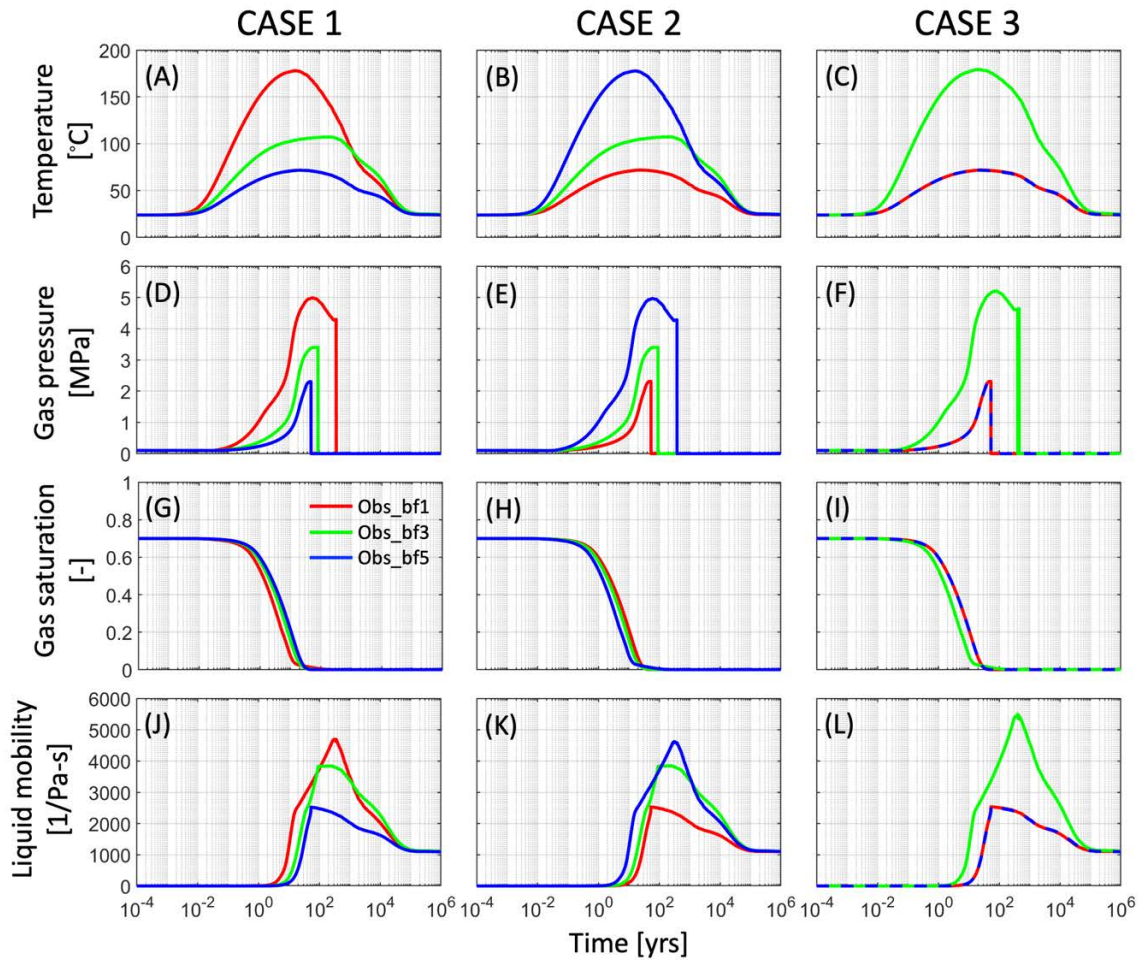
Figure 3-27. Evolution of (A to C) temperature, (D to F) gas pressure, (G to I) gas saturation, and (J to L) liquid mobility at the observation points within the buffer, Obs_bf1, Obs_bf3, and Obs_bf5, surrounding WP1 (west edge), WP3 (middle), and WP5 (east edge), respectively, as shown in Figure 3-1(A) for three cases

As the buffer is heated, the gas pressure increases, and the maximum gas pressure reaches 5.2 MPa (Figure 3-27(D) to Figure 3-27(F)). More heat energy from the greatest heat source results in larger and longer increase of gas pressure because of prolonged presence of gas phase; gas pressurization continues until about 400 years of simulation time near the 99th percentile of heat source. Simultaneously, fluids flow into the buffer from the fully saturated host rock, and liquid mobility changes with the heat pulse. These two processes result in the phase transition of fluids from the gas-liquid two-phase to the liquid single-phase within the buffer that controls the transient perturbation in gas pressure (zero gas pressure when the buffer is fully liquid-saturated). The quicker decrease of gas saturation is observed at the 99th percentile of heat source (Figure 3-27(G) to Figure 3-27(I)) because greater thermal energy enhances the mobility of liquid phase (lessening viscosity) that will facilitate water inflow into the buffer from the fully liquid-saturated host rock (Figure 3-27(J) to Figure 3-27(L)).
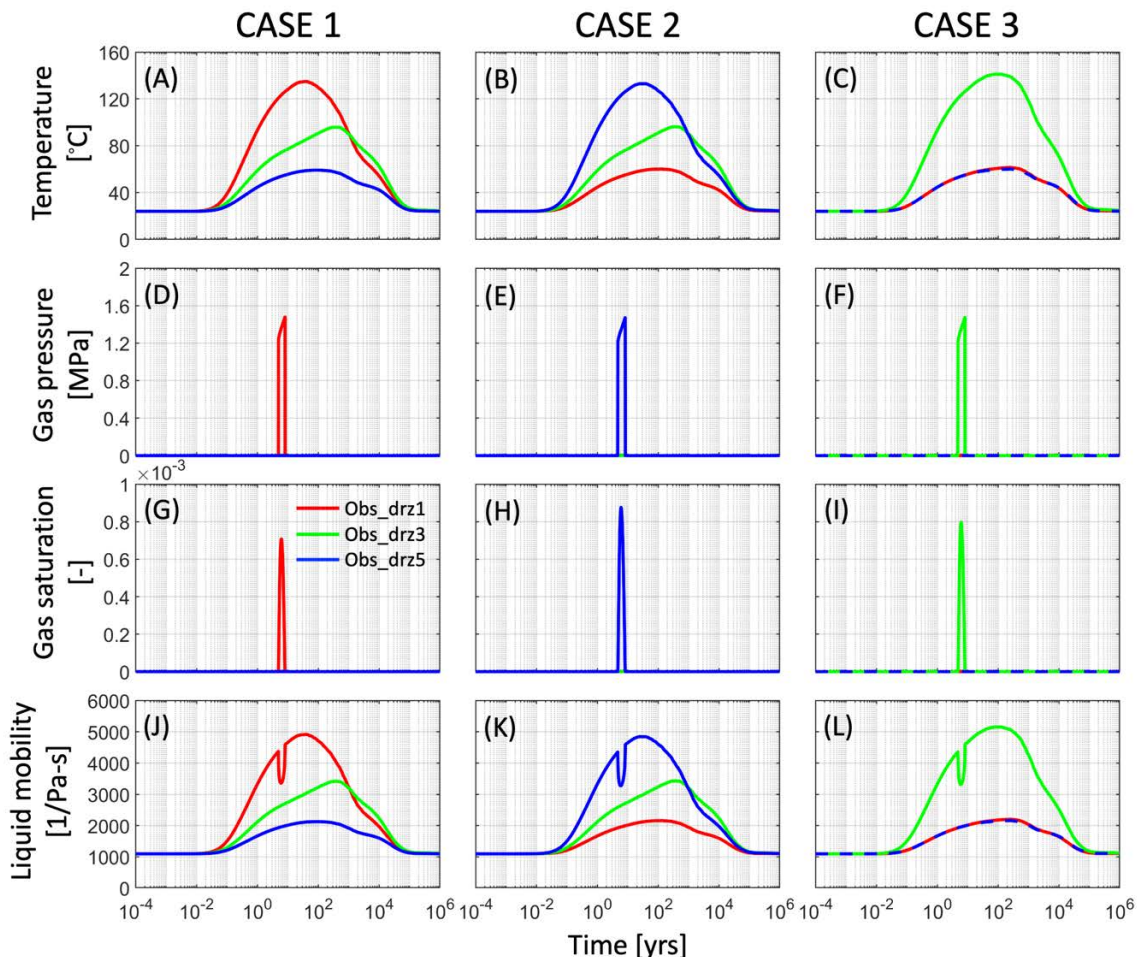
Figure 3-28.   Evolution of (A to C) temperature, (D to F) gas pressure, (G to I) gas saturation, and (J to L) liquid mobility at the observation points within the DRZ, Obs_drz1, Obs_drz3, and Obs_drz5, near WP1 (west edge), WP3 (middle), and WP5 (east edge), respectively, as shown in Figure 3-1(A) for three cases.

Figure 3-28 shows the temporal evolution of the same physical quantities obtained at the observation points within the DRZ cell nearest each waste package for three cases. The temperature changes in a similar way to ones for buffer with lower maximum temperature of about 135 °C at approximately 40 years of simulation time (Figure 3-28(A) to Figure 3-28(C)). The 99th percentile of heat source causes a short presence of gas phase within the DRZ (about 2 years) that generates positive gas pressure up to 1.5 MPa (Figure 3-28(D) to Figure 3-28(I)). Under the fully liquid-saturated state within the DRZ, the liquid mobility is more sensitive to temperature change (Figure 3-28(J) to Figure 3-28(L)). The brief presence of the gas phase reduces the relative permeability of liquid phase that lowers the liquid mobility temporarily.

Once both buffer and DRZ are entirely re-saturated with liquid, gas pressure and saturation will converge to the fully saturated conditions (Figure 3-27(D) to (L) and Figure 3-28(D) to (L), respectively), which implies that the divergence of hydraulic quantities from the observation points is due to the impacts of hydro-thermal behaviors of the repository system as well as the amount of heat energy on near-field coupled heat and fluid flow.

This result indicates that hydro-thermal flow in the buffer at unsaturated conditions and DRZ will be governed by two major hydro-thermal dynamic processes: (1) heat-driven thermal gradients develop outward fluid flow near the waste package and (2) liquid flow into the unsaturated buffer from the adjacent fully saturated host rock, which will lead to more complicated countercurrent flow. Both near-field physical mechanisms depend on local perturbations of temperature and water content corresponding to the amount of heat energy emitted from individual heat sources.

3.2.3.2 Radionuclide transport

If the waste form breach occurs and radionuclides are released, in-situ groundwater flow can play a significant role in long-term radionuclide transport in the far-field from the repository system (Blum et al., 2005; Luo et al., 2000). The PFLOTRAN model solves the local mass-balance by coupling the flow and transport equations, which provides quantitative estimates on transport rates of nuclides and their retardation by sorption-desorption and dissolution-precipitation processes as the canister vitality falls to zero.

Temporal evolution of concentrations of two long-lived radionuclides are shown to quantify the impact of spatial distribution of heat sources and the groundwater flow: Iodine-129 (^{129}I; $t_{1/2} = 1.57 \times 10^7$ year) and Neptunium-237 (^{237}Np; $t_{1/2} = 2.14 \times 10^6$ year). Note that ^{129}I is assumed to have unlimited solubility and to be non-adsorbing while ^{237}Np is solubility-limited and adsorbing.
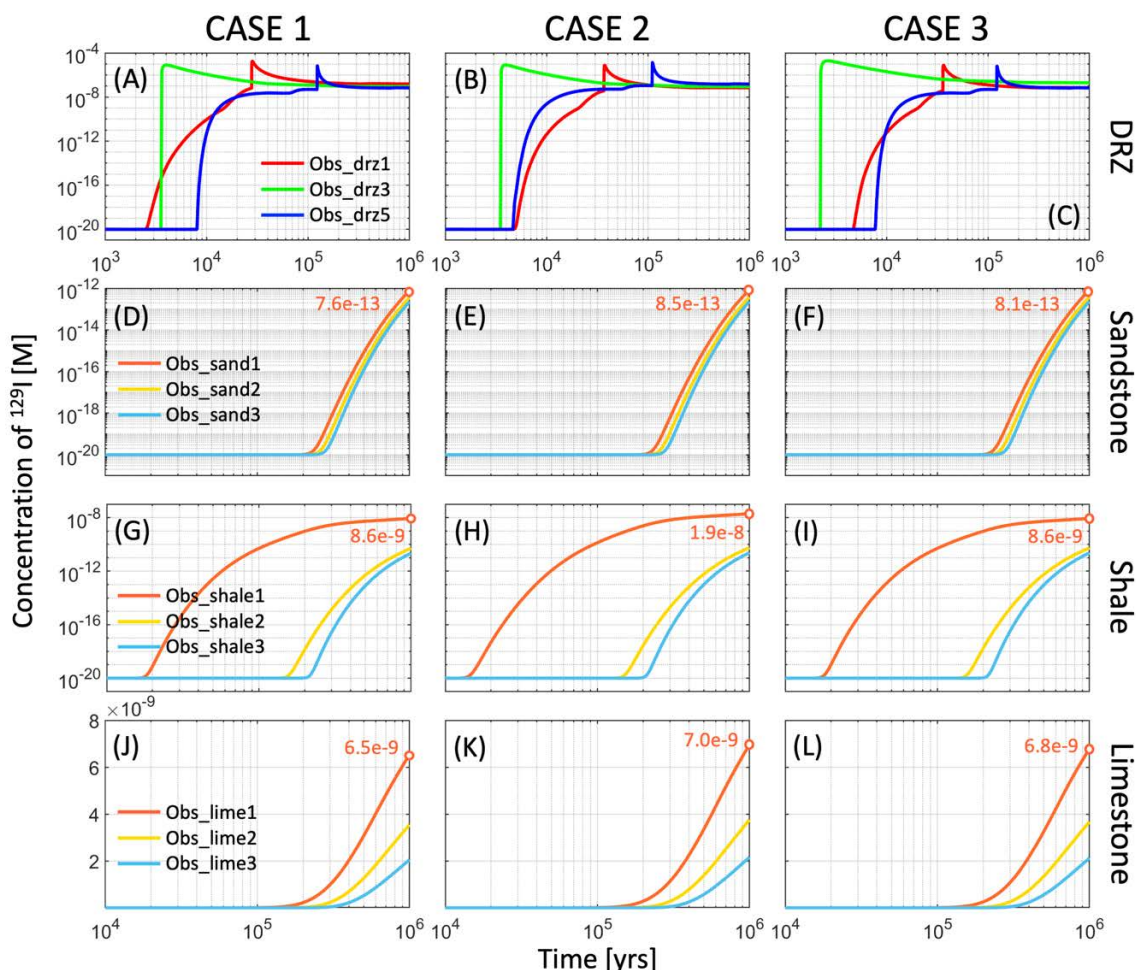
Figure 3-29.   Evolution of Iodine-129 (^{129}I) concentration at the observation points of DRZ (A to C) near WP1 (west edge), WP3 (middle), and WP5 (east edge) (refer to Figure 3-1(A)) as well as of sandstone (D to F), shale (G to I), and limestone (J to L) layers (refer to Figure 3-1(C)) for the three cases.

Figure 3-29 shows the temporal changes of ^{129}I-concentration at the observation points located within the DRZ and layers of upper sandstone, shale, and limestone (Figure 3-1(C)) for the three cases.

The sudden increases of ^{129}I-concentration are observed at the waste package located in the middle of repository for all three cases (Figure 3-29(A) to Figure 3-29(C)) because the degradation rate for individual waste package at each time step is determined by both temperature as well as a probabilistic method that samples the parameter values for the Eq. 3-1 individually for each waste package, based on the same truncated log normal distribution for all three cases.

However, the comparison of ^{129}I-concentration change at the same observation points (the same color lines) for the three cases shows that the onset of waste-form breach occurs earlier when the greatest heat energy is emitted from the 99th percentile of heat sources (e.g., at Obs_drz3 located in the middle of the repository, the fastest release of ^{129}I is observed in CASE3 where hottest heat sources are located in the middle of the repository (refer to Figure 3-25(D)).

In the far-field, the ^{129}I-concentration increases above the background level earlier at the observation points closer to the east edge of the repository (orange lines for all observation point 1 (Obs1) in all cases; (Figure 3-29(D) to Figure 3-29(L)).

After 2×10^5 years of simulation time, ^{129}I reaches the upper sandstone layer, located 425 m above the repository, which is the longest migration of radionuclides to permeable layers in the vertical direction (Figure 3-29(D) to Figure 3-29(F)).

Within the shale layer, the lateral migration of ^{129}I causes the fastest arrival to the observation points (Figure 3-29(G) to Figure 3-29(I)). The vertical migration of ^{129}I in both directions reduces the rate of horizontal ^{129}I transport, so that smaller gaps of the arrival time are observed further away from the repository (yellow and azure lines).

The impact of spatial order of heat source installation is quantified by comparing the magnitude of ^{129}I-concentration at t = 1×10^6 year. The greater heat energy causes quicker release of ^{129}I into the far-field, such that the largest ^{129}I-concentration is observed in CASE 2 where the 99th percentile of heat sources are placed at the east edge of the repository (shortest distance to Obs_sand1, Obs_shale1, Obs_lime1) and so ^{129}I approaches the observation points more quickly with groundwater flow.
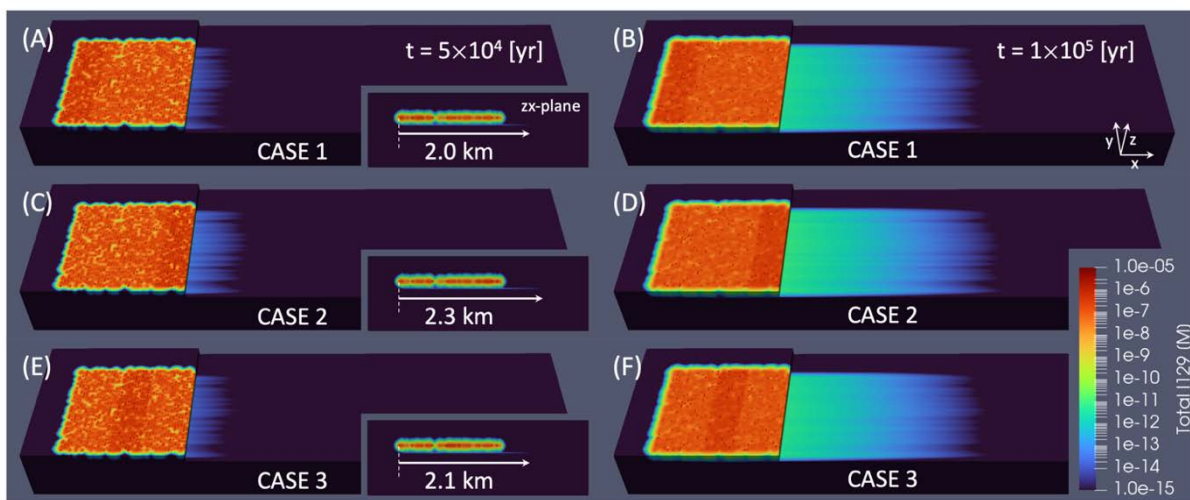
Figure 3-30. **Three-dimensional spatial distribution of ^{129}I-concentration at two times: t = 5×10^4 (left column) and 1×10^5 years (right column). The subset figures show the vertical cross-section (zx-plane) of ^{129}I-concentration at t = 5×10^4 years**

The spatial distribution of ^{129}I-concentration in a three-dimensional domain at t = 5×10^4 and 1×10^5 years confirms that the largest concentrations are observed in the region of 99th percentile of heat sources (Figure 3-30). The longest plume of 1×10^{-15} M concentration along the limestone layer, 160 m below the repository, is observed in CASE 2 (Figure 3-30(C) and Figure 3-30(D), subset plot of Figure 3-30(C)). The location of the hottest waste packages influences the far-field radionuclide transport over time due to impacting the onset of waste form breach and the direction of groundwater flow.
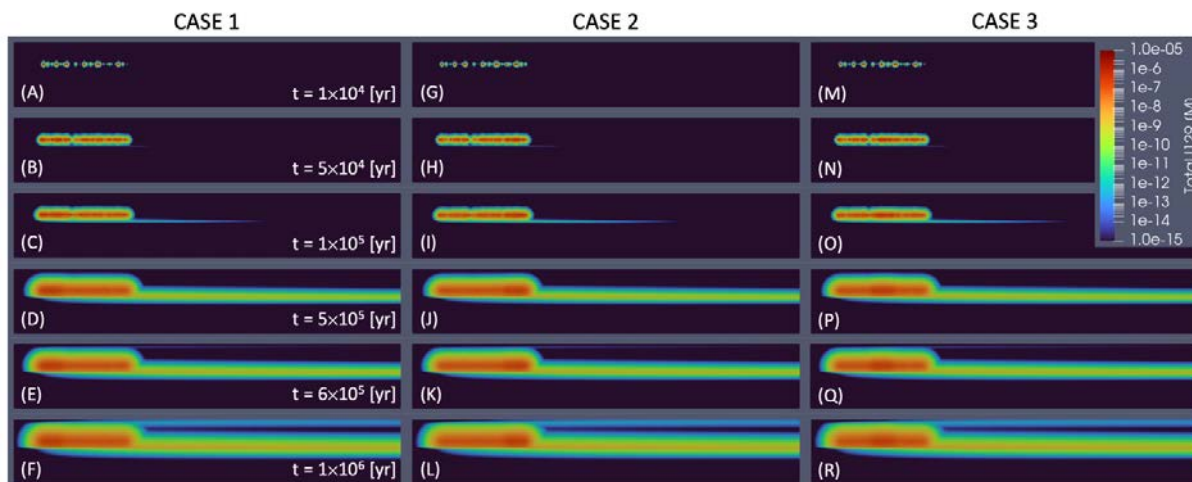
Figure 3-31.   **Two-dimensional vertical cross sections (zx-plane) for spatial distribution of [129]I-concentration at six time-steps for the three cases.**

The vertical distribution of [129]I-concentration at six time-steps are shown in Figure 3-31. At 1×10^4 years, fewer than 50% of the waste packages have breached, and [129]I remains confined to the near field (first row of Figure 3-31). At 5×10^4 years, [129]I has penetrated the highly permeable limestone layer beneath the repository (second row of Figure 3-31). At 5×10^5 years, no plume of [129]I concentration is observed along the upper sandstone layer (fourth row of Figure 3-31), which means that the initial increase of [129]I concentration at Obs_sand1, as observed in Figure 3-29(D) to Figure 3-29(F), is mainly due to the diffusion process. On the other hand, the plume of concentrations above 1×10^{-15} M is observed along the sandstone layer at 6×10^5 years and later (fifth and sixth rows of Figure 3-31), such that the increase of [129]I-concentration at all observation points is governed by advection driven by groundwater flow.
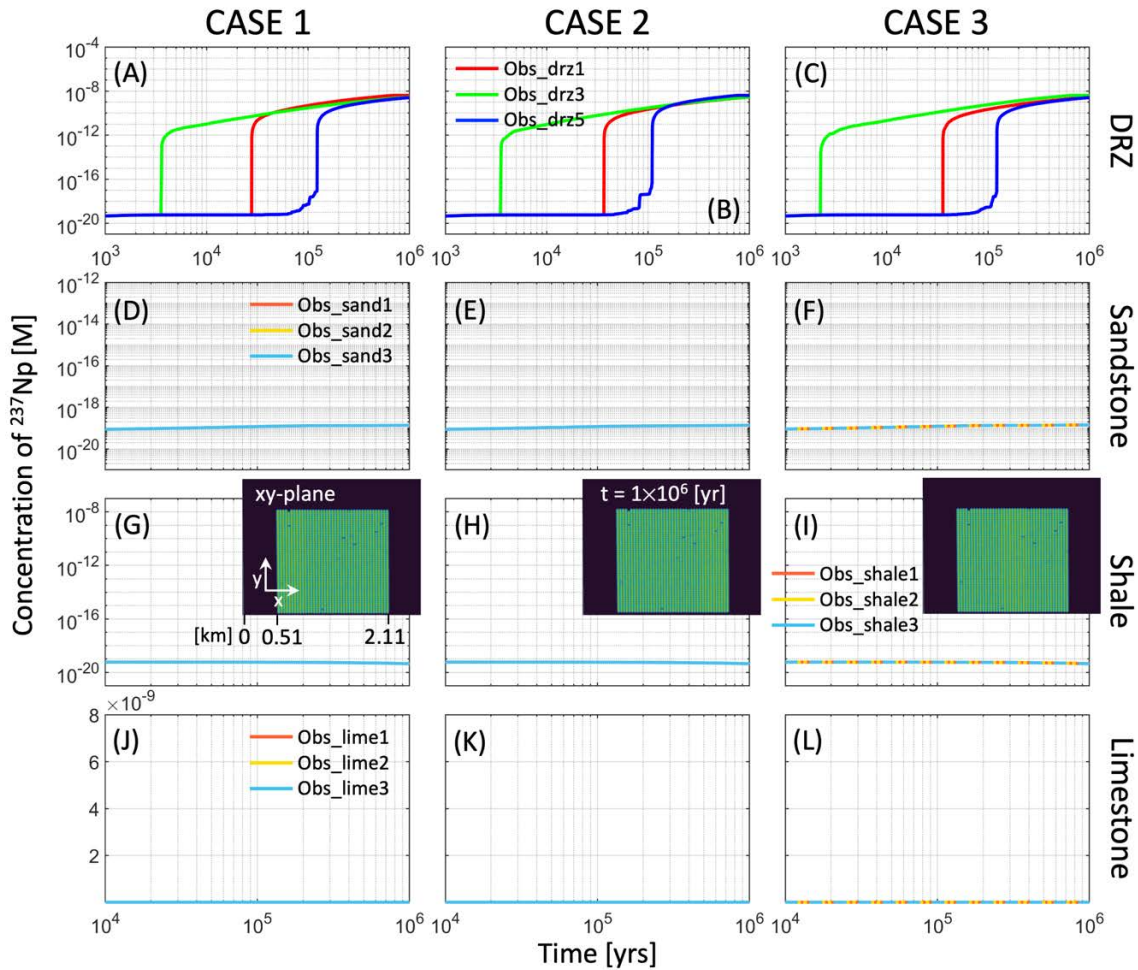
Figure 3-32. Evolution of ^{237}Np concentration at the observation points of DRZ (A to C) near WP1 (west edge), WP3 (middle), and WP5 (east edge) (refer to Figure 3-1(A)) as well as of sandstone (D to F), shale (G to I), and limestone (J to L) layers (refer to Figure 3-1(C)) for the three cases. The subset figures show the spatial distribution of ^{237}Np concentration at the end of simulation run (t = 1×10^6 years). The ranges of ^{237}Np concentration (y-axis) are the same to ones for ^{129}I concentration given in Figure 3-29.

Figure 3-32 shows the temporal changes of ^{237}Np-concentration at the observation points located within the DRZ and layers of upper sandstone, shale, and limestone (Figure 3-1(C)) for three cases.

Again, the earliest increase of ^{237}Np-concentration is observed in the near-field around the middle waste packages (green lines) among three observation points, which is a similar temporal order to one of ^{129}I-concentration (Figure 3-32(A) to Figure 3-32(C)).

In the far-field, no changes occur in ^{237}Np-concentration throughout the 10^6-year simulation because ^{237}Np (and other radionuclide species that adsorb and/or precipitate) remains within the vicinity of the repository (Figure 3-32(D) to Figure 3-32(L)). This result indicates that the chemical and reactive characteristics of radioactive isotopes will control the far-field and long-term transport of radionuclides once the waste form breach occurs.

3.2.4   Future work

Our simulation results show that the spatial distribution of different heat sources will impact the rate of heat-emitting/decaying of the nuclear waste package, which will influence the near-field hydro-thermal fields around the repository, and consequently far-field radionuclide transport after waste form breach occurs. However, the assumption and setting for our model in this study includes the following simplifying assumptions, that may not be realistic for the reasons listed below:

- Nuclear waste packages will be stored sequentially, such that simultaneous heat emission from all waste packages may not be appropriate to describe hydro-thermal flow in the repository system.

- The waste form degradation model assumes a constant spent fuel degradation rate with a fixed specific surface of reaction, not considering transient perturbations in ambient physical conditions around waste packages, to save substantial numerical costs caused by multiphysics-based calculation and iterations to generate degradation rates of thousands of waste packages over time.

- Constant values of hydro-thermal parameters (e.g., permeability, thermal conductivity etc.) assigned for engineered and natural barriers will not represent nonuniform hydro-thermal behaviors potentially driven by various amounts of heat energy from different types of waste packages.

- Pre-defined and constant volume of the DRZ will not capture inelastic mechanical deformation (e.g., healing and sealing) (Tsang et al., 2005), which may not predict the transport rate of radioactive isotopes for long-term field-scale approaches.

Future studies could consider a sequential order of storing waste packages to develop more realistic scenarios of multiple waste-package installation in the geologic repository. In addition, we would like to perform further uncertainty quantification on this shale system, incorporating uncertainty in parameters as well as the waste package placement. We also plan to investigate spatio-temporal statistical methods to understand correlations in the spatial fields over time given the cases of waste package placement.

Recent development of machine learning surrogates for a fuel degradation process model will be incorporated into our PFLOTRAN model to capture spatio-temporal environmental impacts on fuel degradation rates while maintaining the computational efficiency of field-scale repository simulations (Debusschere et al., 2023).

Changes in thermal, hydrological, and geochemical characteristics of the DRZ will affect the overall performance of radioactive waste repositories by redistributing the stress state of the rock and possibly creating additional pathways of radionuclide transport or fluid flow (Tsang et al., 2005; Nasir et al., 2014; Bernier et al., 2017; Zheng et al., 2017). To model more sophisticated coupling processes corresponding to sequential phases of thermal and mechanical loading-unloading., we need to implement hydro-thermal parameter functions and/or mechanical components with full mechanisms or reduced-order approaches as given in previous studies (Sasaki & Rutqvist, 2021; Chang et al., 2022).

3.3   Statistical Study with Uncertain Parameters

As discussed, in Section 3.1, the shale model originally from Sevougian et al. (2019b) was taken, modified, and implemented into the GDSA Workflow. The shale model repository originally consisted of 24-PWR on the west half and 37-PWR waste packages on the east half. This modified shale PA model now only considers the use of 37-PWR waste packages throughout the repository. Coordinates previously used for observation points at waste packages on the west half of the repository were updated due to increased spacing between the 37 PWRs. Additional observation points near the center of the repository

in the shale material layer were placed in order to detect pressure near this region. An open north boundary condition was implemented for the shale PA model (see Section 3.1.1.2).

Three tracers were added into this shale PA model for the GDSA uncertainty quantification and sensitivity analysis (UQ/SA) methods work package. A region was set up around the repository to be used for mass balance calculations as in the crystalline reference case from Swiler et al. (2022). The twelve QoIs that were added into the GDSA Workflow include ^{129}I and ^{237}Np concentrations at 1-million-year simulation time at six observation points (three in upper shale material layer, three in lower sandstone). Additionally, eight sampled epistemic parameters were specified using Dakota within the workflow.

3.3.1   GDSA Workflow Setting for Shale PA

The GDSA Framework (Figure 3-33), along with the NGW, has been increasingly used by GDSA projects in recent years and is referred to as the GDSA Workflow (Mariner et al., 2022). The GDSA Workflow is used to execute the computational shale PA model. There are five main software components in the GDSA Workflow:

- Dakota
    - Allows iterative studies such as sampling, sensitivity analyses, optimization
    - https://dakota.sandia.gov
- PFLOTRAN
    - Multiphysics simulation code that models flow, transport, and related processes
    - https://www.pflotran.org/
- Dakota GUI
    - Provides Graphical User Interface, has QuickStart wizards to generate Dakota input files
    - NGW included in software package
    - https://github.com/snl-dakota/dakota/releases
- NGW
    - Next Generation Workflow that allows the graphical creation of workflows, provides a palette with objects and connections
    - P**ackaged with the Dakota GUI** in the latest distributions (after 6.11)
- ParaView
    - Open-source visualization application that is optimized for handling large data sets
    - Sandia's internal website (https://onestop.sandia.gov/paraview) or for external use (https://www.paraview.org/)

The GDSA Workflow continues to be helpful in organizing, managing, setting up and submitting runs in the graphical environment, compared to traditional methods where the user would set up and run simulations individually. Using the NGW in the GDSA Workflow, the user can set up a workflow on a local machine and execute on the compute nodes of a high-performance computer (HPC).

A workflow is an executable graph of connected components. A component or "node" represents an activity (e.g., executing an external code, extracting a column of numbers from a table). Figure 3-34 shows the Solve_Pflotran workflow within the Dakota GUI for the shale PA. Text boxes in orange font highlight the important nodes linked to each other and describe the purpose of each area of this single

workflow. In the top left of this particular workflow are input parameters and remote resource settings; the bottom left nodes show where each PFLOTRAN source file is pulled from for use within the PFLOTRAN input file; top middle nodes show template processing scripts that help generate the bash script used to submit PFLOTRAN simulations into the HPC queue and a second script that generates the PFLOTRAN input file from a template for a specific run within the study; middle bottom nodes are the remote execution files that submit the generated bash script for PFLOTRAN simulations and a status bash script that help determine if a simulation ran successfully or not; next on the workflow is the remote PFLOTRAN execution that points to a second workflow called HPC_run that handles the actual HPC remote submission (Figure 3-35). Last within this workflow is the response extraction of twelve QoIs previously identified and implemented within the Dakota input file, Run_Dakota, shown in Figure 3-36.

All workflows presented here are linked within the Dakota GUI and once set up, can be run with a click of a button from the Run_Dakota workflow (Figure 3-37). After clicking the play button on the GUI, the Run_Dakota workflow reads in the Run_Dakota input file, generates values for the 50 samples requested using Latin hypercube sampling (LHS) for variables specified (rateSNF, kSand, kLime, kLSand, kDRZ, sNpKd, rateWP, and pShale), and sends these values through the Solve_Pflotran workflow to be inserted within a pflotran.template file that will result in a PFLOTRAN input file specific to each of the 50 runs in the study. These PFLOTRAN simulations are then executed on the HPC and the QoI are extracted.

Using the GDSA Workflow, a 50-sample study varying eight parameters was set up and run on an HPC. The average runtime was 15.7 hours on 1,024 CPU cores, meaning the 50-sample study took 803,840 CPU hours to run to completion.
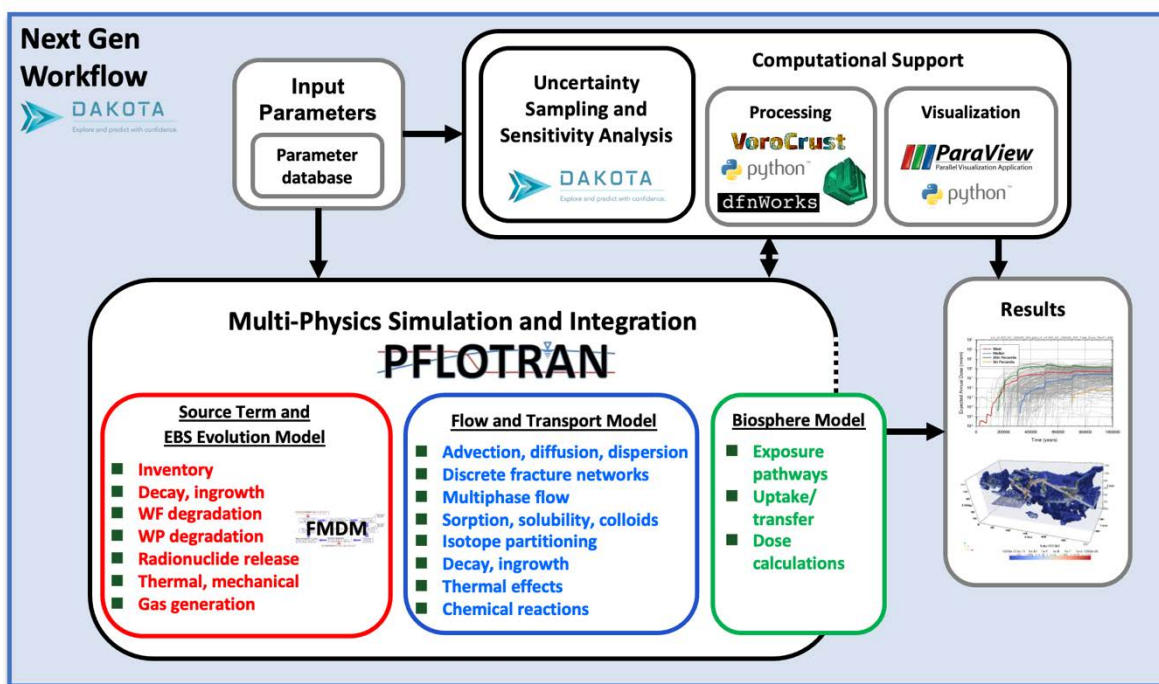
Figure 3-33.   The GDSA Framework.
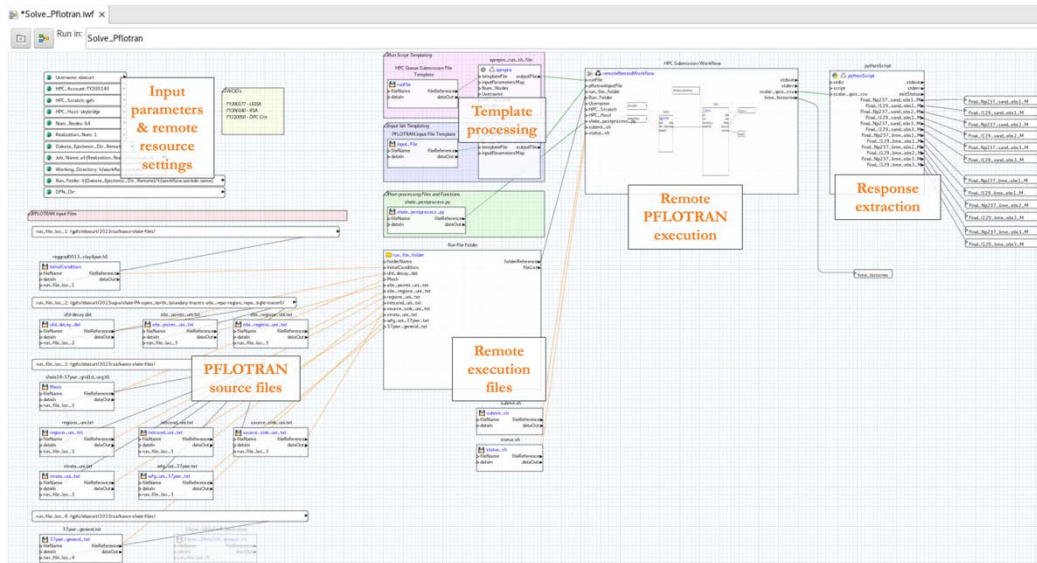
Figure 3-34. Solve_Pflotran workflow within the Dakota GUI for the shale PA GDSA Workflow.
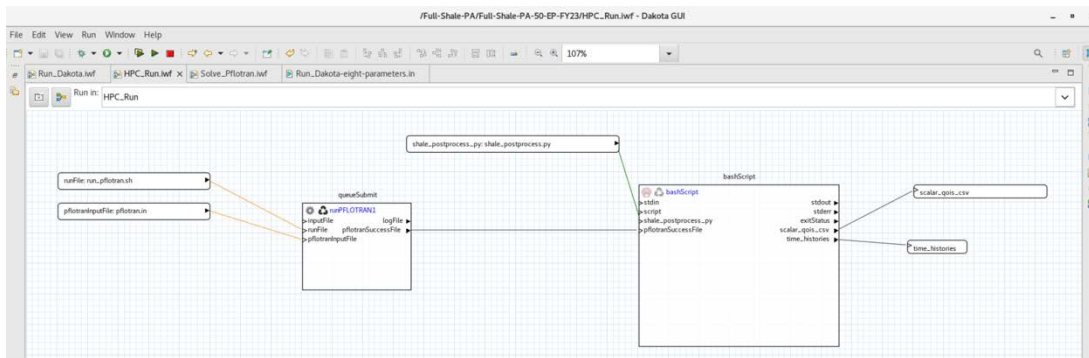
Figure 3-35. HPC_Run workflow within the Dakota GUI for the shale PA GDSA Workflow.

```
*Run_Dakota-eight-parameters.in ×

environment
    tabular_data
        tabular_data_file "tabular.dat"
    output_file "dakota.out"
    error_file "dakota.err"
    write_restart "dakota.rst"
    #read_restart "dakota.rst"
    results_output
        hdf5

method
    id_method "method1"
    sampling
        samples 50 #5 #1
        seed 1337
        fixed_seed
        sample_type
            lhs
        distribution
            cumulative
        model_pointer "model1"

model
    id_model "model1"
    single
        interface_pointer "interface1"
    variables_pointer "variables1"
    responses_pointer "responses1"

variables
    id_variables "variables1"
    active
        uncertain
    loguniform_uncertain = 6
                        # unfdeg  usand_k   lime_k    lsand_k   drz_k     shale_Np_Kd
        lower_bounds    1.e-8     1.e-15    1.e-17    1.e-14    1.e-18    1.26e+5
        upper_bounds    1.e-6     1.e-13    1.e-14    1.e-12    1.e-16    5.37e+7
        descriptors     'rateSNF' 'kSand'   'kLime'   'kLSand'  'kDRZ'    'sNpKd'

        uniform_uncertain = 2 #waste package degradation rate, host rock porosity
        lower_bounds    -5.5      0.1
        upper_bounds    -4.5      0.25
        descriptors     'rateWP' 'pShale'

interface
    id_interface "interface1"
    analysis_drivers "{DRIVER}"
        fork
            parameters_file "params.txt"
            results_file "results.txt"
            file_tag
            file_save
            work_directory
                named "work_dir"
                directory_tag
                directory_save
    asynchronous
        evaluation_concurrency 10 #3 #1

responses
    id_responses "responses1"
    descriptors 'Final_Np237_sand_obs1_M','Final_I129_sand_obs1_M',
                'Final_Np237_sand_obs2_M','Final_I129_sand_obs2_M',
                'Final_Np237_sand_obs3_M','Final_I129_sand_obs3_M',
                'Final_Np237_lime_obs1_M','Final_I129_lime_obs1_M',
                'Final_Np237_lime_obs2_M','Final_I129_lime_obs2_M',
                'Final_Np237_lime_obs3_M','Final_I129_lime_obs3_M'
    response_functions 12
        scalar_responses 12
    no_gradients
    no_hessians
```

Figure 3-36.   Dakota input file within the Dakota GUI for the shale PA GDSA Workflow.
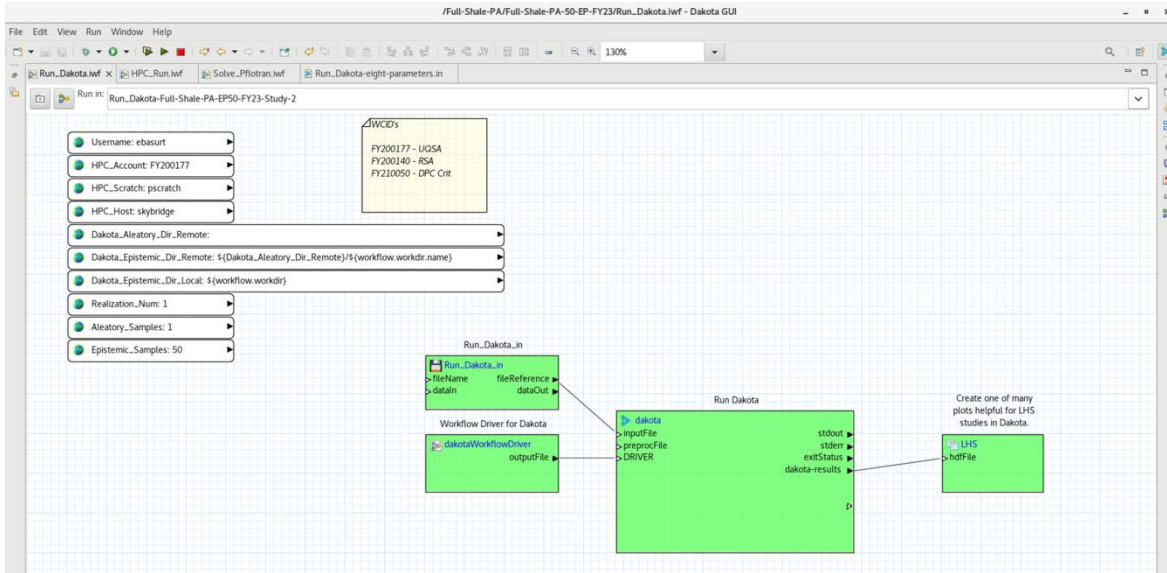
Figure 3-37. **Run_Dakota workflow within the Dakota GUI for the shale PA GDSA Workflow.**

3.3.2 Statistical Study Parameters

The constant inputs for the shale model are shown in Table 3-8 (Mariner et al., 2017; Sevougian et al., 2019b). Parameter values for eight model regions are included in this table and it includes parameter values such as permeability, porosity (ϕ), tortuosity (τ), effective diffusion coefficient, saturated thermal conductivity, heat capacity and grain density. Table 3-9 provides the sampled inputs used for this shale reference case. The parameters included in this table are SNF dissolution rate, mean waste package degradation rate, permeability ranges for five model regions (upper sandstone, limestone, lower sandstone, buffer, and DRZ), porosity of the shale host rock, and Neptunium K_d shale range.

Figure 3-38 shows the eight parameters within the variables section of the Dakota input file used for the shale PA 50-sample study. Parameters and ranges included in this variable block aligns with most parameters and ranges included in Table 3-9. Differences are that the 'rateWP' or mean waste package degradation rate is specified to be uniform uncertain instead of log uniform. Buffer k and Np K_d buffer were not used in this study. Future shale PA studies will consider the use of three additional parameters as included in Figure 3-39. The three additional parameters are buffer permeability 'kBuffer', Np K_d buffer 'bNpKd', and porosity of the buffer 'pBuffer'.

Table 3-8. Constant inputs for the shale reference case.

Model Region	Permeability (m^2)	Porosity ϕ	τ	Effective Diffusion Coefficient[1]	Saturated Thermal Conductivity (W/m/K)	Heat Capacity (J/kg/K)	Grain Density (kg/m^3)
Upper Sandstone[3]	1 x 10^{-13}	0.20	0.58	1.2 x 10^{-10}	3.1	830	2700
Host Rock Shale[2]	1 x 10^{-19}	0.20	0.11	2.2 x 10^{-11}	1.2	830	2700
Silty Shale[2]	1 x 10^{-17}	0.20	0.11	2.2 x 10^{-11}	1.4	830	2700
Limestone[2]	1 x 10^{-14}	0.10	0.04	4.0 x 10^{-12}	2.6	830	2700
Lower Shale[2]	1 x 10^{-20}	0.10	0.04	4.0 x 10^{-12}	1.2	830	2700
Lower Sandstone[3]	1 x 10^{-13}	0.20	0.58	1.2 x 10^{-10}	3.1	830	2700
Buffer[2]	1 x 10^{-20}	0.35	0.23	8.1 x 10^{-11}	3.0	830	2700
Waste Package	1 x 10^{-16}	0.5	1	5 x 10^{-10}	16.7	466	5000

[1] Effective diffusion coefficient $= D_w f\ t\ s$, where the free water diffusion coefficient (D_w) = 1 x 10^{-9} m^2/s (Li & Gregory, 1974) and saturation (s) = 1

[2] $t = \phi^{1.4}$ (Van Loon & Mibus, 2015)

[3] $t = \phi^{1/3}$ (Millington, 1959)

Table 3-9. Sampled inputs for the shale reference case.

Input	Description	Range	Units	Distribution
rateSNF	SNF Dissolution Rate	10^{-8} – 10^{-6}	yr^{-1}	log uniform
rateWP	Mean Waste Package Degradation Rate	10^{-5.5} – 10^{-4.5}	yr^{-1}	log uniform
kSand	Upper Sandstone Permeability	10^{-15} – 10^{-13}	m^2	log uniform
kLime	Limestone Permeability	10^{-17} – 10^{-14}	m^2	log uniform
kLSand	Lower Sandstone Permeability	10^{-14} – 10^{-12}	m^2	log uniform
kDRZ	DRZ Permeability	10^{-18} – 10^{-16}	m^2	log uniform
pShale	Host Rock (Shale) Porosity	0.1 – 0.25	-	uniform
sNpKd	Np K_d Shale	$1.26*10^5 – 5.37*10^7$	m^3kg^{-1}	log uniform

```
variables
    id_variables "variables1"
    active
        uncertain
    loguniform_uncertain = 6
                        # unfdeg  usand_k   lime_k    lsand_k   drz_k    shale_Np_Kd
            lower_bounds  1.e-8   1.e-15    1.e-17    1.e-14    1.e-18   1.26e+5
            upper_bounds  1.e-6   1.e-13    1.e-14    1.e-12    1.e-16   5.37e+7
            descriptors   'rateSNF' 'kSand'  'kLime'   'kLSand'  'kDRZ'   'sNpKd'

        uniform_uncertain = 2 #waste package degradation rate, host rock porosity
            lower_bounds  -5.5    0.1
            upper_bounds  -4.5    0.25
            descriptors   'rateWP' 'pShale'
```

Figure 3-38. Variables specified along with their ranges within the Dakota input file used for the shale PA study.

```
variables
    id_variables "variables1"
    active
        uncertain
    loguniform_uncertain = 8
                        # unfdeg  usand_k   lime_k    lsand_k   buffer_k  drz_k    shale_Np_Kd  buffer_Np_Kd
            lower_bounds  1.e-8   1.e-15    1.e-17    1.e-14    1.e-20    1.e-18   1.26e+5      1.62e+5
            upper_bounds  1.e-6   1.e-13    1.e-14    1.e-12    1.e-16    1.e-16   5.37e+7      1.08e+9
            descriptors   'rateSNF' 'kSand'  'kLime'   'kLSand'  'kBuffer'  'kDRZ'   'sNpKd'      'bNpKd'

        uniform_uncertain = 3 #waste package degradation rate, host rock porosity, buffer porosity
            lower_bounds  -5.5    0.1     0.3
            upper_bounds  -4.5    0.25    0.5
            descriptors   'rateWP' 'pShale' 'pBuffer'
```

Figure 3-39. Variables specified along with their ranges within the Dakota input file to be used for future shale PA studies. Includes additional varibles such as 'kBuffer', 'bNpKd', and 'pBuffer'. Current study assumes constant buffer material properties.

3.3.3 Simulation on an example realization

A single simulation from the 50-sample study is visualized in Figure 3-40 through Figure 3-42 at 1,000,000 years. These visuals include several observation points of interest in this shale PA study that are represented by white spheres and labeled on all figures. Figure 3-40 includes three different views, each is colored by total ^{129}I concentration; Figure (A) shows a y-normal clip through the repository at the y coordinate (817.5 m) of the observation points of interest, along with a visualization of the repository; Figure (B) shows a vertical cross-section (XZ-plane); Figure (C) shows a horizontal cross-section (XY-plane) at the limestone material layer where the higher concentration of ^{129}I resides at 1,000,000 years.

A cumulative distribution function of waste package breach times generated for this single run of the 50-sample study is shown in Figure 3-43. The first waste packages breach at 405 years, 10% (205) of waste packages have breached by 3,300 years, 50% (1,025) of waste packages have breached by 22,400 years, and 99% (2,044) of waste packages have breached by 1,000,000 years. This waste package breach data is useful in helping explain the trends of the observed I-129 concentrations at the distant observation points.

A plot of total ^{129}I molar concentration at various observation points of interest is shown in Figure 3-44. The location of observation points 'pwr_wp2', 'pwr_bf2', 'pwr_drz2' are shown in Figure 3-16. The location of the remaining observation points 'sand_obs1', 'sand_obs2', 'sand_obs3', 'lime_obs1', 'lime_obs2', and 'lime_obs3' are shown in Figure 3-40. At 1-million-year simulation time, the limestone material layer contains the highest concentration of ^{129}I outside the repository region. Observation points 'lime_obs1', 'lime_obs2', and 'lime_obs3' all have ^{129}I concentrations around 10^{-8} M. 'lime_obs3' is the

observation point at the east end of the model domain and has the lowest concentration of the three limestone observation points.

A sensitivity analysis performed on this 50-sample shale PA study will be included in Swiler et al. (2023) and will dig further into the correlation of sampled parameters between each other at the observation points within the model. This sensitivity analysis will help determine what parameters are most important for this shale PA.
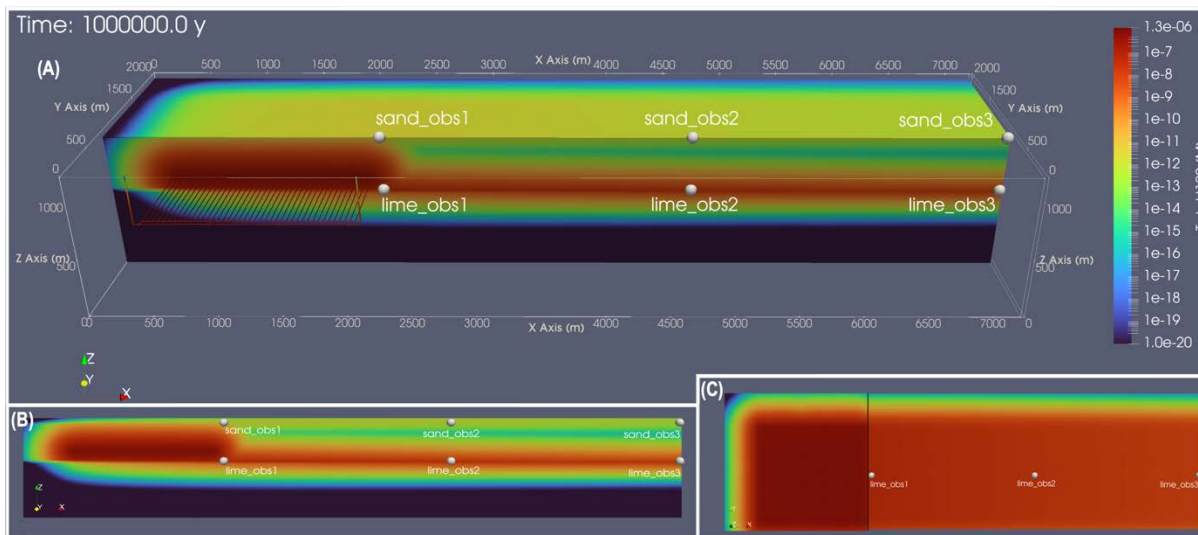
Figure 3-40.   Three views of a single simulation from the 50-sample shale PA study colored by total ^{129}I concentration at 1,000,000 years; Figure (A) shows a y-normal clip through the repository; Figure (B) shows a vertical cross-section (XZ-plane); Figure (C) shows a horizontal cross-section (XY-plane) at the limestone material layer where the higher concentration of ^{129}I resides at 1,000,000 years for this particular simulation.
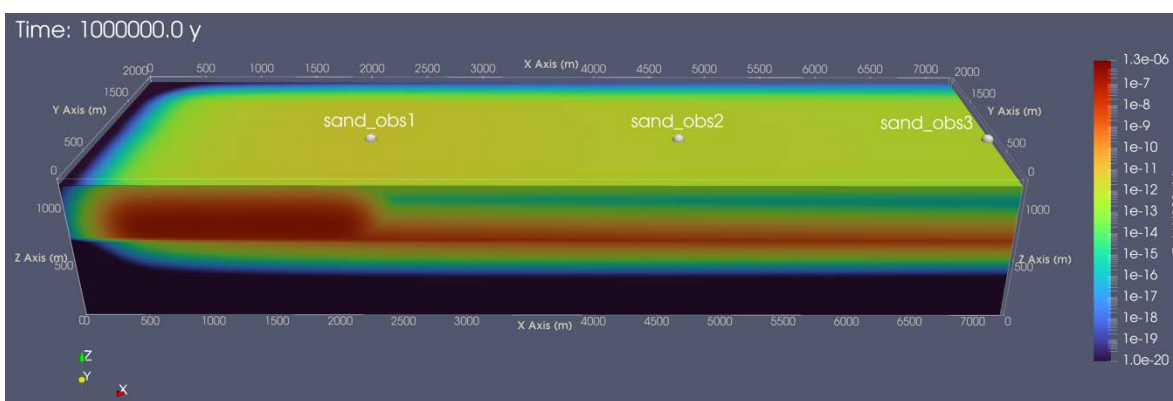
Figure 3-41.   Single simulation from the 50-sample shale PA study colored by total ^{129}I concentration at 1,000,000 years with observation points in the sandstone material layer represented as white spheres and labeled.
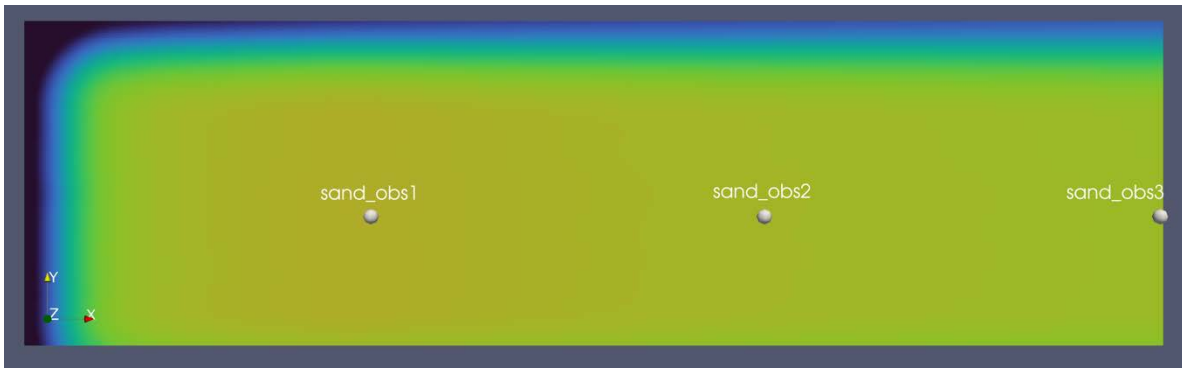
Figure 3-42. Top view of a single simulation from the 50-sample shale PA study colored by total ^{129}I concentration at 1,000,000 years with observation points in the sandstone material layer represented as white spheres and labeled.
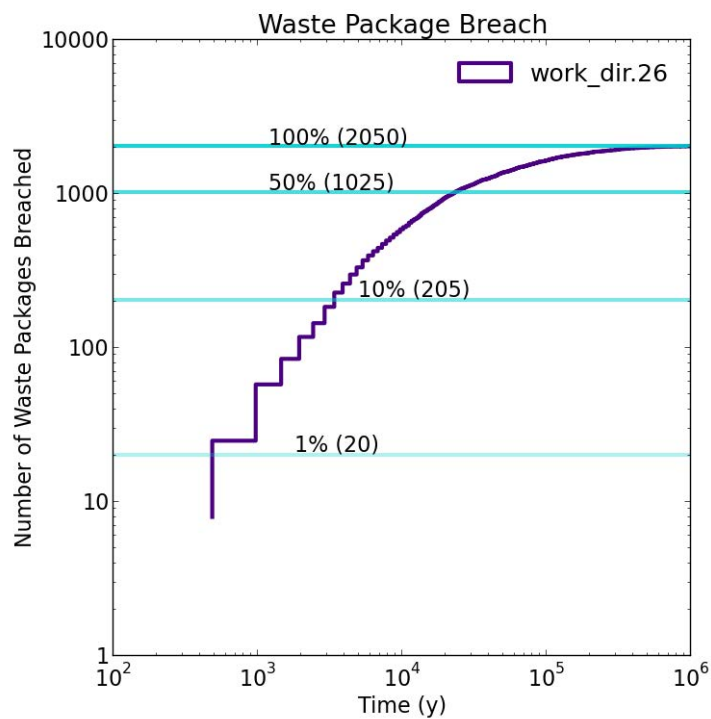
Figure 3-43. Cumulative distribution function (CDF) of waste package breach times for a single run of the 50-sample study.
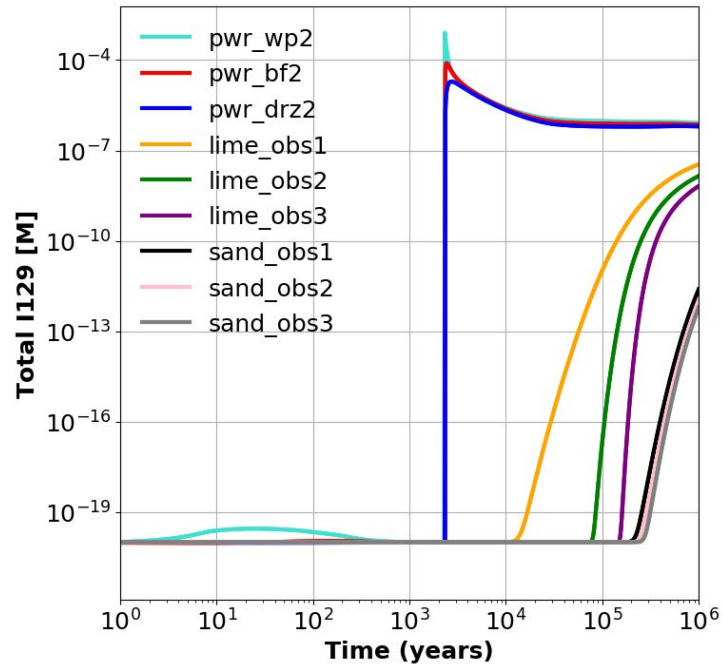
Figure 3-44.   Total ^{129}I concentrations at nine observation points for a single run of the 50-sample study.

This page is intentionally left blank.

4.   UNSATURATED ALLUVIUM MODELLING

4.1   Improved Geological Realism Collaboration with Los Alamos National Laboratories

This year the Geologic Disposal Safety Assessment (GDSA) Repository Systems Analysis (RSA) and the GDSA-Geologic Modeling project at Los Alamos National Laboratories (LANL) initiated a formal collaboration to develop a process to incorporate the results of their unsaturated alluvium geological modelling studies (Gross et al., 2019; 2021, and 2022) into RSA unsaturated alluvium performance assessment (PA) studies. The results of this study will be in separate reports, LaForce et al. (2023b) and Gross et al. (2023) and the workflow is very briefly summarized here.

Initially it was necessary to develop a robust model conversion workflow for converting the LANL geological and simulation models into a format that can be used by Sandia National Laboratory (SNL) researchers for PFLOTRAN (Lichtner et al., 2020) simulations. The first step was an iterative process between the LANL and SNL teams to develop a workflow for converting LaGriT (LANL, 2017) meshes into a format that can be read into PFLOTRAN. A simple test mesh was converted, and the simulation results were benchmarked against previous PFLOTRAN simulations and analytical solutions to validate the workflow.

The second step of the workflow was to convert one of the FEHM (LANL, 2018) simulation models of Gross et al. (2022) for running in PFLOTRAN. Again, it was an iterative process between LANL and SNL to create a mesh populated with heterogenous porosity, permeability, and material types, as well as flow and transport parameters so that identical simulations can be run in FEHM at LANL and PFLOTRAN at SNL.

Running the example FY2022 model for comparative purposes is underway at both SNL and LANL. Future work during this FY will include comparison of PFLOTRAN and FEHM simulations for the example realization, ISO-750 R6, from Gross et al. (2022). Finally, additional simulations will be run on several of the 2022 LANL models that more realistic parameters for gradual radionuclide release utilizing the PFLOTRAN waste form modelling capability.

4.2   Transport Comparison in Unsaturated Zone Model

4.2.1   Small-scale model/mesh development and full-scale model

Two small-scale models using nuclear waste transport (NWT) mode (Figure 4-1) were developed to help resolve tracer concentration oscillations at resaturation that past full-scale model domain simulations have seen in FY22 (LaForce et al., 2022a). The first small-scale model is a nearfield model with a domain size of 50 m in length, 10 m in width, and 100 m in height. This nearfield model consists of 13,237 grid cells with an element size of about 1.67 x 1.5 x 1.67 m and considers half a waste package. The second small scale model has a domain size of 50 m in length, 10 m in width, and 552 m in height. This second model aimed at including all but the lower basin fill (lbf) material layer and consists of 72,044 grid cells with an element size of about 1.67 x 1.5 x 1.67 m and considers half a waste package.

Simulation tests using the small-scale model domains were unsuccessful in running to the final time of 100,000 years. Potential oscillatory convergence warnings in the PFLOTRAN output file were observed within the GENERAL MULTIPHASE FLOW timestep before simulations failed. Small-scale simulation efforts were abandoned once further developments had been made within the NWT mode that included bug fixes and promising improvements.

The full-scale unsaturated zone (UZ) model domain mesh shown in Figure 4-2 and Figure 4-3 is the same as in the FY22 model (LaForce et al., 2022a). This FY's UZ simulations differ that the open northern boundary was implemented for the reasons as stated in Section 3.1.1.2 for the shale reference case. Further developments were also made in PFLOTRAN in GENERAL mode. A previous version of the code could declare false convergence when the solution had actually not converged. Full-scale UZ simulations were run with this updated version of PFLOTRAN and successfully completed the NWT and Global Implicit Reactive Transport (GIRT) mode simulations.
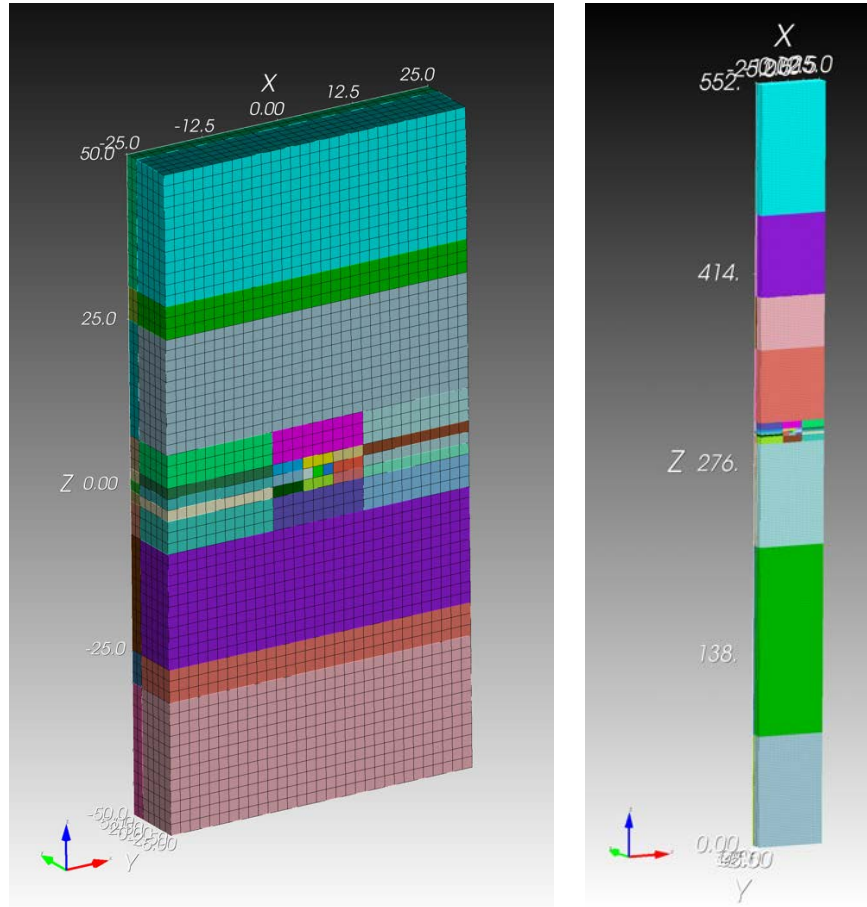
Figure 4-1.   Two small-scale half waste package UZ models. Nearfield UZ model (left) and full-vertical extent model (right).
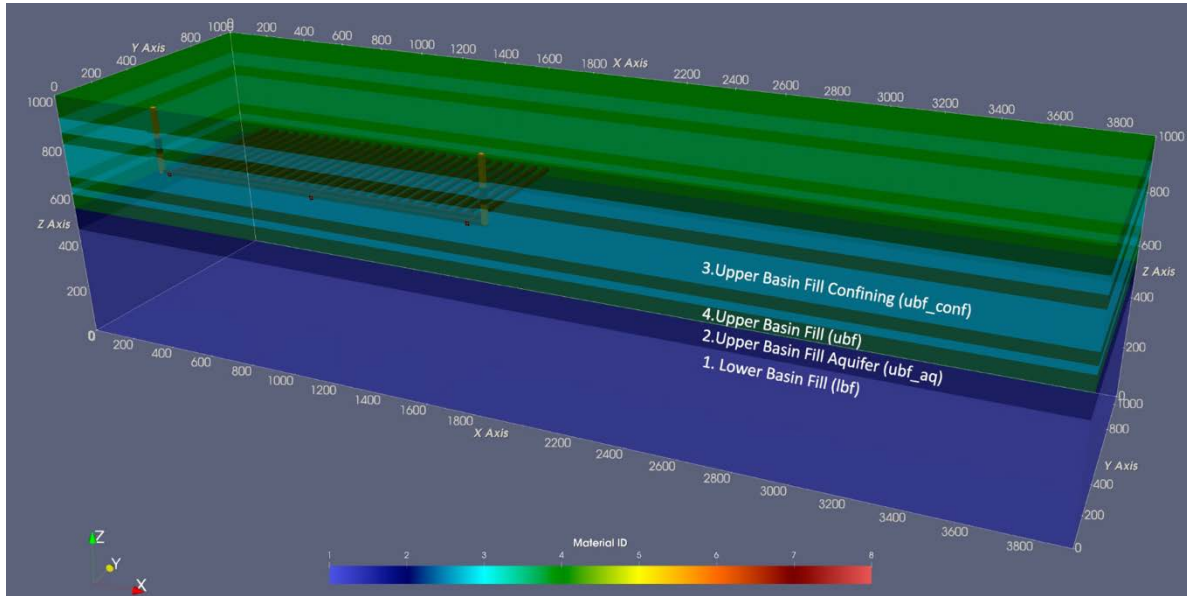
Figure 4-2. Configuration of the repository and natural barrier system generated using Cubit, simulated in PFLOTRAN and visualized on ParaView. Turquoise color (material ID 3) represents the ubf_conf (upper basin fill confining) units (the centermost contains the repository as seen there), green (material ID 4) represents UBF (upper basin fill), dark blue (material ID 2) represents the UBF aquifer, and blue (material ID 1) represents LBF (lower basin fill). Distances along the axes are in meters, where 1000 m is land surface and 0 m is the bottom of the model domain. The left side of the figure represents a western direction.
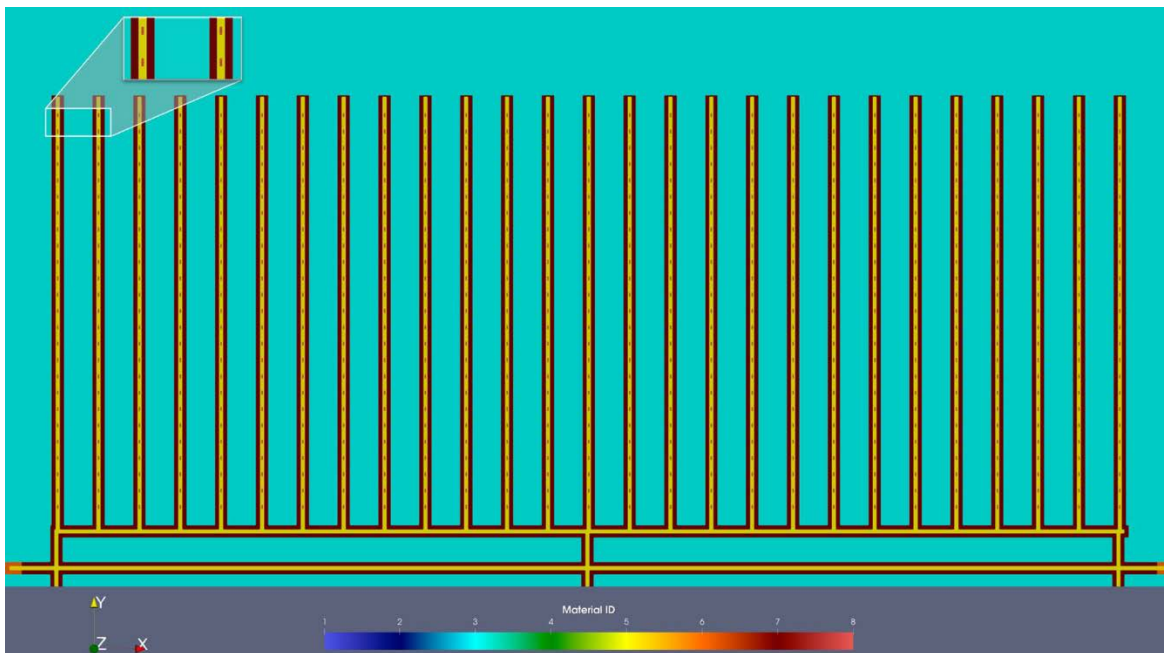
Figure 4-3. XY slice through the repository colored by material ID. The repository is 250 m below the surface. The zoom in box on the top left shows a close-up of four waste packages colored in red, buffer in yellow, disturbed rock zone in burgundy, and ubf_conf in turquoise. Visualized using ParaView.

4.2.2   Difference in GIRT vs NWT Computational Model

Within the PFLOTRAN SUBSURFACE_TRANSPORT block, MODE is a required card. This specific card specifies the transport mode to be employed. Currently there are three transport modes which include GIRT and NWT. GIRT mode specifies fully implicit coupling of transport and reaction. NWT mode uses different primary independent variables from GIRT.NWT can handle complete dry-out of arbitrary cells in the model domain, which is the main difference from GIRT mode. NWT was designed to be used with WIPP flow mode, which is isothermal two-phase flow. The mode assumes equilibrium chemical processes, meaning rates and database files do not need to be provided. NWT – PFLOTRAN Documentation (2023) and GIRT – PFLOTRAN Documentation (2023) provide more information regarding these modes and their usage.

Figure 4-4 provides an example of how GIRT and NWT are specified within the subsurface transport block in the PFLOTRAN input deck. One difference here between the setup of both modes can be seen in the RESTART block. For the GIRT setup, comments are provided that refer to the use of a restart file used that was generated from an initial UZ simulation that had no transport model implemented. The initial GIRT simulation did not include transport due to the inability of GIRT to handle complete dry-out of cells in the model domain. Due to this, the GIRT simulations involve a two-step process. The first step generates checkpoint files at specified times. The checkpoint file of interest ended up being at the 2,200-year timestep, the first time when no grid cells in the model domain had zero liquid saturation. The second step of the GIRT simulation starts at the 2,200 years checkpoint and includes subsurface transport. The NWT mode simulation also uses a RESTART file as seen in the figure, but this is from an initial equilibration run that GIRT also uses in the first step process.

Two other visuals shown in Figure 4-5 show how TRACER1 is specified within the required CHEMISTRY block for GIRT mode and within the specific NUCLEAR_WASTE_CHEMISTRY block for NWT mode. The required card for the CHEMISTRY block is PRIMARY_SPECIES in which TRACER1 is listed as the species for which concentrations will be solved for GIRT mode. The required card for the NUCLEAR_WASTE_TRASNSPORT block is the SPECIES block needed for each transported species in the NWT simulation. Additionally, there are required keywords that need to be specified within the SPECIES block for NWT mode which are: SOLUBILITY, PRECIPITATE_MOLAR_DENSITY, and ELEMENTAL_KD.

Figure 4-6 shows how the CONSTRAINT card is specified for both GIRT and NWT modes. The difference between the two modes here is that for GIRT mode, T is equal to the total aqueous component concentration [mol/L], while in NWT mode it is equal to total bulk concentration [mol/m$^3_{bulk}$]. TRACER1 is listed as a species within the CONCENTRATIONS with a background concentration of $1. \times 10^{-20}$ and a constraint type T.

```
SIMULATION
  SIMULATION_TYPE SUBSURFACE
  PROCESS_MODELS
    SUBSURFACE_FLOW flow
      MODE GENERAL
      OPTIONS
        WINDOW_EPSILON 1.d-3
        CHECK_MAX_DPL_LIQ_STATE_ONLY
        NEWTONTRDC_HOLD_INNER_ITERATIONS
      /
    /
    SUBSURFACE_TRANSPORT transport
      MODE GIRT
      OPTIONS
        SKIP_RESTART
      /
    /
  / #END OF PROCESS_MODELS
   RESTART
      # Restart file used here was generated from previous
      # UZ run with no transport.
      # Checkpoint file at 2,200 years is used because by this
      # time in the simulation there is not a single grid cell
      # with a liquid saturation equal to zero.
      FILENAME ./uz_noTRANS/mesh24TR-2200.0000y.h5
      RESET_TO_TIME_ZERO
   /
END
```

```
SIMULATION
  SIMULATION_TYPE SUBSURFACE
  PROCESS_MODELS
    SUBSURFACE_FLOW flow
      MODE GENERAL
      OPTIONS
        WINDOW_EPSILON 1.d-3
        CHECK_MAX_DPL_LIQ_STATE_ONLY
        NEWTONTRDC_HOLD_INNER_ITERATIONS
      /
    /
    SUBSURFACE_TRANSPORT  nw_transport
      MODE NWT
      OPTIONS
        SKIP_RESTART
      /
    /
  / #END OF PROCESS_MODELS
   RESTART
      FILENAME ./initcon/mesh24TR-1000000.0000y.h5
      RESET_TO_TIME_ZERO
   /
END
```

Figure 4-4.   Example of how GIRT (top) and NWT (bottom) modes are specified within the subsurface transport block in the PFLOTRAN input deck.

```
CHEMISTRY
  PRIMARY_SPECIES
    TRACER1
  /
  TRUNCATE_CONCENTRATION 1.d-22
  OUTPUT
    TOTAL
    TOTAL_SORBED
    all
  /
END
```

```
NUCLEAR_WASTE_CHEMISTRY
  SPECIES
    NAME                  TRACER1
    SOLUBILITY            1.0E20     # [mol/m^3-liq]
    PRECIP_MOLAR_DENSITY 38.61d3     # [mol/m^3-mnrl] (quartz example)
    ELEMENTAL_KD          0.0d0      # [m^3-water/m^3-bulk]
  /
  SPECIES
    NAME                  TRACER2
    SOLUBILITY            1.0E6      # [mol/m^3-liq]
    PRECIP_MOLAR_DENSITY 38.61d3     # [mol/m^3-mnrl] (quartz example)
    ELEMENTAL_KD          0.0d0      # [m^3-water/m^3-bulk]
  /
  OUTPUT
    ALL_SPECIES
    ALL_CONCENTRATIONS
    MINERAL_VOLUME_FRACTION
  /
END
```

Figure 4-5.   **Example of how TRACER1 is specified within the CHEMISTRY block for GIRT mode (top) and within the NUCLEAR_WASTE_CHEMISTRY block for NWT mode (bottom) in the PFLOTRAN input deck.**

```
CONSTRAINT constraint_inventory_initial
  CONCENTRATIONS
   # species_name   concentration  constraint_type
     TRACER1         1.d-20          T
  /
END
```

Figure 4-6.   **Example of how concentrations for TRACER1 is specified within the CONTRAINT card for use within both GIRT and NWT modes in the PFLOTRAN input deck.**

4.2.3   GIRT Simulation Results

PFLOTRAN's GIRT mode simulations fail as saturation approaches zero, which is expected and is the reason why NWT mode was developed. The present simulation only includes the second step of the two-step process discussed above that uses a checkpoint file at 2,200 years generated from the initial first step simulation. The use of the checkpoint file is considered an acceptable approximation to the full simulation including transport because at 2,200 years radionuclides would be in or near the nearly dry waste packages, and without mobile water present there is no mechanism for transport away from them. In FY22, the GIRT mode simulation completed to the final time of 100,000 years from the restart time of

2,200 years in 15.5 hours on 540 cores. The GIRT mode simulation this FY ran to the final time of 100,000 years from the restart time of 2,200 years in 18.7 hours on 540 cores.

Figure 4-7 shows a series of XZ slices through an observation point called "Fwp_inside" which is in the center grid cell of the centermost waste package in the repository. There are subplots for eight periods of time (2,200, 2,300, 2,500, 3,000, 5,000, 7,200, 22,200, 32,200 y) in the 100,000-year simulation for a GIRT mode simulation. Each time includes a visual colored by material ID (top left), aqueous concentration of TRACER1 (bottom left), liquid saturation (top right), and temperature in degrees Celsius (bottom right). In GIRT mode, the initial time at which transport is applied is at 2,200 years, which corresponds to the first time provided in this figure. At this point in time, tracer concentration is not yet visible. By 2,300-year timestep, aqueous concentration for TRACER1 is now visible and located around the "Fwp_inside", liquid saturation in and around the observation point is low, and temperature is in the lower half of the range shown. By 2,500 years, TRACER1 has now begun to transport below the repository due to infiltration driving downward flux. By 3,000 years, tracer concentration has now decreased at the "Fwp_inside" observation point due to the continued infiltration. By 32,200 years, only low concentrations of tracer are visible in and around the "Fwp_inside" observation point and by this time the waste package has liquid saturation around 0.49 and temperatures have nearly returned to initial values.
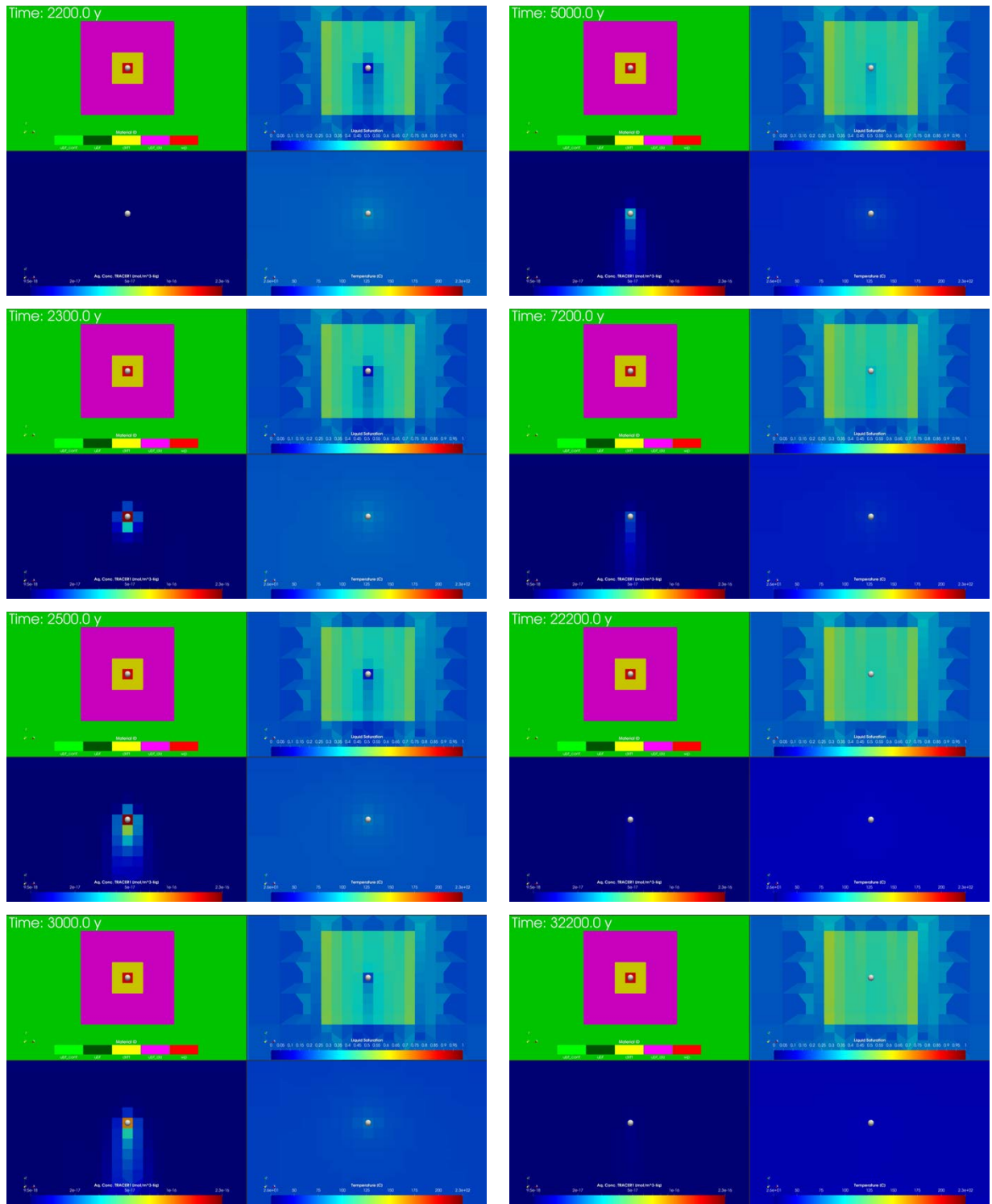
Figure 4-7. A series of XZ slices through the centermost waste package, 'Fwp_inside', which is represented by a white sphere at eight periods of time (2200, 2300, 2500, 3000, 5000, 7200, 22200, 32200 y) in the 100,000-year simulation for GIRT mode. Top left visual is colored by material ID. Bottom left is colored by aqueous concentration of TRACER1. Top right is colored by liquid saturation. Bottom right is temperature °C.

4.2.4   NWT Simulation Attempts

In FY22, a UZ NWT mode simulation completed only 8,463 years of simulation time out of the final time of 100,000 years within the HPC 96-hour time limit on 540 cores. In this FY, the UZ NWT mode simulation ran to the final time of 100,000 years in 19.3 hours on 540 cores. Development of PFLOTRAN in general and bug fixes within NWT have made it possible to run UZ NWT mode simulations up to the intended final time of 100,000 years.

A northern boundary condition was set for the NWT simulation. Previously in FY22, no tracer results were included for NWT mode since simulations were still a work in progress and oscillations in tracer concentration at resaturation were an issue that needed to be resolved.

Oscillations in both aqueous and total bulk tracer 1 concentrations at "Fwp_inside" are still present in most recent simulations even with the corrected NWT mode that has been merged to the master version of PFLOTRAN. Oscillations are believed to be caused by phase-state changes that occur in the waste packages. As the phase state changes, total bulk concentration may be smooth but aqueous concentrations are not since they depend on saturation.

Figure 4-8 shows a series of XZ slices through an observation point called "Fwp_inside" which is in the center grid cell of the centermost waste package in the repository. There are visuals for eight periods of time (0.1, 10, 100, 500, 1,000, 2,000, 5,000, 10,000 y) in the 100,000-year simulation for the NWT mode simulation. Each time includes a subplot colored by material ID (top left), aqueous concentration of TRACER1 (bottom left), liquid saturation (top right), and temperature in degrees Celsius (bottom right). At 0.1 y, tracer concentration is slightly visible in around the waste package region. By the 10-year timestep, aqueous concentration for TRACER1 is now clearly visible in and around "Fwp_inside" with the higher concentration located in the center of this observation point. Liquid saturation in and around the observation point is zero, and temperature is in the high end of the range shown (230 °C). By 100 years, TRACER1 higher concentration surrounds the upper region in the buffer (drift) and ubf_drz regions above "Fwp_inside". Region of zero liquid saturation currently has increased into the buffer and ubf_drz material regions as well. Temperature at the waste package have dropped slightly and the surrounding regions have seen an increase by about 25 °C. By 500 years, tracer has now begun to transport below the repository due to infiltration driving downward flux. By 1,000 years, tracer continues to be transported downward from the repository with concentrations focused in the waste package region. By 2,000 years, a large tracer concentration has now been transported down from the repository region and liquid saturation continues to increase in the region. By 10,000 years, nearly all tracer concentration has now been transported out of the waste package and repository region. Temperatures at his time have reached the lower range in of about 50 °C. Figure 4-9 through Figure 4-16 provide an additional zoomed out view of this specific NWT simulation.
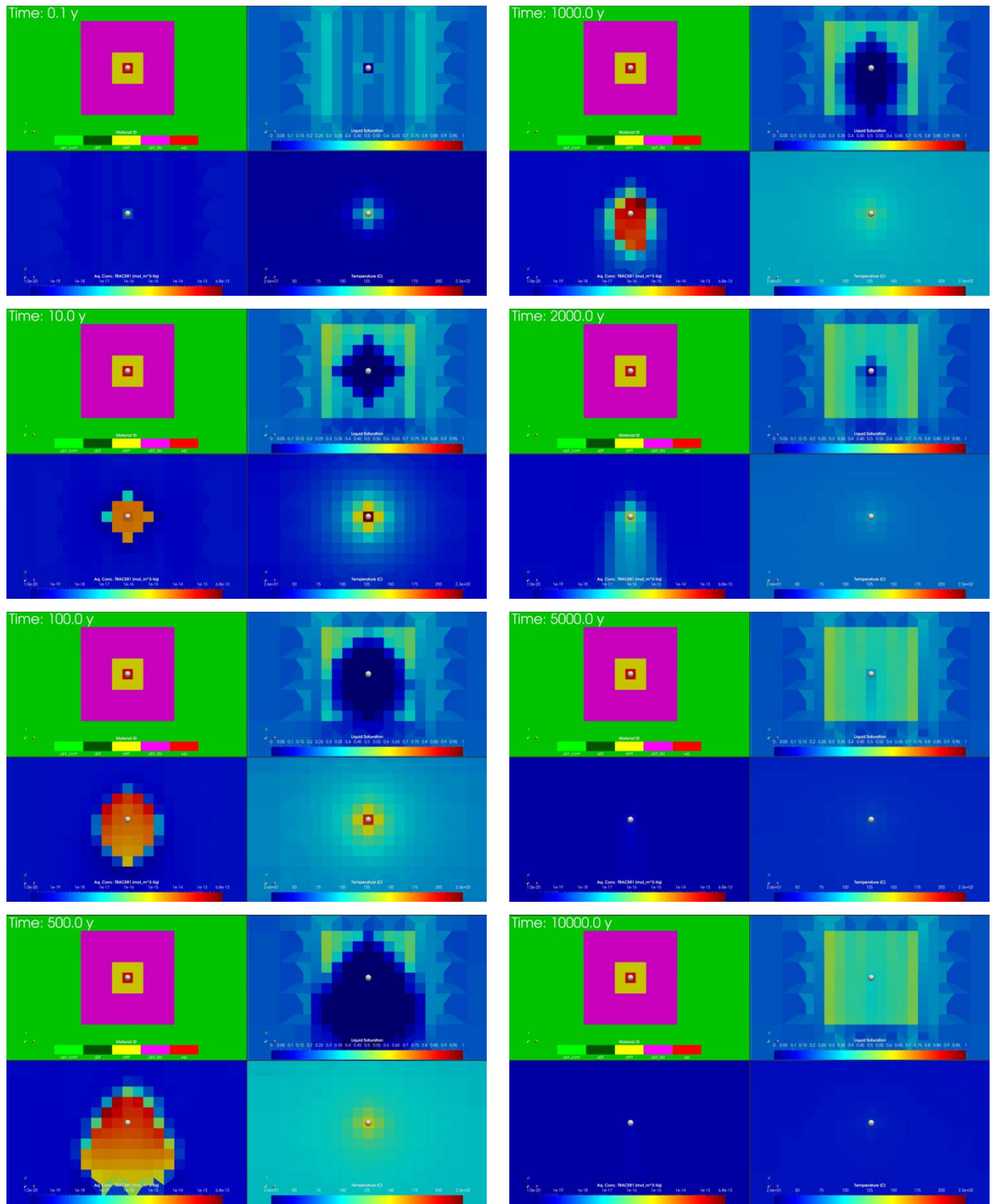
Figure 4-8. A series of XZ slices through the centermost waste package, 'Fwp_inside', at eight points in time (0.1, 10, 100, 500, 1,000, 2,000, 5,000, 10,000 y) in the 100,000-year simulation for NWT mode. Top left visual is colored by material ID. Bottom left is colored by aqueous concentration of TRACER1. Top right is colored by liquid saturation. Bottom right is temperature °C.
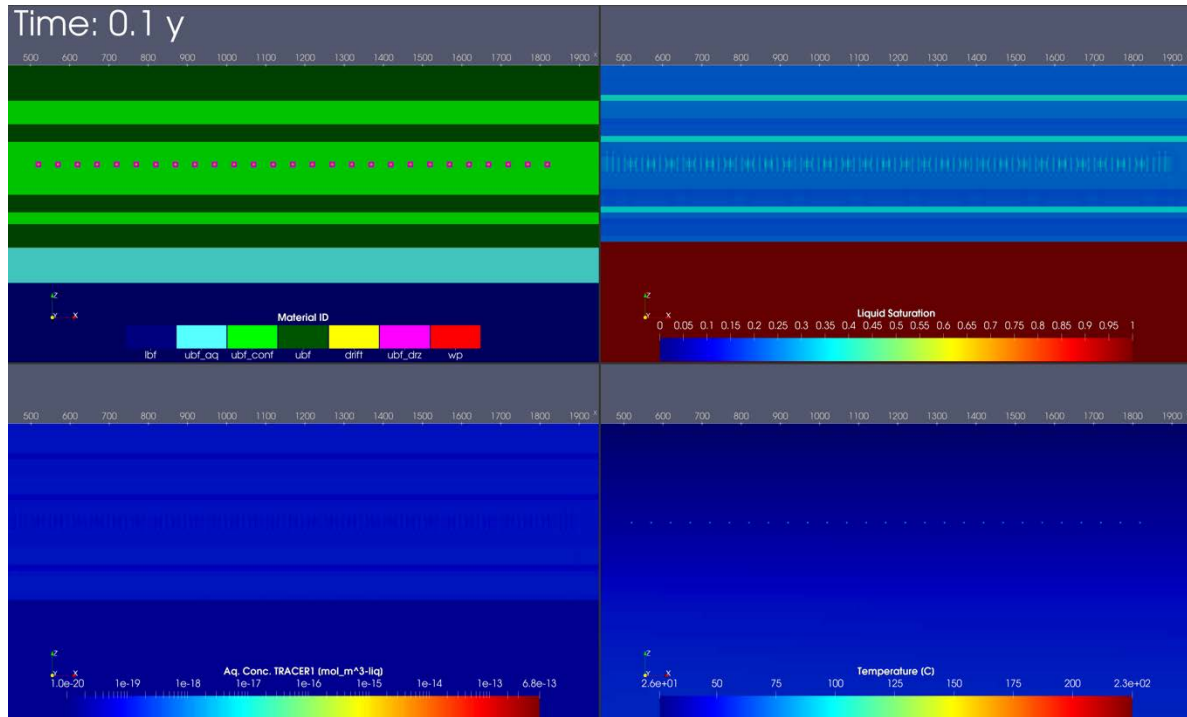
Figure 4-9. **XZ slice through the center of the repository colored by material ID (top left), liquid saturation (top right), aqueous concentration for Tracer1 (bottom left), and temperature °C (bottom right) at 0.1 y for NWT mode simulation.**
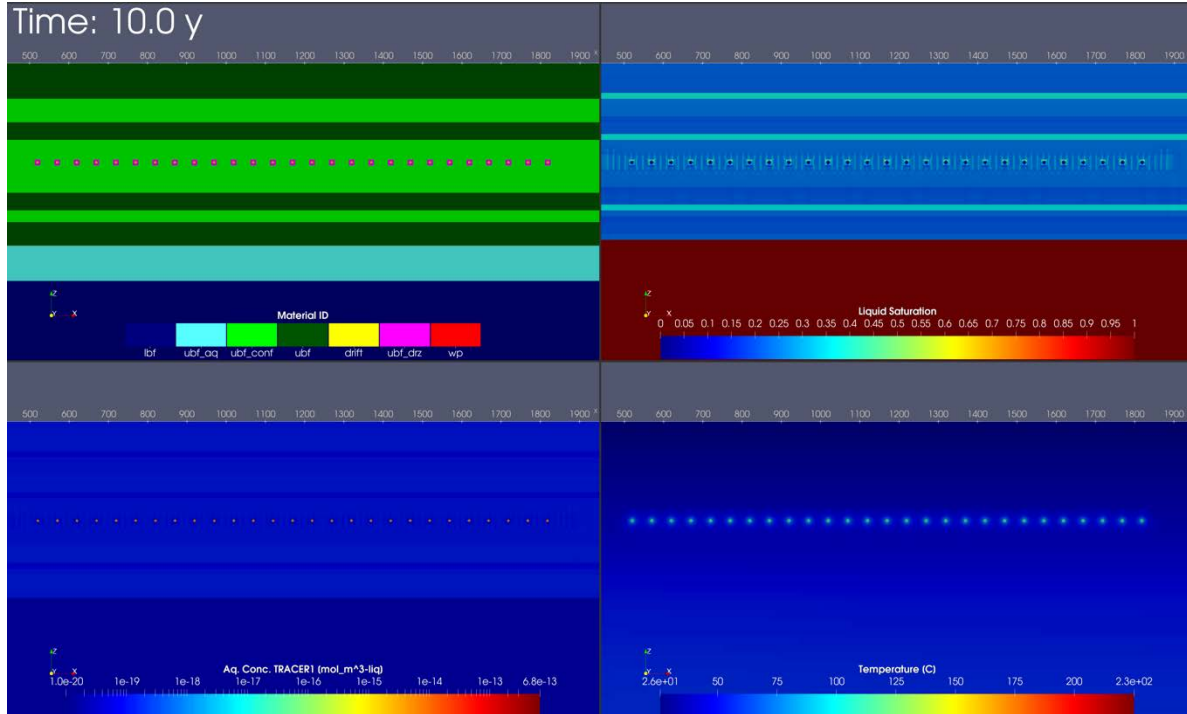
Figure 4-10. **XZ slice through the center of the repository colored by material ID (top left), liquid saturation (top right), aqueous concentration for Tracer1 (bottom left), and temperature °C (bottom right) at 10 y for NWT mode simulation.**
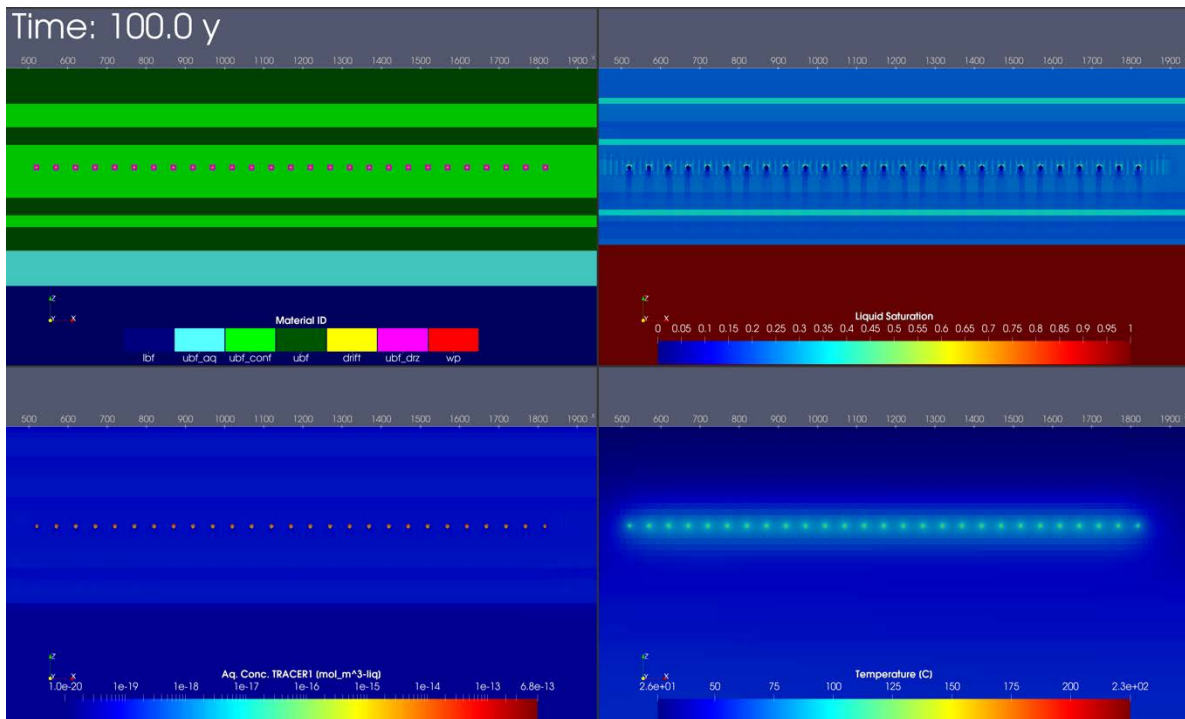
Figure 4-11.   **XZ slice through the center of the repository colored by material ID (top left), liquid saturation (top right), aqueous concentration for Tracer1 (bottom left), and temperature °C (bottom right) at 100 y for NWT mode simulation.**
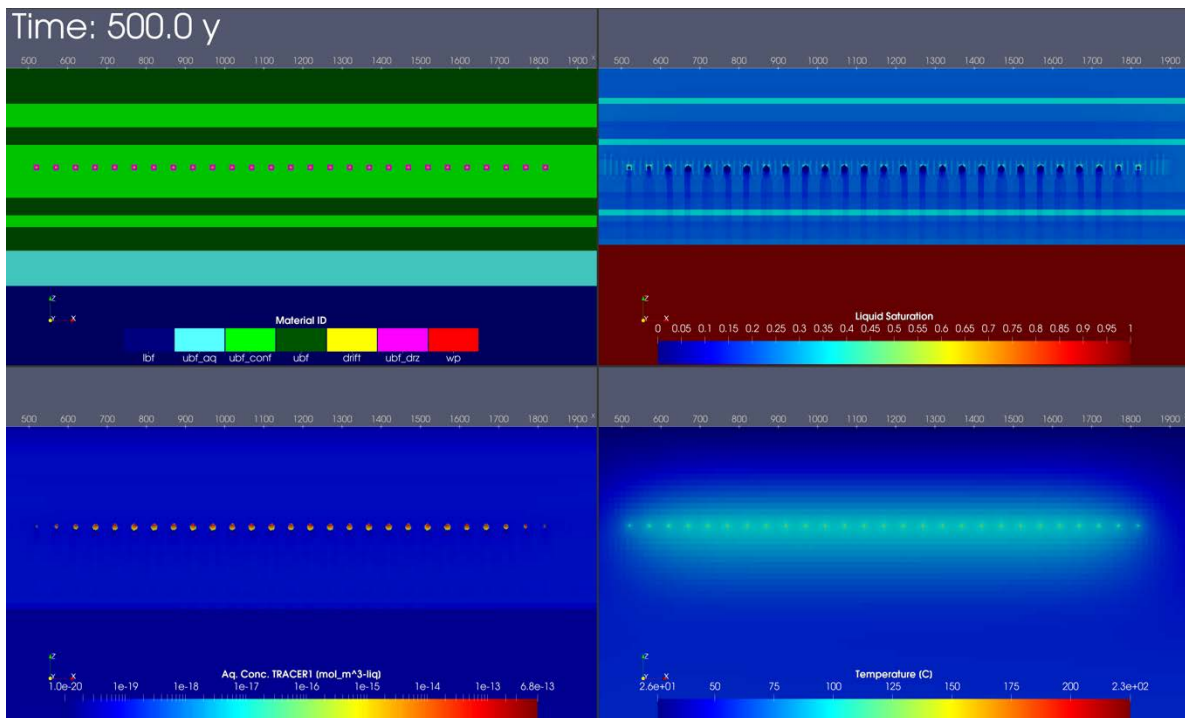
Figure 4-12.   **XZ slice through the center of the repository colored by material ID (top left), liquid saturation (top right), aqueous concentration for Tracer1 (bottom left), and temperature °C (bottom right) at 500 y for NWT mode simulation.**
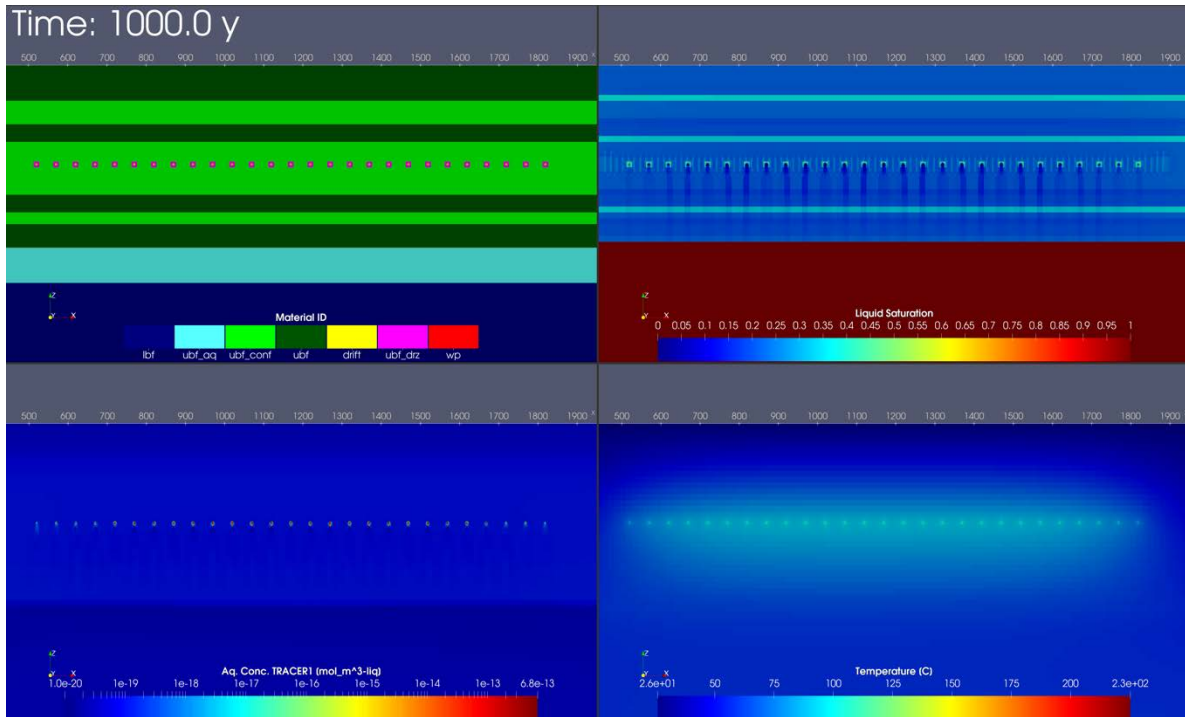
Figure 4-13. XZ slice through the center of the repository colored by material ID (top left), liquid saturation (top right), aqueous concentration for Tracer1 (bottom left), and temperature °C (bottom right) at 1,000 y for NWT mode simulation.
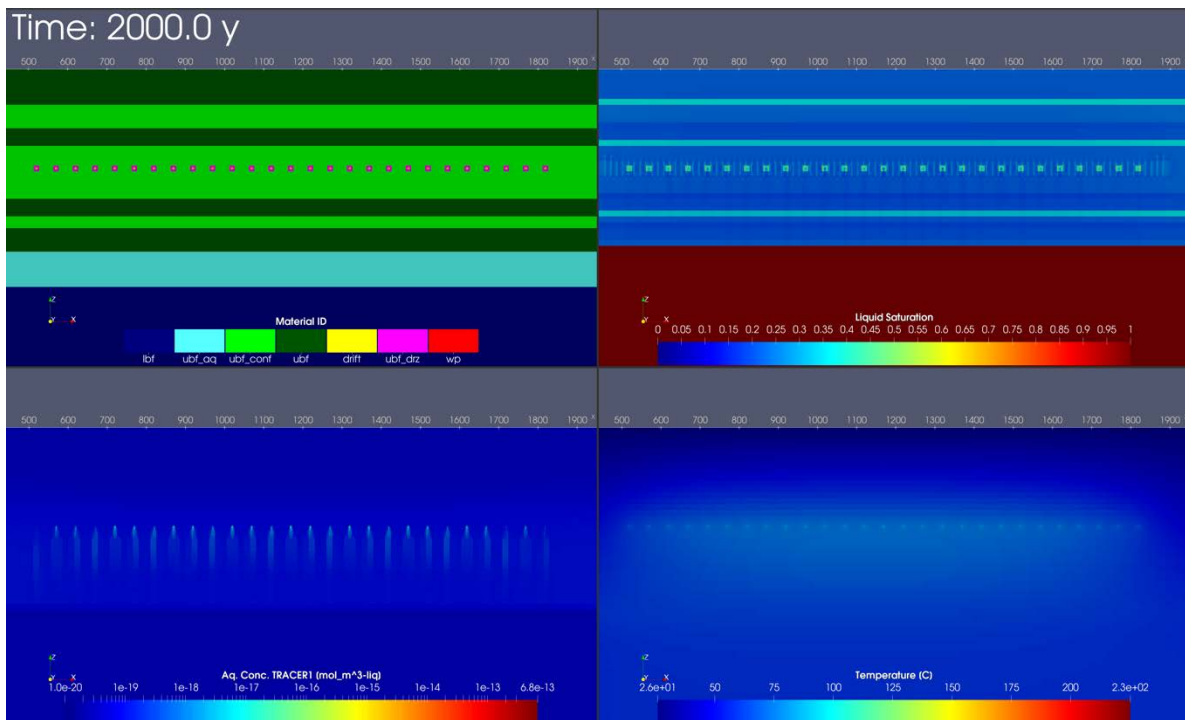
Figure 4-14. XZ slice through the center of the repository colored by material ID (top left), liquid saturation (top right), aqueous concentration for Tracer1 (bottom left), and temperature °C (bottom right) at 2,000 y for NWT mode simulation.
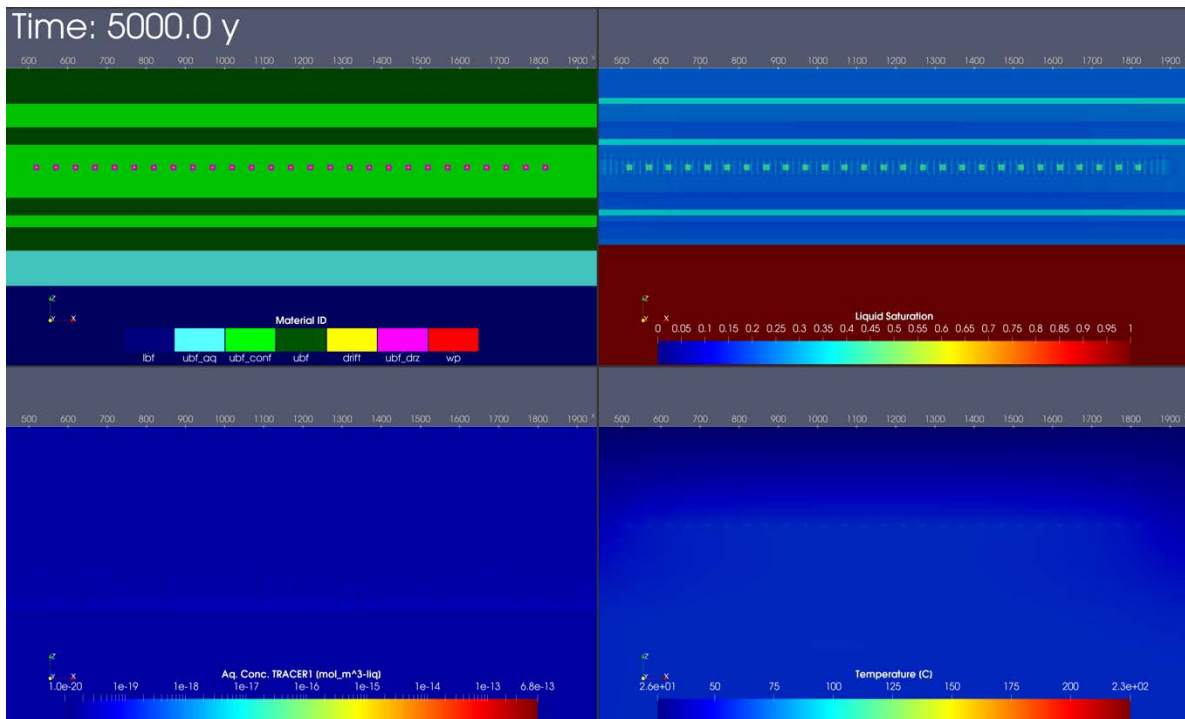
Figure 4-15. XZ slice through the center of the repository colored by material ID (top left), liquid saturation (top right), aqueous concentration for Tracer1 (bottom left), and temperature °C (bottom right) at 5,000 y for NWT mode simulation.
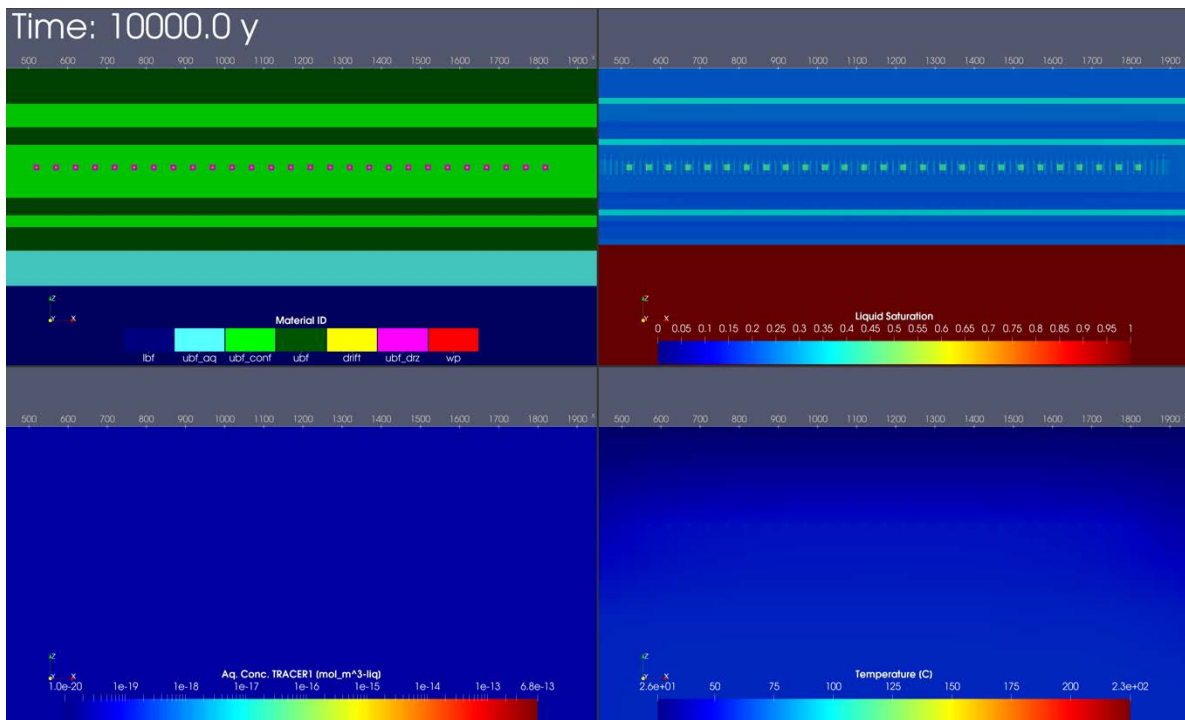
Figure 4-16. XZ slice through the center of the repository colored by material ID (top left), liquid saturation (top right), aqueous concentration for Tracer1 (bottom left), and temperature °C (bottom right) at 10,000 y for NWT mode simulation.

4.2.5   Comparison of Simulation Results

In Figure 4-17, a comparison of tracer concentration at observation point "Fwp_inside" is shown. There are two sets of runs included in this plot. The first set, labeled "Run 1" are for a set of GIRT and NWT simulations that had initial inventory constraint for the tracer set to 10^{-5}. The second, labeled "Run 2" are for GIRT and NWT simulations that ParaView visuals in Figure 4-7 to Figure 4-16 were generated for and had initial inventory constraint for the tracer set to 10^{-20}. The two concentrations that should be compared between GIRT and NWT are the aqueous concentrations for TRACER1. Concentrations peak after shortly after the repository begins to resaturate. As the repository continues to increase in liquid saturation, the aqueous concentration of TRACER1 begins to decrease as it is being transported below the repository due to infiltration driving downward flux.
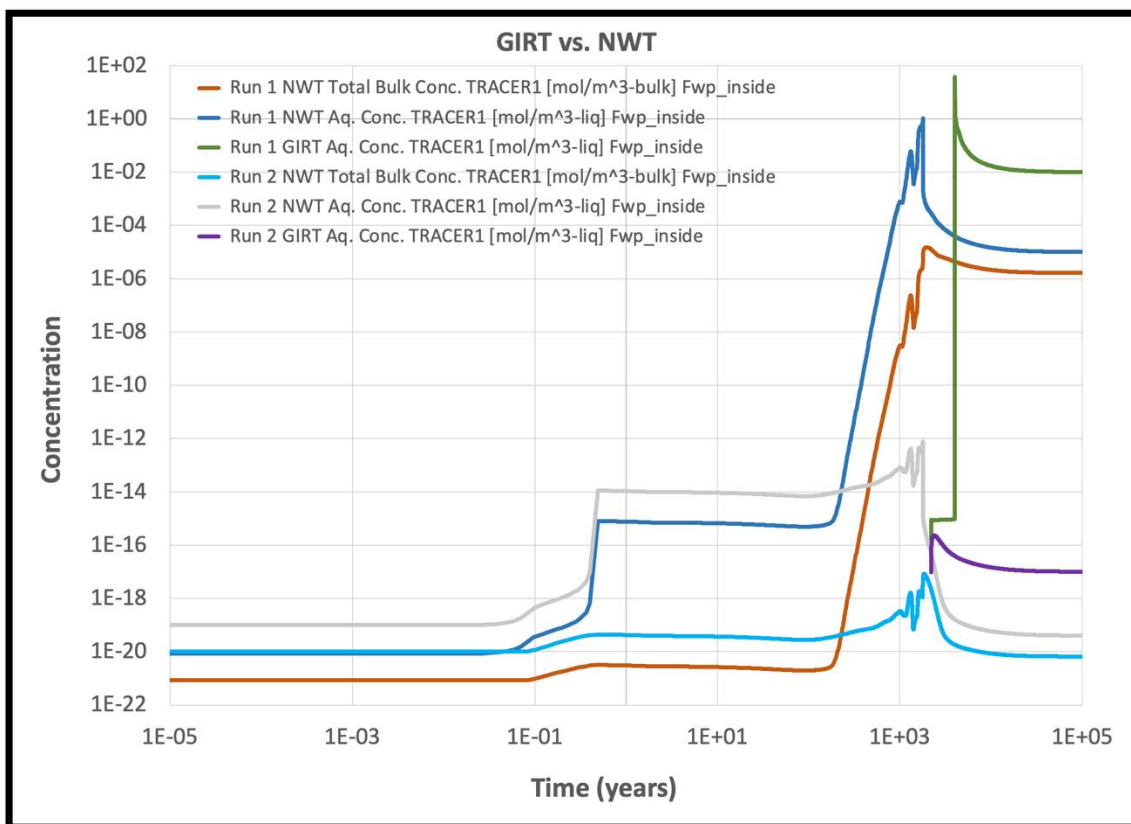
Figure 4-17.   Plot comparing concentration (NWT Total Bulk Concentration [mol/m^3-bulk], NWT Aqueous Concentration [mol/m^3-liq], and GIRT Aqueous Concentration [mol/m^3-liq]) against time in years for TRACER1.

When looking at the series of XZ slices through the centermost waste package observation point "Fwp_inside" for GIRT (Figure 4-7) and NWT (Figure 4-8), there are differences in the NWT transport of TRACER1 concentration during the time of dryout and resaturation that GIRT mode visuals are not able to capture. In the NWT simulation in Figure 4-8, it seems zero liquid saturation in and around the waste package specifically at the 100- and 500-year visuals results in higher tracer concentration just outside of the waste package. As resaturation begins to occur in these regions, tracer concentration begins to be transported below repository bringing the tracer concentration down at "Fwp_inside".

4.2.6   Conclusions and Future Work

This simulation study showed that improvements in PFLOTRAN have allowed the UZ GIRT and NWT mode simulations to complete, while the previous attempt the simulations were too slow. Early in the simulations transport is largely radial from the waste package, but at late time transport is primarily downward to the water table. The results of tracer transport are very different between the GIRT and NWT modes, indicating that the concept of de-coupling the problem in time by using flow-only simulations through dry-out and GIRT transport after dry-out may not be a suitable approximation to the fully coupled problem.

Future work comparing the GIRT with NWT mode should:

- Consider the constraint type unit differences between the modes for a more accurate comparison between the simulation results. This should also be taken into consideration when setting initial tracer concentrations. GIRT uses the unit [M] or [mol/L] for tracer concentrations when T is specified as the constraint type within the CONSTRAINT card.

- Set SNAPSHOT_FILE periodic times in such a way that would allow for ParaView visuals to be compared at the exact same time. The restart file used in GIRT mode at 2,200 years along with the same periodic times specified between the two cases did not allow for the comparison between ParaView visuals to line up at the exact same time.

- Look further at simulation data and determine if oscillations are due to error within the NWT mode or caused by phase state changes that occur in the waste packages.

5.   GEOLOGICAL UNCERTAINTY USING DAKOTA

The long-term scope of this project is to fully incorporate uncertainty in geologic structure within uncertainty quantification (UQ) and sensitivity analysis (SA) for transport modeling of subsurface contaminants from a nuclear waste repository. Towards this goal, the prototype performance assessment (PA) simulations with VoroCrust-Meshing used in LaForce et al. (2022a) are modified and expanded upon to further geologic uncertainty studies. The current study utilizes the next generation workflow (NGW) of Dakota (Swiler et al., 2021). Three pseudo-random geological models are chosen a priori, and the NGW uses Latin Hypercube Sampling (LHS) of four uncertain flow parameters to create a set of thirty samples. The NGW then runs the ninety simulations (thirty on each of the three geological models) and compiles some results which are commonly used in PA uncertainty studies using LHS. Only qualitative sensitivity analysis has been conducted at this time.

The following topics are discussed: (i) the geologic model used for the prototype PA including the model assumptions and simplifications, (ii) a base case example including the workflow used to create each simulation, (iii) a stochastic study and results, and (iv) some conclusions and future work.

5.1   Shale Performance Assessment

A performance assessment example like the Shale PA used in LaForce et al. (2022a), Section 7 is used to conduct UQ and SA that incorporates geologic uncertainties. The workflow presented in LaForce et al. (2022a) provided a starting point for this work; additional capabilities and tools have been added to improve performance and ease of use.

5.1.1   Shale Geologic Framework Model

A Pierre Shale Geologic Framework Model (GFM) was chosen for this work because shale can act as a good geologic barrier for radionuclide transport and thus can be a fitting host rock for a repository. The host shale formation within the Pierre Shale has a thickness of 250 to 589 m making it suitable for hosting spent nuclear fuel (SNF) and a waste repository. The Pierre Shale GFM model has 10 layers; however, as shown in Mariner et al. (2017) and Sevougian et al. (2019b) and discussed in LaForce et al. (2022a), the lowest four layers are unlikely to impact radionuclide transport and are omitted from our studies. The layers used in this work, shown in Figure 5-1, are as follows: a sandstone overburden layer, a host shale layer, a silty shale layer, an underlying shale layer, a limestone aquifer layer, and a lower shale layer. This model has one less layer overlying the host shale layer than the shale PA model in Section 3. That model has separate overburden and sandstone aquifer layers overlying the host shale layer, but they are not separate formations in the shale GFM model used in this section and shown in Figure 5-1.
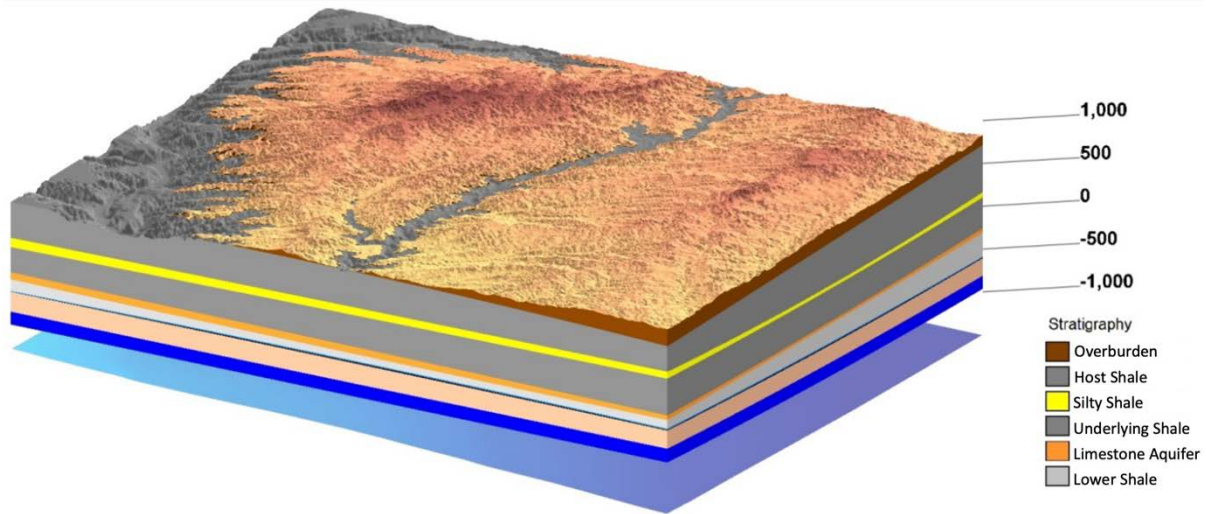
Figure 5-1. **Pierre Shale geologic framework model with stratigraphy at 10x vertical exaggeration scaling (LaForce et al. 2022a, after Sevougian et al, 2019b). The dimensions for the region are 69 km (E-W) by 89 km (N-S).**

5.1.1.1   Modeling Simplifications

The geologic models used in this PA are selected from the GFM model of Pierre Shale presented in Section 5.1.1. As done in LaForce et al. (2022a), smaller, 7 km by 2.5 km, sections are clipped from the larger geologic model. A single overburden surface is chosen that slopes from east to west (positive x-direction), so that is realistic for water to flow downhill in this direction. This is done because the surface topography would be known for a prospective waste disposal site, even if stratigraphy below the surface was poorly constrained. The use of the common surface is a key addition to the work presented in LaForce et al. (2022a). These smaller models will be referred to as geological realizations.

The initial model clipping results are filtered according to three criteria:

- All realizations with incomplete overburden are eliminated, as it is assumed that the selected overburden surface will be present everywhere in the model, and the host shale would not be eroded beneath the overburden.

- The top of the host shale layer must lie at least 5 m beneath the chosen overburden surface. This constraint prevents VoroCrust from making very fine meshes of narrow regions.

- The repository must lie at least 20 m above or below the silty shale layer. This is necessary to ensure that the repository fits the design constraint that it is contained within a shale formation and not near potentially higher-permeability flow paths.

Application of these constraints results in 244 possible realizations such that the surface flow is in the positive x-direction, the host shale is not eroded, and the repository is within a shale formation. Though the screening process allowed for the repository to be in the underlying shale, all models have the repository in the host shale above the silty shale layer. This is another divergence from the Shale PA model in Section 3 of this report, which has the repository located beneath the silty layer.

Of the 244 possible models, the first 100 are chosen for this work. Each model was automatically meshed and monitoring points for quantities of interest (QoI) were appropriately placed, where the correct depth to a given formation is unique to each realization.

A simplified theoretical repository is added to each realization. The structure of the repository within each realization is simplified as done in LaForce et al. (2022a) and the repository and the surrounding damaged area are represented as a single rectangular source. This simplification is done because meshing and running numerous simulations on a VoroCrust mesh containing details of ~2,500 individual waste packages is theoretically possible but not yet feasible for geologic uncertainty studies. Not explicitly including the engineered backfill around each waste package means that this case is likely to over-predict the transport of tracers away from the repository as compared with the model in Section 3, which explicitly includes backfill and waste package properties. With a single representative repository volume, it is impossible to look at uncertainty in engineered properties or waste package degradation time and only far-field QoI can be assessed.

Contaminant transport from the theoretical repository is represented by two tracers with properties representative of ^{129}I, as it is typically the radionuclide that travels the furthest in PA simulations (Mariner et al., 2017; Swiler et al., 2019; LaForce et al., 2020; LaForce et al., 2022a; Section 3, this report). Tracer 1 is instantly released at the start of the simulation, and Tracer 2 is released at a constant rate to represent radionuclide release as the waste packages degrade. The total mass of Tracer 1 represents the instant release of 10% of a theoretical anticipated inventory of ^{129}I in the repository while Tracer 2 represents the remaining 90% of ^{129}I in the inventory, which would diffuse slowly out of the breached waste packages. This is the same transport conceptual model as used in the DECOVALEX Tracer PA cases in Section 2.2 of this report. Both tracers are released at the start of the simulation, which makes this an early-failure scenario. While the previous work in LaForce et al. (2022a) was isothermal, a heat source for the simplified repository was included in this work. The heat source, given by an evolving heat release profile, was calculated from inventory in Carter et al. (2013, Table C-1) using ¼ of the combined 37-PWR waste package and 24-PWR waste package as described in for the shale reference case in Sevougian et al. (2019b, Section 5.3.1).

Monitoring points for Tracer 1 and Tracer 2 were included within multiple layers at locations consistent with the center of the repository, as well as 1 km and 5 km downstream from the repository in potential flow paths (overburden, silty shale, limestone aquifer). For each realization, downstream is in the positive x-direction and flow is driven by a constant liquid pressure gradient in the x-direction applied using boundary conditions.

5.1.2   Model Realization Workflow

To create each model realization and simulate the hypothetical repository within each realization, 7 km by 2.5 km geologic realizations are clipped from the GFM model using a Python script described in Section 5.1.1. The model is grouped by material into volumes using the Los Alamos Grid Toolbox (LaGriT) meshing software. The model volumes are used as input into in the VoroCrust meshing software to create a Voronoi mesh of the realization and enclosed repository. For additional detail about VoroCrust see Section 6. The VoroCrust mesh is used in explicit unstructured mesh mode in PFLOTRAN. Material properties (i.e., flow, heat, and transport properties) and setting needed to run the simulation are included in the PFLOTRAN input deck. The workflow is depicted in Figure 5-2. Note this workflow is like the workflow presented in LaForce et al. (2022a) Section 7.2.4.1.

GFM   LaGriT   VoroCrust Meshing   PFLOTRAN
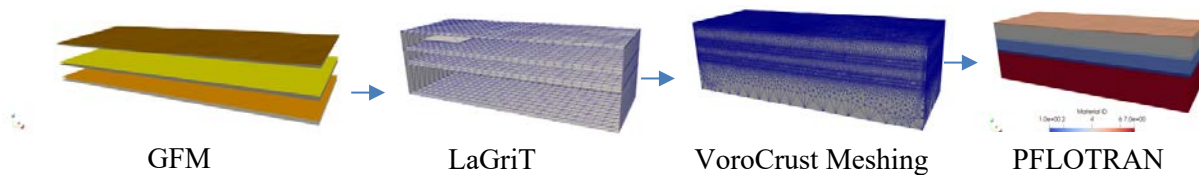
Figure 5-2.   Depiction of workflow used to create and simulate a hypothetical repository.

5.1.3   Base Case Simulation

Using the workflow described in Section 5.1.2, 100 realizations of the geological model were created. Realization 50 was chosen as a base case because it had a visually average layer profile. The base case was run using the parameter values listed in Table 5-1 for 1,000,000 years. The parameter values are consistent with those used in Mariner et al., (2017) and LaForce et al., (2022a), please refer to these references for details on the effective diffusion coefficients used. Two parameters were kept constant throughout the model and thus are not included in Table 5-1; the grain density set to 2700 kg/m^3 and the heat capacity set to 830 J/°C. Within this work, the domain remains saturated and thus no thermal conductivity values for dry soil are included.

Table 5-1.   Base case flow parameter settings as discussed in Section 5.1.3. Regions are listed in order from the surface downwards.

Region	ID	Permeability (m^2)	Porosity	Tortuosity	Effective Diffusion Coefficient (m^2/s)	Thermal conductivity (W/m°C)
Overburden	5	1×10^{-15}	0.20	0.58	2.2×10^{11}	3.1
Host Shale	4	1×10^{-19}	0.20	0.11	2.2×10^{11}	1.2
Silty Shale	3	1×10^{-17}	0.20	0.11	2.2×10^{11}	1.4
Underlying Shale	2	1×10^{-19}	0.20	0.11	2.2×10^{11}	1.2
Limestone	1	1×10^{-14}	0.10	0.04	4.0×10^{12}	2.6
Lower Shale	7	1×10^{-20}	0.10	0.04	4.0×10^{12}	1.2
Repository	6	1×10^{-20}	0.35	0.23	8.1×10^{11}	2.25

The Voronoi mesh created for Realization 50, the base case, is shown in Figure 5-3. The material IDs and permeabilities for the base case are shown in Figure 5-4 with a y-z plane slice through the repository at x=1km also included to show the enclosed repository.
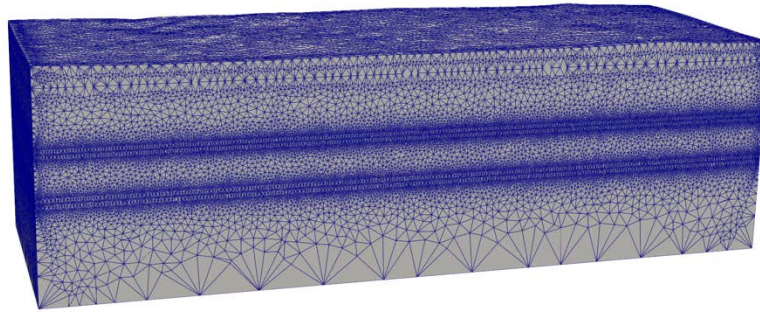
Figure 5-3.   Base case simulation mesh (Realization 50).
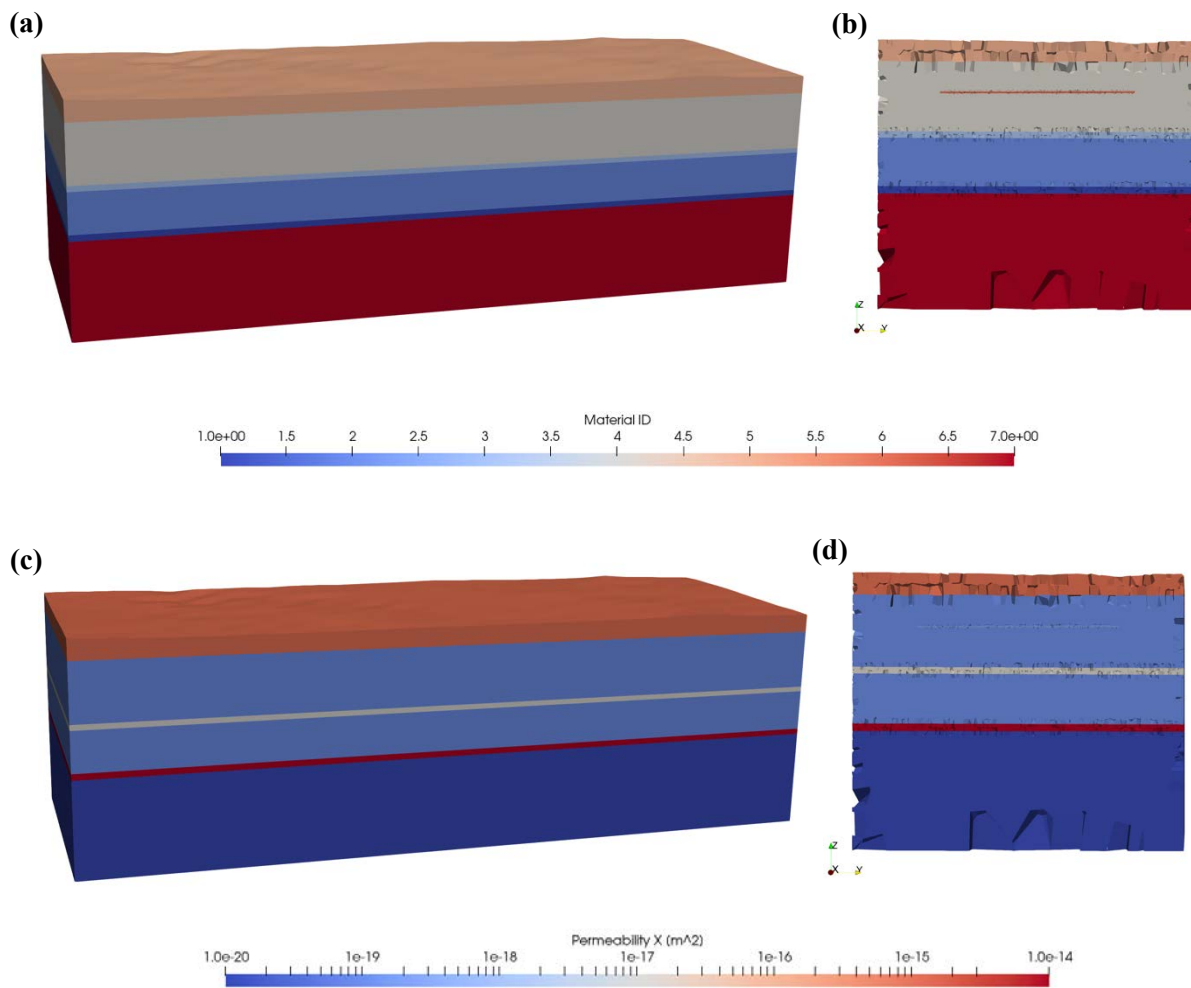
**Figure 5-4.   Base case simulation. Right: (b) and (d) are slices through the repository at x = 1,000
m. Top: (a) and (b) showing regions assigned to material IDs. Bottom: (c) and
(d) show the material dependent permeability.**

5.1.3.1 Base Case Results

The initial condition set for the base case model were based on hydrostatic pressures and a realistic temperature gradient profile. The initial pressures and temperatures for the base case model are shown in Figure 5-5. Snapshots in time at plane x=1 km of the pressure are shown in Figure 5-6, and temperature are shown in Figure 5-7. The temperature in the vicinity of the repository increases until around 500 years then is sustained and diffuses to a larger area. The temperature does not surpass 65 °C and begins to decrease around 30,000 years; however, the temperature does not decrease to the original background temperature within the 1,000,000-year timeframe. The liquid pressure follows a similar trend to the temperature, increasing in the vicinity of the repository until about 500 years and then sustaining higher pressures and the region of higher pressure expanding for some time. However, as opposed to the temperature, the liquid pressure does return to the original background pressure profile. The liquid pressure is near its initial condition by 3,000 years.

Snapshots in time of Tracer 1 (instant release) concentrations at plane x = 1 km are shown in Figure 5-8. Tracer 1 and Tracer 2 (slow release) concentrations at the domain boundary at three snapshots in time are shown in Figure 5-9 and Figure 5-10, respectively. Figure 5-8 through Figure 5-10 show the spread of the tracers from the repository over time. Tracer 1 reaches a threshold concentration of 1×10^{-12} [M] at the surface between 200,000 and 300,000 years while Tracer 2 reaches a concentration of 1×10^{-12} [M] at the surface between 400,000 and 500,000 years. The instant release Tracer 1, though only 10% of the anticipated repository inventory, reaches the surface at concentrations above the threshold of 1×10^{-12} [M] more quickly than Tracer 2, the remaining 90% of anticipated repository inventory, and sustains higher these concentrations at the surface until the final time step of the simulation 1,000,000 years.
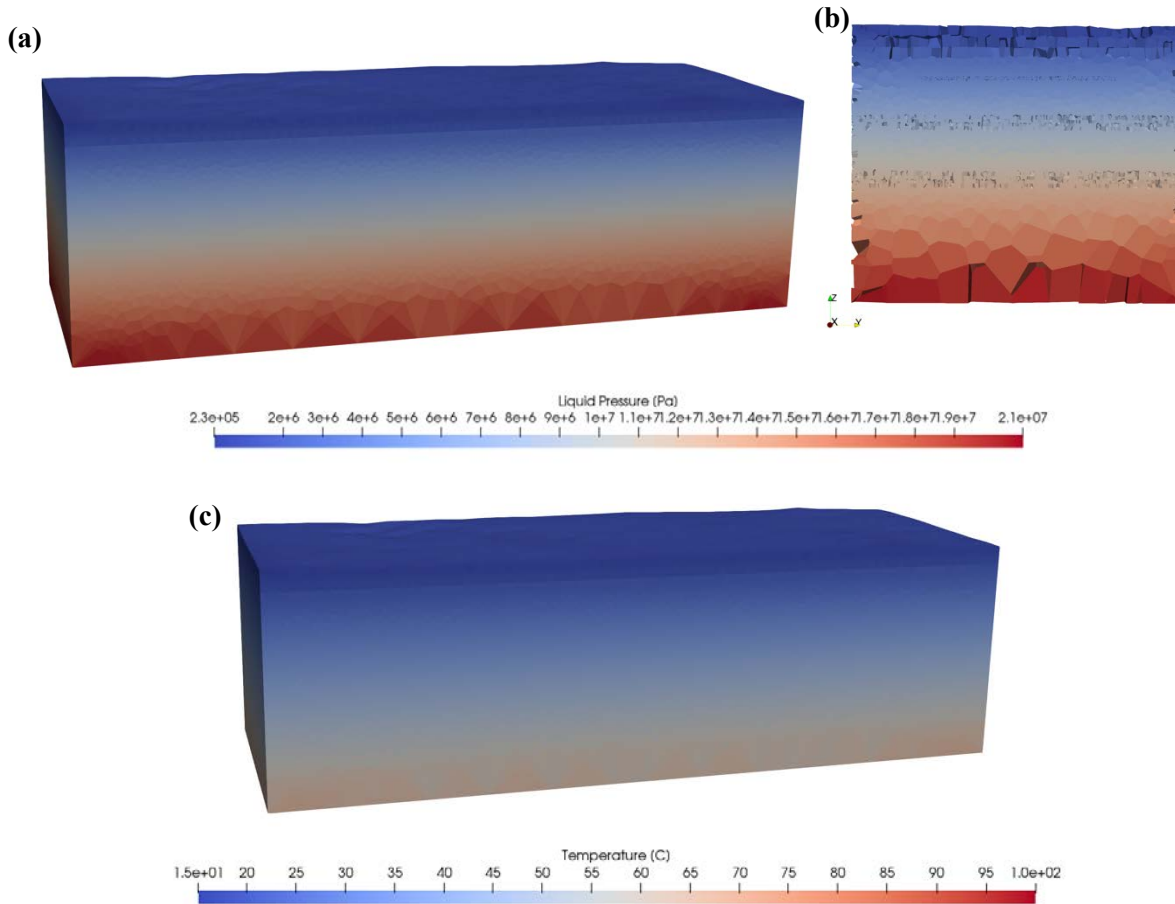
Figure 5-5. **Base case simulation. Top: Initial pressure (a) throughout the domain and (b) at a slice through the repository at x = 1000 m on the right. Bottom: (c) initial temperature.**
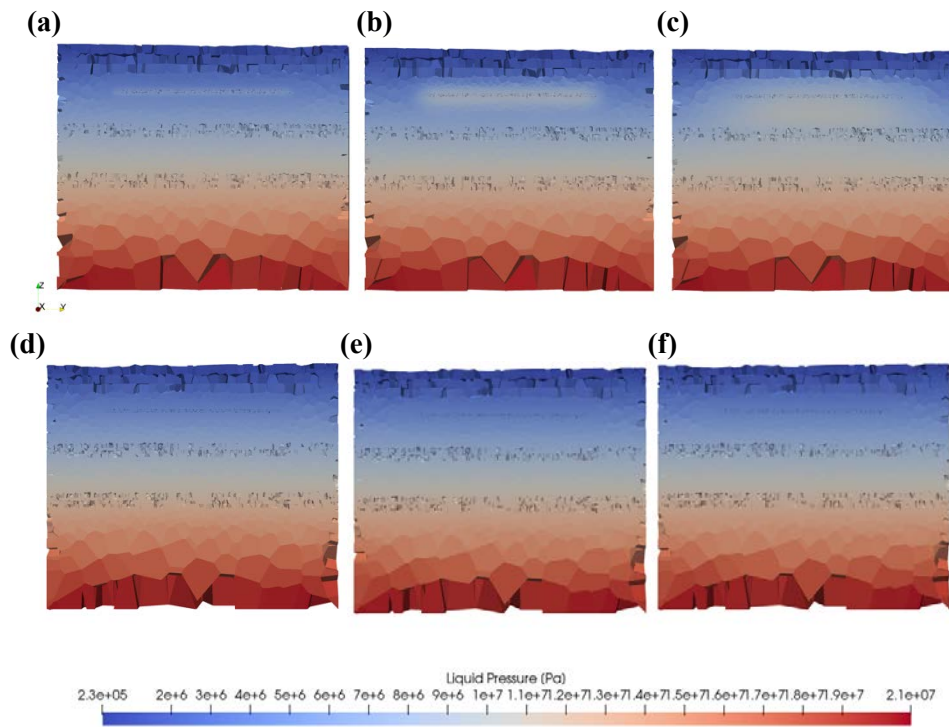
Figure 5-6. **Pressure on the slice through the repository at x = 1,000 m for various snapshots in time. (a) 10 y. (b) 100 y. (c) 1,000 y. (d) 10,000 y. (e) 100,000 y. (f) 1,000,000 y.**
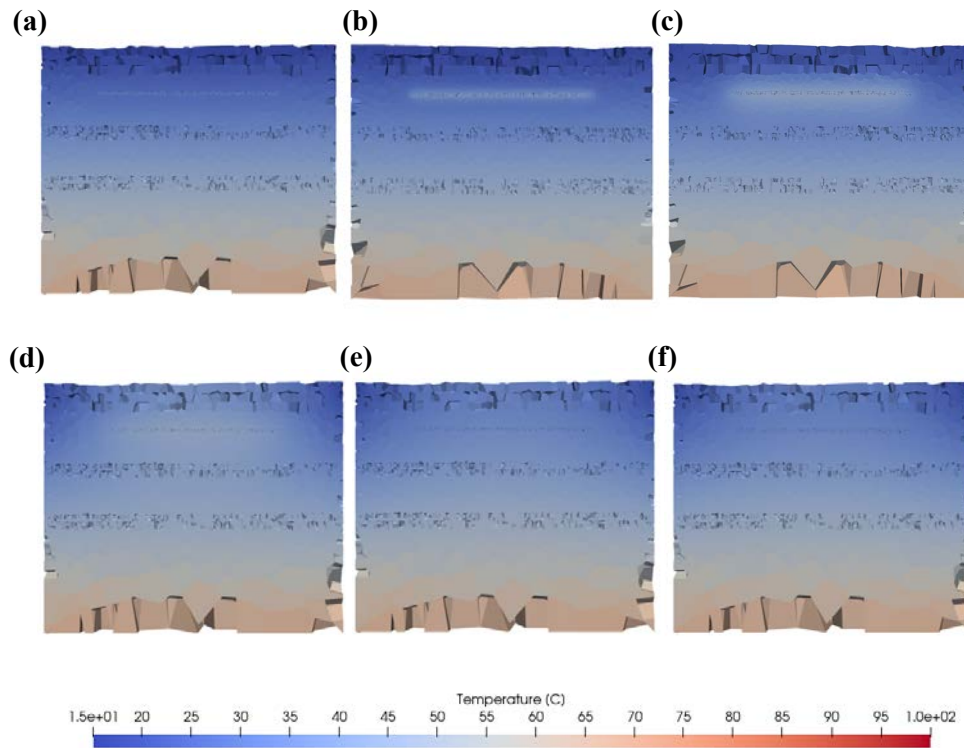
Figure 5-7. Temperature on the slice through the repository at x = 1,000 m for various snapshots in time. (a) 10 y. (b) 100 y. (c) 1,000 y. (d) 10,000 y. (e) 100,000 y. (f) 1,000,000 y.
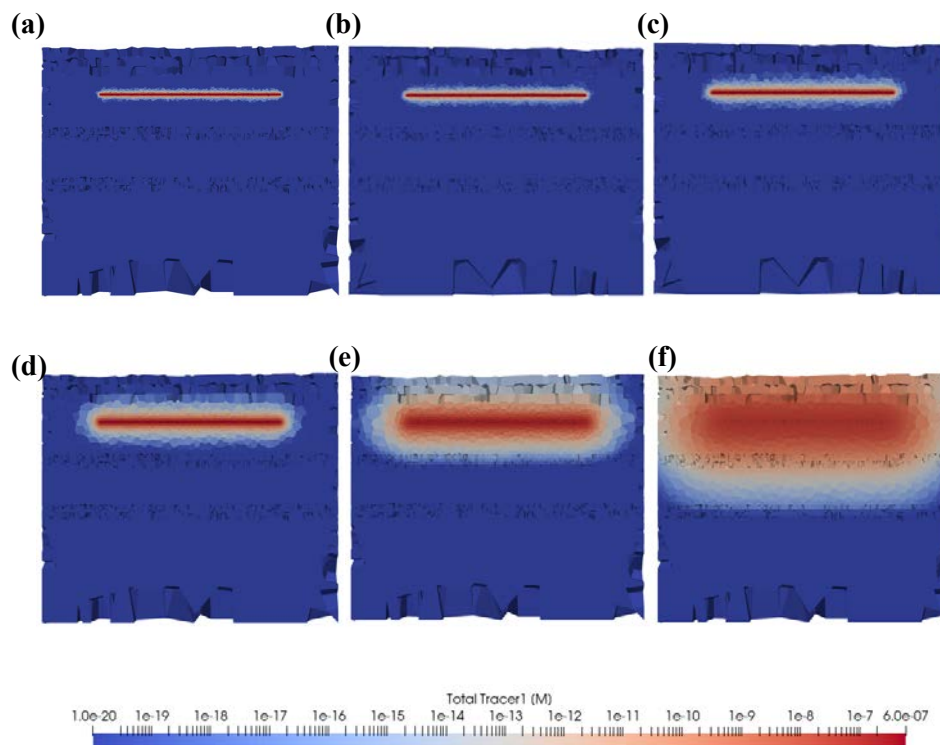
Figure 5-8. Tracer 1 (instant release) on the slice through the repository at x = 1,000 m for various snapshots in time. (a) 10 y. (b) 100 y. (c) 1,000 y. (d) 10,000 y. (e) 100,000 y. (f) 1,000,000 y.
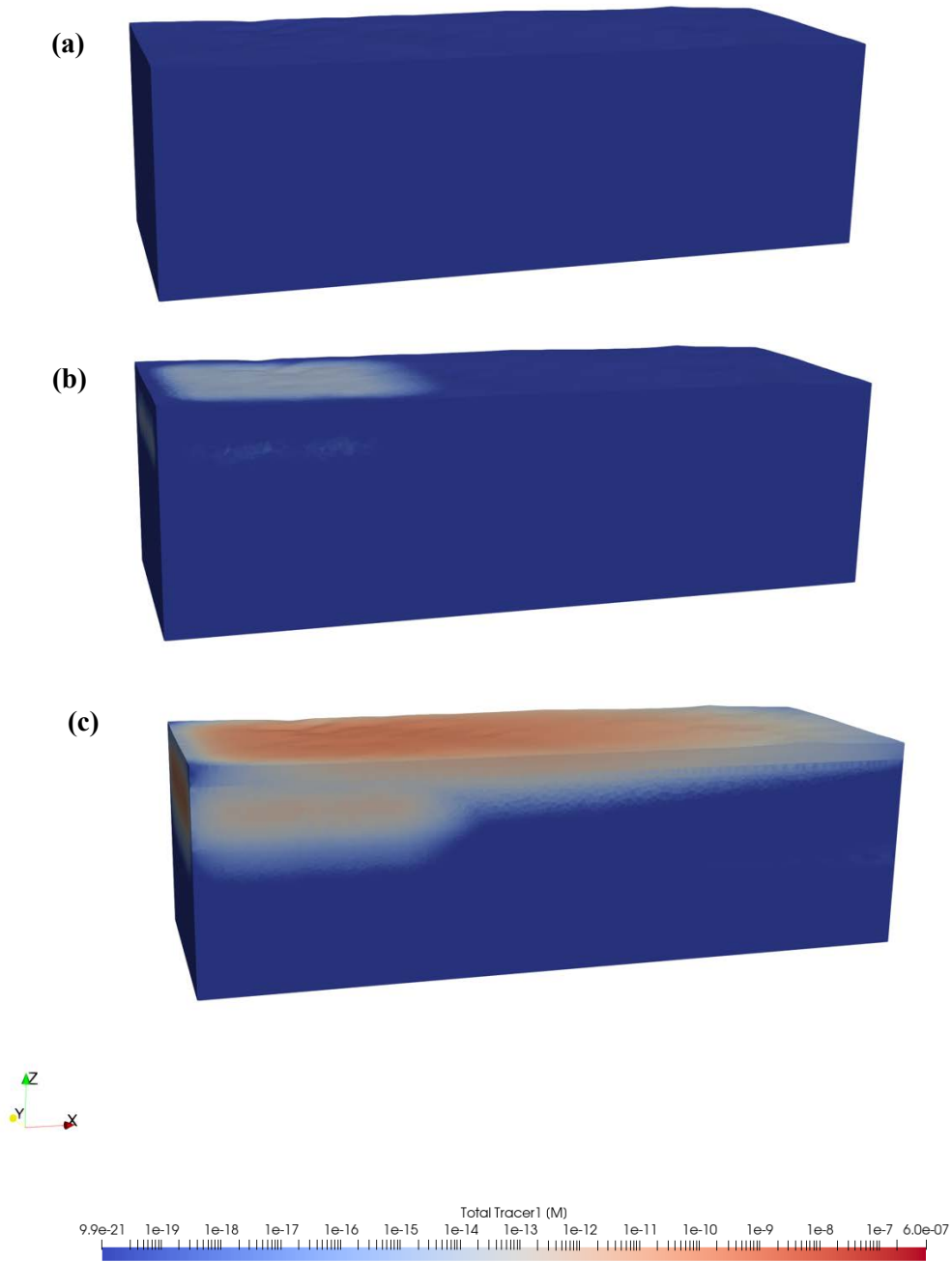
Figure 5-9. **Tracer 1 (instant release) in the reservoir after (a) 10,000 y, (b) 100,000 y and (c) 1,000,000 y.**
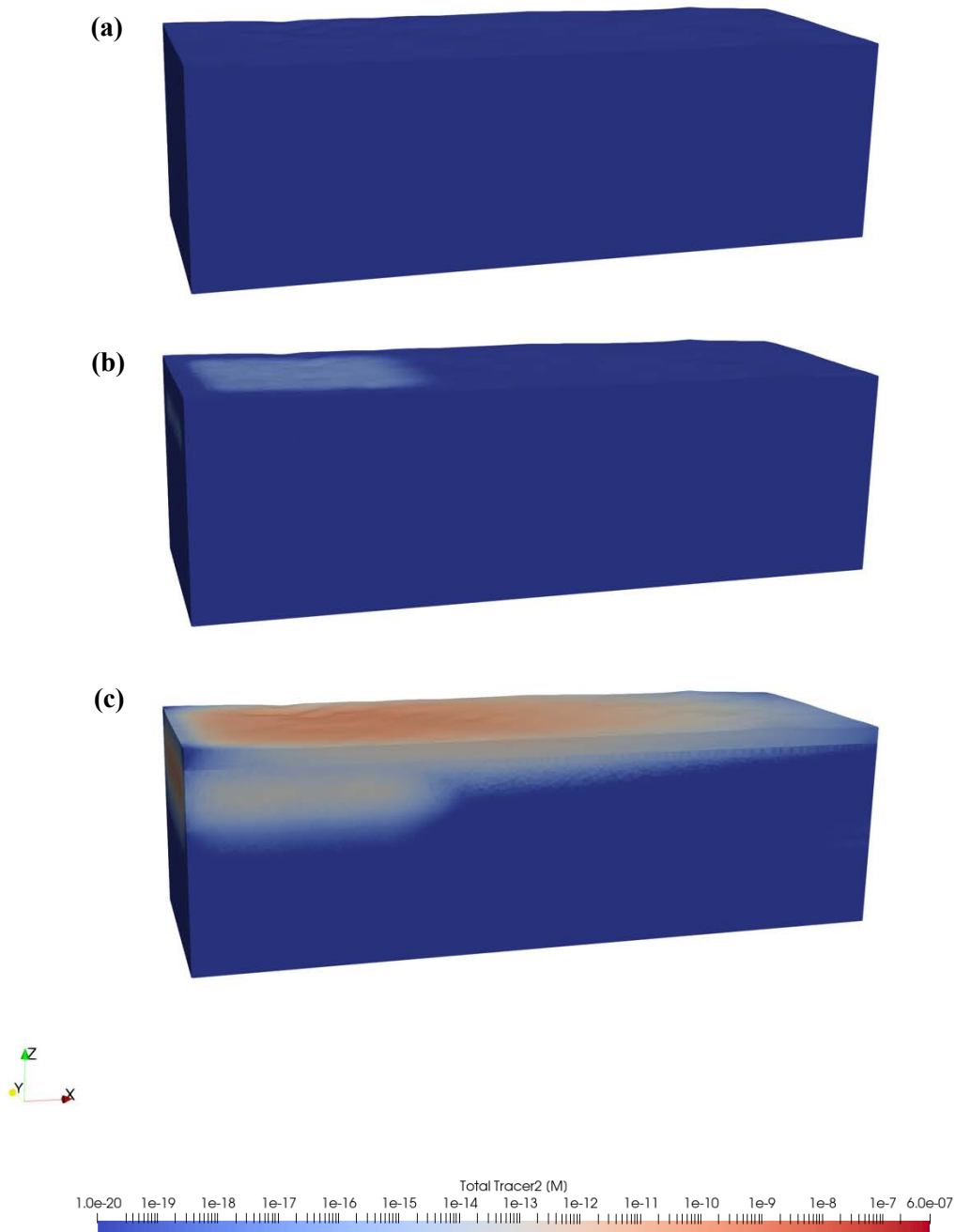
Figure 5-10. Tracer 2 (slow release) in the reservoir after (a) 10,000 y, (b) 100,000 y and (c) 1,000,000 y.

5.1.4   Stochastic Cases

Three simplified geologic repository realizations as described in Section 5.1.1.1 were chosen to demonstrate the workflow and perform an initial prototype PA using Voronoi meshes created using VoroCrust. The geological models with the material regions for the three realizations are shown in Figure 5-11; the surface for each realization is the same but the uncertain topography of the subsurface layers, and consequent thickness of the formations below the surface are different for each model.

The parameters used for the stochastic cases are the same as for the base case described in Section 5.1.2 and Table 5-1 except for four uncertain flow parameters. These flow parameters were sampled thirty times using LHS through the NGW, a tool provided with Dakota, an optimization and UQ software. Details of the NGW used for this study are included in the following section.
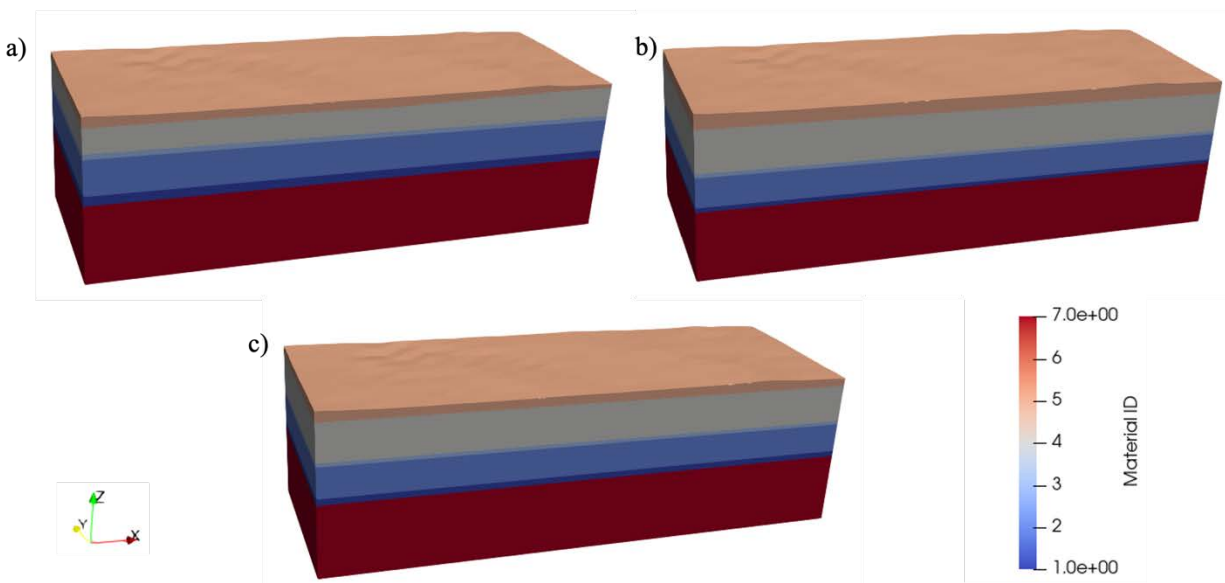
Figure 5-11.   Geological regions for (a) Realization 1, (b) Realization 50, and (c) Realization 100. Material IDs are shown. Realizations 50 and 100 are the most similar, however Realization 50 has the thickest overburden layer.

5.1.4.1   Next-Generation Workflow Implementation

The NGW is a tool accessed through the Dakota GUI that allows the user to create a UQ, SA and/or optimization studies. After the meshes were created using the workflow discussed in Section 5.1.2 with details included in LaForce et al. (2022a, Section 7.2.4.1), the NGW was used to sample the uncertain flow parameters through Dakota, preprocess the PFLOTRAN input deck and run, then connect to the HPC and submit all the runs, gather the results, and provide some LHS default plots. The preprocessing step involved using Dakota's version of APREPRO (An Algebraic Preprocessor for Parameterizing Finite Element Analyses), DPREPRO to put the Dakota selected parameters into a PFLOTRAN template and make a corresponding HPC run script. Additional post processing was done via Python. See Figure 5-12 for an image of one of the NGW pages used for this work.
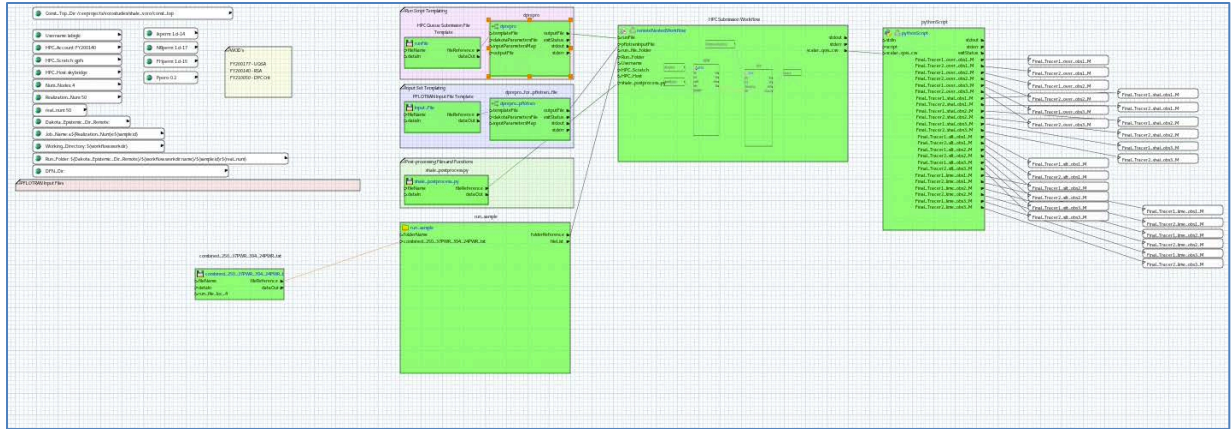
Figure 5-12.   A zoomed-out image of the Next-Generation Workflow tool within the Dakota GUI as discussed in Section 5.1.4.1.

5.1.4.2   Flow Parameter Samples

The four uncertain flow parameters used for this study are: overburden permeability, limestone permeability, silty shale permeability, and host shale porosity. These flow parameters were sampled thirty times using LHS through the NGW Dakota tool with the ranges and distributions shown in Table 5-2. The ranges and distributions are same as used in LaForce et al. (2022a, Section 7) which are based on work in Mariner et al. (2017). The thirty LHS samples given by Dakota are shown in Table 5-3.

Table 5-2.   Sample ranges and distributions.

Parameter	Range	Units	Distribution
Overburden Permeability	10^{-15}-10^{-13}	m^2	log uniform
Limestone Permeability	10^{-17}-10^{-14}	m^2	log uniform
Silty Shale Permeability	10^{-17}-10^{-15}	m^2	log uniform
Host Shale Porosity	0.1-0.25	-	Uniform

Table 5-3.   Samples with flow parameters selected via LHS sampling through Dakota.

Sample	Host Shale Porosity	Overburden Permeability	Silty Shale Permeability	Limestone Permeability
1	0.12139063	3.11E-15	7.19E-16	3.84E-16
2	0.22870578	1.45E-14	1.97E-17	3.57E-17
3	0.14617694	5.73E-15	6.15E-17	7.07E-15
4	0.16667513	1.59E-15	3.69E-17	8.49E-15
5	0.22062529	2.68E-15	2.77E-16	4.98E-15
6	0.10780265	1.13E-15	1.20E-16	9.44E-17
7	0.13229658	4.31E-15	1.97E-16	1.72E-17
8	0.1277154	7.91E-15	1.81E-17	3.12E-15
9	0.16130971	5.87E-14	1.62E-16	4.46E-17
10	0.19901185	9.43E-14	3.98E-16	2.12E-16
11	0.141605	2.31E-15	5.73E-16	1.43E-16
12	0.17635241	4.10E-14	9.64E-16	7.89E-17
13	0.18366407	3.87E-14	4.43E-17	3.37E-15
14	0.11079342	1.95E-15	9.99E-17	6.69E-16
15	0.24931324	1.32E-15	3.26E-16	2.86E-16
16	0.2168157	1.14E-14	1.11E-16	2.95E-17
17	0.13516986	7.28E-14	1.35E-17	1.62E-15
18	0.21314251	5.33E-14	3.26E-17	2.30E-15
19	0.20547574	8.96E-15	7.42E-16	5.94E-16
20	0.23491774	6.49E-15	7.06E-17	5.86E-17
21	0.15796057	1.71E-14	2.44E-17	2.02E-17
22	0.24221612	3.73E-15	2.71E-17	1.35E-15
23	0.23579974	2.57E-14	3.86E-16	1.21E-16
24	0.19057637	5.22E-15	2.28E-16	1.82E-16
25	0.18653726	1.98E-14	5.15E-16	6.14E-15
26	0.10131012	3.12E-14	8.09E-17	9.68E-16
27	0.11606294	2.21E-14	4.65E-17	1.57E-17
28	0.20193138	1.29E-14	1.03E-17	5.01E-16
29	0.17488043	1.54E-15	1.57E-17	1.20E-17
30	0.15259196	8.36E-14	1.46E-16	1.00E-15

5.1.4.3   Quantities of Interest

With three geological realizations and thirty samples of flow parameters, ninety scenarios were simulated. As done for the base case discussed in Section 5.1.2, each of the ninety simplified geological repository scenarios were simulated for 1,000,000 years.

Concentration of ^{129}I at monitoring points downstream of the repository are used as the QoI for determining model sensitivity to input parameters. As described in Section 5.1.1.1, ^{129}I concentrations are represented by Tracer 1, instant release, and Tracer 2, slow release, concentrations. The monitoring points are located at cell centers in the x-z plane midway through the domain in the y -direction, at y = 1.25 km, with four monitoring points in line with the center of the repository, four additional points 1 km downstream from the repository and the final four points located 5 km downstream from the repository. Observation points are at depths near the midpoint of the overburden, host shale, silty shale, limestone aquifer formations. These depths are unique to each model. The observation points used in the study are depicted in Figure 5-13.
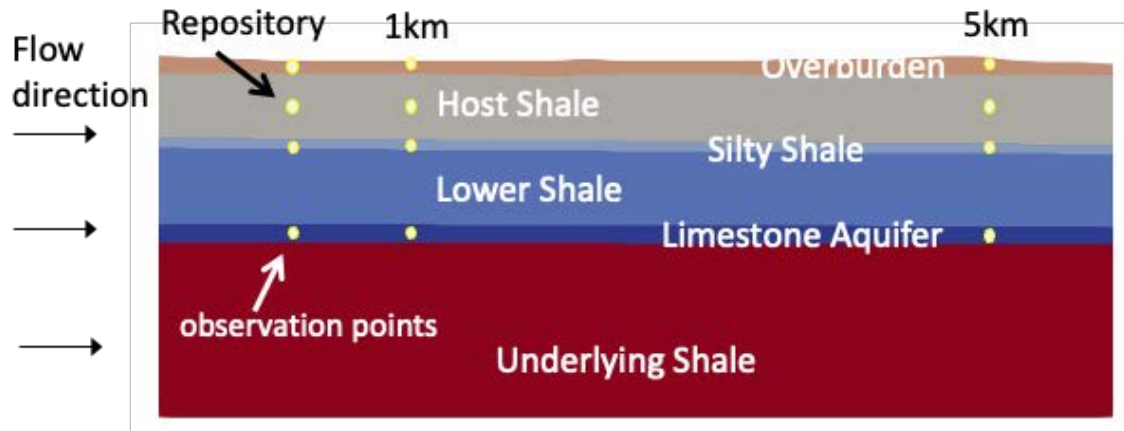
Figure 5-13. **A depiction of the locations of the observation points within the model layers as described in Section 5.1.4. The repository is not shown but the observation point in the center of the repository is labeled. The observations points lie in the x-z plane midway through the model in the y-direction, given by y= 1.25 km.**

5.1.5   Simulation Results

The results for the study described in Section 5.1.4 are presented within this section. The QoI for this work are the Tracer 1 and Tracer 2 concentrations at the observation points shown in Figure 5-13 and discussed in Section 5.1.4.3.

Figure 5-14 and Figure 5-15 show Tracer 1 and Tracer 2 concentrations respectively after 1,000,000 years for all thirty samples and all three geologic realizations for each of the twelve observations points. The results are shown on a semi-log plot. In the overburden layer, concentrations are sensitive to flow parameters, especially for Realization 50. Also, Tracer 1 and 2 concentration levels are more sensitive to variations in flow parameters for Realization 1 than the other two realizations at observation points in the silty shale (silt), host shale (shale) and limestone aquifer (limestone). Conversely, in the silty shale and limestone aquifer, the maximum tracer concentrations are most sensitive to realization of the geological model. At the repository and 1 km downstream, there are higher tracer concentrations in Realization 1 for all thirty sets of flow parameters in both the shale and limestone than any parameter set for Realization 50 or 100. Furthermore, the lowest concentrations for Realization 100 are like the highest concentrations for Realization 50. Realization 1 is the only geological realization sensitive to the flow parameters in the host shale at the repository and 1 km downstream, this may be due to Realization 1 having the thinnest host shale layer as can be seen in Figure 5-11.

To show how the concentrations of Tracer 1 and Tracer 2 evolve over time, two observation points were chosen to highlight. The concentration over time of Tracer 1 at observation point within the overburden at 1 km downstream from the repository for all three realizations are shown in Figure 5-16. The

concentration over time of Tracer 2 at the observation point within the host shale at 5 km downstream from the repository three realizations are shown in Figure 5-17. The observation point within the overburden was chosen because all three realizations show variation due to the parameter sampling at the final time step, see Figure 5-14(b). In contrast, the observation point within the host shale was chosen because only one of the three realizations showed dependence on the sampled flow parameters at the final time, see Figure 5-15(e).

Between 0 and 1,000,000 years for the monitoring points at the overburden at 1 km downstream from the repository and the host shale at 5 km downstream from the repository the variance in concentration levels due to the sampled parameters increases or stays the same; thus, the final time step shows the greatest difference in tracer concentration levels due to sampled flow parameters. Figure 5-16 and Figure 5-17 also show an increase of concentration between the start time and 1,000,000 years later as expected in the simulated nuclear waste repository scenario and seen in previous studies (Mariner et al., 2017; Swiler et al. 2019; LaForce et al. 2020; LaForce et al. 2022a; Section 3, this report).
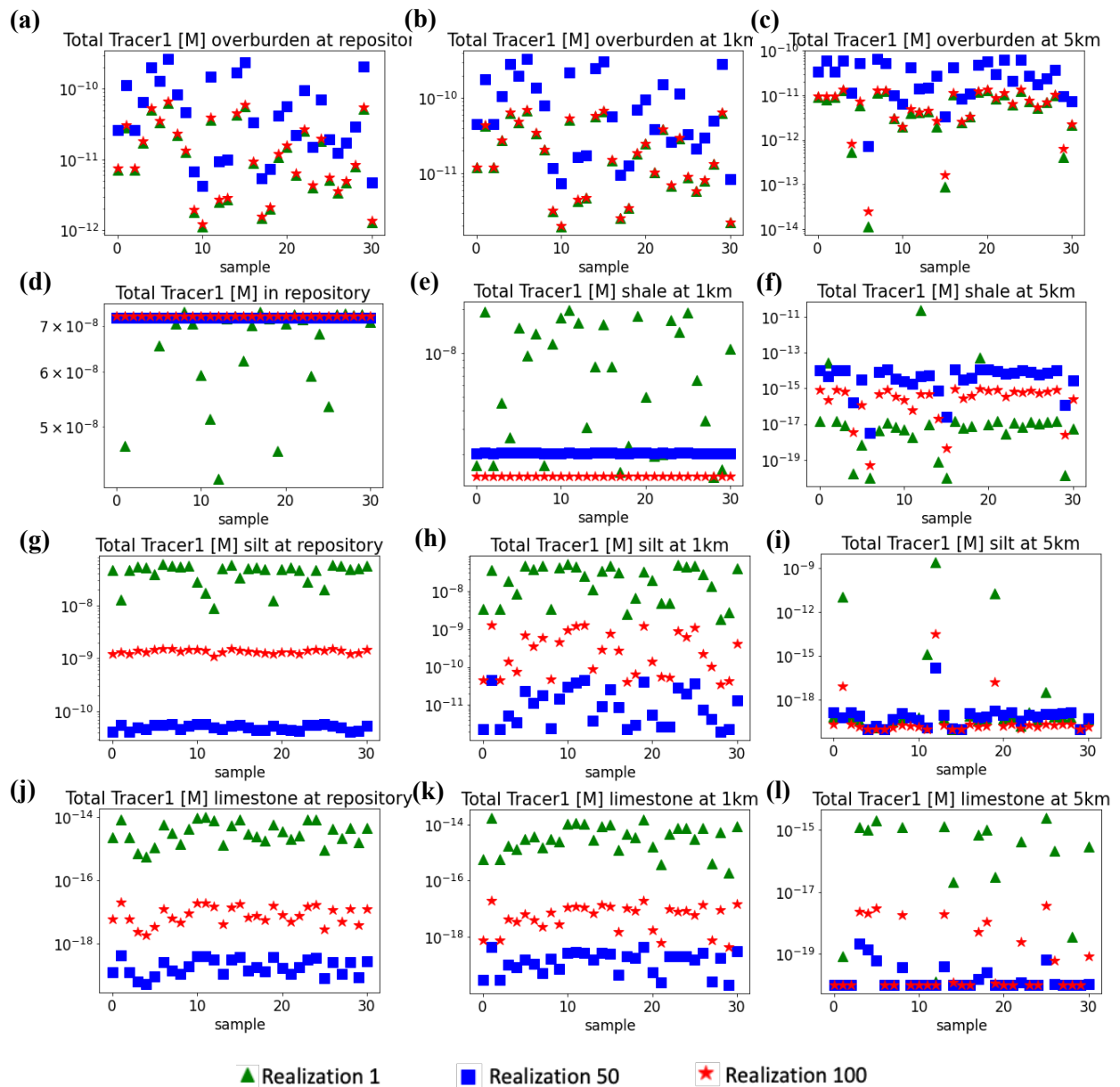
Figure 5-14. **Semi-logarithmic plots of Tracer 1 (instant release) concentration at final time, 1,000,000 years, for all 30 samples at each observation point. Each plot (a)-(l) corresponds to each observation point. Top row: overburden at (a) repository, (b) 1 km downstream, (c) 5 km downstream. Second row: host shale at (d) repository, (e) 1 km downstream, (f) 5 km downstream. Third row: silty shale at (g) repository, (h) 1 km downstream, (k) 5 km downstream. Last row: limestone aquifer at (j) repository, (k) 1 km downstream, (l) 5 km downstream.**
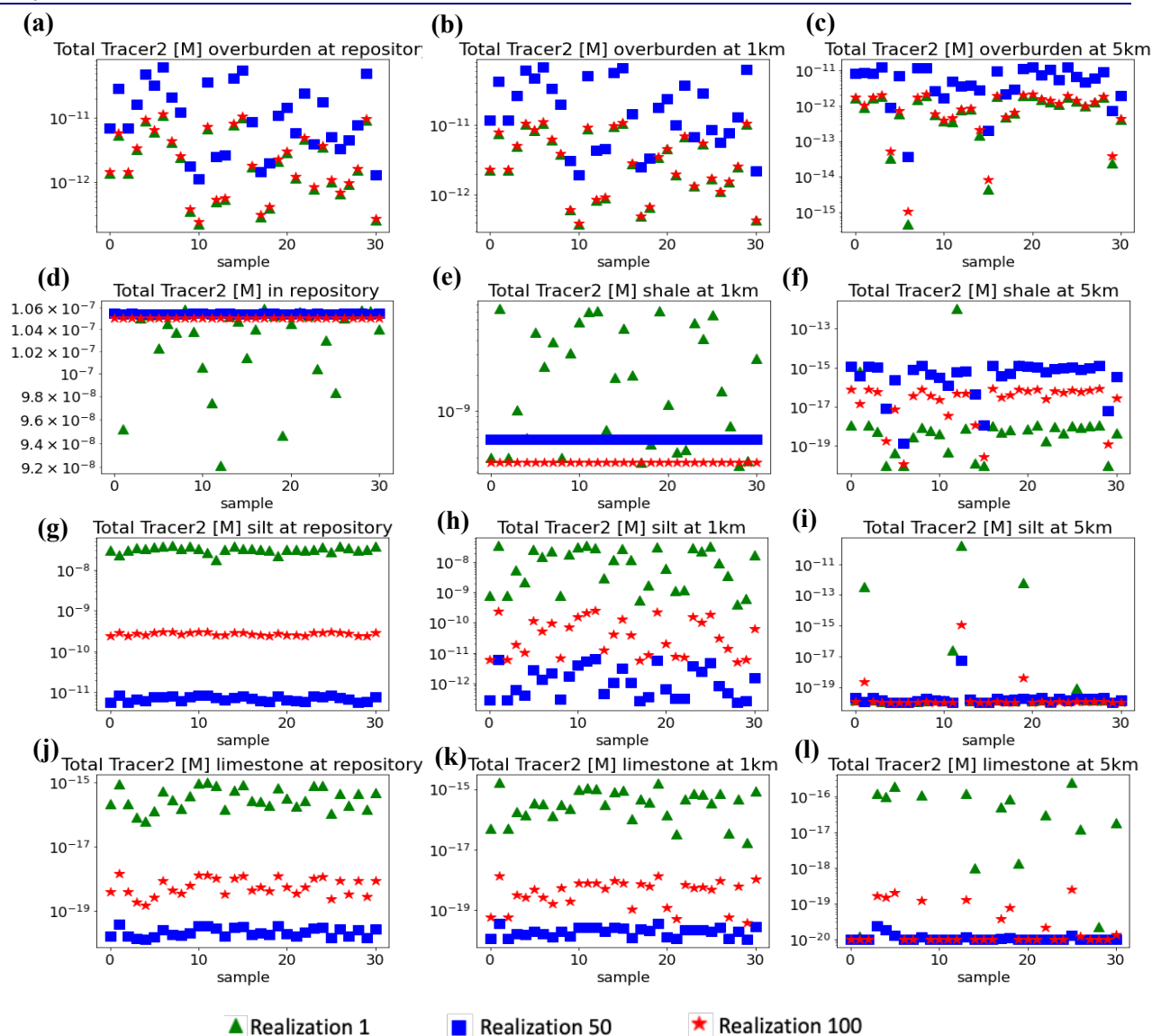
Figure 5-15. **Semi-logarithmic plots of Tracer 2 (slow release) concentration at final time, 1,000,000 years, for all 30 samples at each observation point. Each plot (a)-(l) corresponds to each observation point. Top row: overburden at (a) repository, (b) 1 km downstream, (c) 5 km downstream. Second row: host shale at (d) repository, (e) 1 km downstream, (f) 5 km downstream. Third row: silty shale at (g) repository, (h) 1 km downstream, (k) 5 km downstream. Last row: limestone aquifer at (j) repository, (k) 1 km downstream, and (l) 5 km downstream.**

(a) Realization 1: Tracer 1 [M] Overburden at 1km

(b) Realization 50: Tracer 1 [M] Overburden at 1km

(c) Realization 100: Tracer 1 [M] Overburden at 1km
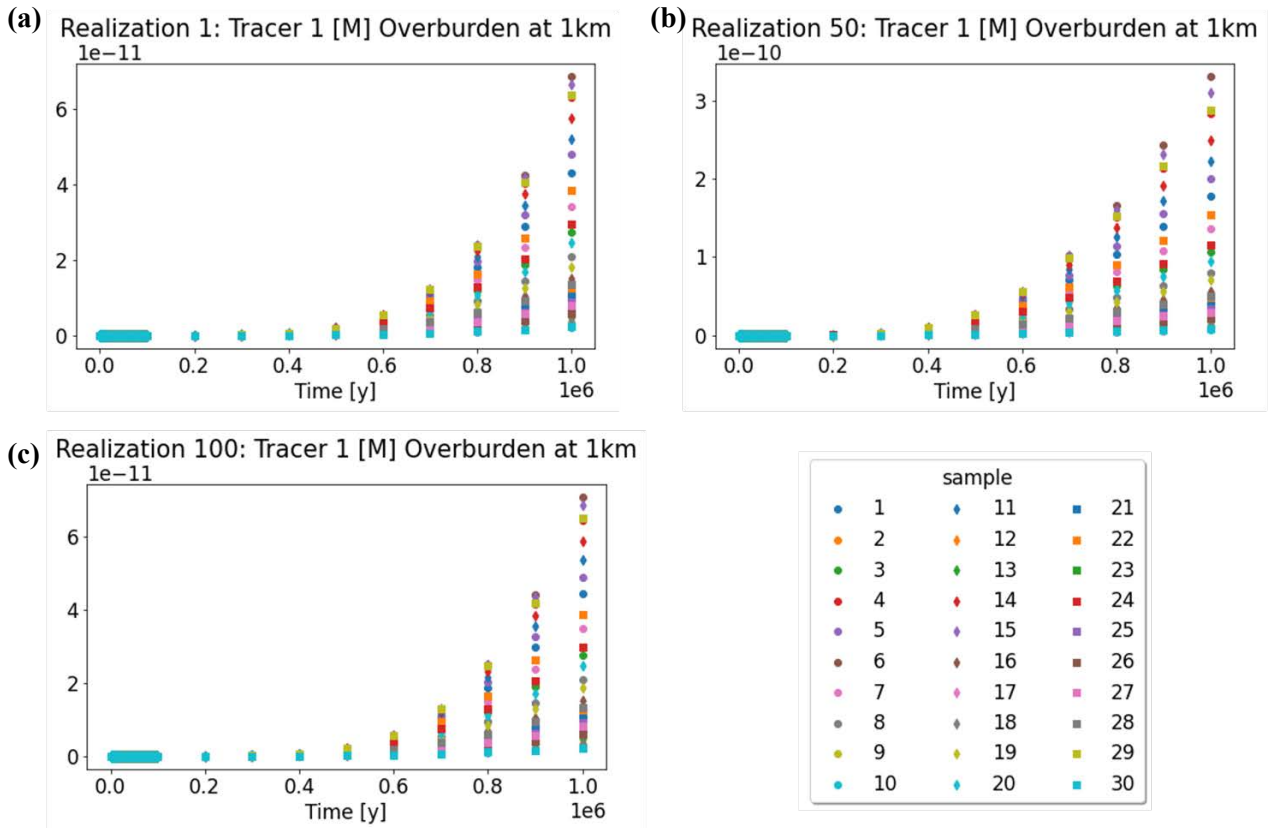
Figure 5-16.   Tracer 1 concentrations [M] over time [y] for all thirty samples for (a) Realization 1, (b) Realization 50, and (c) Realization 100 at the observation point within the overburden at 1 km downstream from the repository as discussed in Section 5.1.5. Note, the scale on the y-axis in plot (b) is an order of magnitude higher than that of plots (a) and (b).
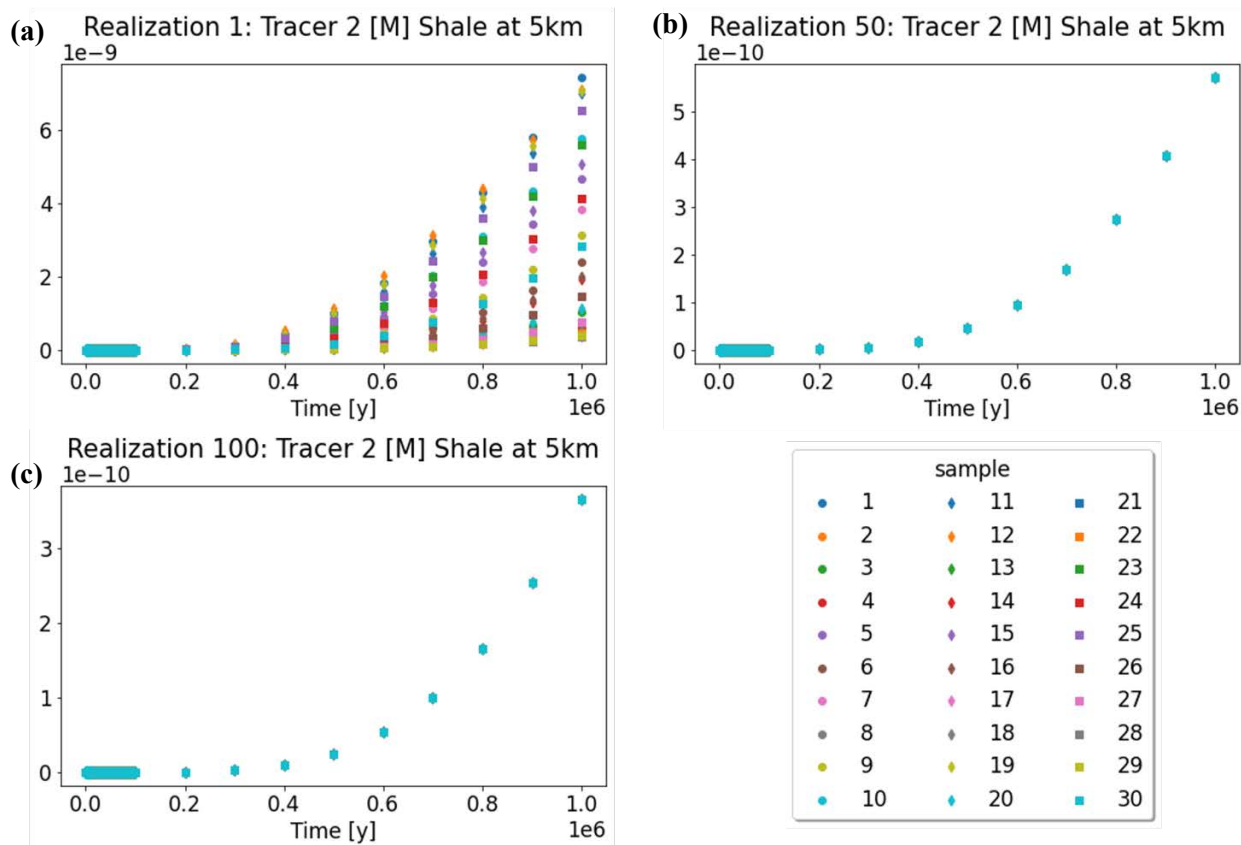
Figure 5-17. Tracer 2 concentrations [M] over time [y] for (a) Realization 1, (b) Realization 50, and (c) Realization 100 at the observation point within the host shale at 5 km downstream from the repository as discussed in Section 5.1.5. Note, the scale on the y-axis in plot (a) is an order of magnitude higher than that of plots (b) and (c).

5.2   Conclusion and Future Work

This section demonstrated how geological structure can be incorporated into Sensitivity Analysis Uncertainty Quantification (SA/UQ) using VoroCrust-meshing for a prototype PA simulation analysis. The first part of this section discussed the model and workflow used to create each geological realization and hypothetical nuclear waste repository. The model was loosely based on the previous shale Geologic Disposal Safety Assessment (GDSA) PA cases (Sevougian et al., 2019b; Swiler et al., 2019; Mariner et al., 2017; LaForce et al., 2022a) and utilized the shale GFM model from Sevougian et al. (2019b). Next, one simulation was chosen as a base case and results from that simulation were discussed in detail. This section concluded with a demonstration of using the NGW of Dakota to conduct sampling via LHS on four flow parameters and run thirty simulations using the sampled parameters on three geological realizations. The NGW of Dakota compiled some results and other results were produced using Python.

The initial study involving three geologic realizations showed that the realization had as much and often more impact on tracer concentrations at the selected monitoring points at and downstream of the repository. Though it is computationally expensive to include the geologic uncertainty in PAs, geological structure is important to include in SA/UQ because it can have a significant impact on QoI.

To continue to quantify the impact of geologic uncertainty within PA, additional work is planned. The next step is to incorporate additional geological realizations into the study since only three of the 100

realizations that were created were used for this initial study; followed by, analyzing the results to obtain quantitative statistical result.

In the long term, this project aims to continue improving automation and robustness of the workflow, incorporate additional realistic features and scenarios including higher resolution within the repository region, and add genuinely uncertain geologic structures.

6.   VOROCRUST DEVELOPMENT AND TESTING

VoroCrust is the first provably correct Voronoi meshing tool. It relies on a sphere packing procedure to ensure capturing the input surfaces as the union of Voronoi faces in the output Voronoi tessellation. VoroCrust is a push button technique that can handle complex geometries (Abdelkader, 2020). It is associated with an automatic feature detection procedure that captures all the details in the input model and ensures the generation of a conforming Voronoi mesh. For PFLOTRAN simulations an orthogonal mesh, where the face between two adjacent cells is orthogonal to the line connecting the two cell seeds is important for the accuracy of the numerical simulation. Without that condition, the two-point flux method used in PFLOTRAN may have a stable simulation, but we cannot ensure its accuracy.

At the beginning of this year, we released the executables of VoroCrust under an open-source license. We are currently releasing the source code itself onto a public Github repository. This required restructuring of many of the VoroCrust classes to enable better maintenance and achieve improved performance. We also added an option for the user to specify a sizing function as an additional constraint for VoroCrust sampling procedure. This allows the user to pass some requirements that are not related to the geometry (e.g., due to physical processes that are in the interior of the domain and need to be finely resolved). Additional software developments were required to track downloads on VoroCrust website, ensure that VoroCrust output is viewable using Paraview and ready to be used by Geologic Disposal Safety Assessment (GDSA) simulations. Finally, creating user manuals to describe the input and the output of each public method in VoroCrust to ease its use by unexperienced users.

A procedure for inserting waste packages as pre-meshed elements is being prototyped in VoroCrust. Currently each waste package is modeled as an independent geometric entity which VoroCrust captures using multiple cells. GDSA performance assessment (PA) models have thousands of waste packages, and the current method would result in too many grid cells to be able to simulate on the mesh. We recognize that waste packages are modeled as boxes and hence we can capture them more efficiently using structured meshes. This requires some significant algorithmic changes to the way VoroCrust operates to merge the structured pre-meshed portion of the mesh with the random unstructured mesh that VoroCrust currently produce to capture the entire model. This year we plan to investigate the proposed method using simple models and increase the complexity gradually to ensure we address all implementation challenges without adding heuristics so we can maintain the guaranteed quality of the meshes VoroCrust currently creates.

On another front, monitoring points are critical to compare simulation results across various meshes for the same model. VoroCrust has capability that allows the user to specify some desired locations for these during the meshing procedure. Unfortunately, some of these points cannot be inserted during the sampling constraints that VoroCrust currently uses to be able to capture the model interfaces properly. This year, we added an option that returns the closest seed to a location if we can't capture the exact point in the final mesh.

6.1   Development and Maintenance

6.1.1   VoroCrust Maintenance

6.1.1.1   Restructure VoroCrust Classes for better maintenance and improved performance.

The goal of this task was to separate the meshing specific code from the other VoroCrust code and place it into its own folders and repositories (i.e., break all dependencies with other source code in the repository and allow the Meshing code to be standalone). We have successfully separated out the meshing component of VoroCrust and obtained an NTESS open-source license for it so that we can provide this

functionality to end users via pre-built binaries available on our website. We have an internal Gitlab repository specifically for the Meshing code that is used to build the binaries to place on the website. We also have a public Sandia GitHub repository that we will share with the public in the future so that anyone who is interested can see and get a copy of our source code.

This restructuring of the meshing code allows us to more easily maintain its source code base, licensing requirements, testing, and syncing. It also reduces the complexity for building and compiling since in the Meshing exclusive code there are less options to consider and include when running the various build stages.

6.1.1.2 Track Webpage Statistics via SiteImprove and Downloads

A goal we had was to monitor how many people are using VoroCrust Meshing. We have accomplished this by releasing our binaries on our website (vorocrust.sandia.gov) and keeping track of how many downloads we have received. Another goal that spawned from this one, is that we wanted to be able to track who was using our software, such as labs, universities, and companies. For this data, we collaborated with the Corporate Web Design and Development Team (CWDDT) who gave us access to a service they use called SiteImprove (Figure 6-1). We have met both goals and can monitor the various data when needed.

The SiteImprove site allows us to view analytics such as how many visitors to our site we had for a given time frame, we can view other data such as their IP address, where they are visiting from (country, state, organization, etc.). One of the most useful things that we can do with this information is generate reports that tells us which labs, universities and companies are interested in VoroCrust (Figure 6-2). Other useful metrics to note are the most and least popular pages, bounce rate, how long it takes pages to load, traffic sources, and what pages the users enter and leave the site from.
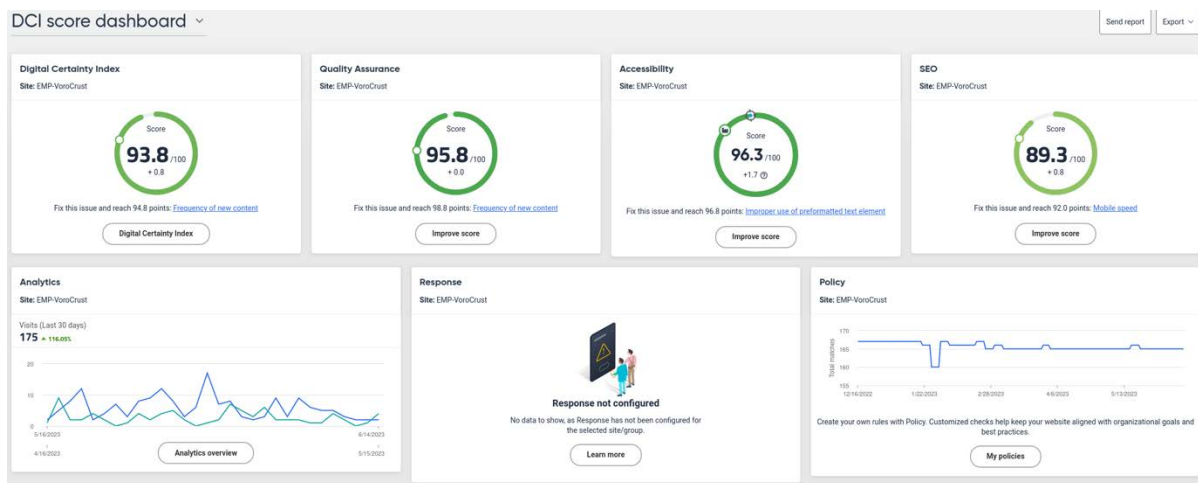
Figure 6-1.   Main page of SiteImprove.

Organizations

Organization	IP address	Visits | % of total
Department 9232 - Advanced Information Technology	5 IPs	14 / 22.6%
Amazon.Com Inc.	4 IPs	12 / 19.4%
Korea Telecom	175.193.91.253	5 / 8.1%
Microsoft Corporation	5 IPs	5 / 8.1%
Valley Electric Association	23.162.0.47	5 / 8.1%

More details

Figure 6-2.   Example of organization data provided by SiteImprove

Using the WordPress site, we can further track download statistics. This gives us a concrete number of people who are using our software. There has been a setback with this, however, since Sandia cyber teams are constantly doing vulnerability checks. They performed a vulnerability check on vorocrust.sanda.gov and part of that was them downloading VoroCrust Meshing software thousands of times (Figure 6-3), so we are now working with CWDDT to do two things:

(1).   Obtain quality download statistics that are indicative of how many actual users there are.

(2).   Prevent this from happening in the future by implementing reCAPTCHAs for each download.

		Title ▲	ID	File	Version	Categories	Tags	↓	★	⚑	🔗	Date posted
☐		vorocrust meshing ubuntu 22.10	848	`vorocrust-meshing-ubuntu2210.zip — 2 MB`	–	–	–	5,222	—	—	—	Published 2022/11/18 at 10:26 am
☐		vorocrust meshing ubuntu 22.04	846	`vorocrust-meshing-ubuntu2204.zip — 2 MB`	–	–	–	2,759	—	—	—	Published 2022/11/18 at 10:26 am
☐		vorocrust meshing ubuntu 20.04	844	`vorocrust-meshing-ubuntu2004.zip — 2 MB`	–	–	–	3,104	—	—	—	Published 2022/11/18 at 10:26 am
☐		vorocrust meshing ubuntu 18.04	842	`vorocrust-meshing-ubuntu1804.zip — 2 MB`	–	–	–	1,991	—	—	—	Published 2022/11/18 at 10:25 am
☐		vorocrust meshing rhel 7	812	`vorocrust-meshing-rhel7.zip — 7 MB`	–	–	–	244	—	—	—	Published 2022/11/10 at 2:30 pm
☐		vorocrust meshing windows 10	810	`vorocrust-meshing-windows10.zip — 244 KB`	–	–	–	713	—	—	—	Published 2022/11/10 at 2:30 pm
☐		vorocrust meshing mac	808	`vorocrust-meshing-mac12-x86.tar.gz — 3 MB`	–	–	–	556	—	—	—	Published 2022/11/10 at 2:28 pm
☐		Title	ID	File	Version	Categories	Tags	↓	★	⚑	🔗	Date posted

Figure 6-3.   Downloads page, showcasing our binaries and how many downloads each have received.

6.1.1.3 Monitor the webpages quality assurance reports and make fixes when things break or changes to improve the site

This goal was created once we gained access to SiteImprove. A weekly quality assurance report is received (Figure 6-4) that details important factors such as broken links, misspellings, number of total pages, etc. This has already been extremely helpful for us, in one case the U.S. patent office changed some of their links and the links we had were broken as a result. The quality assurance report alerted us to this, and we created new, updated links to the patents. This task is ongoing, but we have used these reports to improve our website and the customers experience.

	This check	Last check
Pages	28	28
Pages with broken links	1	1
Pages with broken links (%)	3.57%	3.57%
Links	333	331
Broken links	3	3
Broken links (%)	0.90%	0.91%
Misspellings	1	1
Live report		HTML

Group	Pages	Broken links	Misspellings	Live Report
Pages not currently in a content group	28	3	1	HTML
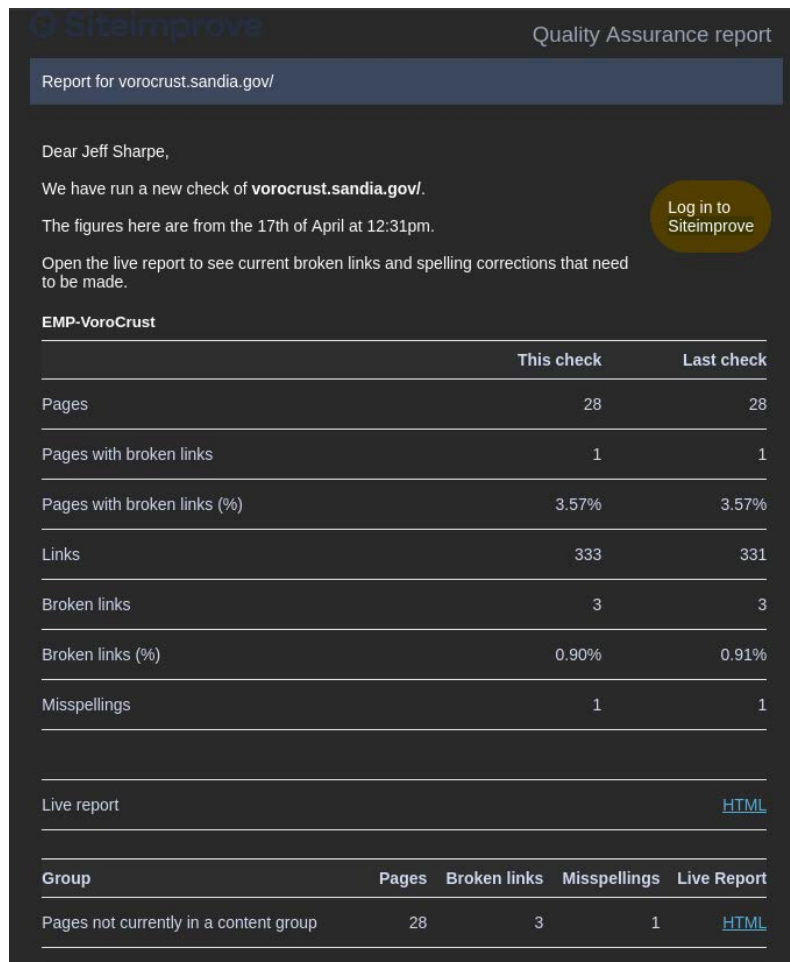
Figure 6-4. **Example of a quality assurance report**

6.1.1.4 Create a user manual, develop nightly tests for new methods and maintain VoroCrust repositories

There are several goals in this task, including creating a manual that users can refer to if they need information about the purpose of VoroCrust Meshing, how to use it, expected inputs and outputs, etc. We also want to get nightly tests in place and continuously maintain the various repositories involved with VoroCrust Meshing.

We have started on the manual creation, and we already have some of this in place on the website, such as how to use our binaries, but we need to collect it all in one online document. We need to also document the functionality of the VoroCrust Meshing software and provide documentation on expected inputs, behavior, and outputs.

We do have nightly tests in place on the VoroCrust Meshing Repository since we have a nightly sync that looks for differences between the main VoroCrust repositories meshing source code and VoroCrust Meshing. When this sync is run, the tests are triggered. However, we don't yet have a nightly test on the main VoroCrust repository. Instead, the tests are executed there when a push or merge is made.

We constantly maintain all involved repositories. For instance, since significant meshing development is done on the main VoroCrust repo, we have a nightly script in place that looks for changes there and transfers them over to the VoroCrust Meshing repo so that it stays up to date. We additionally have a public Sandia Github repository that we update less frequently, a couple of times a year.

6.1.2   VoroCrust Development

6.1.2.1   Implement a procedure for inserting waste packages as pre-meshed elements
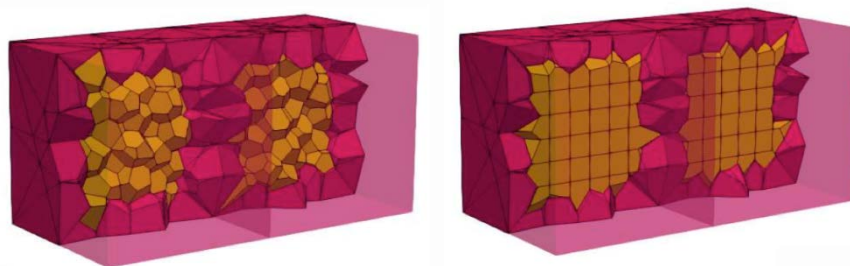
Figure 6-5.   Left: VoroCrust unstructured mesh of an interior feature. Right: Structured mesh of an interior region embedded in the unstructured mesh.

As illustrated in Figure 6-5, VoroCrust has the flexibility to alternate between random and structured Voronoi cells. This FY we are extending this capability to enable efficient insertion of waste packages in each geological domain. This idea is to generate a structured set of seeds representing the waste package and their surroundings using the fewest number of Voronoi cells. Then we insert this set of seeds and protect their neighbor cells with a sphere cover that ensures that the additional seeds VoroCrust inserts, for reconstructing the surfaces of the geological model and for properly meshing the interior of the domain, does not interfere with the embedded structure of the Voronoi cells representing the waste package subregions.

Our initial approach is to let VoroCrust generate a mesh that completely ignores the waste packages, then we would clear some area in the interior, add the structured set of seeds to capture the waste package subregion and fill the surrounding with additional seeds to ensure we have a good quality mesh at the end. Unfortunately, that approach did not work robustly since it ignores the sizing function associated with the packages this could result in a wild variation of the cell sizes in the proximity of the waste package subregion and that resulted in a mesh with poor quality.

To fix this issue we are now implementing another approach that collects the sizing function from the waste package domain and ensures that VoroCrust satisfies it during the meshing procedure. We then insert the seeds representing the packages after the surface meshing step and before adding additional seeds in the interior.

This approach assumes that the waste packages are inserted far enough from the surface and that they do not need additional points to be represented in the VoroCrust mesh. Future work is needed to address this challenge.

6.1.2.2 *Improve the robustness of imposing monitoring points across multiple VoroCrust mesh realizations of the same geological model*

To compare numerical simulations across different meshes, it is desired that all meshes share a set of Voronoi seeds in the same locations. This FY, we added source code to improve the robustness of this operation in VoroCrust. In the past, VoroCrust would attempt adding a Voronoi seed at a specific location, if not successful, it would ignore it and move on after reporting that failure to the user. This FY, instead of simply ignoring it, VoroCrust attempts inserting a seed as close as possible. Finally, it reports that new location back to the user.

6.1.2.3 *Make visualization and simulation possible using Paraview with VoroCrust Exodus meshes*

This task has two parts:

(1). Using Paraview to view VoroCrust Meshing meshes

(2). Using Paraview to verify meshes will work for GDSA simulations utilizing other simulators, such as FEHM or TOUGH2.

Part 1 is complete. This task arose because the newer versions of Paraview were not displaying VoroCrust meshes, whereas the previous versions would. The problem was that the newest versions of Paraview (5.10+) do not support Polyhedral meshes. We raised this issue with the Paraview developers. This is a known issue and the Paraview team are working on resolving this. The work around until then is to install a plugin called **LegacyExodusReader** and use that to view VoroCrust Meshing's Exodus (.**exo**) files, as shown in Figure 6-6 and Figure 6-7.
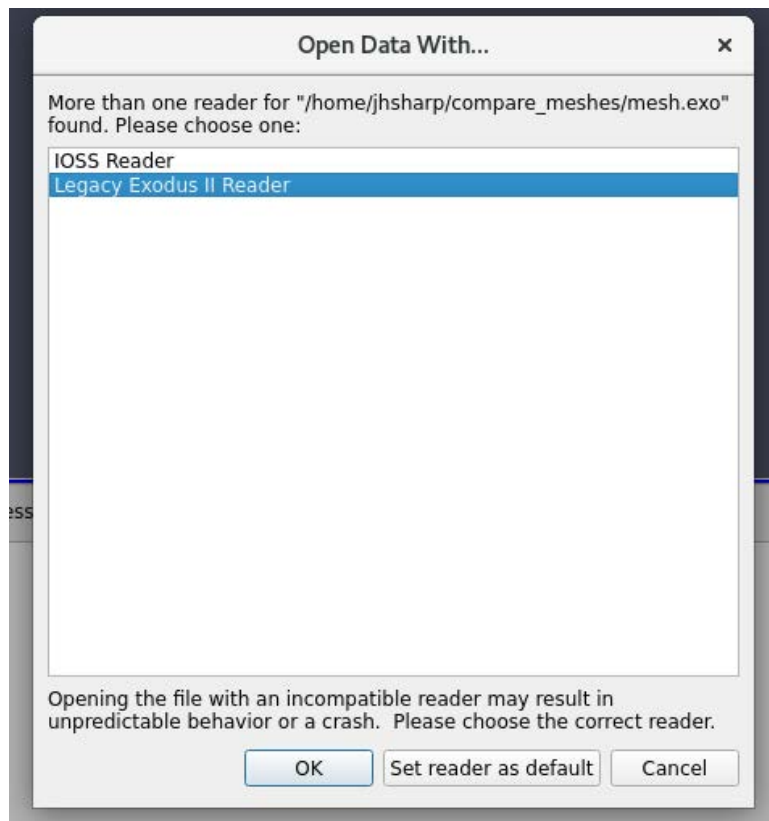
Figure 6-6. **Once the LegacyExodusReader plugin is downloaded, when you open an Exodus file select it.**
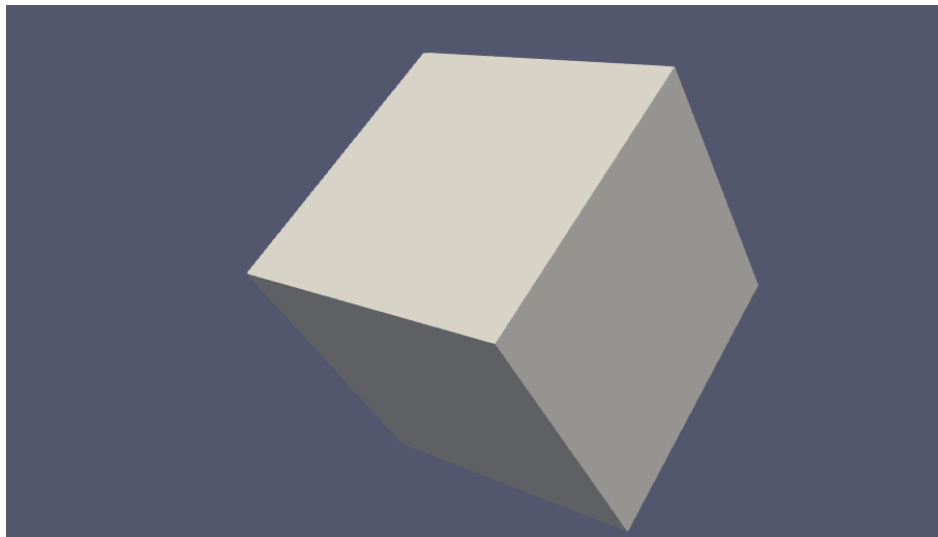
Figure 6-7.   How our meshes look in Paraview using the LegacyExodusReader.

Part 2 is in progress. The goal of this task is to make our Exodus II meshes conform to the Exodus standard meshing data structure. Once complete, VoroCrust meshes will have all information necessary for utilization in other simulation software (e.g., Amanzi (Mercer-Smith, 2020; Coon et al., 2019) and Sierra Mechanics). The template we are using is the open-source LaGriT software meshes (LANL Grid Toolbox, 2021)

We have downloaded and compiled the Amanzi ATS software to further investigate why our meshes do not work for simulation purposes. This is the software used by the group that reported that we are missing necessary data for the simulations. There are some complexities here to figure out such as it seems that XML and VTK files are needed to run Amanzi, or at least some of the Python scripts that are part of the Amanzi ATS suite.

One thing that Amanzi users have highlighted is that we need is side-set data. LaGriT meshes contain this data in the correct format. One possible solution is to incorporate this into our pipeline to generate the side set data for our meshes in post processing. This is an ongoing task.

6.2   Study of Simulation Accuracy on Voronoi Meshes

It has been established that utilizing unstructured VoroCrust Voronoi meshes results in high accuracy in PFLOTRAN simulation results as compared with analytical benchmark solutions (LaForce et al., 2020, Section 6.3.3; LaForce et al., 2021, Section 6.2). Simulations on VoroCrust meshes have been proved to be as (LaForce et al., 2020) or more (LaForce et al., 2023c) accurate than simulations on hexahedral meshes of similar resolution. However, this accuracy comes at an additional computation cost. Simulations on unstructured polyhedral meshes are intrinsically more computationally-intensive and typically simulations take about three times as long as simulations on hexahedral meshes for the same level of grid resolution (LaForce et al., 2020).

Thus, unstructured Voronoi meshes are not a one-size-fits-all solution for simulating subsurface flow problems. There are scenarios where flexed hexahedral meshes give acceptable simulation results and so Voronoi meshes may not be worth the computational cost, unless there are other reasons for utilizing unstructured meshing (e.g., automated meshing or inability to mesh geological features accurately with hexahedral grid flexing). However, in other scenarios, utilizing unstructured meshing may be the only way to obtain an accurate simulation result. As detailed studies of simulations on Voronoi meshes remain

relatively rare in the literature it is not clear where it is imperative to use unstructured meshes to obtain an accurate solution, and cases when Voronoi meshes are likely not worth the additional computational cost.

In this section, a series of simulations on structured hexahedral and randomly-generated VoroCrust Voronoi (Abdelkader, 2020) meshes will be conducted and the simulation results compared. Simulations for 2D single-phase flow and transport with analytical solutions will be compared with hexahedral, flexed hexahedral and VoroCrust Voronoi meshes. Finally, simulations for viscous-unstable gas flow, which are notoriously difficult to simulate using structured meshes will be compared to experimental data.

6.2.1   Sources of Simulation Error

Two important sources of numerical error in subsurface flow simulations are the grid causing preferential flow directions and non-orthogonal fluxes between cells. Though the two are often conflated and may occur simultaneously, they have different causes:

- Simulations on a structured grid may exhibit artificial **preferential flow directions** because the grid structure systemically biases the calculated flow field. This is caused by overestimating the flux perpendicular to cell faces and under estimating flux in other directions. Preferential flow may occur on an ideal block hexahedral mesh (which is a special case of a Voronoi mesh) despite a having orthogonal fluxes everywhere.

- **Non-orthogonal fluxes** occur in simulations on a mesh with poorly scaled grid cells due to distorting the grid to capture geological or engineered features. A non-orthogonal flux occurs when the calculated flux is not perpendicular to the face connecting neighboring cells. By definition, non-orthogonal fluxes cannot occur on meshes that are Voronoi, but can occur in simulations on tetrahedral, general polyhedral, or flexed hexahedral meshes.

6.2.2   Quantitative Comparison of Results

In order to quantify acceptable versus unacceptable simulated solutions, it is necessary to have measurements of error in terms of the goals of a particular simulation model. Several measurements of simulation error are utilized in this work that can be used to determine global error of a simulation or error at a particular point in time or space. The first is the pointwise error, or error at a particular grid cell in the mesh. Point-wise relative (units of observations) L2 error, ER, is defined as:

$$ER = \frac{(Q_{an,i} - Q_{sim,i})^2}{Q_{an,i}}$$

Eq. 6-1

where $Q_{an,i}$ is the analytical solution for the quantity of interest and $Q_{sim,i}$ is the simulated solution at cell center i in the domain. This error metric is primarily useful for simulations where Q is positive and large everywhere in the domain, such as when Q is the pressure.

When the initial or far-field conditions for Q are zero, such as in simulations where Q is tracer or saturation, the relative error given in Eq. 6-1 may be large because the analytical quantity $Q_{an,i}$ is small, and the absolute L2 point-wise error metric is more useful. The absolute L2 error (units of observation variance), EA, is given by:

$$EA = (Q_{an,i} - Q_{sim,i})^2$$

Eq. 6-2

Two types of qualitative comparisons are made utilizing the pointwise errors: (1) plots of error for every i in the simulation domain at a snapshot in time (or steady state) and (2) plots of the simulated error ER(t) or EA(t) at a particular location of interest as a function of time.

Global error metrics are utilized to quantitatively assess the average quality of the simulation across the entire domain. The root mean squared (RMS) error of the simulation (units of observations) at some or all points in the simulation domain, RMS_{dom}, at a snapshot in time (or steady state) is defined as

$$RMS_{dom} = \sqrt{\frac{\sum_{i=1}^{N}(Q_{an,i} - Q_{sim,i})^2}{N}}$$

      Eq. 6-3

where the sum is over every grid cell center i in the simulation or region of interest.

For time-dependent problems it is useful to consider the RMS error of the simulated solution at a single point as a function of time. The error at a single point as function of time, $RMS_{i,t}$, is given by:

$$RMS_{i,t} = \sqrt{\frac{\sum_{t=1}^{T}(Q_{an,i}(t) - Q_{sim,i}(t))^2}{T}}$$

      Eq. 6-4

where i denotes the location of interest in the simulation domain and the sum is over every output timestep $t = 0,\ldots,T$ in the simulation.

6.2.3   2D single-phase flow between a source and sink

A five-spot well pattern is a common petroleum reservoir development strategy that provides a 2D benchmark problem with an analytical solution for single-phase flow of an incompressible fluid. This benchmark is frequently used to study grid orientation effects because the dominant direction of flow is diagonally to the grid cell faces of a structured hexahedral mesh, so it represents a numerically challenging simulation with a simple analytic solution.

In a five-spot injection pattern, four injection wells are located at the corners of a square domain and the production well sits in the center (https://glossary.slb.com/en/terms/f/five-spot.aspx). If the assumption is made that a large array of five-spot well patterns are repeated and that identical volumes of fluid are injected and produced at constant rate, then the equation for the pressure in the reservoir in the centermost array is (Bear, 1988):

$$P_{inj}(x,y) = \left(\frac{-Q\rho\mu}{4\pi kh}\right)\ln\left[(x-x_{inj})^2 + (y-y_{inj})^2\right]$$
$$P_{prod}(x,y) = \left(\frac{Q\rho\mu}{4\pi kh}\right)\ln\left[(x-x_{prod})^2 + (y-y_{prod})^2\right]$$
$$P = P_o + P_{inj} + P_{prod}$$

      Eq. 6-5

Where:

- (x_{inj}, y_{inj}) is the location of the injection well

- (x_{prod}, y_{prod}) is the location of the production well

- Q is injection/extraction rate in m^3/sec

- ρ is liquid density in kg/m^3

- μ is liquid viscosity in Ps

- k is permeability in m^2

- h is vertical thickness of the reservoir in m

- P_o is initial reservoir pressure in Pa

For the benchmark problem, the fluid parameters are constant density $\rho = 10^3$ kg/m^3, reference pressure $P_o = 10^6$ Pa, and constant viscosity of $\mu = 10^{-3}$ Pa-s. The fixed liquid injection/extraction rate is $Q = 3.0 \times 10^{-5}$ m^3/sec (30.0 g/sec) and h = 0.02 m. Using the symmetry of the analytical solution, it is sufficient to simulate ¼ of the rectangular domain containing the five-spot well pattern by utilizing all closed boundaries, one injector at the lower left-hand corner and one producer at the upper right-hand corner. In the benchmark problem the ¼ five-spot domain is a 1 × 1 m square so that $(x_{inj}, y_{inj}) = (0,0)$ and $(x_{prod}, y_{prod}) = (1,1)$.

6.2.3.1   Isotropic domain analytical solution

For the isotropic simulations the x and y direction permeabilities are k $= 5.0 \times 10^{-12}$ m^2. The analytical solution is shown in Figure 6-8.
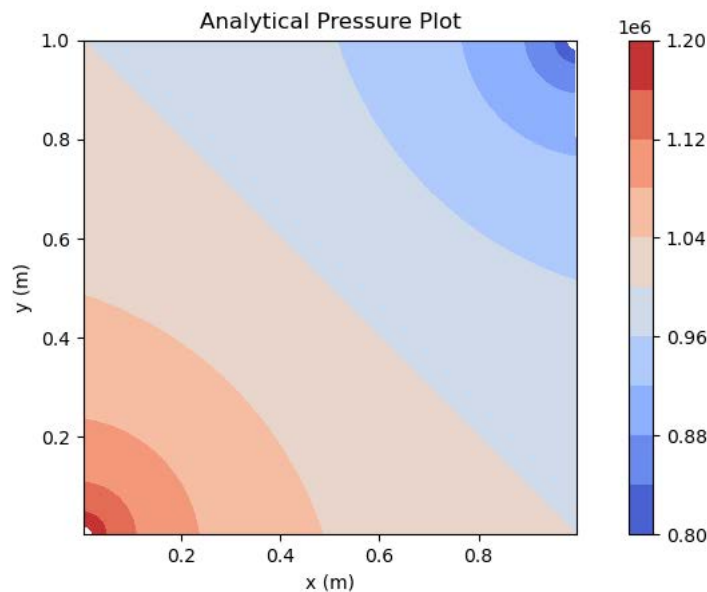
Figure 6-8.   **Analytical solution for isotropic five-spot benchmark problem.**

6.2.3.2   Anisotropic domain analytical solution

For the anisotropic simulations the x direction permeability is $k_x = 10^{-12}$ m^2 and the y direction permeability is $k_y = 10^{-11}$ m^2 so that the average permeability is $(k_x k_y)^{0.5}$ and the y-coordinate in the analytical solution is transformed so that y = y $(k_x/k_y)^{0.5}$. The analytical solution is shown in Figure 6-9.
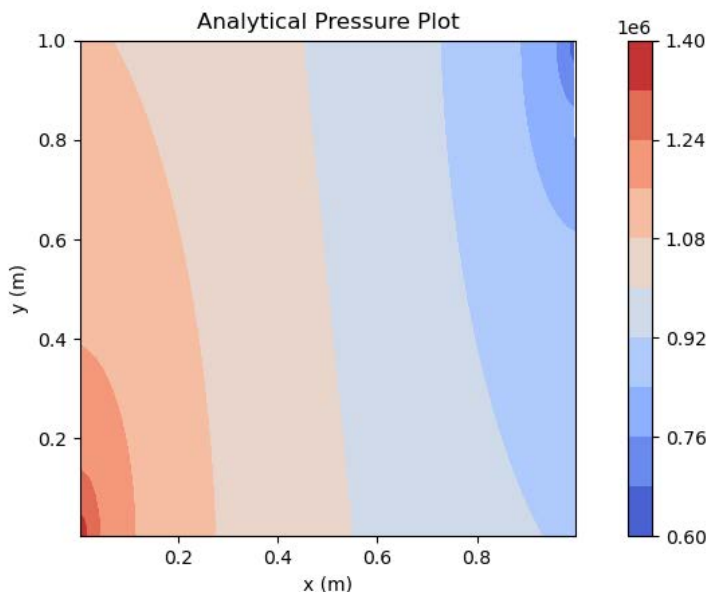
Figure 6-9.   Analytical solution for anisotropic five-spot benchmark problem with $k_x/k_y = 0.1$.

6.2.3.3   Simulation model parameters

All simulations are in TH mode, though they are set to isothermal conditions and this example is fully water-saturated. A slightly compressible fluid formulation was necessary to allow the simulations to converge, as a fully incompressible single-phase problem in a closed domain is an extraordinarily difficult numerical problem. The liquid phase has exponential function compressibility given by DENSITY EXPONENTIAL with $\rho = 10^3$ kg/m^3, reference pressure $P_o = 10^6$ Pa and compressibility 10^{-10} Pa^{-1}. It was also necessary to ramp up the injection rate over the first day of the simulation to the steady-state liquid injection/extraction rate. As the simulation includes only ¼ of the five-spot domain the injection rate is scaled by 0.25 so that the injection/extraction rate is $Q = 7.5 \times 10^{-6}$ m^3/sec (7.5 g/sec). Gravity is omitted from the simulation model and simulations are run for two days.

6.2.3.4   Simulation meshes

All VoroCrust-Meshing Voronoi meshes are three-dimensional (3D) and isotropic, so the 2D benchmark problems are all simulated in 3D. Hexahedral meshes are three cells thick in the z-direction for conceptual consistency with the Voronoi meshes. Similar number of grid cells are used when possible, so that the simulation meshes are of similar resolution and the comparison is not biased by different levels of numerical diffusion. Hexahedral meshes in this study are always approximately isotropic.

Four simulation meshes are constructed to study the impact of gridding on these benchmark problems. All meshes have dimensions $1 \times 1 \times 0.02$ m. The first two meshes are simply the simulation domain as a box with no interior features, while the second two have a fracture of width 0.02 m artificially introduced into the domain at an angle of -30º from the y-axis and intersecting the y=0 boundary of the domain at x=0.809 m. The fracture feature does not have different properties from the rest of the domain.

- Figure 6-10 shows the first simulation mesh, a structured hexahedral mesh of the simulation domain with 150 cells in the x and y direction and 3 cells vertically, for a total of 67,500 perfectly cubic cells that are 6.67×10^{-3} m on a side. This mesh is a special-case of a Voronoi mesh.

- Figure 6-11 shows the second simulation mesh, a randomly generated Voronoi mesh of the simulation box with 69,963 general polyhedral cells.

- Figure 6-12 shows the third simulation mesh, a hexahedral mesh that has been flexed in the x-direction to conform exactly to the fracture feature. The mesh is not flexed in the y-direction. This mesh has 68,400 distorted hexahedral cells.

- Figure 6-13 shows the fourth simulation mesh, a randomly generated Voronoi mesh that conforms exactly to the fracture feature. This mesh has 94,720 general polyhedral cells. This mesh has more grid cells than the others because VoroCrust requires additional cells to resolve the two faces of the fracture.

Table 6-1.   Simulation meshes for five-spot benchmark problem. Simulation times are on 24 cores of a Linux parallel super-computer. RMS error is calculated using Eq. 6-2.

Mesh name	Cells	Isotropic Five-spot computation time (min)	Isotropic Five-spot RMS error in pressure (Pa)	Anisotropic Five-spot computation time (min)	Anisotropic Five-spot RMS error in pressure (Pa)
Hexahedral cubes	67,500	0.153	50.19	0.219	88.39
Voronoi	69,963	4.48	53.35	3.79	91.76
Hexahedral flexed to fracture	68,400	0.251	19.97	0.266	105.03
Voronoi with fracture	94,720	5.88	40.04	7.10	71.55
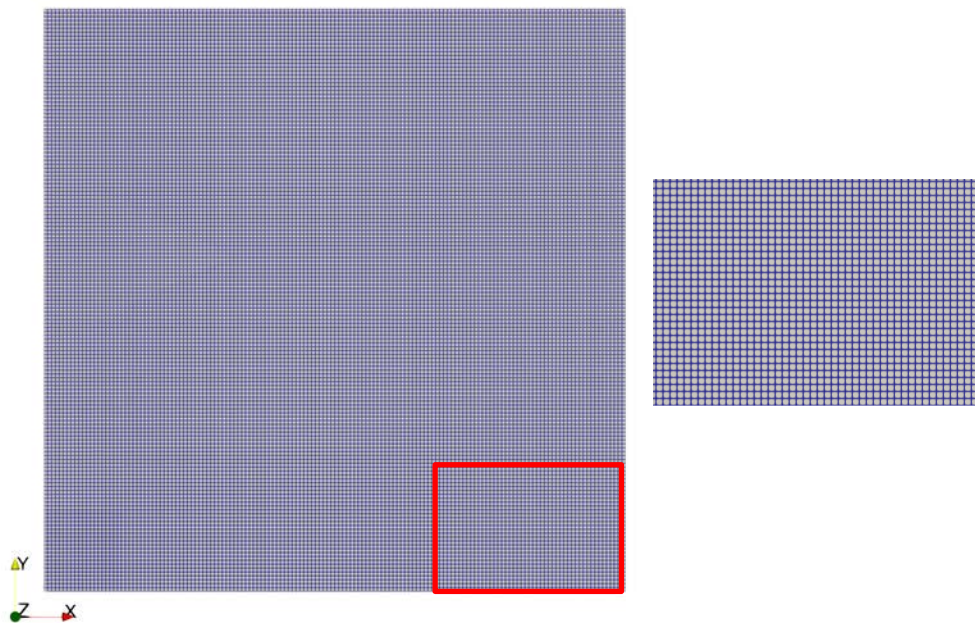
Figure 6-10.   Structured hexahedral mesh of the simulation domain with 67,500 perfectly cubic cells. Right: top-down view of the full simulation mesh. Left: detail of the mesh in the area indicated by the red box.
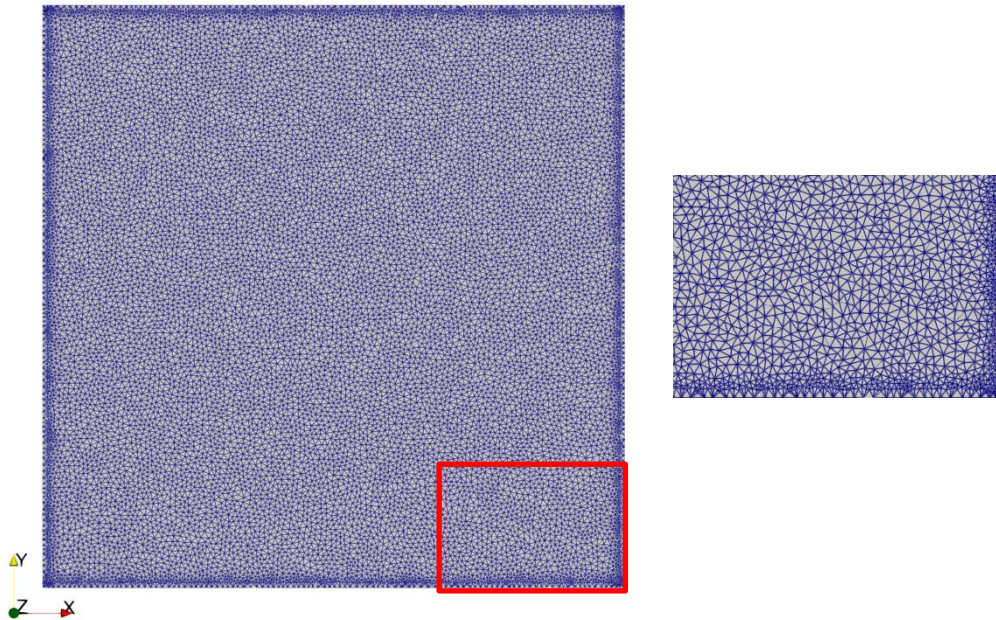
Figure 6-11. **Randomly-generated Voronoi mesh of the simulation domain with 69,963 polyhedral cells. Right: top-down view of the full simulation mesh. Left: detail of the surface mesh in the area indicated by the red box.**
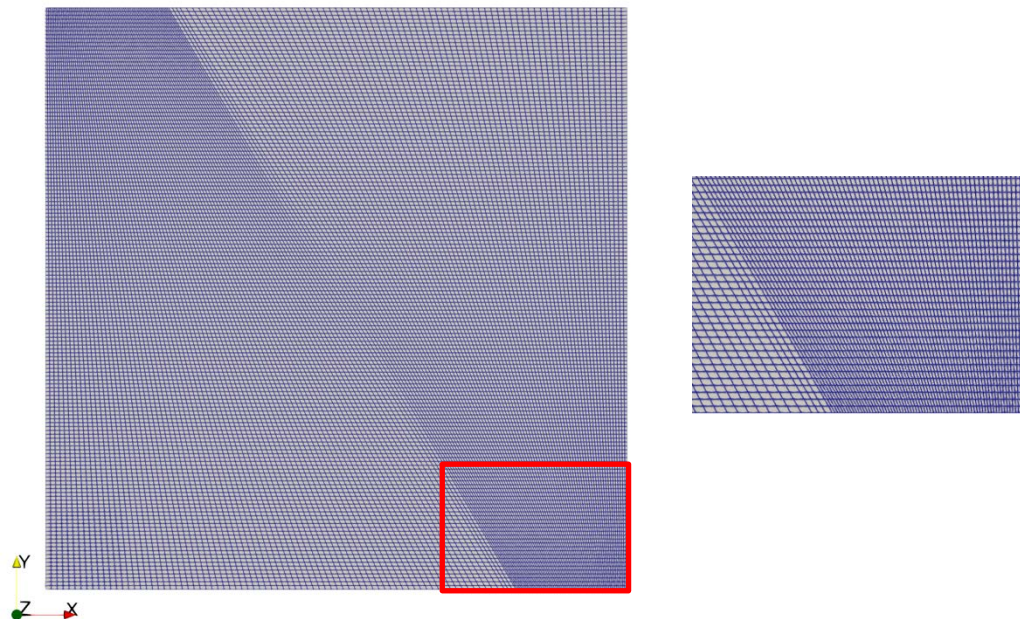
Figure 6-12. **Structured hexahedral mesh flexed to capture the fracture in the simulation domain with 68,400 distorted hexahedral cells. Right: top-down view of the full simulation mesh. Left: detail of the mesh in the area indicated by the red box.**
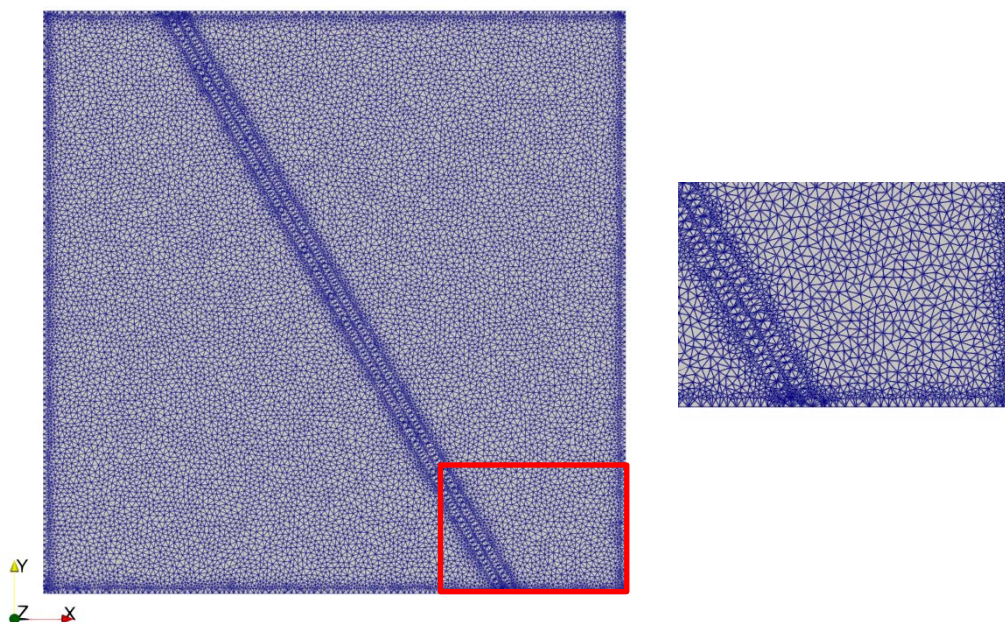
Figure 6-13. Randomly-generated Voronoi mesh of the fractured simulation domain with 94,720 polyhedral cells. Right: top-down view of the full simulation mesh. Left: detail of the surface mesh in the area indicated by the red box.

6.2.3.5 Isotropic simulation results

The isotropic five-spot benchmark simulation is run to steady state on each of the four simulation meshes. The pressure contours are shown on the left side of Figure 6-14. Errors are computed $r > 0.05$ m away from the injection and production wells. This is because the simulated injector and producer are at the center of the cells at the corner of the domain, not true point sources at (0,0) and (1,1), so that the error is expected to be larger here and could dominate the global error in the solution. The error subplots on the right side of Figure 6-14 show blank spots in this radial area on pointwise plots, and the RMS errors in Table 6-1 are calculated based only on the regions shown.

All four simulation results are excellent, with the greatest RMS error being 53 Pa for the Voronoi mesh. The three simulation meshes that are Voronoi (hexahedral cubes, Voronoi and Voronoi with fracture) all show similar trends, however the Voronoi mesh simulations take over 20 times as long to simulate the problem (see Table 6-1). This is due in part because the simulation on the hexahedral meshes uses the default Newton and Linear solvers, while the Voronoi mesh simulations require the slower, but more robust NTRDC Newton solver and the FGMRES with CPR preconditioner linear solver. The pressure contours of the simulated solutions are indistinguishable on subplots (a), (c) and (g) on left side of Figure 6-14. While subplots (b), (d) and (h) on left side of Figure 6-14 show that error is very low in the interior of the domain and increases towards the wells, with the highest error at the production well. The lower error in the Voronoi mesh with the fracture is likely due to the higher number of grid cells in the mesh.

However, the flexed hexahedral mesh has low pointwise error everywhere, and the lowest global RMS error of 19.97 Pa. This is even though the pressure contours for 0.96, 1.0 and 1.04 $\times 10^6$ Pa on subfigure (e) on the left side of Figure 6-14 are visibly distorted by the mesh. The flexing of the grid cells more closely aligns the grid cells in the center of the domain with the pressure isopotentials (thus making the dominant flow direction across cell faces), which improves the calculation of the fluxes in the center of the domain. The result is lower pointwise error near the wells, as shown on subfigure (f) on the right side of Figure 6-14.

The result of this benchmark problem is highly counter-intuitive. The pressure field in the simulation on the flexed hexahedral mesh 'looks bad' but has global RMS less than half the other meshes and the lowest local error at the wells, which are likely to be the points of greatest interest in a simulation study.
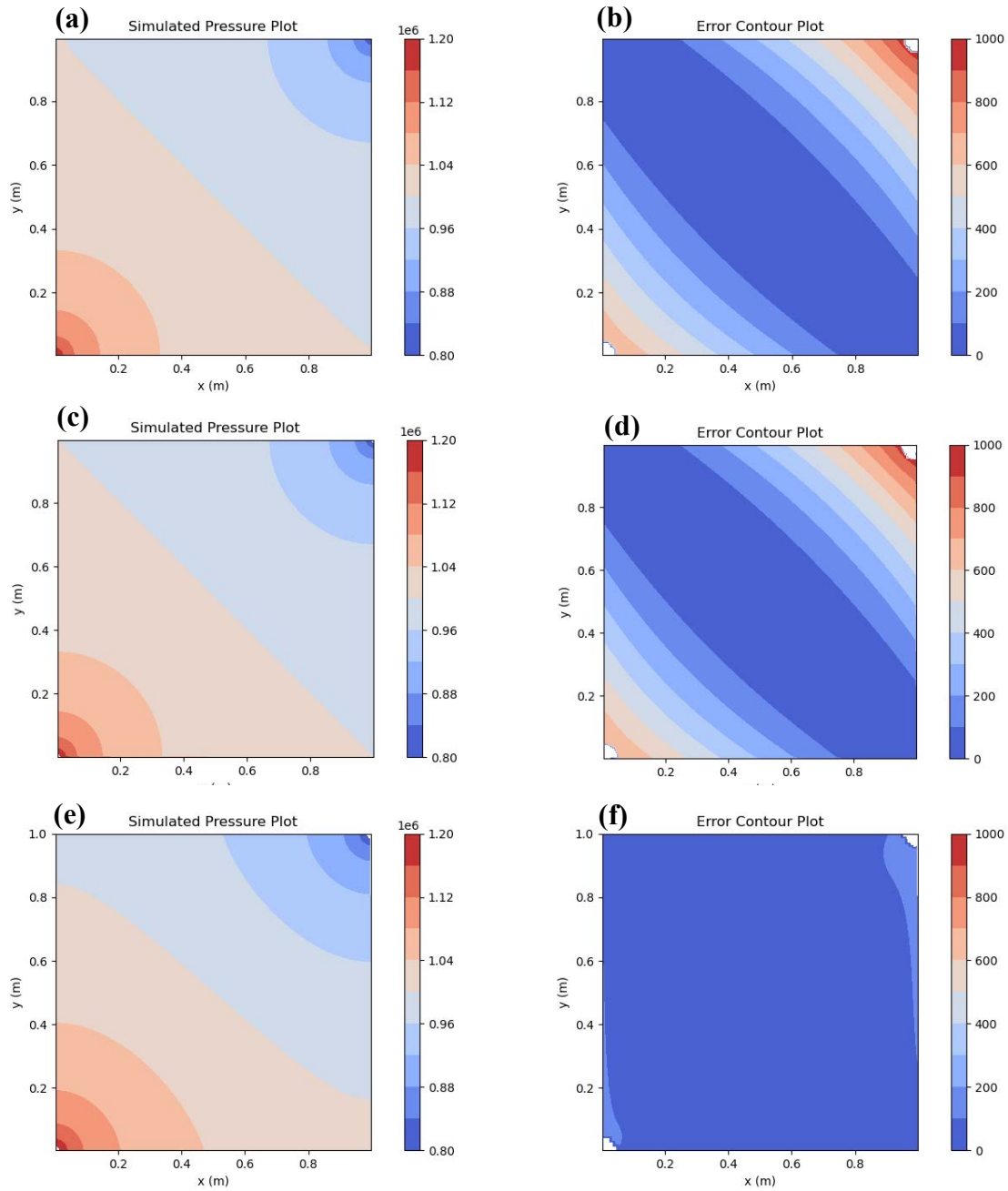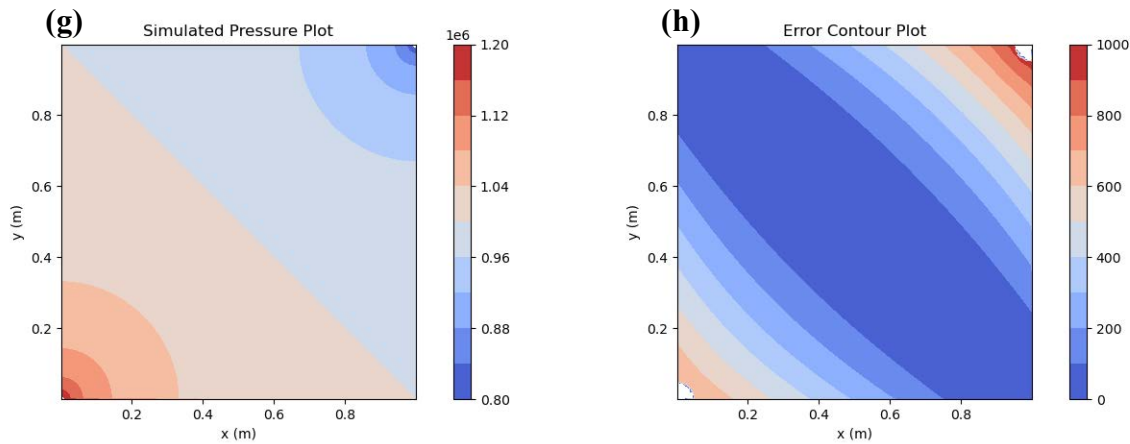
Figure 6-14. Simulation results for isotropic five-spot benchmark problem. (a) Simulated liquid pressure (Pa) on ideal hexahedral mesh. (b) Pointwise absolute error in the liquid pressure on ideal hexahedral mesh. (c) Simulated liquid pressure (Pa) on Voronoi mesh. (d) Pointwise absolute error in the liquid pressure on Voronoi mesh. (e) Simulated liquid pressure (Pa) on flexed hexahedral mesh. (f) Pointwise absolute error in the liquid pressure on flexed hexahedral mesh. (g) Simulated liquid pressure (Pa) on Voronoi mesh with fracture. (h) Pointwise absolute error in the liquid pressure on Voronoi mesh with fracture.

6.2.3.6   Anisotropic simulation results

As in the isotropic case, the RMS errors in Table 6-1 are calculated $r > 0.05$ m away from the wells. All of simulations have higher error for in the anisotropic case than the isotropic case, as shown by the larger scale in the error bar for the pointwise error plots on the right of Figure 6-15. For this case, flow from left to right dominates away from the wells.

Local error in the structured meshes are highest at the top and bottom boundaries of the domain, and the pressure contours in both hexahedral mesh simulations are more linear than the analytical solution in Figure 6-9. The pressure field in the center of the domain is nearly aligned with the grid cell boundaries in the ideal hexahedral mesh, though comparison of the hexahedral mesh simulation in subplot (a) of Figure 6-15 and the analytical solution in Figure 6-9 reveals that the pressure contours are more vertical than the analytical solution. The flexed hexahedral mesh has the highest RMS global error and has significant error over much of the simulation domain. This is because in this example the flexing of the hexahedral mesh near the fracture causes flow to be diagonal to the grid cell boundaries in the center of the domain and the pressure contours in subplot (e) of Figure 6-15 are more diagonal than the analytical solution in Figure 6-9.

Local error in the two Voronoi meshes follow a fundamentally different trend than the structured meshes. Simulations on these meshes, shown on sublots (c) and (g) on the left of Figure 6-15 have pressure contours that more rounded than the analytical solution in Figure 6-9, and the highest local errors are on the center right and left side of the domain. This is likely because the simulation does not use PFLOTRAN's full-tensor permeability capability, and few of the grid cell faces are aligned with the x- and y-permeabilities. The Voronoi meshes again have similar RMS error to each other, indicating that introduction of the fracture has not impacted the quality of the simulation mesh for this benchmark problem. The lower error in the Voronoi mesh with the fracture is again likely due to the higher number of grid cells in the mesh. The simulation time for the two Voronoi meshes is again over 20 times longer than the hexahedral mesh of similar accuracy (see Table 6-1).

In this example, the simulation result on the flexed hexahedral mesh has the highest RMS error and high local error across much of the domain, including near the wells. The other three simulations all have similar RMS error, show mild distortion of the pressure contours, and have regions of higher local error away from the injection and production wells. This result is opposite what was seen in the isotropic benchmark and demonstrates that it is not only the mesh itself, but also the simulation parameters that impact whether a particular mesh is well-suited for a simulation.
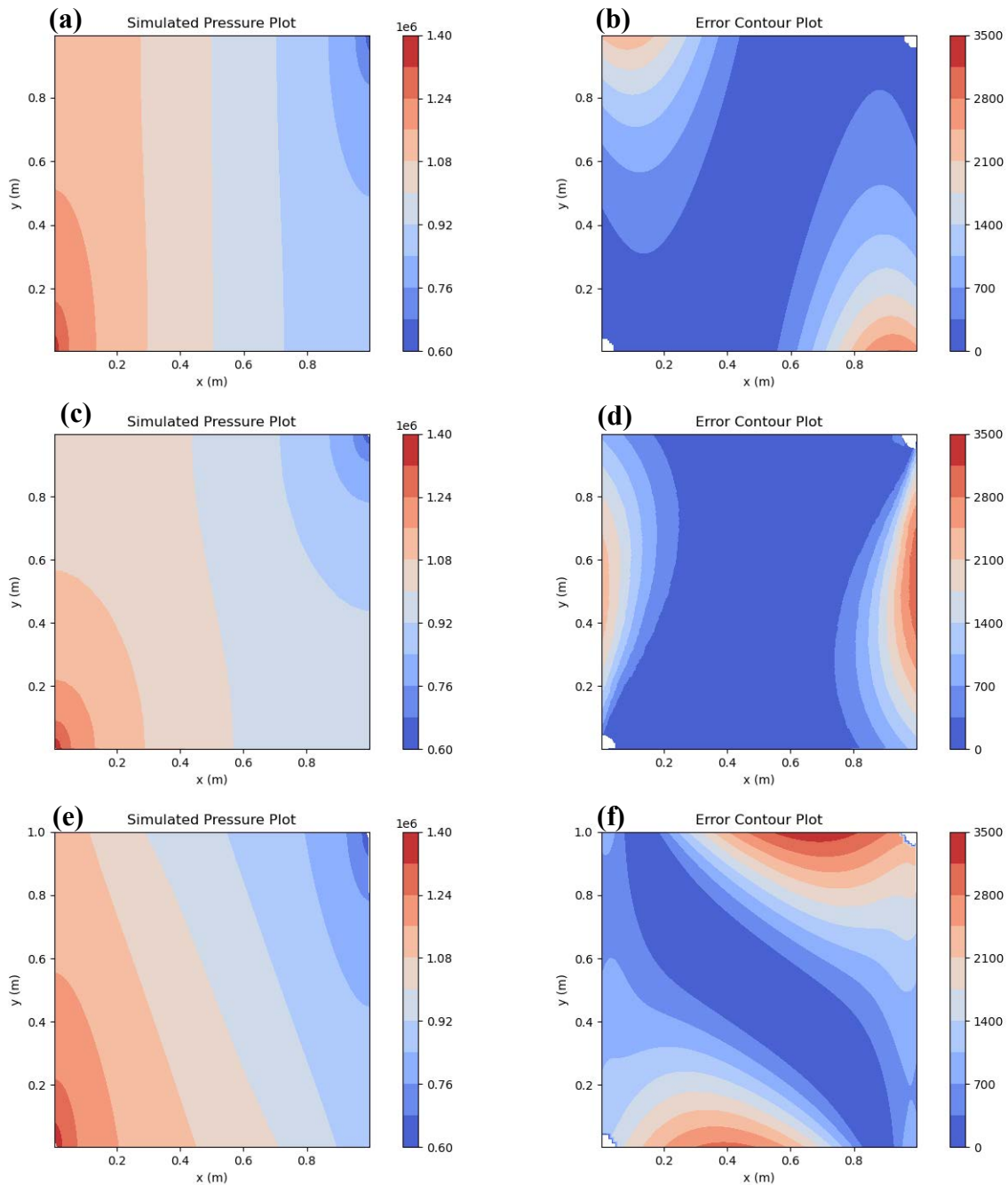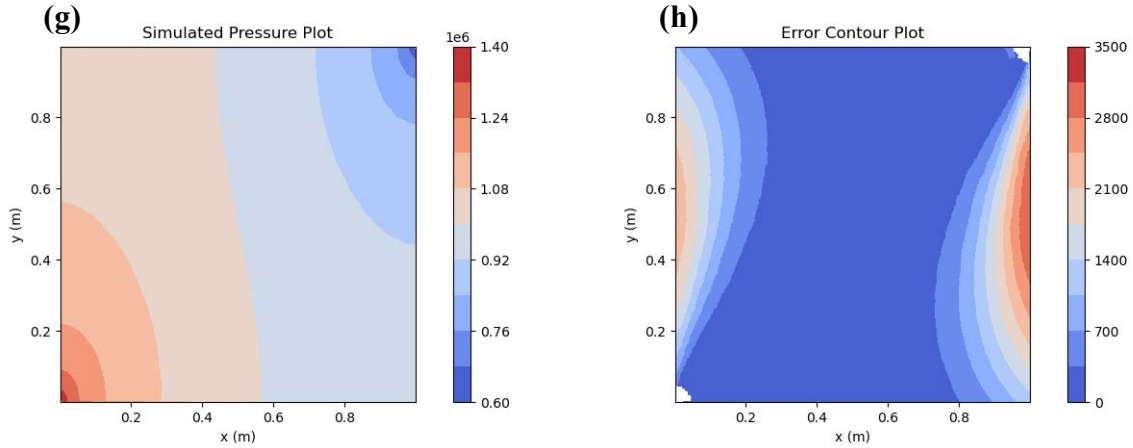
Figure 6-15. Simulation results for anisotropic five-spot benchmark problem. (a) simulated liquid pressure (Pa) on ideal hexahedral mesh. (b) Pointwise absolute error in the liquid pressure on ideal hexahedral mesh. (c) simulated liquid pressure (Pa) on Voronoi mesh. (d) Pointwise absolute error in the liquid pressure on Voronoi mesh. (e) simulated liquid pressure (Pa) on flexed hexahedral mesh. (f) Pointwise absolute error in the liquid pressure on flexed hexahedral mesh. (g) simulated liquid pressure (Pa) on Voronoi mesh with fracture. (h) Pointwise absolute error in the liquid pressure on Voronoi mesh with fracture.

6.2.4 Tracer Transport from a Line Source

LaForce et al. (2023a) considered a benchmark problem for DECOVALEX Task F2-salt that is representative of transport of radionuclides through the overburden as the result of shaft-seal failure. This problem was also simulated in Section 2.2.9 of the FY21 RSA report (LaForce et al., 2021) but is revisited for quantitative analysis here. The benchmark models transport of tracers through a 2-D semi-infinite domain with constant, unidirectional flow and tracer entering the domain from a line source. The 2-D domain represents idealized overburden sediment, while the line source represents the intersection of the shaft with the overburden. The setup of the benchmark problem and its solution are discussed in detail in Section 3.3.2.2 of Batu (2006) and LaForce et al. (2023a) and so are only briefly discussed here.

6.2.4.1 Analytical Model

The analytical model is based on Example 3-9 of Batu (2006). The assumptions of the analytical model are (after Batu, 2006):

(1). Unidirectional steady-state groundwater velocity field with flow in the x-direction. The domain is assumed to be water-saturated.

(2). Solute source is located at x = 0, planar and perpendicular to the velocity of the flow field.

(3). Source concentration is a function of z-coordinate and time through an exponential function.

(4). The medium is infinite in the x-direction and z is in the range (0, Z).

The governing equation is:

$$\frac{\partial C}{\partial t} = \frac{D_x}{R_d}\frac{\partial^2 C}{\partial x^2} + \frac{D_z}{R_d}\frac{\partial^2 C}{\partial z^2} - \frac{U}{R_d}\frac{\partial C}{\partial x} - vC \qquad \text{Eq. 6-6}$$

The initial condition is

$$C(x,z,0) = 0 \qquad \text{Eq. 6-7}$$

and the boundary condition is

$$C(0,z,t) = \begin{cases} C_m \exp(\gamma t) & D_1 < z < D_1 + 2B \\ 0 & \text{otherwise} \end{cases} \qquad \text{Eq. 6-8}$$

In this equation C_m is the initial tracer concentration at the source, U is the groundwater seepage velocity, v is the interstitial velocity, γ is the chemical decay rate of the source, R_d is the retardation factor, D_1 is the distance of the source from the z = 0 axis, D_2 is the distance from the z = Z outer boundary of the model, and B is the half-length of the planar source. $R_d = 1$ for flow without adsorption and $\gamma = 0$ for a constant rate tracer source for the benchmark problem. Dispersion is anisotropic and directional dispersion is $D_x = D^* + U\alpha_l$ and $D_z = D^* + U\alpha_t$.

All parameters are shown in Table 6-2. They are identical to Batu (2006) except that the height of the porous media has been increased to 20 m to make simulating the problem faster, as discussed in the next section. As the problem is 2D, the increased thickness does not impact the analytical solution. The series solution to this benchmark problem is challenging to compute numerically in regions of low concentration. The analytical solution shown has n = 500 terms of the series. In computing the analytical solution, if the tracer concentration is less than 10^{-20} [kg/m^3] it is set to this value, which is consistent with the background tracer concentration in the simulated solution. The analytical tracer concentration near the source after five years is shown in Figure 6-16a.

Table 6-2. **Parameters for 2D benchmark from DECOVALEX Task F2 salt. Height and permeability are only needed for simulations.**

Parameter	Value
Distance to source, D_1 [m]	1000
Half-width of source, B [m]	5
Width of the model in z-direction, Z [m]	2,010
Length of the model in x-direction, X [m]	9,000
Interstitial velocity [m/day]	0.15
Longitudinal dispersivity, a_l [m]	21.3 (+ 3.7)
Transverse dispersivity, a_t [m]	4.3 (+ 3.7)
Diffusion coefficient, D^* [m²/day]	0.0
Concentration at source, C_m [kg/m³]	1.0
Porosity [-]	0.25
Permeability [m²]	1×10^{-12}
Height*, h [m]	20

*Height is increased from Batu (2006) benchmark.

(a)

(b)

(c)

(d)
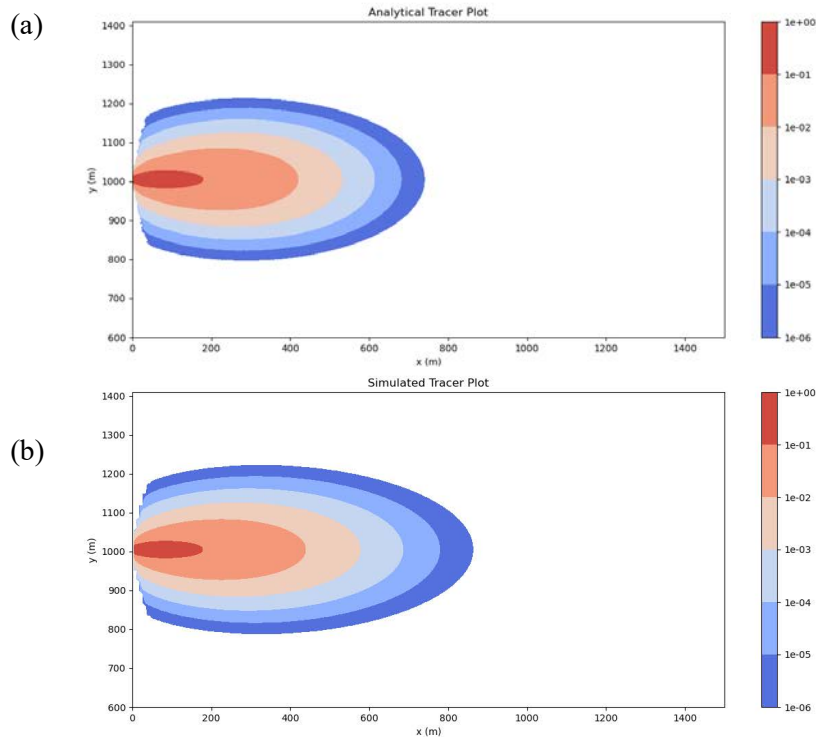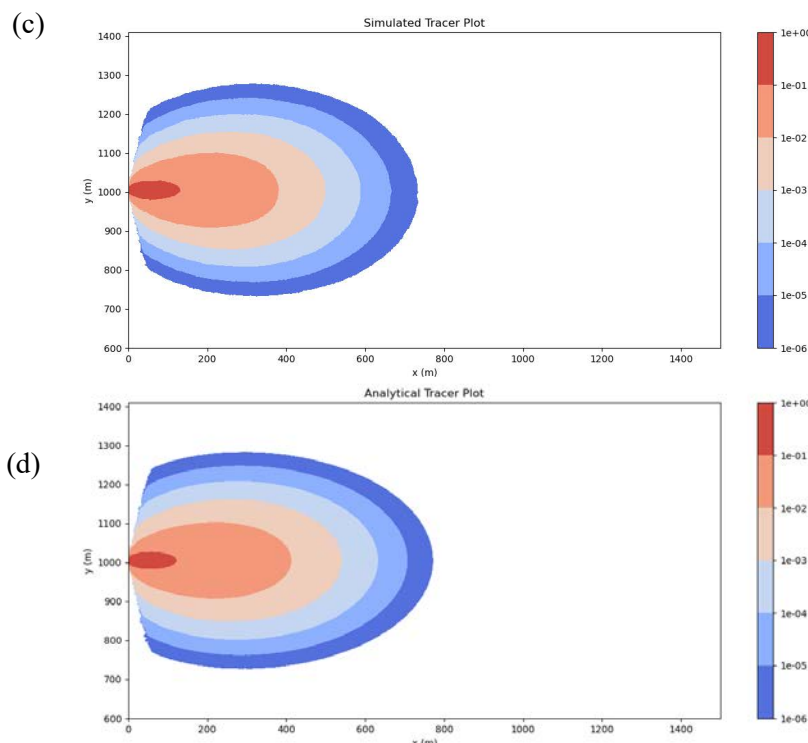
**Figure 6-16.   Batu (2006) benchmark problem tracer concentration above 10^{-6} [kg/m^3] after 5
years [kg/m3]. (a) Analytical tracer distribution for the benchmark problem as
given. (b) Simulated solution on hexahedral mesh. (c) Simulated solution on Voronoi
mesh. (d) Analytical tracer distribution for the benchmark problem with dispersion
increased to include approximate level of numerical dispersion in the hexahedral
mesh simulation.**

6.2.4.2   Simulated Solutions

The domain for the analytical solution is infinite in the x-direction (flow direction). The simulation
domain extends to X = 4000 m downstream of the line source. The part of the plume with concentration
above 10^{-6} [kg/m^3] extends to a maximum distance of 1,674 m after 5 years of simulation, or just over 1/3
of length of the domain, which is sufficient to mimic an infinite-acting reservoir. This threshold was
chosen because 10^{-6} [kg/m^3] equates to 1 part per billion (ppb) which is at or below the threshold for
measuring tracers or potentially dangerous subsurface contaminants. The background tracer concentration
in the simulation is set to 10^{-20} [kg/m^3].

The vertical mesh thickness was increased from 10 to 20 m. This is because over 1.5 million grid cells
were required to mesh the original benchmark due to the high anisotropy of the 4000 × 2010 × 10 m
domain. Increasing vertical thickness to h = 20 m reduced the number of cells in the VoroCrust Voronoi
mesh to 426,544 and does not impact the solution to the benchmark problem. As in the previous
benchmark problems, the hexahedral domain was given vertical thickness of 3 cells and the size of the
grid in the x and y directions was chosen to be 7.5 m so that the grid cells are nearly cubic (7.5 × 7.5 ×
6.67 m) and the number of grid cells in the mesh was similar to the Voronoi mesh at 426,390.

The simulation time for the hexahedral mesh is 0.9 minutes, while the simulation on the Voronoi mesh is
2.9 min, about three times slower. The simulated solutions are shown for tracer concentrations above 10^{-6}
[kg/m^3] (1 ppb) in Figure 6-16 (b) and (c). As can be seen, both simulated solutions over-estimate the
extent of the plume in Figure 6-16 (a) in the longitudinal direction. They both also under-estimate the
concentration of the plume near the source. This is the inevitable consequence of having numerical

dispersion in addition to the physical longitudinal and transverse dispersion given in Table 6-2. The increased dispersion is particularly pronounced in the flow direction on the hexahedral mesh. Truncation error in space on the structured mesh is expected to be on the order of R = (Δx - Δt)/2 (Aziz and Settari, 1979). For the structured mesh Δx = 7.5 and in both simulations the maximum timestep size is used, Δt = 0.1 y, for all except the first few timesteps of the simulations. Thus, on the structured mesh R = 3.7 m, which is the same order of magnitude as the physical dispersion.

Figure 6-16 (d) shows the analytical solution with both longitudinal and transverse dispersion increased by 3.7 m to account for numerical dispersion. This analytical solution is more like the simulations and will be used for qualitative and quantitative comparison of simulation error.

The simulation of the plume on the Voronoi mesh under-estimates the analytical tracer plume extent in Figure 6-16 (d), indicating that the numerical dispersion in the Voronoi mesh is likely lower than the dispersion estimated. However, the shape of the contours in the simulated solution are like the analytical plumes both with and without accounting for numerical dispersion. Conversely, the plume computed using a hexahedral mesh is more elongated in the flow direction than either analytical plume, an indication that this benchmark is sensitive to grid orientation effects on the structured mesh.

6.2.4.3   Error in Simulated Solutions

Local error

Pointwise error is calculated using Eq. 6-1 and Eq. 6-2 at t = 5 yr over the slice of the domain x = (10,1400) m, y = (600,1410) m, below the line y = 4x + 1010 and above the line y = 4x +1000. This subset of the domain contains the plume of concentrations above 10^{-6} [kg/m^3] for the analytical simulation and both simulations. It also eliminates the areas of small-x that are upstream of the plume where tracer concentration is very low and the analytical solution is challenging to compute. Simulated tracer plume and local errors on the hexahedral mesh simulation are shown in Figure 6-17, while the simulated plume and local errors in the Voronoi mesh simulation are in Figure 6-18.

As can be seen, in both simulations the relative and absolute error show very similar trends. Absolute L2 point-wise error is only shown for errors above 10^{-10} [kg/m^3] and is only above this threshold within the simulated plumes. Thus, in this case the EA metric is more informative.

Absolute error in both simulations is above 10^{-3} kg/m^3 near the center of the plume immediately downstream of the source from around x = (0,50) m for the Voronoi mesh, and from around x = (0,100) m for the hexahedral mesh, where the region of highest concentration is over-estimated by both simulations relative to the analytical solution with increased dispersion. However, further downstream of the source the two simulations have a fundamentally different trend in simulation error. In the simulation on the hexahedral mesh there are regions of high simulation errors above and below (at larger and smaller y) the source where tracer concentration is under-estimated by the simulation due to the plume being elongated by the grid orientation effects of the structured mesh. The simulation on the Voronoi mesh has second region of increased error from on the order of 10^{-5} from x = (300,400) m due to under-estimation of the plume extent in the x direction because the numerical dispersion on the Voronoi mesh appears to be smaller than the value estimated based on the hexahedral mesh. There is also scatter in the error near the center of the plume. This must be caused by the random nature of the mesh and would be slightly different for another realization of the mesh, though the trend would be the same.
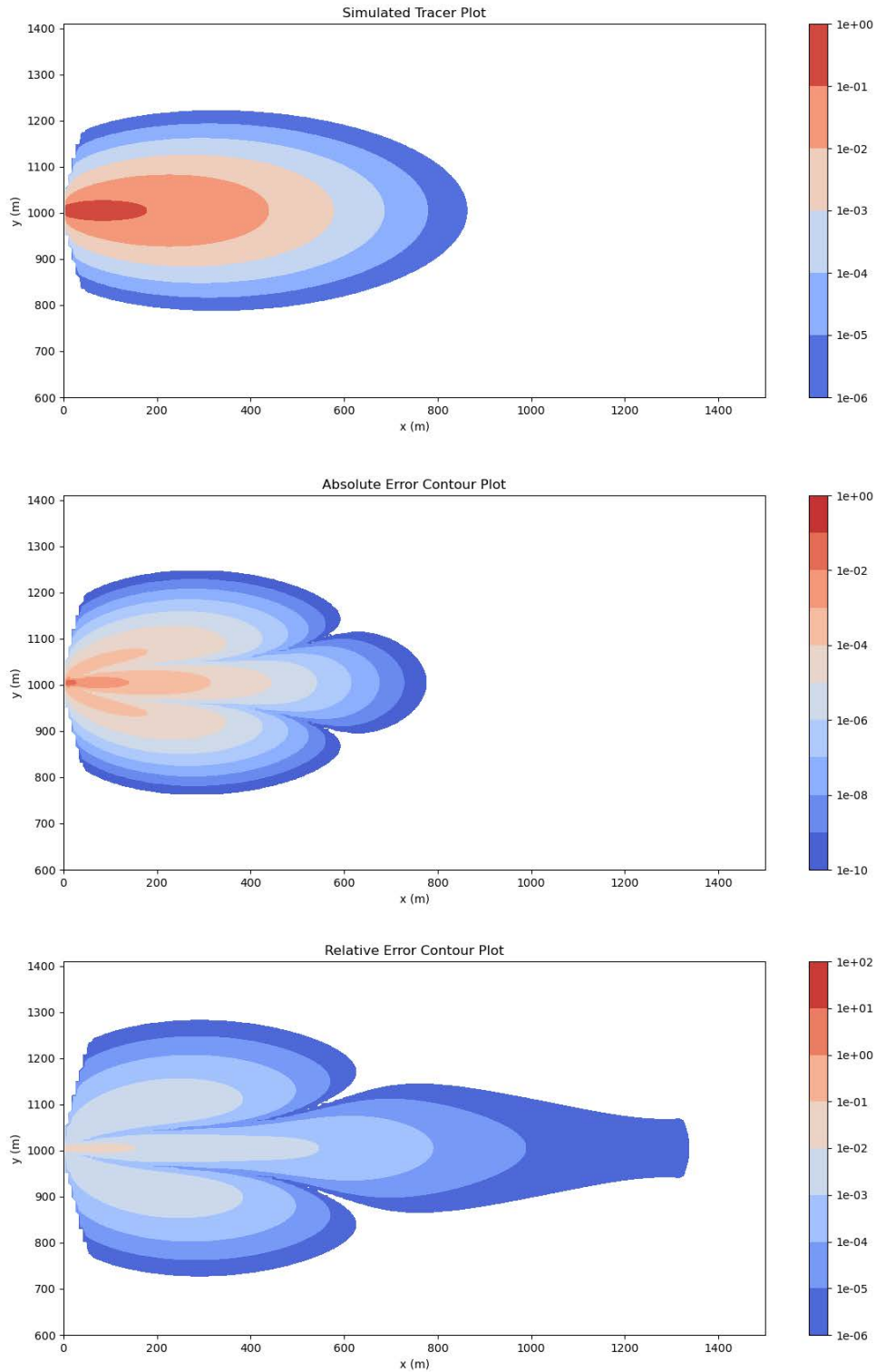
Figure 6-17.   **Simulation of Batu (2006) benchmark problem on the hexahedral mesh after 5 years. Top: Simulated solution for concentrations above 1×10^{-6} [kg/m^3]. Middle: Absolute error in tracer concentration [kg/m^3] Bottom: Relative error in tracer concentration [-].**
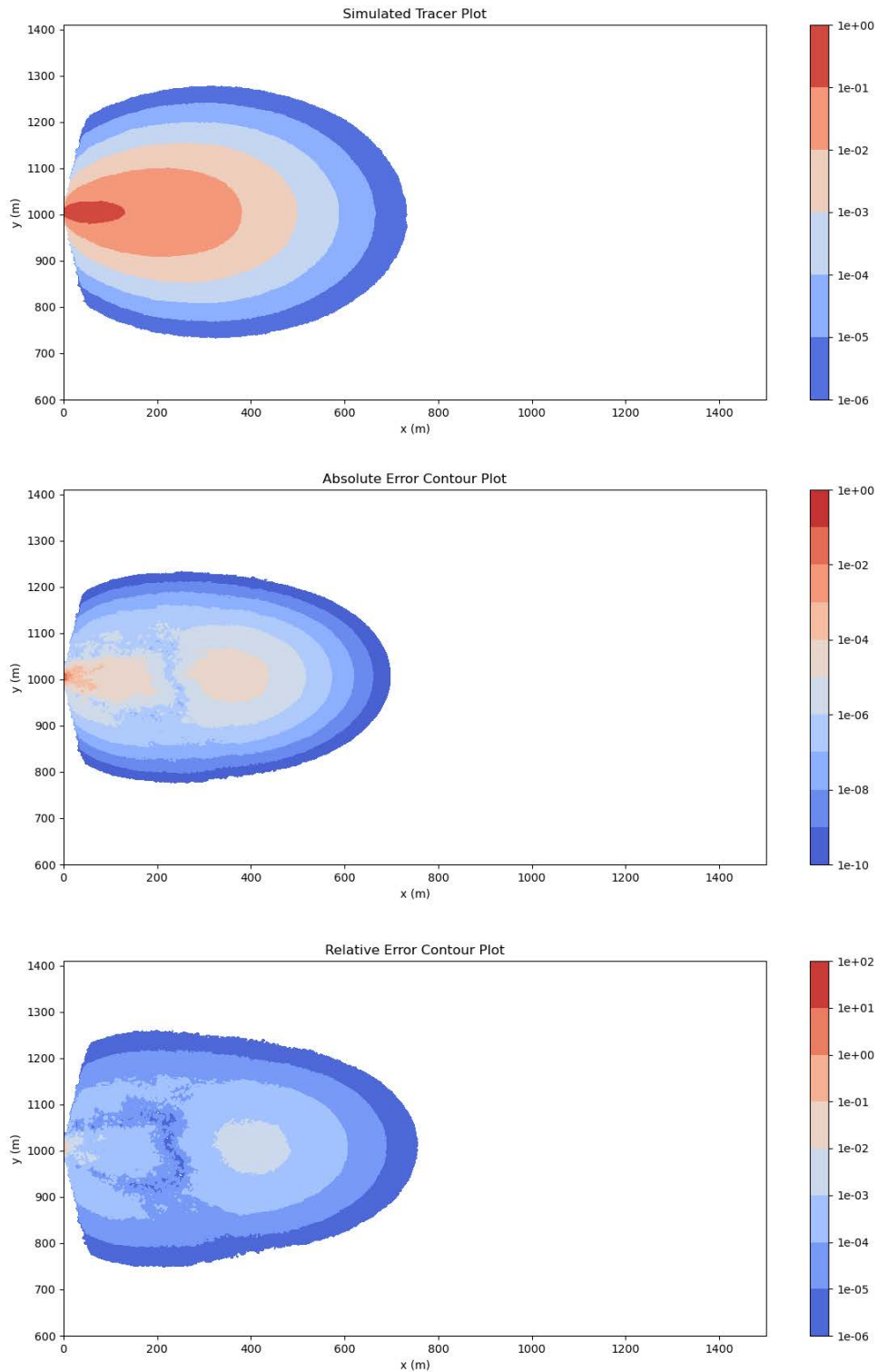
Figure 6-18. **Simulation of Batu (2006) benchmark problem on the Voronoi mesh after 5 years. Top: Simulated solution for concentrations above 10^{-6} [kg/m^3]. Middle: Absolute error in tracer concentration [kg/m^3] Bottom: Relative error in tracer concentration [-].**

RMS global error

RMS_{dom} error is calculated at t= 5 yr using Eq. 6-3. The global error is only computed the region between x = (10,1400) m, y = (600,1410) m, below the line y = 4x + 1010 and above the line y = 4x +1000, which are shown in Figure 6-17 and Figure 6-18. This is to prevent numerical errors on very low concentrations outside the tracer plume from dominating global error estimate. For the hexahedral mesh RMS_{dom} = 1.7 × 10^{-5} [kg/m^3], while the error on the Voronoi mesh is RMS_{dom} = 1.6 × 10^{-5} [kg/m^3]. Thus, in the global sense the quality of the two simulations is the same. Again, this is a counter-intuitive result because the simulation on the Voronoi mesh 'looks more like' the analytical solution.

Error as function of time

In the field, subsurface tracers (or contaminants) are typically measured as time series at one or more wells, which are represented as points in the domain. In monitoring groundwater for tracers, the two key quantities of interest are capturing the breakthrough time when the tracer arrives at the well and the shape of the tracer breakthrough curve. Thus, for tracer problems such as this benchmark, the global error may be of less interest than the local error at points as a function of time.

Sixteen prospective observation locations are defined for this benchmark, as shown in Table 6-3. The observation points are 50, 100, 200 and 500 m downstream of the source and at y = 1005, 1055, 1100 and 1200 m. These points were chosen to estimate error directly in the advective path of the plume (y = 1005 m) and at three distances away from the plume center.

Figure 6-19 shows the simulated and analytical tracer plots for the four observation points that are x = 200 m downstream of the source. None of the observation points are guaranteed to be exactly in either mesh, so the closest point to the desired location and the analytical solution is computed at the grid cell center for comparison. The simulation on the hexahedral mesh shows a clear trend of overpredicting the tracer concentration in the line of advective flow at (200,1005) and then underpredicting it with increasing severely with increasing distance from the plume center in the y-direction. A similar trend is observed for the Voronoi mesh, but the under and over-prediction of the plume are much smaller. Throughout the simulations, the error time series in Figure 6-19 for the Voronoi mesh is nearly two orders of magnitude smaller than the hexahedral mesh error at the points (200,1005) and (200,1100). This qualitative analysis indicates that the Voronoi mesh simulation is more accurate in time than the hexahedral mesh simulation.

RMS_{time} error is calculated based on simulation output every 0.1 year from tracer breakthrough at the observation point until the end of the simulation at 10 y. As can be seen in Table 6-3 the RMS_{time} error is smaller on the Voronoi mesh simulation at every observation point except for the point (500,1055). At five of the observation points with highest concentration: (50,1005), (100,1005), (200,1005), (50,1055), (100,1055), the RMS_{time} error on the Voronoi mesh is an order of magnitude smaller than the hexahedral mesh simulation. Furthermore, the RMS_{time} error on the Voronoi simulation is relatively consistent at all the locations in the mesh, while the error in the hexahedral simulation is highest at points with higher concentration. This result indicates that the Voronoi mesh simulation has superior accuracy using the RMS_{time} error metric.

Table 6-3 also shows the difference between the simulated and analytical tracer breakthrough time for both simulations. Breakthrough time is an indication of simulation quality with practical significance in the field, as collecting monitoring well data is expensive and time-consuming, but it is critically important to capture breakthrough time of tracers as they are a primary measurement of travel time of fluids in the reservoir. Breakthrough time is defined as when the tracer concentration exceeds 1×10^{-6} [kg/m^3] or 1 ppb. As can be seen in Table 6-3, on the hexahedral mesh simulation the error in simulated breakthrough time has a general trend of increasing with distance from the source in x and y and reaches a maximum of predicting breakthrough 1.7 years later than the analytical solution at the point (200,1200). Conversely, the error in the simulated breakthrough time on the Voronoi mesh is never greater than 0.3 years and is

relatively consistent across the simulation domain. This result indicates that the Voronoi mesh simulation also has superior accuracy using the breakthrough time error metric. Thus, the additional computation time (2.9 min instead of 0.9 min) to simulate on the Voronoi mesh is necessary to get an accurate solution according to the point-wise error metrics.

Table 6-3. Error in Batu (2006) simulated result at 16 observation points. RMS error is calculated using Eqn. 6.4. Errors are calculated from breakthrough time when tracer concentration exceeds 1×10^{-6} [kg/m^3] until the end of the simulation at 10 y. Error is only calculated for points with maximum concentration above 1×10^{-5} [kg/m^3]. Breakthrough time is based on output steps 0.1 y apart, so that is the resolution of this estimate. Positive change in breakthrough time means the analytical solution predicted later breakthrough than the simulation.

Observation point	Hexahedral mesh simulation results			Voronoi mesh simulation results		
	Maximum Tracer [kg/m^3]	RMS error [kg/m^3]	Breakthrough (t_{an}- t_{sim})	Maximum Tracer [kg/m^3]	RMS error [kg/m^3]	Breakthrough (t_{an}- t_{sim})
(50,1005)	2.49×10^{-1}	6.21×10^{-2}	0	1.82×10^{-1}	9.11×10^{-3}	0
(100,1005)	1.55×10^{-1}	3.55×10^{-2}	0.1	1.18×10^{-1}	6.85×10^{-3}	0.1
(200,1005)	1.04×10^{-1}	2.05×10^{-2}	0.4	8.06×10^{-2}	4.96×10^{-3}	0.2
(500,1005)	4.48×10^{-2}	5.34×10^{-3}	0.7	3.38×10^{-2}	2.37×10^{-3}	-0.1
(50,1055)	2.45×10^{-2}	1.03×10^{-2}	0.1	1.87×10^{-2}	9.90×10^{-4}	0.1
(100,1055)	4.31×10^{-2}	1.15×10^{-2}	0.2	4.06×10^{-2}	1.35×10^{-3}	0.2
(200,1055)	4.89×10^{-2}	3.21×10^{-3}	0.4	5.06×10^{-2}	2.51×10^{-3}	0.3
(500,1055)	3.25×10^{-2}	1.89×10^{-3}	0.7	2.80×10^{-2}	1.94×10^{-3}	-0.1
(50,1100)	2.23×10^{-3}	1.37×10^{-3}	0	1.90×10^{-3}	5.03×10^{-4}	0.2
(100,1100)	7.01×10^{-3}	3.90×10^{-3}	0	6.47×10^{-3}	9.28×10^{-4}	0.3
(200,1100)	1.62×10^{-2}	6.63×10^{-3}	0.2	1.43×10^{-2}	1.02×10^{-3}	0.2
(500,1100)	1.73×10^{-2}	2.04×10^{-3}	0.4	1.65×10^{-2}	1.39×10^{-3}	-0.1
(50,1200)	1.74×10^{-5}	-	-	2.04×10^{-5}	-	-
(100,1200)	7.84×10^{-5}	-	-	7.64×10^{-5}	-	-
(200,1200)	4.11×10^{-4}	2.32×10^{-4}	-1.7	4.20×10^{-4}	1.24×10^{-4}	0.1
(500,1200)	1.80×10^{-3}	6.72×10^{-4}	-0.7	2.03×10^{-3}	1.80×10^{-4}	-0.1
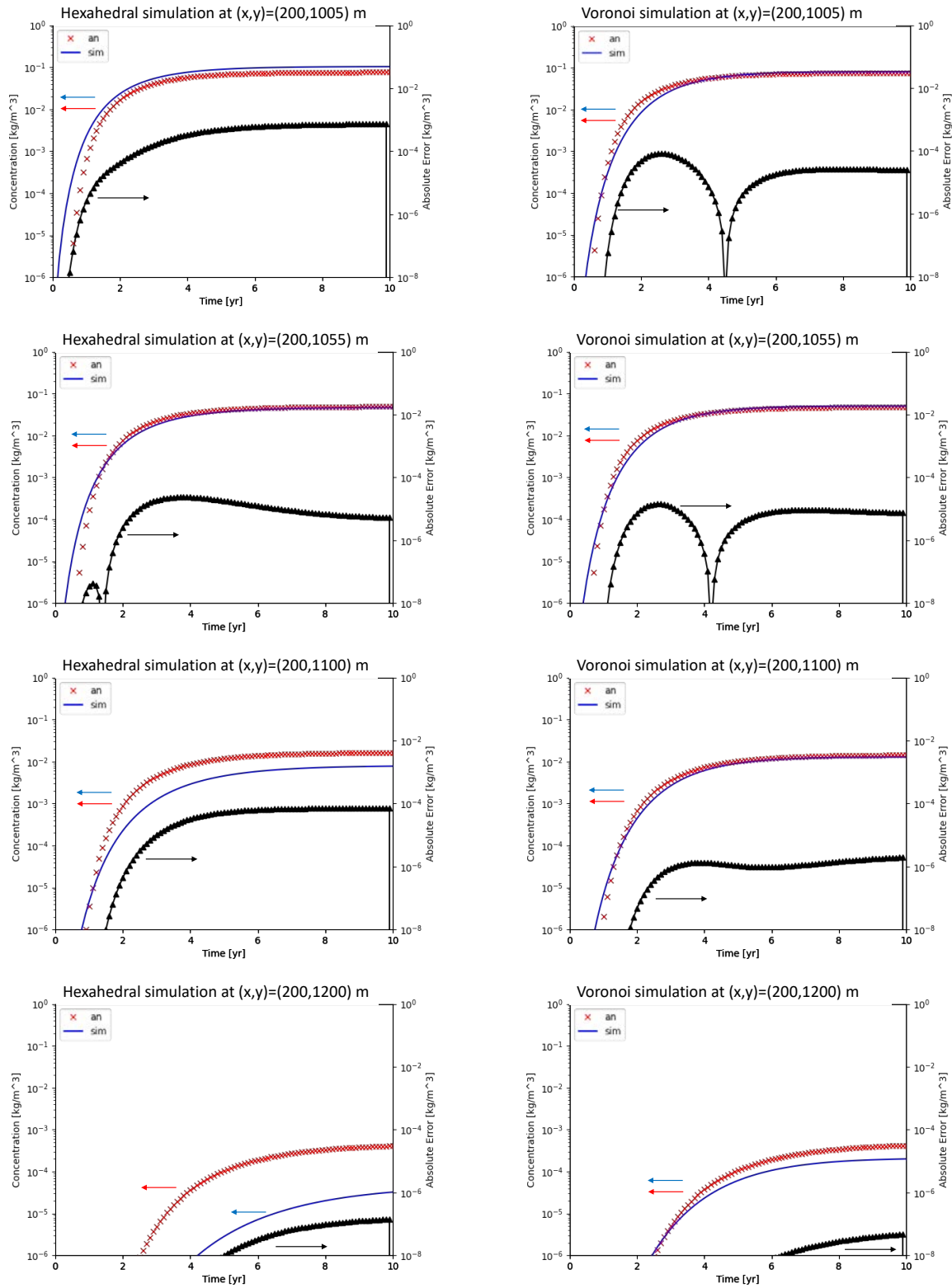
Figure 6-19.   Simulated and analytical tracer concentration and pointwise absolute error at the four observation points 200 m downstream of the tracer source. Left: Simulations on the hexahedral mesh. Right: Simulations on the Voronoi mesh.

6.2.5 Fingering in gas injection

In this section PFLOTRAN simulations on hexahedral and Voronoi meshes are run on experiments of unstable gas flow in a 2D micromodel from Wang et al. (2013). Fingering phenomena occur in unstable displacements such as gas injection for geological storage or hydrogen gas leakage from a nuclear waste canister in the subsurface. Gas fingering is notoriously difficult to simulate using conventional (finite difference, finite volume, finite element) reservoir simulators. Structured meshes have a smoothing effect on gas fingers, so that the extent of the gas plume is typically under-predicted and its thickness may be overpredicted.

It has been observed in previous PFLOTRAN simulations of CO_2 injection on VoroCrust Voronoi meshes have gas fingering patterns that 'look like' the type of fingers that are expected for this unstable displacement (LaForce et al., 2023c; LaForce et al., 2021). Simulations in LaForce et al. (2023c) were run on three realizations of the mesh and the gas fingers were demonstrably triggered by the random nature of the mesh. However, the simulations in that work were too complex to do a rigorous analysis of whether the gas fingers were physically meaningful or if they were numerical artefacts of the unstructured mesh.

6.2.5.1 Experimental study

The experimental conditions in Wang et al. (2013) were chosen so that the displacements span the crossover from capillary to viscous fingering of CO_2 into the liquid phase. Wang et al. (2013) used a 2D micromodel with x and y dimension 1.2 × 1.2 cm and depth of 35 µm (0.0035 cm). The discontinuous rate (constant rate) experimental results of Wang et al. (2013) are reproduced in Figure 6-20. All experiments were run until quasi-steady state and the final CO_2 saturation in the micromodel was calculated. They observed three distinct flow regimes:

- At low injection rates (logCa < −6.61), the displacements are characteristic of capillary fingering. CO_2 enters the domain as a uniform front with clusters of entrapped water. At later time the CO_2 flowpath transitioned into one gradually narrowing finger leading to the outlet.

- At high injection rates (logCa > −5.21), displacements are characteristic of viscous fingering. The CO_2 entered the pore network as narrow fingers distributed over the entire width of the domain and from inlet to outlet.

- At the two intermediate injection rates (logCa = −5.91, −5.21), crossover from capillary to viscous fingering was observed. There was a large decrease in the quasi-steady state CO_2 saturation for these two experiments.

Some of the experimental conditions of Wang et al. (2013) are reproduced in Table 6-4, while the injection rates and capillary number of eight of the displacements are in Table 6-5.

Table 6-4.   Experimental conditions from Wang et al. (2013).

Pressure [MPa]	9.0
Temperature [ºC]	41.0
CO_2 viscosity [mPa·s]	0.036
Water viscosity [mPa·s]	0.64
Log M	-1.25

Table 6-5.   **The eight discontinuous-rate experiments from Wang et al. (2013).**

Experiment number	Q (μL/h)	v (m/d)	Log Ca [-]	PVI to quasi-steadystate [-]
1	10	0.57	-7.61	1
2	50	2.83	-6.91	4
3	100	5.67	-6.61	6
4	500	28.33	-5.91	13
5	1000	56.67	-5.61	31
6	2500	141.67	-5.21	97
7	5000	283.35	-4.91	120
8	7500	425.03	-4.73	193
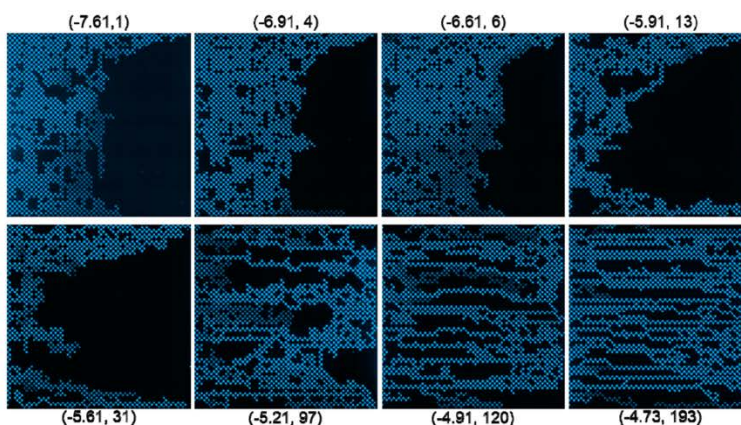
Figure 6-20.   **Gas fingering in the constant-rate injection experiments of Wang et al. (2013, Figure 1)**

6.2.5.2   *Numerical model*

As in the previous example, it was necessary to increase the vertical thickness of the VoroCrust simulation model to have a tractable simulation mesh size. The simulation domain is $1.2 \times 1.2 \times 0.035$ cm and the Voronoi mesh has 37,289 cells.

The structured mesh model is of a similar size, at $100 \times 100 \times 4$ grid cells for a total of 40,000 cells. Each grid cell has dimensions $0.012 \times 0.012 \times 0.00875$ cm, so mesh is nearly isotropic. Though the experiment was quasi-2D, the simulations have gravity included, as gas override is observed when gravity is included in the simulation on both meshes. The mesh is four grid cells tall (instead of the usual three) to allow additional cells to capture gravity override more accurately.

6.2.5.3   *Simulation results*

Three of the experiments are simulated on Voronoi and hexahedral meshes, as shown in Figure 6-21. The structured mesh simulation is unable to capture the gas fingering phenomena in any of the experiments, as anticipated. In this case the only way to achieve even qualitative consistency with the experimental results is to utilize the unstructured Voronoi mesh.

The Voronoi mesh simulations show fingering effects, but the transition from viscous to capillary fingering appears to take place at a lower rate, with the fingers in the simulation of the 0.57 m/d experiment appearing (left) most like the experimental data from 5.67 m/d (middle) and the simulation of 5.67 m/d (middle) appearing most like the 425 m/d experiment (right). This could be due to the impact of relative permeability parameters chosen, or discrepancies in gas phase density and viscosity between the simulation and experiment, or the increased thickness of the simulation model, and is an area of continuing research.
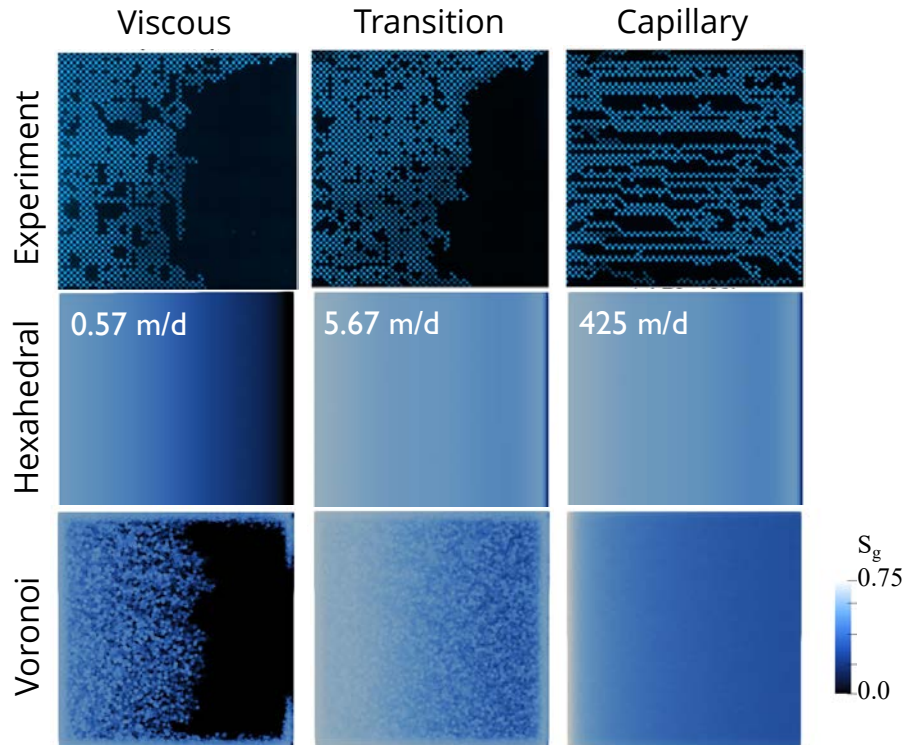
Figure 6-21. **Top: Gas fingering in the constant-rate injection experiments of Wang et al. (2013) at quasi-steady state, shown in Table 6-5. Middle: simulation with same rates on a hexahedral mesh. Bottom: simulation on a Voronoi mesh.**

6.2.5.4 Future work

There remain open questions about the ability to simulate gas fingering on unstructured Voronoi meshes in a quantitatively accurate way. Wang et al. (2013) plot the average gas saturation in the model as a function of capillary number at quasi-steady state, and a comparison of the simulated average gas saturations against these experimental results would quantitatively evaluate the quality of the simulated results against the experiments.

In addition to investigating the obvious discrepancies in gas phase density, the unknown relative permeability of the fluids in the micromodel, and the possible impacts of having increased the thickness of the simulation domain for computational convenience, there is one additional complexity that could potentially impact the ability to simulate gas fingering on VoroCrust meshes. Additional simulations on a finer mesh (not shown) indicate that the simulated transition between gas fingering (observed in the v = 0.57 and 5.67 m/d cases) and a relatively uniform gas invasion front (observed in the v = 425 m/d case) takes place at a different flowrate for a finer mesh. This indicates that it may be necessary to match the Voronoi average grid cell size to the anticipated average finger width to quantitatively match the gas fingering phenomena.

It is also an area of future work to see if small heterogeneities can be introduced into the structured model to trigger fingering. Some possible heterogeneities that could be investigated are small variations in the initial saturation, gas injection boundary condition, or permeability/porosity of the porous media.

6.2.6   Conclusions and Future Work

This series of benchmark examples has demonstrated that there are simulations where it is imperative to use unstructured meshes to obtain an accurate solution. However, in many cases, there is no one-size-fits-all solution. The most suitable mesh for a given simulation depends not only on the simulation domain but also three considerations:

- If the mesh must be distorted to capture geometric features of the domain: The flexed hexahedral mesh was fine for the isotropic five-spot example but had high error for the anisotropic five-spot example.

- The quantity of interest (e.g., global vs local error): The global error between the two meshes on the tracer benchmark Batu (2006) was similar, but the error as a function of time some specific points of interest and calculated tracer breakthrough time were much higher for the hexahedral than the Voronoi mesh.

- The physics and complexity of the simulation: It was not possible to trigger unstable gas fingering from the Wang et al. (2013) using a structured hexahedral mesh, while the Voronoi mesh triggered fingers.

Future work could include quantitatively matching the final gas saturations presented in the Wang et al. (2013) experimental results and conducting additional simulation studies. Of particular interest is the Elder problem, in which the simulated solution is known to converge to different solutions for different levels of resolution in the mesh.

This page left intentionally blank.

7.   Summary and Conclusions

This report describes specific activities in FY23 associated with the Geologic Disposal Safety Assessment (GDSA) Repository Systems Analysis (RSA) work package within the Spent Fuel and Waste Science and Technology (SFWST) Campaign. The overall objective of the GDSA RSA work package is to develop generic deep geologic repository concepts and system performance assessment (PA) models in several host-rock environments, and to simulate and analyze these generic repository concepts and models using the GDSA Framework toolkit, and other tools as needed.

The GDSA RSA and FRAMEWORK work packages have continued to lead Task F1-crystalline and Task F2-salt of the DECOVALEX 2023 project on behalf of the SFWST campaign. Development of the task specification is complete, and the final version, revision 10, has been made publicly available. The Sandia National Laboratory (SNL) simulations on both tasks are largely complete and a comparison of the SNL modeling results with partner teams is underway. We have applied to the DECOVALEX-2027 sponsors for a task continuation for the next four years. If successful, the next stage will focus on adding complexity to the two PA models, sensitivity analysis (SA), and uncertainty quantification (UQ).

In FY24 the GDSA RSA and Sensitivity Analysis and Uncertainty Quantification (SA/UQ) teams decided to focus on updating the shale/argillite PA model. The 2019 version of the shale PA model was updated and implemented in the Next Generation Workflow (NGW) of Dakota. The main modifications were to consider more realistic and increased thermal output scenarios and changing the model to include an open northern boundary. Two studies were conducted on the updated model. The first was a deterministic study on the distribution of heat in the repository that included waste packages with thermal output representative of in-inventory dual-purpose canisters (DPCs). This study demonstrated that configuration of the waste packages in the repository impacted fluid flow in the nearfield and had a small, but perceptible, impact on transport of radioactive transport in the far-field. The second shale PA study was to develop and run a set of 50 stochastically-generated realizations in support of the SA/UQ work package.

Two parallel projects were conducted on unsaturated alluvium (UZ) modelling this year. The first was a collaborative study with Los Alamos National Laboratory (LANL), which focused on utilizing their highly heterogeneous geological models in PFLOTRAN simulations. The models were successfully converted between the simulators, and exemplar simulations utilizing the PFLOTRAN waste form module to model more realistic release of radionuclides were conducted. The second UZ task was continuing to work on adding tracer transport to this numerically challenging problem. Simulations with PFLOTRAN's new nuclear waste transport (NWT) transport mode were able to complete but showed unphysical oscillations during the resaturation process. Several improvements to the NWT mode were developed by the GDSA PFLOTRAN Development work package, but the problem was not fully resolved.

A simplified shale PA model with VoroCrust meshes and uncertainty in the locations of geological horizons was continued this year. The workflow was implemented in the NGW module of Dakota. A nested sampling approach was implemented wherein three geological models were chosen and simulations of 30 realizations of sampled flow parameters were run on each. Though the representation of the repository is still significantly simplified from the full shale PA model, this study demonstrates an automated method for including geological uncertainty in PA simulation modelling and the importance of including geological uncertainty in PA simulations.

Finally, VoroCrust simulation and development continued in FY24. The open-source version of VoroCrust was improved and developments were made to make it more accessible to users. Software was added to the website to track downloads and the IP addresses of people downloading the software. Work has also been done towards developing the capability to individually mesh small features, such as waste packages, that will enable utilization of VoroCrust in full-complexity PA simulations. A series of

benchmark problems were run on VoroCrust meshes, to establish the accuracy and computation time of simulations on these meshes in comparison with the hexahedral meshes we have traditionally used in GDSA simulations. The results of this study were that PFLOTRAN simulations on VoroCrust simulations are always at least as accurate as hexahedral meshes, and that the additional computation time required for Voronoi mesh simulations is highly problem dependent.

7.1   Future Work

Future work in FY24 will continue to focus on developing the technical bases for representing generic repository concepts in GDSA Framework simulations for deep geologic disposal in any of four possible host-rock environments: argillite, crystalline, bedded salt, and unsaturated zone formations. The following tasks are of particular interest:

- Write the final DECOVALEX 2023 reports and papers for publication in collaboration with our international partner teams. If we are approved by the DECOVLAEX sponsors to continue the task in DECOVALEX-2027, then we will write a new task specification and continue to lead the task for a further four years.

- Work closely with the SA/UQ work package to continue to develop the shale PA case. This will entail sampling waste package heat, and possibly radionuclide inventory, to allow for random distribution of representative waste packages in the repository. We will also continue to look at additional sampled flow parameters and quantities of interest near the repository.

- Continue working on incorporating geostatistical heterogeneity into the unsaturated alluvium model and working with the GDSA PFLOTRAN Development work package on PA-scale simulations in the new NWT transport mode.

- Conducting uncertainty analysis on the simplified VoroCrust shale PA model with uncertainty in geological structure in collaboration with the SA/UQ work package. This will involve improving realism of the simulation model and quantitative uncertainty analysis on the simulation results.

- Continued development of VoroCrust capability to mesh small features such as waste packages, and utilization of it in models of increasing complexity to work towards a full PA model mesh.

8.   References

Abdelkader, A., Bajaj, C. L., Ebeida, M. S., Mahmoud, A. H., Mitchell, S. A., Owens, J. D., & Rushdi, A. (2020). VoroCrust. *ACM Transactions on Graphics*, *39*(3), 1–16. https://doi.org/10.1145/3337680

Anttila, M. (2005). *Radioactive Characteristics of the Spent Fuel of the Finnish Nuclear Power Plants*. Working Report 2005-71. Posiva Oy, Olkiluoto, Finland.

Ayachit, U. (2015). The ParaView Guide: A Parallel Visualization Application. Kitware, ISBN 978-1930934306

Aziz, K. and Settari, A. (1979). *Petroleum Reservoir Simulation*. Applied Science Publishers, 476 p.

Batu, V. (2006). *Applied Flow and Solute Transport Modelling in Aquifers*. CRC Taylor and Francis.

Bear, J. (1988). *Dynamics of Fluid in Porous Media*. New York 1972.

Bernier, F., Lemy, F., De Cannière, P., & Detilleux, V. (2017). Implications of safety requirements for the treatment of THMC processes in geological disposal systems for radioactive waste. *Journal of Rock Mechanics and Geotechnical Engineering*, *9*(3), 428–434. https://doi.org/10.1016/j.jrmge.2017.04.001

Bertrams, N., Bollingerfehr, W., Eickemeier, R., Fahland, S. Flügge, J., Frenzel, B., Hammer, J., Kindlein, J. Liu, W., Maßmann, J., Mayer, K.-M., Mönig, J., Mrugalla, S., Müller-Hoeppe, N., Reinhold, K., Rübel, A., Schubarth-Engel- schall, N., Simo, E., Thiedau, J., Thiemeyer, T., Weber, J.R., Wolf, J. (2020a). *Grundlagen zur Bewertung eines Endlagersystems in flach lagernden Salzformationen (S1) - Ergebnisse aus dem Vorhaben RESUS*. BGE TEC 2020a.

Bertrams, N., Bollingerfehr, W., Eickemeier, R., Fahland, S. Flügge, J., Frenzel, B., Hammer, J., Kindlein, J. Liu, W., Maßmann, J., Mayer, K.-M., Mönig, J., Mrugalla, S., Müller-Hoeppe, N., Reinhold, K., Rübel, A., Schubarth-Engel- schall, N., Simo, E., Thiedau, J., Thiemeyer, T., Weber, J.R., Wolf, J. (2020b). *Grundlagen zur Bewertung eines Endlagersystems in steil lagernden Salzformationen (S2) - Ergebnisse aus dem Vorhaben RESUS*. BGE TEC 2020b.

Beuth, T., Bracke, G., Buhmann, D., Dresbach, C., Keller, S., Krone, J., Lommerzheim, A., Mönig, A., Mrugalla, S., Rübel, A., and Wolf, J. (2012). *Szenarienentwicklunng: Methodic und Anwendung. Bericht zum Arbeitspaket 8. Vorläufige Sicherheitsanalyse für den Standort Gorleben*, Gesellschaft für Anlagen und Reaktorsicherheit (GRS) mbH, GRS-284, Köln, ISBN 978-3-939355-60-1.

Blum, P., Mackay, R., Riley, M. S., & Knight, J. (2005). Performance assessment of a nuclear waste repository: Upscaling coupled hydro-mechanical properties for far-field transport analysis. *International Journal of Rock Mechanics and Mining Sciences*, *42*(5–6), 781–792. https://doi.org/10.1016/j.ijrmms.2005.03.015

Bollingerfehr, W., Filbert, W., Pöhler, M., Tholen, M., and Wehrmann, J. (2008). *Konzeptionelle Endlagerplanung und Zusammen- stellung des endzulagernden Inventars (Design planning of a final repository and summary of the inventory to be stored) – Project ISIBEL*, Peine, April 2008.

Bollingerfehr, W., Buhmann, D. and Doerr, S. (2017). *Evaluation of methods and tools to develop safety concepts and to demonstrate safety for an HLW repository in salt*. Final Report (No. TEC-03-2017-AB). DBE Technology GmbH.

Bollingerfehr, W., Bertrams, N., Buhmann, D., Eickemeier, R., Fahland, S., Filbert, W., Hammer, J., Kindlein, J., Knauth, M., and Wenting, L. (2018). *Concept developments for a generic repository for heat-generating waste in bedded salt formations in Germany*. Synthesis Report (No. BGE TEC 2018-13). BGE TECHNOLOGY GmbH.

Carter, J., Luptak, A. J., Gastelum, J., Stockman, C. T., and Miller, A. (2013). *Fuel Cycle Potential Waste Inventory for Disposition*. FCR&D-USED-2010-000031 Rev 6. Savannah River National Laboratory, Aiken, SC.

Chang, K., LaForce, T., & Price, L. L. (2022). Hydro-thermal impacts on near-field flow and transport in a shale-hosted nuclear waste repository. *Tunnelling and Underground Space Technology*, *130*, 104765. https://doi.org/10.1016/j.tust.2022.104765

Chang, K., Nole, M., & Stein, E. (2021). Reduced-order modeling of near-field THMC coupled processes for nuclear waste repositories in shale. *Computers and Geotechnics*, *138*, 104326. https://doi.org/10.1016/j.compgeo.2021.104326

Cho, D.K., N.Y. Ko, Y.K. Koh, J.S. Kwon, I.Y. Kim, J.W. Kim, J.H. Ryu, K.W. Park, C.K. Park, T.J. Park, M.H. Baik, S. Yoon, M. Lee, S.Y. Lee, J.K. Lee, J.O. Lee, J. Lee, C. Lee, S. Jung, J. Jeong, and S.H Ji. (2016). *A Safety Case of the Conceptual Disposal System for Pyro-processing High-Level Waste Based on the KURT Site (AKRS-16): VI Models and Data, KAERI/TR-6732/2016.*

Coon, E.T., Svyatsky, D., Jan, A., Kikinzon, E., Berndt, M., Atchley, A., Harp, D., Manzini, G., Shelef, E., Lipnikov, K., Garimella, R., Xu, C., Moulton, D., Karra, S., Painter, S., Jafarov, E., & Molins, S. (2019). *Advanced Terrestrial Simulator.* [Computer software]. https://github.com/amanzi/ats. https://doi.org/10.11578/dc.20190911.1.

Debusschere, B., Seidl, D. T., Berg, T. M., Chang, K. W., Leone, R. C., Swiler, L. P., & Mariner, P. E. (2023). Machine learning surrogates of a fuel matrix degradation process model for performance assessment of a nuclear waste repository. *Nuclear Technology*, 1–24. https://doi.org/10.1080/00295450.2023.2197666

DOE (U.S. Department of Energy). (2012). *Used Fuel Disposition Campaign Disposal Research and Development Roadmap*. FCR&D-USED-2011-000065, REV 1, U.S. DOE Office of Nuclear Energy, Used Fuel Disposition, Washington, D.C.

Freeze, G., Gardner, P., Vaughn, P., Sevougian, S.D., Mariner, P., Mousseau, V. and Hammond, G. (2013). *Enhancements to Generic Disposal System Modeling Capabilities*. FCRD-UFD-2014-000062. SAND2013-10532P. Sandia National Laboratories, Albuquerque, NM.

GIRT (Global Implicit Reactive Transport) — PFLOTRAN documentation. (2023.). Retrieved 7/26/23. https://www.pflotran.org/documentation/user_guide/cards/simulation/subsurface_transport_modes/global_implicit_reactive_transport_card.html#global-implicit-reactive-transport-card

Gonzales, S. and K.S. Johnson, (1985). *Shales and Other Argillaceous Strata in the United States*. ORNL/Sub/84-64794/1. Oak Ridge National Laboratory, Oak Ridge, Tennessee.

Gross, M., Bussod, G., Gable, C., Kelley, R., Lavadie-Bulnes, A., Milazzo, D., Miller, E., Miller, T., Roback, R., Stauffer, P.H., and Swanson, E. (2019). *Progress report on the development of a geologic framework model capability to support GDSA*. Technical Report LA-UR-19-27943, Los Alamos National Lab., Los Alamos, NM.

Gross, M., Guiltinan, E, Milazzo, D., Miller, T., Swanson, E., Miller, E., Lavadie-Bulnes, A., and Stauffer, P.H. (2021). *Advances in 3D Geologic Modeling of Alluvial Basins with a Focus on Facies and Property Modeling*. Technical Report LA-UR-21-29521, Los Alamos National Lab., Los Alamos, NM.

Gross, M., Guiltinan, E, Milazzo, D., Miller, T., Swanson, E., Miller, E., Lavadie-Bulnes, A., and Stauffer, P.H. (2022). *Incorporating Heterogeneity into 3D Geologic Models for the Alluvial Basin Reference Case*. Technical Report LA-UR-22-26137, Los Alamos National Laboratories. Los Alamos, NM.

Gross, M., Alberts, E., Miller, T.A., Guiltinan, E., Swager, K., LaForce, T., and Stauffer, P. (2023). *Prototype Workflow for 3D Geologic Modeling and Flow and Transport Simulations of a Generic Alluvial Basin for use in GDSA Repository Systems Analysis*. Technical Report LA-UR-23-xxxxx. Los Alamos National Laboratories. Los Alamos, NM.

Hammond, G. E., Lichtner, P. C., & Mills, R. T. (2014). Evaluating the performance of parallel subsurface simulators: An illustrative example with PFLOTRAN. *Water Resources Research*, *50*(1), 208–228. https://doi.org/10.1002/2012wr013483

Hyman, J. D., Karra, S., Makedonska, N., Gable, C. W., Painter, S. L., and Viswanathan, H. S. (2015). dfnWorks: A discrete fracture network framework for modeling subsurface flow and transport. *Computers & Geosciences*, *84*, 10–19. https://doi.org/10.1016/j.cageo.2015.08.001

Jones, P., Chang, K.W., Hardin, E. (2021). *DPC Disposal Thermal Scoping Analysis*. SAND2021-7515R, Sandia National Laboratories, Albuquerque, NM, USA.

LaForce, T., Chang, K.W., Perry, F.V., Lowry, T.S., Basurto, E., Jayne, R., Brooks, D., Jordan, S., Stein, E., Leone, R., and Nole, M. (2020). *GDSA Repository Systems Analysis Investigations in FY2020*. M2SF-20SN010304052, SAND2020-12028 R. Sandia National Laboratories, Albuquerque, NM.

LaForce, T., Basurto, E., Chang, K.W., Jayne, R., Leone, R., Nole, M., Perry, F.V., and Stein, E., (2021). *GDSA Repository Systems Analysis Investigations in FY2021*. SAND2021-11691 R. Sandia National Laboratories, Albuquerque, NM

LaForce, T., Basurto, E., Chang, K.W., Ebeida, M., Eymold, W., Faucett. C., Jayne, R., Kucinski, N., Leone, R., Mariner, P., and Perry, F.V. (2022a). *GDSA Repository Systems Analysis Investigations in FY2022*. SAND2022-12771 R. Sandia National Laboratories, Albuquerque, NM

LaForce, T., Jayne, R., Leone, R., Marine, P., Stein, E., Nguyen, S., and Frank, T. (2022b). D*ECOVALEX-2023 Task F Specification Revision 9.* SAND2022-10439R. Sandia National Laboratories, Albuquerque, NM.

LaForce, T., Jayne, R.S., Leone, R., Marine, P., Stein, E., Nguyen, S., and Frank, T. (2023a). D*ECOVALEX-2023 Task F Specification Revision 10.* SAND2023-04005R. Sandia National Laboratories, Albuquerque, NM.

LaForce, T., Gross, M., Miller, T.A., Guiltinan, E., Milazzo, D., Stauffer, P.H., Swanson, E., Alberts, E., Bourret, S., Hyman, J., and Swager, K. (2023b). *Unsaturated Alluvium Disposal Modelling with Improved Geological Realism*. SAND2023-XXXX. Sandia National Laboratories, Albuquerque, NM.

LaForce, T., Ebeida, M. S., Jordan, S., Miller, T. A., Stauffer, P. H., Park, H., Leone, R., & Hammond, G. E. (2023c). Voronoi meshing to accurately capture geological structure in subsurface simulations. *Mathematical Geosciences*, *55*(2), 129–161. https://doi.org/10.1007/s11004-022-10025-x

Li, Y., & Gregory, S. M. (1974). Diffusion of ions in sea water and in deep-sea sediments. *Geochimica Et Cosmochimica Acta*, *38*(5), 703–714. https://doi.org/10.1016/0016-7037(74)90145-8

Lichtner, P.C., & Hammond, G.E. (2012). Quick Reference Guide: PFLOTRAN 2.0: Multiphase-Multicomponent-Multiscale Massively Parallel Reactive Transport Code. LA-CC-09-047, Los Alamos National Laboratory, Los Alamos, NM, USA.

Lichtner, P. C., Hammond, G. E., Lu C., Karra, S., Bisht, G., Andre, B., Mills, R. T., Kumar, J., Frederick, J. M. (2020) PFLOTRAN Web page. http://www.pflotran.org

Los Alamos National Laboratory (LANL). (2017). Los Alamos grid toolbox, LaGriT. http://lagrit.lanl.gov.

Los Alamos National Laboratory (LANL). (2018). *Finite element heat and mass transfer code, FEHM*. https://fehm.lanl.gov/

Los Alamos National Laboratory (LANL). (2021). Los Alamos Grid Toolbox (LaGriT). https://lagrit.lanl.gov/

Luo, S., Ku, T., Roback, R., Murrell, M. T., and McLing, T. (2000). In-situ radionuclide transport and preferential groundwater flows at INEEL (Idaho): decay-series disequilibrium studies. *Geochimica et Cosmochimica Acta*, *64*(5), 867–881. https://doi.org/10.1016/s0016-7037(99)00373-7

Mariner, P. E., Gardner, W. P., Hammond, G. E., Sevougian, S. D. and Stein, E. (2015). *Application of Generic Disposal System Models*. SAND2015-10037R. FCRD-UFD-2015-000126. Sandia National Laboratories, Albuquerque, NM.

Mariner, P. E., Stein, E., Frederick, J. M., Sevougian, S. D., Hammond, G. E., and Fascitelli, D. G. (2016). *Advances in Geologic Disposal System Modeling and Application to Crystalline Rock*. FCRDUFD-2016-000440. SAND2016-96107R. Sandia National Laboratories, Albuquerque, NM.

Mariner, P. E., Stein, E., Frederick, J. M., Sevougian, S. D., and Hammond, G. E. (2017). *Advances in Geologic Disposal System Modeling and Shale Reference Cases*. SFWD-SFWST-2017-000044 / SAND2017-10304R. Sandia National Laboratories, Albuquerque, NM.

Mariner, P. E., Stein, E., Sevougian, S. D., Cunningham, L. J., Frederick, J. M., Hammond, G. E., Lowry, T. S., Jordan, S., and Basurto, E. (2018). *Advances in Geologic Disposal Safety Assessment and an Unsaturated Alluvium Reference Case*. SFWD-SFWST-2018-000509. SAND2018-11858R. Sandia National Laboratories, Albuquerque, NM.

Mariner, P. E., Connolly, L. A., Cunningham, L. J., Debusschere, B. J., Dobson, D. C., Frederick, J. M., Hammond, G. E., Jordan, S. H., LaForce, T., Nole, M. A., Park, H. D., Perry, F. V., Rogers, R. D., Seidl, D. T., Sevougian, S. D., Stein, E., Swift, P. N., Swiler, L. P., Vo, J., and Wallace, M. G. (2019). *Progress in Deep Geologic Safety Assessment in the U.S. since 2010*. M2SF-19SN010304041, U.S. Department of Energy, Spent Fuel and Waste Science and Technology Campaign, Office of Spent Fuel and Waste Disposition, Washington, DC.

Mariner, P.E., Nole, M.A., Basurto, E., Berg, T.M., Chang, K.W., Debusschere, B.J., Eckert, A.C., Ebeida M.S., Gross, M., Hammond, G.E., Harvey, J., Jordan, S.H., Kuhlman K.L., LaForce, T., Leone, R.C., McLendon III, W.C., Mills, M.M., Park, H.D., Perry, F.V., Salazar III, A., Seidl, D.T., Sevougian, S.D., Stein, E., and Swiler, L.P. (2020). *Advances in GDSA Framework Development and Process Model Integration*. SAND2020-10787 R. Sandia National Laboratories, Albuquerque, NM.

Mariner, P.E., Berg, T.M., Chang, K.W., Debusschere, B.J., Eckert, A.C., Harvey, J., LaForce, T., Leone, R.C., Mills, M.M., Nole, M., Park, H.D., Perry, F.V., Seidl, D.T., Swiler, L.P. (2021). *GDSA Framework Development and Process Model Integration FY2021*. SAND2021-12626R, Sandia National Laboratories, Albuquerque, NM.

Mariner, P.E., Debusschere, B.J., Fukuyama, D.E., Harvey, J.A., LaForce, T.C., Leone, R.C., Perry, F.V., Swiler, L.P., Taconi, A.M. (2022), *GDSA Framework Development and Process Model Integration FY2022*. SAND2022-14304 R

Mercer-Smith, J. A. (2020). *Amanzi–ATS: Modeling Environmental Systems across Scales*. United States. https://doi.org/10.2172/1657092

Millington, R. J. (1959). Gas diffusion in porous media. *Science*, *130*(3367), 100–102. https://doi.org/10.1126/science.130.3367.100-a

Nasir, O., Fall, M., & Evgin, E. (2014). A simulator for modeling of porosity and permeability changes in near field sedimentary host rocks for nuclear waste under climate change influences. *Tunnelling and Underground Space Technology*, *42*, 122–135. https://doi.org/10.1016/j.tust.2014.02.010

Nole, M., Beskardes, G.D., Fukuyama, D., Leone, R.C., Park, H.D., Paul, M., Salazar, A., Hammond, G.E., and Lichtner, P.C. (2023). Recent Advancements in PFLOTRAN Development for the GDSA Framework. Sandia National Laboratories. M3SF-23SN010304101 SAND2023-XXXXX R.

NWT — PFLOTRAN documentation. (2023). Retrieved 7/26/23. https://www.pflotran.org/documentation/user_guide/cards/simulation/subsurface_transport_modes/nuclear_waste_transport_card.html#nuclear-waste-transport-card

Perry, F.V., Kelley, R.E., Dobson, P.F. and Houseworth, J.E. (2014). *Regional Geology: A GIS Database for Alternative Host Rocks and Potential Siting Guidelines*. LA-UR-14-20368, FCRD-UFD-2014-000068. Los Alamos National Laboratory, Los Alamos, New Mexico.

Perry, F.V. and Kelley, R.E. (2017). *Regional Geologic Evaluations for Disposal of HLW and SNF: The Pierre Shale of the Northern Great Plains*. SFWD-SFWST-2017-000119. U.S. Department of Energy, Spent Fuel and Waste Technology. Los Alamos Unlimited Release LA-UR-17-27829. 31 p.

Rechard, R. P., Goldstein, B., Brush, L.H., Blink, J.A., Sutton, M., and Perry, F.V. (2011). *Basis for Identification of Disposal Option for Research and Development for Spent Nuclear Fuel and High-Level Waste*. FCRD-USED-2011-000071. SAND2011-3781P, Sandia National Laboratories, Albuquerque, New Mexico.

Sasaki, T., & Rutqvist, J. (2021). Estimation of stress and stress-induced permeability change in a geological nuclear waste repository in a thermo-hydrologically coupled simulation. *Computers and Geotechnics*, *129*, 103866. https://doi.org/10.1016/j.compgeo.2020.103866

Sassani, D. Birkholzer, J., Camphouse, R., Freeze, G., Stein, E. (2021). *SFWST Disposal Research R&D 5-Year Plan- FY2021 Update*. SAND2021-12491 R. Sandia National Laboratories, Albuquerque, NM and Lawrence Berkeley National Laboratory.

Sevougian, S. D., Freeze, G. A., Gross, M., Lee, J., Leigh, C. D., Mariner, P. E., MacKinnon, R. J. and Vaughn, P. (2012). *TSPA Model Development and Sensitivity Analysis of Processes Affecting Performance of a Salt Repository for Disposal of Heat-Generating Nuclear Waste*. FCRD-UFD-2012-000320 Rev. 0, U.S. Department of Energy, Office of Used Nuclear Fuel Disposition, Washington, DC.

Sevougian, S. D., Freeze, G. A., Vaughn, P., Mariner, P. E., and Gardner, W.P. (2013). *Update to the Salt R&D Reference Case*. FCRD-UFD-2013-000368, SAND2013-8255P. Sandia National Laboratories, Albuquerque, NM.

Sevougian, S. D., Freeze, G. A., Gardner, W. P., Hammond, G. E. and Mariner, P. E. (2014). *Performance Assessment Modeling and Sensitivity Analyses of Generic Disposal System Concepts*. FCRD-UFD-2014- 000320, SAND2014-17658. Sandia National Laboratories, Albuquerque, NM.

Sevougian, S. D., Stein, E., Gross, M., Hammond, G. E., Frederick, J. M. and Mariner, P. E. (2016). *Status of Progress Made Toward Safety Analysis and Technical Site Evaluations for DOE Managed HLW and SNF*. SAND2016-11232 R; FCRD-UFD-2016-000082, Rev. 1. Sandia National Laboratories, Albuquerque, NM.

Sevougian, S. D., Stein, E., LaForce, T., Perry, F. V., Lowry, T. S., Cunningham, L. J., Nole, M., Haukwa, C. B., Chang, K. W. and Mariner, P. E. (2019a). *GDSA Repository Systems Analysis Progress Report*. SAND2019-5189R. Sandia National Laboratories, Albuquerque, NM.

Sevougian, S. D., Stein, E., LaForce, T., Perry, F. V., Nole, M., Haukwa, C. B., and Chang, K. W. (2019b). *GDSA Repository Systems Analysis FY19 Update*. SAND2019-11942R. Sandia National Laboratories, Albuquerque, NM.

Shelton, S.M. (1934). Thermal conductivity of some irons and steels over the temperature range 100 to 500 $^{\circ}$C. Bureau of Standards Journal of Research, 12(4/6), 441–450.

Shurr, G.W. (1977). The Pierre Shale, Northern Great Plains: A Potential Isolation Medium for Radioactive Waste. Open-File Report 77-776. *United States Geological Survey*, Reston, Virginia.

Skroch, M., Owen S. J., Staten, M.L., Quadros, R.W., Hanks, B., Clark, B., Hensley, T., Ernst, C., Morris, R., McBride, C., Stimpson, C., Perry, J., Richardson, M., and Merkley, K. (2021). CUBIT geometry and mesh generation toolkit 15.9 user documentation. Technical Report SAND2021-12663 W, Sandia National Laboratories. Albuquerque, NM.

Swiler, L.P., Helton, J.C., Basurto, E., Brooks, D.M., Mariner, P.E., Moore, L.M., Mohanty, S., Sevougian, S.D., and Stein, E.R. (2019). *Status Report on Uncertainty Quantification and Sensitivity Analysis Tools in the Geologic Disposal Safety Assessment (GDSA) Framework*, SAND2019-13835R.

Swiler, L.P., Basurto, E., Brooks, D.M., Eckert, A.C., Leone, R., Mariner, P.E., Portone, T., Smith, M. L., and Stein, E.R. (2021). *Uncertainty and Sensitivity Analysis Methods and Applications in the GDSA Framework (FY2021)*, SAND2021-9903R

Swiler, L.P., Basurto, E., Brooks, D.M., Eckert, A.C., Leone, R., Mariner, P.M., Portone, T., and Smith, M.L. (2022), Uncertainty and Sensitivity Analysis Methods and Applications in the GDSA Framework (FY2022). SAND2022-11220 R.

Swiler, L.P., Basurto, E., Brooks, D.M., Leone, R., Mariner, P.E., and Portone, T. (2023). Uncertainty and Sensitivity Analysis Methods and Applications in the GDSA Framework (FY2023). Technical Report SAND2023-XXXX, Sandia National Laboratories. Albuquerque, NM.

Tsang, C., Bernier, F., & Davies, C. (2005). Geohydromechanical processes in the Excavation Damaged Zone in crystalline rock, rock salt, and indurated and plastic clays—in the context of radioactive waste disposal. *International Journal of Rock Mechanics and Mining Sciences*, *42*(1), 109–125. https://doi.org/10.1016/j.ijrmms.2004.08.003

Van Loon, L. R., & Mibus, J. (2015). A modified version of Archie's law to estimate effective diffusion coefficients of radionuclides in argillaceous rocks and its application in safety analysis studies. *Applied Geochemistry*, *59*, 85–94. https://doi.org/10.1016/j.apgeochem.2015.04.002

Vaughn, P., Sevougian, S. D., Hardin, E. L., Mariner, P. E., and Gross, M. (2013). *Reference Case for Generic Disposal of HLW and SNF in Salt, in Proceedings of the 2013 International High-Level Radioactive Waste Management Conference*. Albuquerque, NM, April 28 – May 2, 2013, American Nuclear Society, La Grange Park, Illinois. (www.ans.org).

Wang, Y., Zhang, C., N, W., Oostrom, M., Wietsma, T., Li, X., & Bonneville, A. (2012). Experimental Study of Crossover from Capillary to Viscous Fingering for Supercritical CO_2–Water Displacement in a Homogeneous Pore Network. *Environmental Science & Technology*, *47*(1), 212–218. https://doi.org/10.1021/es3014503

Yu, L., Weetjens, E., Sillen, X., Vietor, T., Li, X., Delage, P., Labiouse, V., & Charlier, R. (2014). Consequences of the Thermal Transient on the Evolution of the Damaged Zone Around a Repository for Heat-Emitting High-Level Radioactive Waste in a Clay Formation: a Performance Assessment Perspective. *Rock Mechanics and Rock Engineering*, *47*(1), 3–19. https://doi.org/10.1007/s00603-013-0409-4

Zhang, C., Conil, N., & Armand, G. (2017). Thermal effects on clay rocks for deep disposal of high-level radioactive waste. *Journal of Rock Mechanics and Geotechnical Engineering*, *9*(3), 463–478. https://doi.org/10.1016/j.jrmge.2016.08.006

Zheng, L., Rutqvist, J., Xu, H., & Birkholzer, J. (2017). Coupled THMC models for bentonite in an argillite repository for nuclear waste: Illitization and its effect on swelling stress under high temperature. *Engineering Geology*, *230*, 118–129. https://doi.org/10.1016/j.enggeo.2017.10.002